High-resolution Vat-photopolymerization-based 3D Printing of Biocompatible Materials for Organ-on-a-chip Applications and Capillarics

Vahid Karamzadeh

DEPARTMENT OF BIOMEDICAL ENGINEERING

MCGILL UNIVERSITY

MONTREAL,

QC, CANADA

A THESIS SUBMITTED TO McGill UNIVERSITY

IN PARTIAL FULFILLMENT OF THE REQUIREMENTS OF THE DEGREE OF DOCTOR OF PHILOSOPHY

Dedicated to
Mahsa Amini
, other women who suffered in my country,
and to “Women, Life, Freedom”

زن، زندگی، آزادی

Acknowledgment

I am extremely grateful for the opportunity to express my sincere appreciation to the individuals who contributed to the completion of my PhD thesis.

First and foremost, I would like to express my deepest gratitude to my supervisor, Dr. David Juncker, for providing me with continuous guidance, unwavering support, and the confidence to explore new ideas during my doctoral studies. Dr. Juncker's availability and willingness to offer his wisdom and vision have been invaluable in developing my skills in critical thinking, research ethics, experiment design, and scientific writing. I will always be thankful for the last few years that I spent in Juncker lab at McGill. I am also grateful to my Ph.D. advisory committee members, Dr. Christopher Moraes, Dr. Luc Mongeau, and Dr. Louis Collins for their invaluable insights, detailed discussions, and helpful advice provided during our Ph.D. meetings.

I would like to extend my thanks to the Biomedical Engineering department staff, particularly Pina Sorrini, Trang Tan, and Sabrina Teoli, for their consistent availability and helpfulness. I am also grateful to our lab manager, Pammy Lo, for her contributions to the lab's smooth functioning.

I would also like to acknowledge the Fonds de Recherche du Québec – Nature et technologies (FQRNT) Doctoral fellowship, which provided financial support during my PhD.

The PhD was a long, and sometimes difficult, journey. I would not have finished it without the support of a great group of colleagues running alongside me. I was fortunate to be surrounded by brilliant lab mates who made my Ph.D. journey more enjoyable. I want to express my appreciation to Molly Shen for always being willing to offer support and help in developing ideas, as well as to Dr. Ahmad Sohrabi for the outstanding collaboration on one of my PhD projects. I am also grateful

to my labmates Alia Alameri, Dr. Hossein Ravanbakhsh, Dr. Felix Lussier, Dr. Andy NG, Dr. Mohamed Yafia, Dr. Oriol Ymbern Llorens, Bisan Samara, Geunyong Kim, Zijie Jin, Edward Zhang, Yiannis Paschalidis, Yonatan Morocz, and others who made Juncker lab a fun place and created so many wonderful memories, both inside and outside the lab. I am also grateful to the outstanding undergraduate students who worked with me and taught me how to become a better mentor. Special thanks to Weiqi Han, Peter Chimienti, and Celia Zhu.

I want to express my deepest appreciation to my family members, especially my dad, who always believed in me, my sister Mahsa, who has been much more than a sibling to me, my niece Elara for bringing more joy to my life by being born, and my brother-in-law Dr. Nima for his valuable feedback and advice. I am also extremely grateful to my brother Moe for his unwavering support and encouragement throughout my academic journey. I also want to express my heartfelt gratitude to my mom, who has been my true hero and the driving force behind my academic success. I would like to thank my dear friend Sara for her continuous inspiration, motivation, and unwavering support. Her faith in me and encouraging words have helped me to navigate through the most difficult times of my research. I am incredibly grateful for her presence in my life.

Lastly, I would like to say a huge thank you to my friends, both in Montreal and around the world, for their love and support. Your presence and encouragement have been invaluable to me during my academic journey.

Abstract

Vat-photopolymerization (VP)-based 3D printing has emerged as a high-throughput 3D printing method, offering high-resolution fabrication of complex geometries. While biocompatible resins, hydrogels, and elastomers have been successfully developed for VP printing, there remains a lack of suitable biomaterials that can fulfill the necessary requirements for some specific applications. Polyethylene glycol diacrylate (PEGDA) has gained attention as an alternative material to polydimethylsiloxane (PDMS). Multiple groups have developed PEGDA-250 formulations capable of 3D printing microfluidic channels as small as 20 μm^2. However, the current formulations lack certain characteristics necessary for some microfluidic and organ-on-a-chip (OoC) applications. For example, these formulations are hydrophobic or only mildly wettable (>65°), which falls outside the optimal hydrophilicity range for microfluidic capillaric circuits (CCs). Additionally, PEGDA-250 does not provide sufficient cell attachment, and due to its low molecular weight, it has low gas permeability. In addition, PEGDA-250 is a rigid and non-degradable material that may not be suitable for some tissue engineering (TE) applications that require mechanical properties similar to soft tissues.

Citrate-based elastomers have garnered considerable attention due to their biocompatibility, and degradability. One promising citrate-based biomaterial is poly(octamethylene maleate (anhydride) citrate) (POMaC) elastomer, which is a photo-curable elastomer and has been used as a key component of implantable sensors and TE. However, the current fabrication methods for POMaC involve multiple photolithography steps that hinder its use. 3D printing could provide an alternative solution to these limitations.

This dissertation focuses on the development of biocompatible formulations suitable for VP 3D printing of OoC and microfluidic CCs. To address the limitations of current materials, novel inks were developed based on PEGDA-250 and POMaC, both of which demonstrated enhanced properties suitable for various biomedical applications. This dissertation first presents the development of a hydrophilic ink through co-polymerization of PEGDA-250 monomer with hydrophilic crosslinkers. Using the developed ink, digital manufacturing (DM) of monolithic, fully functional, and intrinsically hydrophilic CCs was achieved. 3D printing supports advances in capillary valve design, embedded conduits with circular cross-sections that prevent bubble trapping, as well as interwoven circuit architectures used for immunoassays. Additionally, external paper capillary pumps are replaced with an integrated 3D printed gyroid structure, realizing fully functional, monolithic CCs. Next, a novel biocompatible, nanoporous ink formulation was developed using a non-reactive PEG as porogen to increase the nanoporosity of 3D-pritned parts. 3D-printed nanoporous substrates seeded with endothelial cells lead to fourfold coverage compared to nonporous ones. Finally, we introduced a tumor-on-a-chip model comprising a 3D printed microporous gyroid scaffold for growing stromal cells in 3D around a central opening filled with hydrogel and a cancer cell spheroid.

Finally, an ink for 3D VP 3D printing based on biodegradable, elastic POMaC that matches tissue softness (<1000 kPa) was developed for TE applications. Moreover, it was 3D printed not only using DLP printers (~$15K), but using low-cost LCD 3D printers (~300$) into complex gyroid scaffolds with features as small as 80 μm. To demonstrate biocompatibility, we cultured endothelial cells on the 3D printed scaffolds, and also confirmed biodegradability *in vitro*. The POMaC ink enables assembly-free DM of this material, and with the use of low-cost 3D printers could greatly facilitate the rapid prototyping of devices for OOC and TE.

This dissertation has contributed to the development of novel 3D printable photocurable inks for TE and microfluidic applications. Through the use of VP 3D printing method, this work has achieved improved functionality and tunability in biocompatible inks, paving the way for the development of more functional microfluidic and OoC devices. While progress has been made in addressing the current limitations of formulations for microfluidics and OoC applications, further optimization is still required to achieve sub-hundred micron embedded microfluidic channels using an LCD 3D printer. Future work includes designing inks with a tunable porosity from nano to micro range and using multi-material 3D printing approach, to create more functional heterogeneous objects using developed inks.

Résumé

L'impression 3D par photopolymérisation en cuve (VP) s'est imposée comme une méthode d'impression 3D à haut rendement, offrant une fabrication à haute résolution de géométries complexes. Bien que des résines biocompatibles, des hydrogels et des élastomères aient été développés avec succès pour l'impression par photopolymérisation en cuve, il n'existe toujours pas de biomatériaux appropriés pouvant répondre aux exigences de certaines applications spécifiques. Le diacrylate de polyéthylène glycol (PEGDA) a attiré l'attention en tant que matériau alternatif au polydiméthylsiloxane (PDMS). Plusieurs groupes ont développé des formulations de PEGDA-250 capables d'imprimer en 3D des canaux microfluidiques aussi petits que 20 μm2. Toutefois, les formulations actuelles ne présentent pas certaines caractéristiques nécessaires à certaines applications microfluidiques et d'organes sur puce (OoC). Par exemple, ces formulations sont hydrophobes ou seulement légèrement mouillables (>65°), ce qui est en dehors de la plage d'hydrophilie optimale pour les circuits capillaires microfluidiques (CC). En outre, le PEGDA-250 ne permet pas une fixation suffisante des cellules et, en raison de son faible poids moléculaire, il présente une très faible perméabilité aux gaz. En outre, le PEGDA-250 est un matériau rigide et non dégradable qui peut ne pas convenir à certaines applications d'ingénierie tissulaire (TE) qui nécessitent des propriétés mécaniques similaires à celles des tissus mous et une dégradation lente.

Les élastomères à base de citrate ont fait l'objet d'une attention considérable ces dernières années en raison de leur biocompatibilité et de leur dégradabilité. Un biomatériau prometteur à base de citrate est l'élastomère poly(octaméthylène maléate (anhydride) citrate) (POMaC), qui est un élastomère photodurcissable et qui a été utilisé avec succès comme composant clé de capteurs implantables et de TE. Cependant, les méthodes actuelles de fabrication du POMaC impliquent de

multiples étapes de photolithographie qui entravent son utilisation. L'impression 3D pourrait apporter une solution alternative à ces limitations.

Cette thèse se concentre sur le développement de formulations biocompatibles adaptées à l'impression 3D de POMaC et de CC microfluidiques. Pour répondre aux limites des matériaux actuels, de nouvelles encres ont été développées à base de PEGDA-250 et de POMaC, qui ont toutes deux démontré des propriétés améliorées convenant à diverses applications biomédicales. Cette thèse présente tout d'abord le développement d'une encre hydrophile à base de PEGDA par copolymérisation du monomère avec des réticulants hydrophiles. En utilisant l'encre développée, la fabrication numérique (DM) de CC monolithiques, entièrement fonctionnels et intrinsèquement hydrophiles a été réalisée. L'impression 3D permet des avancées dans la conception de valves capillaires, de conduits intégrés avec des sections transversales circulaires qui empêchent le piégeage des bulles, ainsi que d'architectures de circuits entrelacés utilisés pour les immunodosages. En outre, les pompes capillaires externes en papier sont remplacées par une structure gyroïde intégrée imprimée en 3D, ce qui permet de réaliser des CC monolithiques entièrement fonctionnels. En outre, une nouvelle formulation d'encre biocompatible et nanoporeuse a été mise au point en utilisant un PEG non réactif comme porogène. Les substrats nanoporeux imprimés en 3D et ensemencés de cellules endothéliales ont permis de quadrupler la couverture par rapport aux substrats non poreux. En outre, l'encre a été utilisée pour développer une plateforme OOC pour la co-culture de sphéroïdes avec des cellules de soutien.

Une encre à base de POMaC, qui contrairement au PEGDA-250 est biodégradable, est élastique et correspond à la souplesse des tissus (<1000 kPa) a été développée pour les applications TE. De plus, nous introduisons l'utilisation d'imprimantes 3D LCD à très faible coût (<300$) et démontrons leur potentiel en fabriquant des échafaudages en POMaC aussi petits que 80 µm ainsi

que des structures gyroïdes complexes. Pour démontrer la biocompatibilité, nous avons cultivé des cellules endothéliales sur les échafaudages imprimés en 3D et confirmé la biodégradabilité in vitro. L'encre POMaC permet une DM sans assemblage de ce matériau, et avec l'utilisation d'imprimantes 3D à faible coût, elle pourrait grandement faciliter le prototypage rapide de dispositifs pour l'OOC et la TE.

Cette thèse a contribué au développement de nouvelles encres photocurables imprimables en 3D pour les applications TE et microfluidiques. Grâce à l'utilisation de la méthode d'impression 3D VP, ce travail a permis d'améliorer la fonctionnalité et l'accordabilité des encres biocompatibles, ouvrant ainsi la voie au développement de dispositifs microfluidiques et OOC plus fonctionnels. Bien que des progrès aient été réalisés dans la résolution des limites actuelles des formulations pour les applications microfluidiques et OOC, une optimisation supplémentaire est encore nécessaire pour obtenir des canaux microfluidiques intégrés de moins de cent microns à l'aide d'une imprimante 3D LCD. Les travaux futurs comprennent la conception d'encres avec une porosité accordable de la plage nano à micro et la combinaison d'encres avec une approche d'impression 3D multi-matériaux, afin de créer des objets hétérogènes plus fonctionnels.

Preface and Contribution of Authors

In accordance with the "Guidelines for Thesis Preparation," this thesis is organized as a collection of manuscripts written by the candidate in collaboration with co-authors. **Chapter 1** presents a general introduction to the thesis topic and outlines its scope. **Chapter 2** serves as an introduction to multi-material bioprinting methods and their applications. **Chapter 3** updates the content of **Chapter 2**, incorporating recent references and information relevant to the PhD thesis. **Chapters 4, 5, and 6** detail the obtained results, which include the fabrication of monolithic CCs using VP 3D printing and hydrophilic ink (**Chapter 4**), the development of porous PEGDA-based ink for OoC applications (**Chapter 5**), and the development of an ink based on POMaC for VP 3D printing (**Chapter 6**). **Chapter 7** offers an in-depth and comprehensive scholarly discussion of all the findings from the thesis. The concluding chapter provides a summary of the thesis contributions, highlights their significance, and explores potential directions for future work.

In this dissertation, I explored the development of biocompatible formulations for VP 3D printing of OoC and microfluidic CCs. Novel inks based on PEGDA-250 and POMaC were developed, demonstrating enhanced properties for various biomedical applications. A hydrophilic PEGDA-based ink was created, enabling digital manufacturing of monolithic, fully functional, and intrinsically hydrophilic CCs. In addition, a novel biocompatible, nanoporous ink formulation was developed using a non-reactive PEG as porogen. 3D-printed nanoporous substrates seeded with endothelial cells lead to fourfold coverage compared to nonporous ones. Furthermore, a POMaC-based ink was developed for tissue engineering applications. The use of low-cost LCD 3D printers demonstrated the potential for rapid prototyping of devices for OoC and tissue engineering, with scaffolds as small as 80 μm and complex gyroid structures.

The manuscripts are based on experiments conceived and executed by the candidate who also collected and analyzed the data. Furthermore, the candidate was responsible for interpreting the findings. Professor Juncker, the PhD supervisor, appears as a co-author on all the manuscripts to reflect his supervisory role and involvement with result interpretation and manuscript editing.

In **Chapter 2**, which reviews emerging technologies in multimaterial bioprinting, the candidate, H. Ravanbakhsh, and G. Bao contributed equally to the work. The candidate and H. Ravanbakhsh prepared the outline. The candidate wrote and prepared the figures for the sections related to VP bioprinting, LIFT bioprinting, and commercial 3D bioprinters. The candidate also contributed to parts of the introduction, application, future perspective, and conclusion sections.

In **Chapter 4**, where I introduce DM of CCs, the author and A. Sohrabi contributed equally to the work. Both wrote the manuscript and revised it based on Professor Juncker's feedback. I contributed to the development, characterization, and optimization of the CCInk and its application for CCs (Figure 1, Figure 2, Figure 3, and Figure 4). The author also developed the gyroid capillary pump (Figure 6) and contributed to the multilayer MCR and development of CCs with circular channels. A. Sohrabi developed and designed the chip for the assay. M. Shen appears as a co-author due to her assistance with spotting the membrane.

In **Chapter 5**, where I develop a porous PEGDA-based ink, I designed, conducted, and analyzed the experiments, wrote the manuscript, and revised it with feedback from Professor Juncker. M. Shen appears as a co-author due to his contribution in conducting experiments for the cytotoxicity assay and the co-culture platform. F. Lussier appears as a co-author due to his assistance with the fluorescence diffusion test.

In **Chapter 6**, where I develop VP-POMaC for VP 3D printing, I designed, conducted, and analyzed the experiments, wrote the manuscript, and revised it with feedback from Professor Juncker. M. Shen appears as a co-author due to his contribution in conducting experiments for the cytotoxicity assay and 3D cell culture. H. Ravanbakhsh appears as a co-author for his initial assistance with photorheology and compression testing as well as his help with the synthesis of POMaC. A. Sohrabi appears as a co-author for his help in measuring two time points for swelling.

List of Abbreviations

3D	Three-Dimensional
AA	Acrylic Acid
BAPO	Phenylbis(2,4,6-Trimethylbenzoyl) Phosphineoxide
CC	Capillaric Circuit
CDV	Capillary Domino Valve
CLIP	Continuous Liquid Interface Production
CNC	Computer Numerical Control
DLP	Digital Light Processing
DM	Digital Manufacturing
DMD	Digital Micromirror Device
ECM	Extracellular Matrix
FDM	Fused-Deposition Modeling
FEP	Fluorinated Ethylene Propylene
GCP	Gyroid Capillary Pump
GelMA	Gelatin Methacryloyl
HEMA	2-Hydroxyethyl Methacrylate
HUVEC	Human Umbilical Vein Endothelial Cell
ISO	International Organization for Standardization
ITX	Isopropyl Thioxanthone
KSM	Kenics Static Mixer
LAB	Laser-Assisted Bioprinting
LAP	Lithium Phenyl-2,4,6-Trimethyl Benzoyl Phosphinate
LCD	Liquid-Crystal Display

LIFT	Laser-Induced Forward Transfer
MA	Methacrylic Acid
MCR	Microfluidic Chain Reaction
MMP	Matrix Metalloproteinase
MW	Molecular Weight
NaOH	Sodium Hydroxide
NIR	Near-Infrared
NPS	2-Nitrophenyl Phenyl Sulfide
OoC	Organ-on-a-Chip
PA	Photoabsorber
PCL	Poly(E-Caprolactone)
PDMS	Polydimethylsiloxane
PEG	Polyethylene Glycol
PEGDA	Polyethylene Glycol Diacrylate
PEGDMA	Polyethylene Glycol Dimethacrylate
PEGDME	Poly(Ethylene Glycol) Dimethyl Ether
PFA	Perfluoroalkoxy
PI	Photoinitiator
POMaC	Poly(Octamethylene Maleate (Anhydride) Citrate)
PU	Polyurethane
PVA	Poly(Vinyl Alcohol)
RBV	Retention Burst Valve
SEM	Scanning Electron Microscope
SLA	Stereolithography
SLS	Selective Laser Sintering

SV Stop Valve

TE Tissue Engineering

TMPS Triply Periodic Minimal Surface

TMPTA Trimethylolpropane Triacrylate

TPO Diphenyl(2,4,6-Trimethylbenzoyl) Phosphine Oxide

TPP Two-Photon Polymerization

TV Trigger Valve

UV Ultraviolet

VP Vat Photopolymerization

Table of Contents

List of Figures

List of Tables

Chapter 1

1. Chapter 1: Introduction

Vat photopolymerization (VP), also known as stereolithography (SLA), is an additive manufacturing (AM) technology that creates three-dimensional objects by curing liquid photopolymer resins layer by layer using a light source, typically ultraviolet (UV) or visible light[1]. Although VP 3D printing enables high-throughput fabrication of intricate geometries with high resolution, there is still a need for suitable photocurable materials that meet specific application requirements, such as hydrophilicity and biocompatibility in resins, hydrogels, and elastomers.

Polydimethylsiloxane (PDMS) is a prevalent material for fabricating microfluidic and organ-on-a-chip (OoC) devices due to its biocompatibility, transparency, and oxygen permeability[2]. While some groups have attempted to 3D print PDMS, it remains challenging to print embedded channels with dimensions smaller than 100 microns[3–6]. Additionally, PDMS absorbs small hydrophobic molecules, leading to inaccurate drug toxicity and efficacy assessments[7]. Polyethylene glycol diacrylate (PEGDA) has emerged as a promising alternative to PDMS for microfluidic and OoC applications[8–12]. However, current PEGDA-250 formulations exhibit limitations, such as suboptimal hydrophilicity and insufficient cell attachment. To overcome these limitations, hydrophilic formulations compatible with high-resolution 3D printing techniques like VP printing are needed, as well as resins that promote cell attachment, biocompatibility, and nanoporosity. PEGDA-250's rigidity and non-degradability may also restrict its use in tissue engineering applications.

Citrate-based elastomers like poly(octamethylene maleate (anhydride) citrate) (POMaC) offer biocompatibility, degradability, and tunable mechanical properties, making them attractive for biomaterial applications[13–15]. Although current POMaC fabrication methods involve multiple photolithography steps, 3D printing could provide an alternative solution. However, existing POMaC formulations face challenges in 3D printing intricate structures due to slow reactions and high viscosity. These limitations can be addressed by developing novel PEGDA-250 and POMaC inks for VP 3D printing in OoC and microfluidic applications. These enhanced formulations could improve properties suitable for various biomedical applications, paving the way for future advancements in the field.

1.1 Scope of the thesis

The aim of my thesis is to develop novel 3D printable photocurable inks based on PEGDA-250 and POMaC for OoC and microfluidic applications. Through the use of VP 3D printing method, this work improves functionality and tunability of these materials, paving the way for the development of more functional microfluidic and OOC devices.

In **Chapter 2**, we delve into the realm of bioprinting, a sub-discipline within the rapidly evolving field of biofabrication, which focuses on the fabrication of functional biomimetic constructs. Various three-dimensional bioprinting techniques have been adapted to print cell-laden bioinks; however, single-material bioprinting techniques often struggle to reproduce the intricate compositions and diversity found in native tissues. As an emerging approach, multi-material bioprinting allows for the creation of heterogeneous, multi-cellular constructs that more accurately replicate their host microenvironments compared to single-material methods. In this chapter, we provide a brief overview of bioprinting modalities, discuss their adaptation for multi-material bioprinting, and analyze the advantages and challenges associated with both custom-designed and

commercially available technologies. We present a perspective on how multi-material bioprinting unlocks new opportunities in tissue engineering, tissue model engineering, therapeutics development, and personalized medicine. This chapter serves as a foundation for understanding the advancements and potential of multi-material bioprinting techniques in the broader context of biofabrication and its applications.

In **Chapter 3**, I concentrate on reviewing capillary microfluidics, DM, and photocurable bioinks for VP 3D printing, with a particular emphasis on synthetic inks such as PEGDA and POMaC. This chapter aims to fill the gaps in background knowledge not addressed in the previous chapter and provides a solid foundation for the forthcoming sections of the thesis.

In **Chapter 4**, we introduce the digital manufacturing (DM) of monolithic, fully functional, and intrinsically hydrophilic CCs. We employ light engine additive manufacturing to 3D print CCs using a PEGDA ink co-polymerized with acrylic acid crosslinkers, optimized for printability and hydrophilicity. We present a new, robust capillary valve design and embedded conduits with circular cross-sections that prevent bubble trapping. We also demonstrate complex interwoven circuit architectures, particularly for use in immunoassays. Furthermore, we eliminate the need for external paper capillary pumps by incorporating an integrated 3D printed gyroid structure, realizing fully functional, monolithic CCs. Consequently, a computer-aided design file can be transformed into a CC using light engine 3D printing within a few minutes. This development paves the way for low-cost, distributed DM of fully functional, ready-to-use microfluidic systems. This chapter showcases the innovative use of digital manufacturing techniques to overcome current limitations in microfluidic capillaric circuit fabrication and applications.

In **Chapter 5**, we introduce a novel PEGDA ink that is biocompatible and nanoporous thanks to the incorporation of a non-reactive porogen. We assess the material's cytotoxicity on

various cell lines and examine its influence on cell attachment. Our findings reveal that 3D-printed nanoporous substrates, when seeded with endothelial cells, result in a fourfold increase in coverage compared to nonporous counterparts. Furthermore, we showcase the practical application of this material by employing it to create an OoC platform suitable for sustaining long-term co-culture for up to 14 days.

In **Chapter 6**, we present POMaC formulations tailored for light-based 3D printing using cost-effective liquid-crystal display printers, enabling the fabrication of complex 3D structures with 80 μm resolution and adjustable mechanical properties. To date, only simple, low-resolution structures have been achieved via photolithography processes using POMaC, a biocompatible, biodegradable, and soft elastomer that is photocurable and theoretically suitable for VP 3D printing. We demonstrate the creation of optically transparent submillimeter structures, including intricate gyroids, using a budget-friendly desktop 3D printer (< USD 300). Additionally, we employ an optimized POMaC formulation to 3D print constructs with mechanical properties similar to skeletal and heart muscle tissues. We also demonstrate the usability of 3D-printed POMaC substrates for mammalian cell culture. This POMaC ink facilitates assembly-free, automated DM of biodegradable materials, paving the way for rapid prototyping in organ-on-chip and tissue engineering platforms.

In **Chapter 7**, I will provide an in-depth and comprehensive scholarly discussion of all the findings from our research on utilizing VP 3D printing for various photocurable formulations and their applications. Through the development of suitable polymers, we showcase how the potential of materials like POMaC and PEGDA, as well as technologies such as capillary microfluidics and organ-on-a-chip, can be expanded, building on the results presented in previous chapters. This

chapter synthesizes our discoveries, providing an overarching understanding of the advancements made within the field.

In **Chapter 8**, I conclude by summarizing the contributions of this thesis to science. In addition, we discuss the limitations of presented methods and formulations as well potential future work avenues that could address those limitations.

1.2 References

1. Li, W. *et al.* Recent Advances in Formulating and Processing Biomaterial Inks for Vat Polymerization-Based 3D Printing. *Adv. Healthc. Mater.* 2000156 (2020) doi:10.1002/adhm.202000156.

2. Raj M, K. & Chakraborty, S. PDMS microfluidics: A mini review. *J. Appl. Polym. Sci.* **137**, 48958 (2020).

3. Gonzalez, G., Chiappone, A., Dietliker, K., Pirri, C. F. & Roppolo, I. Fabrication and Functionalization of 3D Printed Polydimethylsiloxane-Based Microfluidic Devices Obtained through Digital Light Processing. *Adv. Mater. Technol.* **5**, 2000374 (2020).

4. Krongauz, V. V. Crosslink density dependence of polymer degradation kinetics: photocrosslinked acrylates. *Thermochim. Acta* **503**, 70–84 (2010).

5. Bartnikowski, M., Dargaville, T. R., Ivanovski, S. & Hutmacher, D. W. Degradation mechanisms of polycaprolactone in the context of chemistry, geometry and environment. *Prog. Polym. Sci.* **96**, 1–20 (2019).

6. Bhattacharjee, N., Parra-Cabrera, C., Kim, Y. T., Kuo, A. P. & Folch, A. Desktop-Stereolithography 3D-Printing of a Poly(dimethylsiloxane)-Based Material with Sylgard-184 Properties. *Adv. Mater.* **30**, 1–7 (2018).

7. Naderi, A., Bhattacharjee, N. & Folch, A. Digital Manufacturing for Microfluidics. *Annu. Rev. Biomed. Eng.* **21**, 325–364 (2019).

8. Warr, C. *et al.* Biocompatible PEGDA Resin for 3D Printing. (2020) doi:10.1021/acsabm.0c00055.

9. Gong, H., Bickham, B. P., Woolley, A. T. & Nordin, G. P. Custom 3D printer and resin for 18 μm × 20 μm microfluidic flow channels. *Lab Chip* **17**, 2899–2909 (2017).

10. Zhang, R. & Larsen, N. B. Stereolithographic hydrogel printing of 3D culture chips with biofunctionalized complex 3D perfusion networks. *Lab Chip* **17**, 4273–4282 (2017).

11. Urrios, A. *et al.* 3D-printing of transparent bio-microfluidic devices in PEG-DA. *Lab Chip* **16**, 2287–2294 (2016).

12. Kuo, A. P. *et al.* High-Precision Stereolithography of Biomicrofluidic Devices. *Adv. Mater. Technol.* **4**, 1–11 (2019).

13. Montgomery, M. *et al.* Method for the Fabrication of Elastomeric Polyester Scaffolds for Tissue Engineering and Minimally Invasive Delivery. *ACS Biomater. Sci. Eng.* **4**, 3691–3703 (2018).

14. Zhao, Y. *et al.* A Platform for Generation of Chamber-Specific Cardiac Tissues and Disease Modeling. *Cell* **176**, 913-927.e18 (2019).

15. Zhang, B. *et al.* Biodegradable scaffold with built-in vasculature for organ-on-a-chip engineering and direct surgical anastomosis. *Nat. Mater.* **15**, 669–678 (2016).

Chapter 2

2. Chapter 2: Emerging Technologies in Multi-material Bioprinting

This chapter is based on: Emerging technologies in multi-material bioprinting, Ravanbakhsh*, H., **Karamzadeh*, V**., Bao*, G., Mongeau, L., Juncker, D., & Zhang, Y. S., Advanced Materials 33 (49) (2021): 2104730.

2.1 Abstract

Bioprinting, within the emerging field of biofabrication, aims at the fabrication of functional biomimetic constructs. Different three-dimensional bioprinting techniques have been adapted to bioprint cell-laden bioinks. However, single-material bioprinting techniques oftentimes fail to reproduce the complex compositions and diversity of native tissues. Multi-material bioprinting as an emerging approach enables the fabrication of heterogeneous multi-cellular constructs that replicate their host microenvironments better than single-material approaches. Here, we briefly review bioprinting modalities, discuss how they are being adapted to multi-material bioprinting, as well as analyze their advantages and challenges, encompassing both custom-designed and commercially available technologies. The review offers a perspective of how multi-material bioprinting opens up new opportunities for tissue engineering, tissue model engineering, therapeutics development, and personalized medicine.

Keywords: biofabrication; 3D printing; bioprinting; multi-material; commercial bioprinters

2.2 Introduction to bioprinting modalities

Three-dimensional (3D) printing refers to the fabrication of constructs from a digital 3D model in a layer-wise[1] or volumetric[2] programmed manner. The flexibility, versatility, and functionality of 3D printing enable the fabrication of exquisite and intricate structures[3–5] with details as small as hundreds of nanometers[6]. Here we focus on one sub-category of 3D printing, designated 3D bioprinting[7,8], in which a combination of cells, growth factors, or biomaterials (i.e., bioink[9]) may be used as the printing material for additive manufacturing of biological constructs[10]. As part of the rapidly evolving field of biofabrication, 3D bioprinting is being explored for a broad range of applications within tissue engineering[11,12], regenerative medicine[13], organ-specific tissues[14], patient-specific grafts[15], tissue model engineering[16], and drug screening[17]. The most frequently used technologies for 3D bioprinting include nozzle-based and laser/light-based techniques. Extrusion[18] and inkjet[19] are arguably the most common modalities of nozzle-based bioprinting at the moment, while laser-induced forward transfer (LIFT)[20] and vat-photopolymerization[21] are the two frequently used for laser/light-based 3D bioprinting[22].

Extrusion bioprinting involves fabrication on a bioprinting platform using bioinks extruded from one or several nozzle(s) (**Figure 2.1A**). The extrusion process may be pressure-controlled, with the bioink entrained by means of pneumatic actuation, or flow rate-controlled with the bioink forced by mechanical impulses through syringes[23]. Solidification of the bioprinted structures as they are delivered is obtained through physical, chemical, or photo-crosslinking[24]. Extrusion bioprinting is relatively inexpensive, straightforward, and convenient. It has been embodied, for example, within handheld and portable devices[25–29]. But such convenience must be traded off against significant challenges. Nozzle extrusion necessarily entails a high level of shear stress near the fluidic channel walls. Excessive shear, particularly in high-viscosity bioinks, jeopardizes cell

viability[30]. High-resolution bioprinting often requires small-diameter nozzles. The greater shear required imposes a limit on bioink flow rate and throughput. This problem may be addressed through the use of printable shear-thinning biomaterials[31], for which the viscosity decreases under shear stress. But shear-thinning bioink materials that meet all design requirements are often difficult to find. Further notable challenges of extrusion methods include difficulties in finding stable in situ crosslinking methods for non-shear-thinning bioinks, as well as low printing resolution[32] in relation to other methods, and complications in the fabrication of free-standing constructs[33,34]. These shortcomings have spurred many enhancements, notably co-axial/core-shell bioprinting[35], described in Section 2.4.1.3, and embedded bioprinting[36], in Section 2.4.13.

Inkjet bioprinting (**Figure 2.1B**), similar to home/office inkjet printing, delivers small droplets of bioink to a substrate and can produce high-resolution voxelated constructs[37]. Unlike the extrusion method where shear-thinning bioinks with a broad range of viscosities can be used, inkjet bioprinters are mainly designed to work with low-viscosity bioinks[38]. The deposition of droplets/voxels is controlled either by thermal, piezoelectric, or electromagnetic actuation[39,40]. Short thermal pulses within the printhead result in gasification of the bioink, and the subsequent pressure increase causes the ejection of droplets. Piezoelectric actuators impart acceleration to the bioink to trigger controlled droplet ejection. Electromagnetic inkjet bioprinters use solenoid-actuated valves within the nozzle to regulate the extrusion of droplets[41]. Inkjet approaches are faster than extrusion. Yet, they are typically not suited for the fabrication of thick structures, and not used as broadly for multi-material bioprinting. The printability of bioinks for inkjet bioprinters is usually determined by the Ohnesorge number, $Oh = \mu/\sqrt{\rho\sigma R}$, where μ is the viscosity, ρ is the density, σ is the surface tension, and R is the characteristic length scale for the flow, which can be taken as the radius of the orifice of the printing nozzle[42]. This dimensionless number represents

the ratio of viscous forces to inertia and surface tension. A material with an Ohnesorge number between 0.1 to 1 is usually deemed printable via the inkjet method[42]. For a given bioink composition, the ejected droplet size is mainly determined by nozzle dimensions. The printing speed mainly depends on the frequency of the pulsated heating or piezoelectric motion. Inkjet printing speed and droplet size are therefore controlled independently.

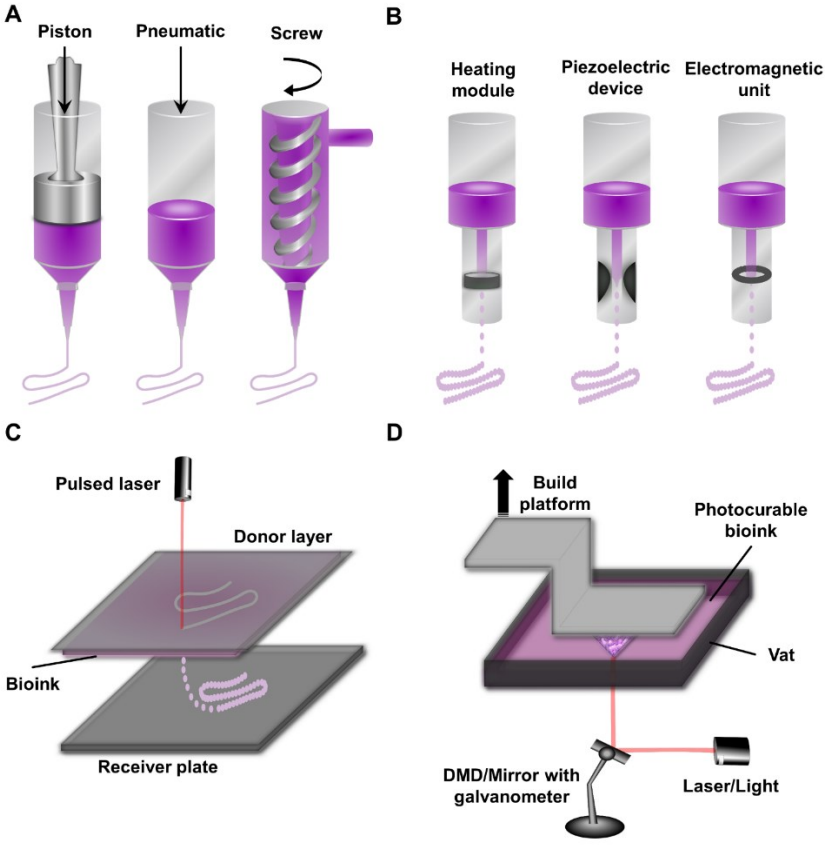

Figure 2.1. Schematic showing the different bioprinting modalities. A) Extrusion. B) Inkjet. C) LIFT. D) Vat-photopolymerization.

In LIFT bioprinting (**Figure 2.1C**), the bioink is initially deposited as a thin layer on the bottom of a substrate, termed the donor layer. Upon irradiation of the donor layer surface with a pulsed laser, droplets are created and transferred onto the receiver plate in a voxelated fashion[20]. The LIFT method is both highly accurate and fast. A range of bioinks is available for LIFT[20], despite

restrictions in viscosity (values should fall between 1 to 300 mPa s) and crosslinking mechanisms[22,43]. At the time of this review, LIFT is not suitable for the high-throughput fabrication of multi-material or multi-cellular constructs[44]. It is not often used for high-aspect-ratio constructs.

In vat-photopolymerization bioprinting (**Figure 2.1D**), the fabrication process involves the selective exposure of liquid photocurable bioink in a vat to ultraviolet (UV), visible, or near-infrared (NIR) light[45–48]. Three light-patterning methods have mainly been used for vat-photopolymerization: (i) one single programmed laser beam, such as in conventional stereolithography (SLA); (ii) digital light processing (DLP); or (iii) two-photon polymerization (TPP). The programmed pattern in the precursor vat is illuminated by the laser beam and solidifies. Once each layer is crosslinked, the build platform moves to a neighboring position to allow the fabrication of the next layer.

Other commonly used vat-photopolymerization bioprinting methods include DLP and conventional SLA. These methods are able to fabricate constructs with details only of a few tens of micrometers[49]. In the DLP method, the projected light is usually masked using an array of mirrors termed the digital micromirror device (DMD). This allows the simultaneous illumination of one entire layer. Pixels are either exposed or blocked to obtain the desired shape outline. Other devices scan a laser beam along the horizontal axis to rapidly solidify the bioink across each plane[50,51]. The speed of DLP bioprinting is greater than that of conventional SLA or TPP as it is not limited by layer geometrical complexity (XY area), but rather by layer thickness and exposure time. However, the accuracy of DLP is limited by the pixel size of the projected image. Thus, the printed surface area must be traded off against the level of detail along the horizontal axes (XY). Light intensities in DLP-based 3D bioprinting are often lower than that in other vat-photopolymerization printers. Nevertheless, some high-resolution DLP light engines deliver light

energy densities within the same range as SLA laser beams (>100 mW/cm^2) and solidify bioinks within hundreds of milliseconds. In these two methods, the XY resolution is primarily determined by the projected pixel or laser beam spot size, bioink reaction kinetics, and the diffusion of free radicals[52]. The vertical resolution is mainly dictated by the light penetration depth, itself a function of the absorbance/scattering of the ink, and the layer thickness[53]. Both SLA and DLP technologies can generate bioconstructs with high cell densities (>2×10^7 cell/mL)[54–56]. Limitations include phototoxicity, UV-triggered mutations, photoinitiator toxicity, and insufficient choice of photocurable bioinks.

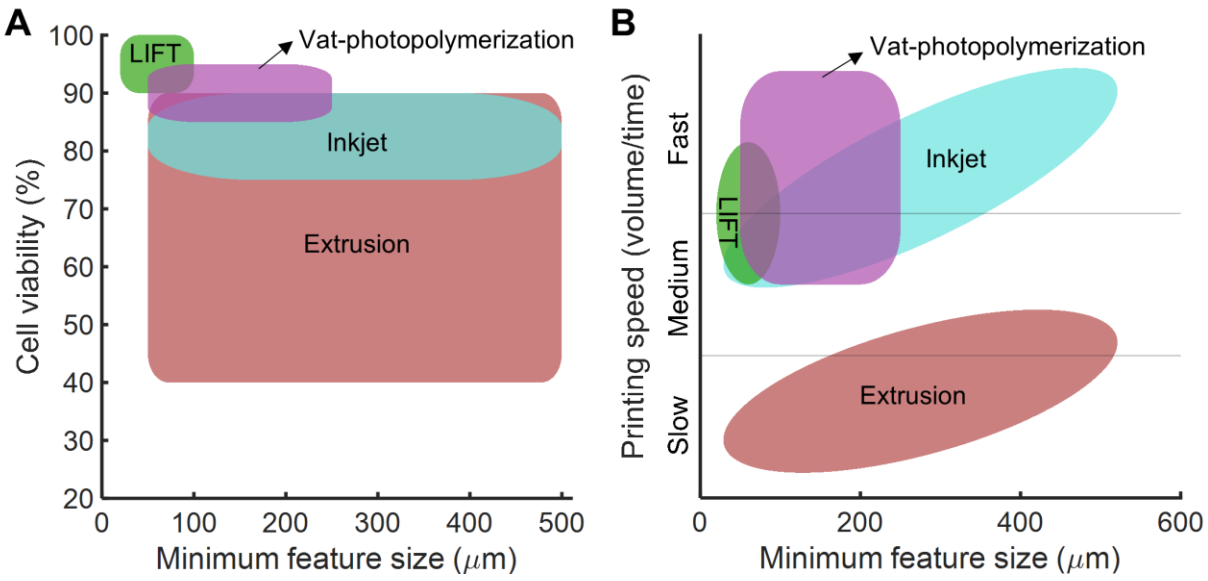

Figure 2.2. **Comparison of different bioprinting methods.** A) Cell viability versus minimum feature size. In nozzle-based techniques, the excessive shear stress applied to the cells significantly decreases the cell viability, whereas in light/lased-based methods, the overall cell viability is higher. The light/laser-based methods are also more capable of generating well-defined constructs with higher resolutions. B) Printing speed versus minimum feature size. Despite its simplicity, the extrusion method is generally the slowest modality among the four primary bioprinting techniques. Inkjet and vat-photopolymerization are the two fastest methods, and LIFT is considered a medium-speed method[32,38,43,49,57–61].

The use of TPP for 3D bioprinting has been less common due to lower cell viability, insufficient throughput for bioprinting of large constructs, and a limited number of efficient biocompatible water-soluble photoinitiators[62]. Most TPP 3D bioprinters are based on femtosecond lasers operating in the NIR wavelength range. They enable the fabrication of 3D microstructures with submicron details[63]. Due to the operational mechanism of TPP, high-throughput 3D bioprinting of cell-laden hydrogels requires a high-speed scanning system[64]. In TPP, the spatial resolution is largely dictated by the laser irradiation intensity (~TW/cm^2) and exposure time, which primarily depends on the initiating efficiency of TPP photoinitiators[65,66].

The performances of these four primary bioprinting modalities according to feature size, cell viability, and printing speed are shown in **Figure 2.2**. As mentioned before, nozzle-based techniques, especially the extrusion-based method, deliver a relatively lower average cell viability rate. Viscosity of a bioink, which depends on the molecular weight and concentration of the dissolved polymers, also plays an important role in the efficacy of the bioprinting methods. Particularly for extrusion bioprinting, structures with high fidelity can be bioprinted when viscous bioinks with high yield strengths are utilized, although oftentimes they would still go through another crosslinking step post-bioprinting[42]. However, higher viscosity values usually induce higher shear stresses and lower cell viability[67]. This trade-off needs to be considered when live cells are used in a biofabrication process. If viscous bioinks are adopted in conventional extrusion bioprinting, the cell viability declines due to the high shear stresses. In the inkjet technique, low-viscosity bioinks are used with high cell viability, but additional polymerization is almost always needed to yield a crosslinked construct with a high yield strength that resists the deformation due to gravity[68]. Recently, an acoustic droplet ejection approach has been employed in conjunction with the inkjet printing to reduce shear stress on the bioink[69]. In embedded bioprinting, where low-

viscosity bioinks are also employable, higher cell viability and smaller feature sizes can be achieved. As a result, the ranges of cell viability and feature sizes for the extrusion method are considerably larger than those of the other methods (**Figure 2.2A**). Laser/light-based methods, i.e., LIFT and vat-photopolymerization, generally yield high cell viability values as well as better bioprinting resolutions and faster bioprinting speeds[47,49].

Bioprinter selection must consider the limitations of the intrinsic printing mechanism. Printing speed and detail resolution are shown for various techniques in **Figure 2.2B**. No modality is absolutely preferable over other methods in terms of printing speed. In general, extrusion bioprinting is slower, while inkjet and vat-photopolymerization technologies provide faster fabrication paces[43]. The range of bioink viscosities available for extrusion bioprinters is greater than that for inkjet bioprinters[70]. The lower viscosities in inkjet bioprinting yield higher flow rates and thus increased printing speeds. For nozzle-based techniques, the printing speed considerably affects detail resolution[71], unless it is increased through the addition of multiple nozzles. According to the Hagen–Poiseuille law[72], nozzle diameter, nozzle length, bioink viscosity, and bioink flow rate affect detail resolution in extrusion bioprinting. In newly developed volumetric 3D bioprinting[2] and xolography[73], the resolution does not necessarily affect the printing speed. Inspired by cell patterning[74] and cell packing approaches[75], recent efforts have been devoted to exploiting acoustic and ultra-sound impulses to organize and pattern cells within printed layers[76,77]. Overall, the selection of bioprinting technology depends on the targeted application and the required detail resolution. Although printing speed, cell viability, and resolution are important, other key features, such as flexibility, accessibility, operability, and cost-effectiveness, should also all be considered. These aspects are discussed in Section 6.

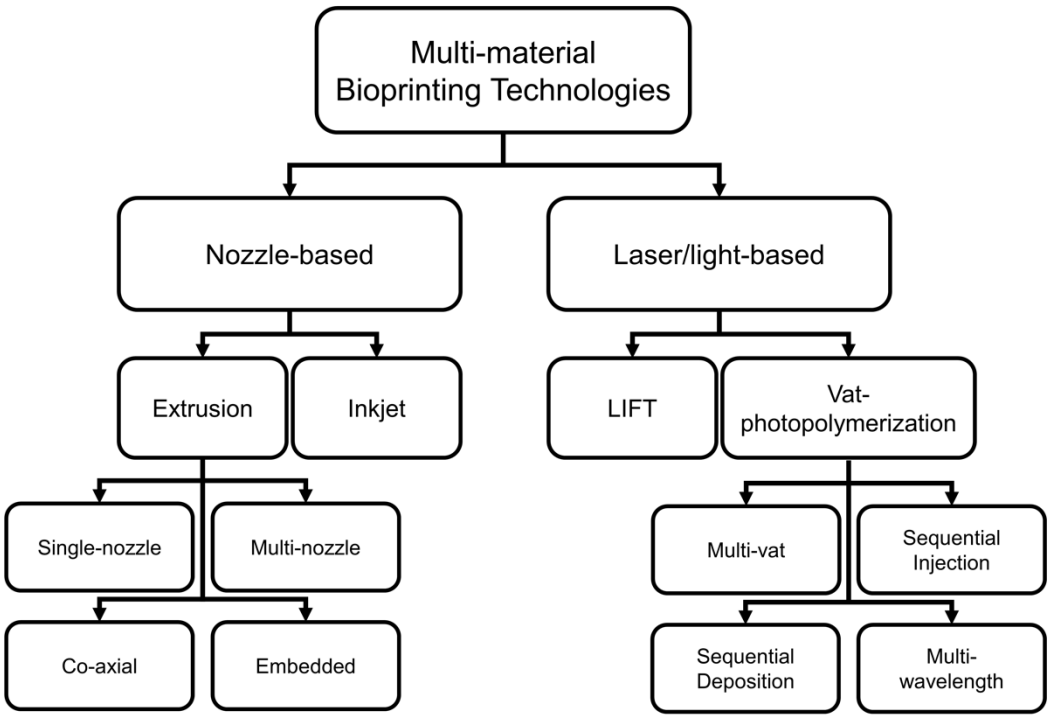

Figure 2.3. Classification of multi-material bioprinting technologies.

The capability of fabricating multi-cellular/multi-material constructs is of paramount significance as the native human tissues and organs possess heterogenous cellular and extracellular structures. Recently, tremendous attempts have been made to design multi-material bioprinters, encompassing a broad range of technologies, from open-source desktop platforms[78] to standalone commercial bioprinters[79]. Several surveys have been published with discussions on multi-material additive manufacturing[80,81]. However, these reviews have devoted scant attention to the multi-material printing of cell-laden bioinks, i.e., bioprinting. Other reviews with a focus on biomedical applications of 3D printing[3,82,83] have brief discussions on multi-material methods, principally emphasizing the material design rather than its technology. Other recently published reviews describe microfluidics-assisted bioprinting[44]. Extrusion-based multi-material bioprinting has been hailed as one of the main applications of microfluidic systems[84]. But the salient evolution of multi-material bioprinting both in nozzle-based and laser/light-enabled technologies over the last few

years, along with the upsurge of available multi-material commercial bioprinters, entails the need to recapitulate the recent advances.

Herein, we classify (**Figure 2.3**) and summarize the state-of-the-art multi-material bioprinting approaches mostly developed over the past 5 years. Recent advances in multi-material bioprinting are critically discussed, broken down along the four dominant technologies presented above. A section on applications of multi-material bioprinting is included. Commercial multi-material bioprinters are presented as they are key for translation to clinical applications. Perspectives on opportunities for future discoveries conclude the review.

2.3 Multi-material bioprinting concept

Multi-material bioprinters are generally better-suited than conventional bioprinters for the fabrication of constructs that mimic the heterocellular structures of native tissues[85–87], enabling for example the incorporation of graded composition and properties or environmental adaptations[88–90]. The versatility added to biofabrication methods via the development of multi-material bioprinting has already led to improved sacrificial supports[91], multi-functional systems[92], vascularized structures[93], customizable tissues and organs[94], and advanced spatiotemporal control[95].

At the onset, it is useful to clarify some important definitions. Multi-component bioink refers to mixtures of two or more different biomaterials making up one single-phase homogenous bioink[96,97]. Once properly crosslinked, such bioinks may yield multi-network or single-network structures. Composite bioinks are, specifically, multi-phase materials composed of two or more immiscible components[98]. The most common types of composite bioinks are fabricated through the incorporation of nanoparticles/nanofibers in hydrogel matrices[99–101]. Composite bioinks may have isotropic or anisotropic properties, depending on the spatial distribution and orientation of

the additives[97]. Multi-material 3D bioprinting designates the sequential/simultaneous bioprinting of two or more (bio)inks in a programmed manner to achieve region-specific features and performances. Accordingly, each (bio)ink may be single-/multi-component, single-phase, or composite.

As for conventional bioprinting, various advanced materials have been developed for multi-material modalities to achieve either superior properties, proper crosslinking, or better biomimicry[102]. Many are hydrogel polymers in view of their intrinsic characteristics, such as hydrated microenvironment, facilitated crosslinking mechanisms, cytocompatibility, printability, and vast rheological properties over different temperatures. Chemically modified bioinks, e.g., methacrylated polymers[103,104], are widely employed since they offer precisely controllable crosslinking regimes[105]. The polymer molecular weight and concentration significantly affect bioink performance[106]. The gelation mechanism of a hydrogels is a critical factor in multi-material bioprinting, where multiple bioinks are to be crosslinked in a compliant manner. Physically and chemically crosslinked hydrogels follow different gelation regimes[107]. Special attention should be, therefore, devoted to bioinks with different crosslinking mechanisms when concomitantly employed in multi-material bioprinting. Composite biomaterials, as described above, are another category of advanced materials that have been developed and used in multi-material bioprinting. One of the main advantages of composite bioinks is their enhanced printability and functionality. The reader is referred to our previous review for more details about composite bioinks[97].

Due to the employment of multiple materials, interactions at the interfaces of materials must be considered. A strong interfacial adhesion can improve the toughness and fatigue-resistance of bioprinted constructs[108]. Different bioprinted parts are commonly bonded by using materials that can be crosslinked via the same covalent or ionic crosslinkers[109]. Other methods employing

supramolecular forces such as guest-host interactions have also been explored[110]. But, it is challenging to bond hydrogels to materials from a different family, especially elastomers and thermoplastics, in a multi-material (bio)printing process. Recent advances in hydrogel adhesives shed light on new ways to design material interfaces in bioprinting. For example, hydrogels and elastomers can be strongly bonded by using free-radical polymerizations[111], topological adhesion[112], bridging polymers[113], or catechol chemistry[114]. Thermoplastics can also be functionalized with certain specific functional groups to allow hydrogel bonding[115]. However, it is to be emphasized that most existing hydrogel adhesion strategies suffer from cytocompatibility issue, and the cytotoxicity are dose-dependent. Cell-friendly strategies, such as bio-orthogonal click chemistry[116], could be a potential remedy. While this review is focused on multi-material bioprinting technology, the reader is referred to reviews covering the design and applications of hydrogel adhesion elsewhere[117–119].

2.4 Multi-material bioprinting technologies

Over recent years, four types of bioprinting technologies have been exploited to fabricate multi-material products. Multi-material bioprinting has grown from the use of rather cumbersome tools to a well-integrated and automated process. In this section, the latest efforts for advancing the field of multi-material bioprinting are reported with a focus on technology. Broader studies about 3D printing are at times included when they have the potential to be adapted for 3D bioprinting.

2.4.1 Extrusion bioprinting

Extrusion bioprinting is the most popular method for multi-material bioprinting[3]. Many innovative concepts have been demonstrated for the fabrication of multi-material constructs. In multi-material extrusion bioprinters, the printhead comprises cartridges (reservoirs), mixers, tubing, and nozzles. Nozzle delivery may be divided into single-nozzle[120] and multi-nozzle[121]

technologies. Conventional single- and multi-nozzle technologies are among the most prevalent, accessible, and easy-to-implement technologies. In single-nozzle bioprinters, there is essentially one printhead consisting of only one nozzle. Different concentrations of bioinks may be sequentially extruded or mixed within the printhead. The use of only one nozzle for multiple materials requires the same working temperature for all the (bio)inks, which is not always feasible. More importantly, single-nozzle delivery increases the risk for cross-contamination. Multi-nozzle bioprinters have one or multiple printheads, each of which is equipped with one or several nozzles. Simultaneous delivery through several nozzles tends to increase fabrication speed. Co-axial nozzles[122–124] enable the fabrication of multi-layer/core-shell constructs through the simultaneous and concentrically collocated extrusion of different bioinks. These are often needed for bioinks with rapid crosslinking mechanisms, e.g. those based on or containing alginate. Embedded bioprinting[125] is helpful for making freeform structures that are difficult to fabricate using classic extrusion methods, or for using low-viscosity bioinks that are not compatible with other extrusion-based methods. Co-axial and embedded bioprinting techniques can be potentially used with either single-nozzle and multi-nozzle bioprinters.

2.4.1.1 Single-nozzle bioprinting technology

Extrusion of different bioinks through one single nozzle remains the baseline for multi-material bioprinting. Multi-reservoir systems and mixers are the two most common related modalities. In the former, several reservoirs of bioinks are connected to the nozzle within the printhead (**Figure 2.4A-D**). The multi-material construct is fabricated following sequential or simultaneous activation of multiple reservoirs, resulting in the alteration of the feed. This method is well-illustrated by a pneumatically controlled bioprinter consisting of seven reservoirs[126]. This bioprinter may be used with a broad range of bioinks, including shear-thinning and conductive biomaterials. Its solenoid valve technology enables precise bioink flow control and rapid switch

between bioinks. As for most extrusion techniques, with the exception of embedded bioprinting, the smallest feature size is limited to around 100-200 μm. The nozzles' inner surface properties may also affect the switching rate between bioinks. For example, Cameron et al. used a readily available single-nozzle printhead mounted on a commercial bioprinter (**Figure 2.4E, F**)[127] to show that switching between bioinks is faster when a hydrophobic coating, e.g., silicone, is used for the nozzles' inner channels. Much work is needed to further explore the influence of nozzle coatings on the effectiveness of multi-material bioprinting and the viability of encapsulated cells.

Microfluidic devices facilitate switching between bioinks when following a multi-reservoir approach[84,123,128,129]. Since the flow of bioinks in microchannels is often laminar (i.e., with a low Reynolds number), microfluidic devices work as switches that deliver bioinks sequentially with minimal mixing. Switching rate, however, is limited by the system's compressibility [130]. Longer transient periods tend to reduce the sharpness of the edges in the printed structures.

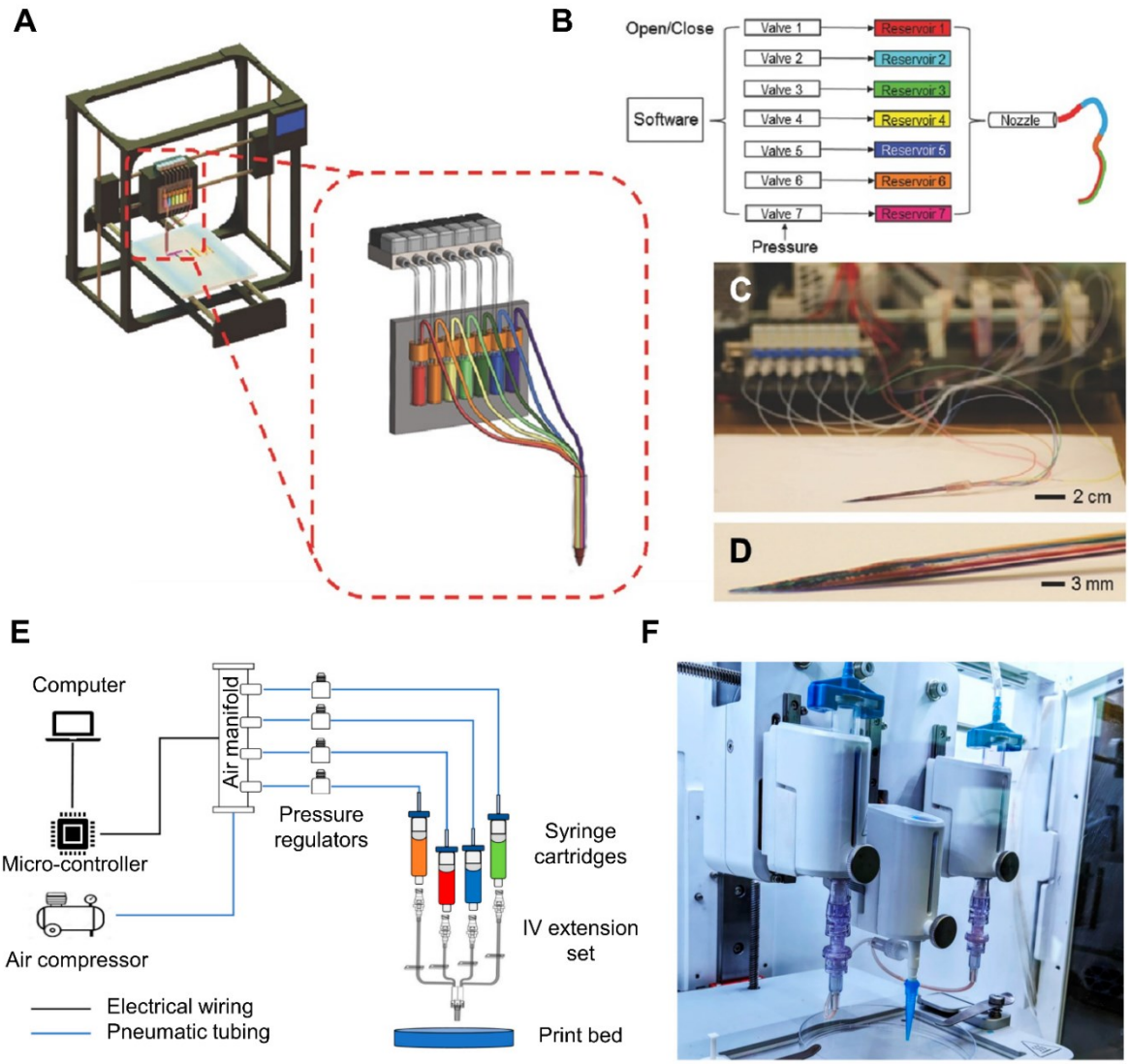

Figure 2.4. Single-nozzle multi-material bioprinting technologies. A, B) Schematic illustration of the multi-reservoir technique. Each cartridge is actuated using a separate pneumatic valve. C, D) Optical image of the valves and the printhead setup. Reproduced with permission.[126] Copyright 2017, Wiley-VCH. E, F) Schematic configuration of a multi-material single-nozzle printhead assembled on a commercial 3D bioprinter, and its photograph. Adapted under the terms of the CC-BY Creative Commons Attribution 4.0 International license (https://creativecommons.org/licenses/by/4.0).[127] Copyright 2020, The Authors, published by Multidisciplinary Digital Publishing Institute.

While implementing the multi-reservoir system is simple, this method is not functional for systematically fabricating constructs with continuous gradient properties. Various mixers have

been used to overcome this shortcoming by blending two or more bioinks in different concentrations to facilitate multi-material printing[130]/bioprinting[131] jobs. The mixers are divided into two general categories; active and passive[132]. Active mixers, such as the so-called "on-the-fly" designs[133], consist of either a motor-driven impeller or an acoustic source (**Figure 2.5A, B**)[134], in which the mixing capacity can be finely controlled through changing the input power. The active mixers have been studied using computational models to anticipate the mixing capabilities[135,136]. Passive mixers operate by introducing turbulent cross-stream flows using geometrical discontinuities or sharp edges within the microchannels (**Figure 2.5C**)[137]. An important problem with passive mixers is the limited capability of mixing bioinks on small scales. The solution to this problem is employing microfluidic mixers, a popular category of passive mixers commonly used in multi-material bioprinters. Bioink volumes as small as 10^{-9} to 10^{-18} L can be properly mixed in a controlled manner using microfluidic mixers[44]. The mechanism of mixing in such devices is based on transitioning the flow of bioink from laminar to turbulent (i.e., high Reynolds numbers)[129,137,138]. The reader is referred to another recent review for a more comprehensive insight into microfluidics-based 3D bioprinting[44].

Passive mixers are generally easier to integrate and more biocompatible as they induce less shear stress to the encapsulated cells[139]. However, it is impossible to tune the mixing capacity of passive mixers without changing the input bioinks' flow rates[133]. Changing the flow rates, on the other hand, may adversely affect the bioprinting quality. Furthermore, the mixing capacity of microfluidic devices highly depends on the viscosity of the bioink, as well as the length, diameter, and geometry of the microchannels. The small-scale mixing issue mentioned above becomes more serious when viscous bioinks are employed. In such situations, the mixing capacity significantly declines. Kenics static mixers (KSM) were recently used to facilitate the continuous chaotic

printing of multi-material structures (**Figure 2.5D-H**)[140]. Using this technology, multi-lamellar fibers with a well-defined internal microarchitecture were created by exploiting the mixing capacity of chaotic flows (**Figure 2.5E**), which importantly were highly predictable. These fibers can be used to bioprint defined multi-material structures featuring large interfacial areas. This KSM technology is growing fast[141,142] to overcome the limitations of mixing viscous bioinks in passive microfluidic mixers.

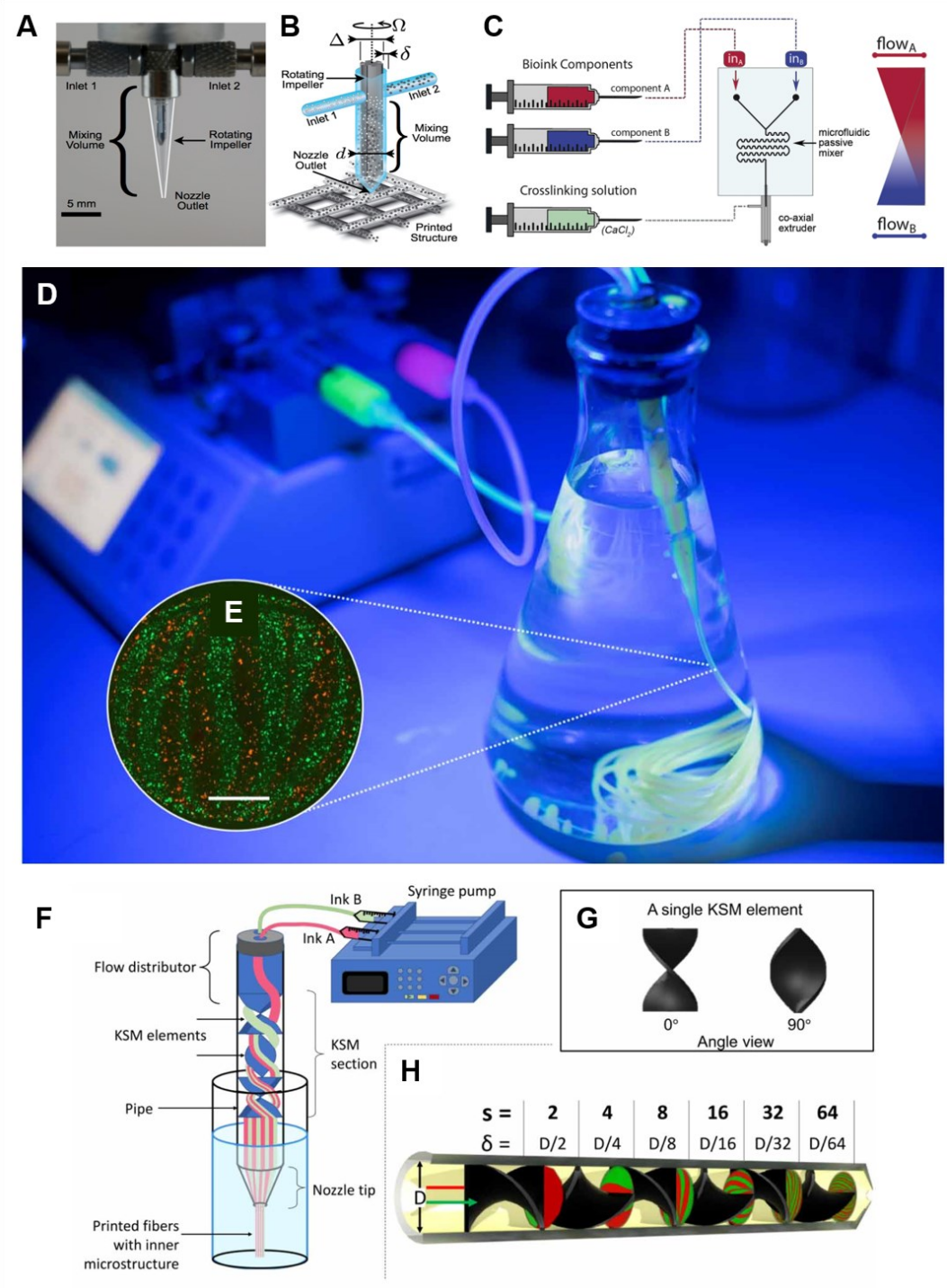

Figure 2.5. Different types of mixers used for multi-material bioprinting. A, B) Photograph and schematic of an impeller-based active mixer used for blending two bioinks. Reproduced with permission.[133] Copyright 2015, The Authors, published by National Academy of Sciences. C) Schematic design of a passive microfluidic mixer. Reproduced with permission.[137] Copyright 2019, Institute of Physics. D) Continuous chaotic printing experimental setup. E) Cross-section of the multi-lamellar printed fiber. Scale

bar: 250 μm. F) Schematic of the experimental design for the chaotic printing of two inks using a KSM and a syringe pump. G) Side views of KSM at two different angles. H) Illustration of flow splitting action in a six-element KSM with a diameter of D. The distance between lamellae is shown by δ. Reproduced under the terms of the CC-BY Creative Commons Attribution 4.0 International license (https://creativecommons.org/licenses/by/4.0).[140] Copyright 2020, The Authors, published by Institute of Physics.

2.4.1.2 Multi-nozzle bioprinting technology

One drawback of the single-nozzle technology is the risk of cross-contamination as the (bio)inks flow in one nozzle. Multi-nozzle multi-material bioprinters are utilized to resolve this shortcoming and increase the throughput. In such technology, one or more printheads with an array of nozzles are implemented for delivering various bioinks[143]. Compared to single-nozzle bioprinters, more complex features at a faster pace and a larger build volume can be fabricated when multi-nozzle technology is employed. Depending on the design complexity, each of the bioinks can flow through one nozzle or every nozzle. In the latter case, a more meticulous design of microfluidic channels is essential to ensure synchronized delivery of the bioinks to the bioprinting platform. A basic method in which each nozzle is dedicated to only one bioink was demonstrated in 2014[144]. In this work, four nozzles were mounted on separate printheads, each independently controlled along the Z-axis. Heterogenous 3D constructs with interpenetrating vasculature were successfully bioprinted, taking advantage of the fugitive properties of Pluronic F-127. In 2016, a multi-nozzle printer, named integrated tissue–organ printer (ITOP), with the capability of printing four different materials, including two bioinks, was proposed[145]. As shown in **Figure 2.6A**, this single-printhead multi-dispensing module consisted of four microscale nozzles connected to separate repositories and air pressure controllers. The researchers could successfully bioprint different organ models such as ear cartilage, skeletal muscle, and mandible bone with the aid of polycaprolactone (PCL) as the supporting material (**Figure 2.6B**) and Pluronic

F-127 as the sacrificial compartment. While elegant, the designed bioprinter is not able to fast-switch between the bioinks. The prolonged transient period results in a lower sharpness in the edges and hinders the construction of intricate multi-material tissue models.

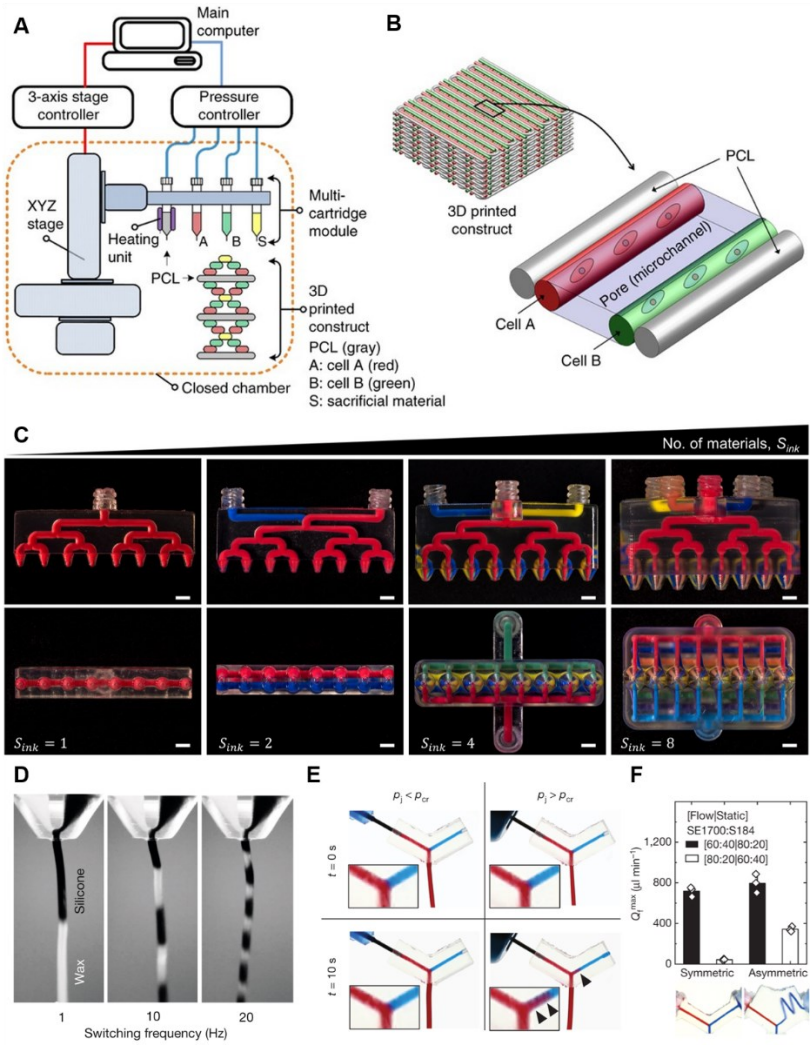

Figure 2.6. Multi-nozzle multi-material 3D printing technologies. A) The Integrated tissue-organ printer setup consisting of four separate nozzles. B) Schematic of 3D-printed basic pattern with multiple bioinks and the supporting PCL ink. Reproduced with permission.[145] Copyright 2016, Springer Nature. C) Optical images of top and side views of multi-nozzle printheads with various types of inks. D) Generating voxelated multi-material filaments at an increasing switching frequency, where only one of the nozzles is shown. E) Comparing the effect of subcritical and supercritical pressures in the occurrence of backflow. F) The effect

of using asymmetric microfluidic channels on the maximum flow of the active channel (Q_f^{max}), where only one of the nozzles is shown. Reproduced with permission.[146] Copyright 2019, Springer Nature.

Pneumatic actuators are reliable instruments to achieve fast switching between the inks[126,146]. Recently, Lewis and colleagues built a multi-material multi-nozzle 3D printer (**Figure 2.6C**), which was actuated through a series of pneumatic solenoids, enabling fast switching between the inks (up to 50 Hz)[146]. In this design, a maximum of eight different materials could flow in the nozzles by means of a microfluidic system. They used pressure-driven flows in merging microfluidic channels to achieve seamless switching between the inks (**Figure 2.6D**). One common concern with the advanced multi-nozzle designs that may negatively influence the operation of the 3D printer is the backflow from the active channel to the static channels due to the higher pressure at the junction of the channel. Pressures below the maximum critical pressure values for the active channel (P_{cr}) were used to successfully prevent the backflow into the static channels (**Figure 2.6E**). Also, it was reported that increasing the channel length for lower-viscosity inks and using asymmetric configurations could effectively mitigate the backflow (**Figure 2.6F**). Although these conclusions are derived for general multi-material 3D printing, the same concept can be potentially expanded to multi-material 3D bioprinters, with consideration of the presence of the cells.

2.4.1.3 Co-axial bioprinting technology

Co-axial nozzle (**Figure 2.7A**) is a mechanism for bioprinting multi-material core-shell structures[123,124,147,148], such as vascular constructs[149], heterogenous microfibers[150], and tumor models[151]. This technique enables the user to fabricate hollow structures with compositional and geometrical complexities. Co-axial nozzles are specifically suitable for bioinks that rapidly crosslink upon mixing with the crosslinker. Alginate is the most popular hydrogel used in co-axial bioprinters in conjunction with calcium chloride ($CaCl_2$) as the physical crosslinker. For example,

a handheld co-axial system of extrusion was developed to print multi-material structures, which resembled the brain's cortical tissue[26]. Gellan gum and the proper crosslinkers (calcium and magnesium ions) were used to print the multi-material brain-like structures through this co-axial configuration. While convenient, this method has certain limitations in resolution, accuracy, reproducibility, and production rate, which are attributed to the lack of full automation. By reconfiguring the nozzles in the co-axial design, multi-layered tubular tissues can be fabricated. This configuration was achieved by concentrically placing three nozzles with different diameters inside each other and simultaneously bioprinting a mixture of alginate, gelatin methacryloyl (GelMA), and eight-arm poly(ethylene glycol) (PEG)-acrylate with a tripentaerythritol core (PEGOA)[152]. As shown in **Figure 2.7B**, $CaCl_2$ was used in the inner nozzle to ionically crosslink the bioink. The double-layer tubular construct was subsequently crosslinked again by UV light to form a stable structure. Using this design, the users can continuously alter the shape, size, and the

number of layers in a single step without changing the nozzle. These circumferentially multi-layered constructs can be used as human cannular tissue models.

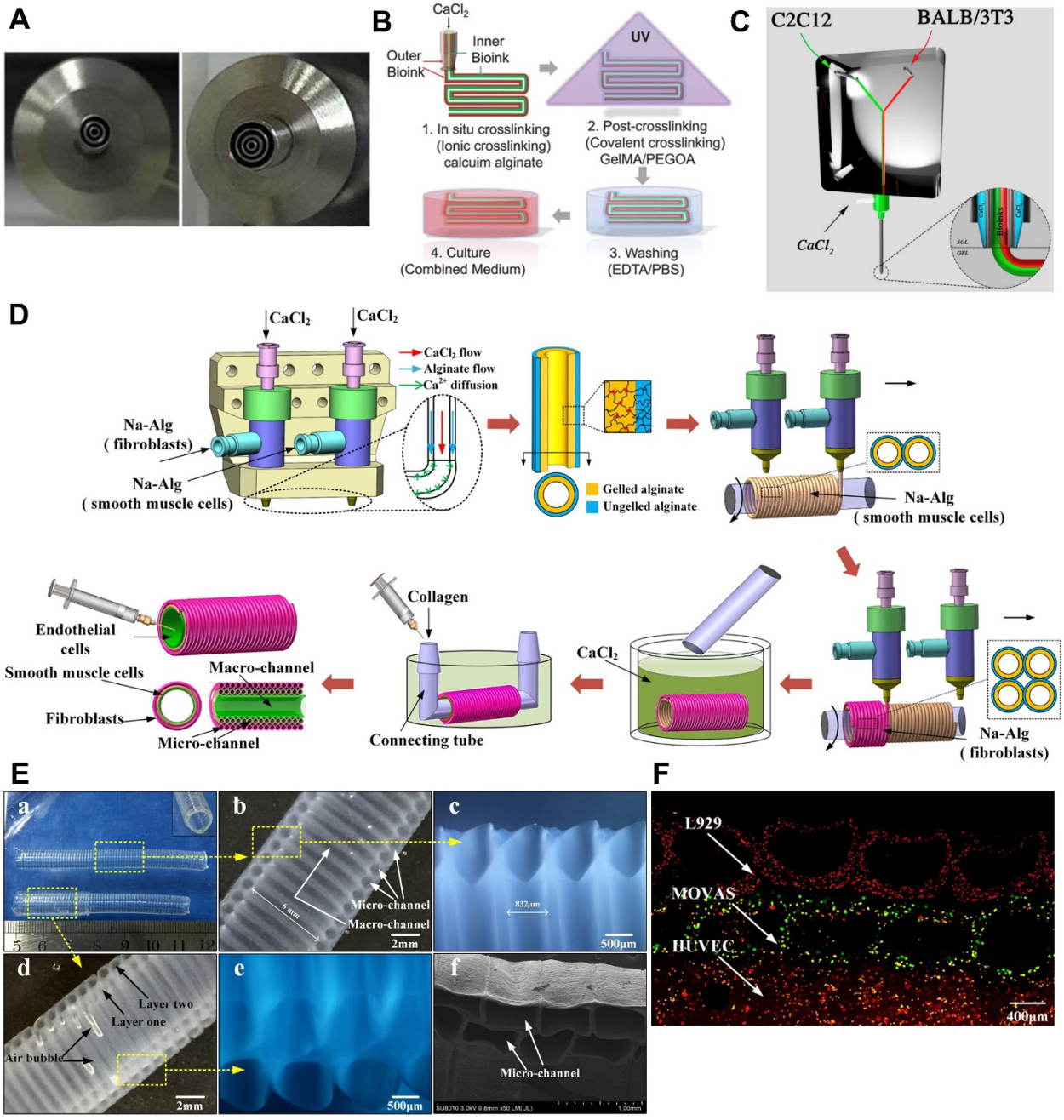

Figure 2.7. Co-axial multi-material bioprinting technologies. A) Custom-designed multi-layered co-axial nozzles with various diameters. Reproduced under the terms of the CC-BY Creative Commons Attribution 4.0 International license (https://creativecommons.org/licenses/by/4.0).[153] Copyright 2017, The

Authors, published by Springer Nature. B) Schematic illustration of multi-material bioprinting of a tubular tissue using a blend of PEG and PEGOA in GelMA/alginate as the bioink. Reproduced with permission.[152] Copyright 2018, Wiley-VCH. C) Using microfluidic systems to achieve a crosslinked Janus flow pattern of multiple cell-laden bioinks via a co-axial nozzle. Reproduced with permission.[85] Copyright 2017, Elsevier. D) A multi-scale fluidic system used for biofabricating vessel-like structures made of alginate. E) Multi-scale perfusable vessel-like constructs, (a) Samples of single-layer and double-layer constructs, (b, c) Photographs of the single-layer construct, (d, e) Photographs of the double-layer construct, (f) Scanning electron microscopy of the longitudinal section. F) Bioprinted multi-cellular vessel-like structures (red: L929, green: MOVAS, and orange: HUVEC). Reproduced with permission.[154] Copyright 2017, American Chemical Society.

Microfluidic printheads can be coupled with co-axial extruders to add more versatility to the bioprinters. Costantini et al. used this technology to achieve a Janus flow pattern of mouse myoblast (C2C12) and fibroblast (BALB/3T3) cell-laden bioinks in the printhead (**Figure 2.7C**)[85]. The compartmentalized bioprinted structure was used to study how fibroblasts could expedite the myogenic differentiation. Microfluidic printheads in conjunction with co-axial nozzles are also beneficial in fabricating more complicated configurations, such as multi-compartmental fibers[155]. Furthermore, by implementing an innovative approach with the aid of co-axial nozzles, a configuration of multi-scale fluidic systems (i.e., macrochannels and microchannels) for fabricating multi-level vascularized tissue constructs was proposed[154]. As depicted in **Figure 2.7D**, two co-axial nozzles were used to bioprint two types of cell-laden alginate bioinks (with fibroblasts and smooth muscle cells) along a rotating rod. The inner nozzles contained $CaCl_2$ as the crosslinker. After bioprinting, the rod was removed, and the double-layer spiral construct was soaked in the $CaCl_2$ bath so that the outer surface was fully crosslinked. Collagen solution was then injected in the macrochannel to enhance the adhesion of endothelial cells, which were seeded to resemble the vascular network. The method was used to fabricate single- and multi-layer vessel-like constructs (**Figure 2.7E**). Also, multi-cellular vessel-like structures containing mouse fibroblasts (L-929),

mouse vascular smooth muscle cells (MOVSMCs), and human umbilical vein endothelial cells (HUVECs) were successfully fabricated (**Figure 2.7F**). In the fabrication process, the constructs should be manually translocated between each step to receive proper crosslinking. As a result, the main drawback of this method is the increased risk of contamination. One possible improvement to such technology is automating the system and eliminating the manual translocation of the construct.

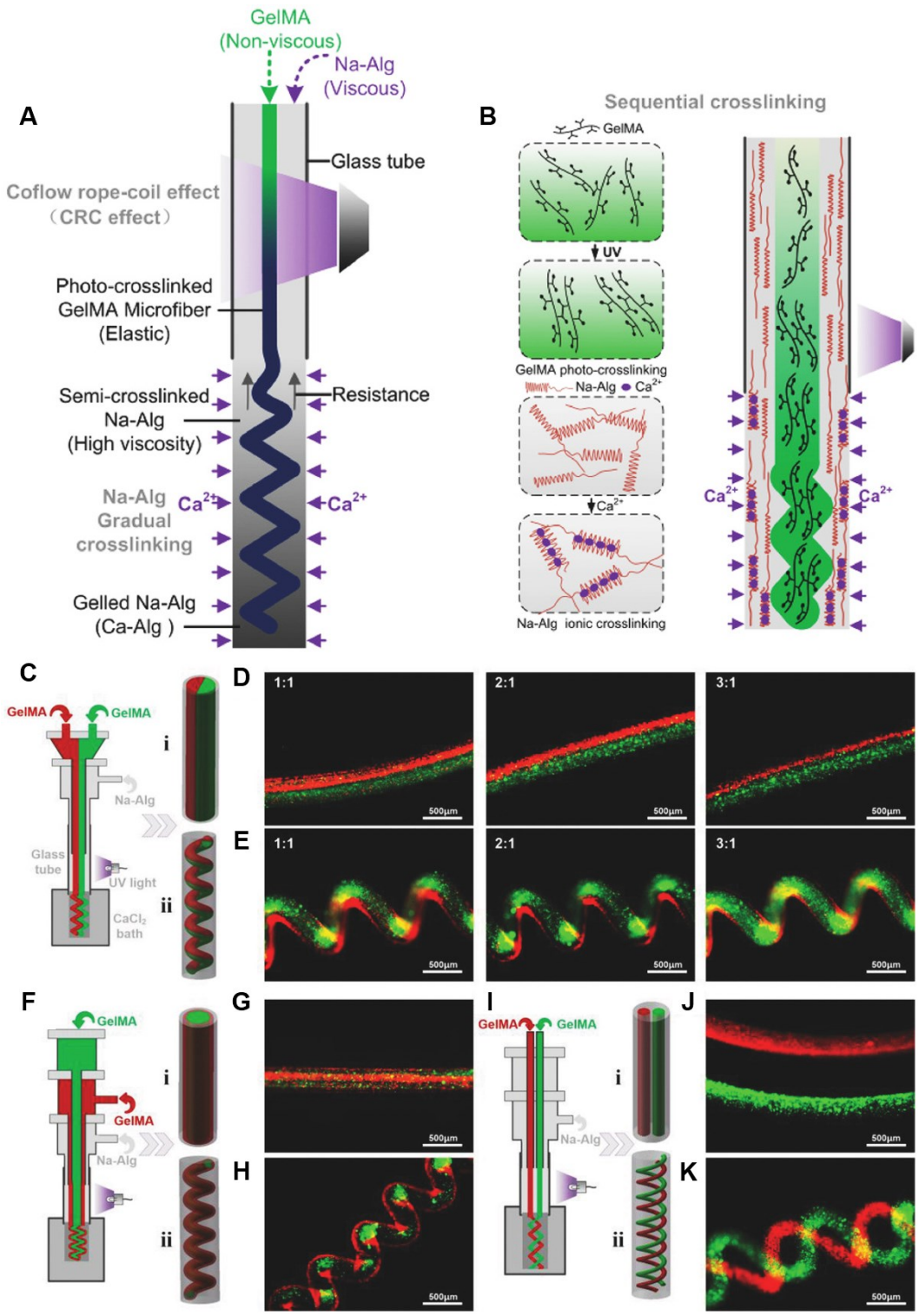

Figure 2.8. Fabrication of multi-material microfibers. A) Schematic illustration of the co-axial nozzle for the fabrication of GelMA microfibers based on the co-flow rope-coil effect. B) Two-step sequential crosslinking of the microfibers. By changing the setup and adjusting the flow rates, microfibers with

different morphologies were obtained: C, D, E) Janus structures, F, G, H) multi-layer patterns, and I, J, K) paractic configurations. Reproduced with permission.[156] Copyright 2018, Wiley-VCH.

The liquid rope-coil effect has been recently exploited as an excellent method for creating multi-material constructs[157,158]. Using this approach, Shao et al. employed co-axial multi-material bioprinting to fabricate GelMA microfibers with various morphologies[156]. Non-viscous GelMA was surrounded by viscous alginate in the nozzle, forming a laminar co-axial flow. The nozzle was connected to a transparent tube to provide enough room for a sequential crosslinking process (**Figure 2.8A, B**). As the first step of crosslinking, the co-axial flow was exposed to the UV light, which fully solidified the GelMA compartment, resulting in the formation of GelMA microfibers flowing inside alginate. The second step of crosslinking was subjecting the sheath layer to $CaCl_2$. Once alginate rapidly solidified, the velocity of the GelMA compartment dominated, and the microfibers began to coil inside the alginate matrix. By adjusting the flow rates of GelMA and alginate solutions, the nozzle diameters, and the concentration of the GelMA phase, a variety of microfiber shapes was achieved. A similar methodology was used with different cell-laden hydrogels as the core bioinks to achieve multi-compartmental microfibers (**Figure 2.8C-K**). Using HUVEC-laden GelMA as the core bioink in the co-axial configuration proved that endothelial cells could migrate towards the border of GelMA coils after 12 days of culture. Other types of cells can be used through similar co-culture systems to study the effect of microfiber shape on the interaction between the cells.

2.4.1.4 Embedded bioprinting technology

In the embedded printing approach, the hydrogel (bio)ink, which is not printable via conventional 3D printing techniques, is extruded into a liquid-like or gel-like bath that supports the fidelity of the printed structure. Besides the ability to fabricate freeform constructs, embedded printing is very effective for printing extremely low-viscosity inks through employing the aqueous

two-phase system (ATPS)[159,160]. One of the earliest works using the concept of embedded printing was reported in 2011[161]. Therein, fugitive ink filaments were printed in a photocurable hydrogel bath to form omnidirectional patterns, e.g., vascularized constructs. Later on, in 2015, an upsurge in the field of embedded bioprinting occurred by three concurrent papers. The guest-host complexes were exploited to print structures within self-healing support hydrogels through supramolecular assembly[162]. The other approach employed granular hydrogels as the supporting bath to create large-aspect-ratio 3D structures[163]. A freeform reversible embedding of suspended hydrogels (FRESH) method, which relied on the supporting bath's thermoreversible properties, was also reported in the same year[164]. Very high resolutions, down to 20 μm, have been achieved for acellular inks using the upgraded versions of the embedded printing technique[165]. This capacity is attributed to the compatibility of the embedded printing method with low-viscosity inks and the presence of a supporting matrix, which enhances the fidelity of the printed structures.

Since the embedded bioprinting job is performed inside a supporting bath, the rheological and mechanical properties of this substrate should be precisely controlled. In addition to the importance of the nozzle's inner diameter, which is also critical in conventional extrusion-based bioprinting, the nozzle tip's outer diameter is a crucial factor determining the bioprinting fidelity. A needle with a large outer diameter may disturb an excessive amount of hydrogel in the bath and preclude its recovery, which eventually results in bubble-formation or lower resolution. The nozzle's rigidity is also critical considering that nozzles with low stiffness may bend or break while moving inside the viscous hydrogel bath[125]. Embedded bioprinting can work with lower ranges of viscosity values for the bioinks comparing to other extrusion modalities. However, the existence of the supporting bath in embedded bioprinting sets practical limits on the bioink flow rate and the nozzle displacement. Particularly, since the nozzle's fast movement may agitate the supporting bath and

damage the bioprinted structure, the average printing speed is generally lower than other extrusion methods.

As for multi-material embedded bioprinting, we employed a multi-nozzle technology to perform embedded multi-material bioprinting in a Pluronic F-127 bath[125]. A set of 27G needles were bundled together and placed in metal-tube supports in a telescopic fashion so that the needles do not fail during printing. This multi-material bioprinter could print cell-laden structures with an acceptable switching rate between the materials. One impediment in this design is the limitation in the number of clustered needles, which restricts the versatility of the multi-material bioprinting. Therein, alginate with different colors was used to illustrate the feasibility of multi-material bioprinting. However, using materials with diverse rheological properties entails a custom design for each of the nozzles, which makes the multi-material embedded bioprinting a cumbersome job. The thermosensitive rheological properties of the supporting bath should also be precisely designed so that different bioinks can be properly embedded. These complications also made the embedded bioprinting technology a challenging technique for fabricating multi-material constructs. Although significant advancements have been reported in the embedded bioprinting method[165], this technique is in the early stages of development, and more effort is needed to foster its maturation for multi-material bioprinting.

2.4.2 Inkjet bioprinting

Inkjet bioprinters are perhaps the most affordable type of bioprinter and can be easily modified from commercially available two-dimensional (2D) ink-based paper-printers at a low cost[166]. However, the pricings for commercially available inkjet bioprinters are generally more expensive than extrusion or vat-photopolymerization bioprinters. One advantage of inkjet bioprinting is that it can obtain higher printing resolutions (up to 50-75 μm) compared to extrusion-based

bioprinters[38], as already mentioned. While the droplet size is usually predetermined by the printing nozzle and the viscosity of the bioink used, the resolution can be changed by the movement speed between the nozzle and the stage, bioink surface energy (contact angle between the droplet and the substrate), and the polymerization speed post-printing. For bioinks with higher viscosities (greater than 1,000 mPa s), stronger jetting mechanisms, such as highly localized acoustic pressure, can be utilized to reach ~100-μm resolution[167]. The multi-material inkjet bioprinters can rapidly and precisely deposit multiple bioinks to form heterogeneous constructs with gradient properties by spatially varying the droplet sizes of biomaterials, cells, and growth factors[168]. Another feature of the inkjet technology is that it works with bioinks with low viscosities on the order of 10 mPa s [70]. Unlike single-nozzle bioprinters, multi-material inkjet bioprinters usually do not share printheads (i.e., each material has its own nozzle)[169]. Therefore, there is limited chance for cross-contamination during the bioink switches.

Multi-material inkjet bioprinting technology has been long-explored for building tissues and their models. Some pioneer works can be traced back to as early as 2003, where organic molecules and aggregates have been shown to be able to patten onto solid supports and form stable and functional cellular assemblies[170,171]. A fairly complex printhead design, such as a 3-by-3 parallel nozzle array, was demonstrated to be a feasible way to create heterogeneous engineered tissues. The high-precision dispensing ability is especially beneficial for drug screening and development[40]. It has been demonstrated that this technology can dispense different compounds into 384-well plates for high-throughput tests, such as biochemical assay, cell-based reporter-gene assay, and cytotoxicity assay, with clean and reproducible results[172].

One main limitation of this technology is the difficulty in fabricating cellular constructs with clinically relevant sizes. This is caused by the fact that the mechanical strengths of compatible

bioinks are generally low prior to necessary crosslinking, which limits the maximum building heights of the printed constructs[38]. Due to this reason, constructs with high aspect ratios are also difficult to fabricate. Efforts have been made to overcome those challenges. For example, an inkjet bioprinting platform printed a silk fibrin/alginate bioink on a motorized stage[173]. When the bioink was collected on the stage, it gradually moved the bioprinted construct into a cell-friendly crosslinker bath while the fabrication continued for the part which was still out of the crosslinker solution. This method offers high cell viability (evidenced by greater than a 6-fold increase in metabolic activity) and high-aspect-ratio shapes (height-to-width ratio greater than 1). Other limitations of inkjet bioprinters include the incompatibility of bioinks with high cell densities (greater than 1×10^6 cells/mL) due to viscosity issues and relatively low printing fidelity compared to the vat-photopolymerization method[38]. For more technical and translational aspects of inkjet bioprinting, we refer the readers to other excellent reviews[41,68,174].

2.4.3 LIFT bioprinting

Although the LIFT technology was invented in the 1980s[175], it has rarely been applied for the fabrication of complex multi-cellular and multi-material constructs. Specific printing parameters associated with each cell-laden hydrogel comprise one of the greatest challenges of the LIFT method that limit its use in multi-material bioprinting[176]. Koch et al. designed a multi-material LIFT bioprinter using a carrier for transferring different cells coated on the donor slides (**Figure 2.9A**)[177,178]. They deposited human skin cell lines and mesenchymal stem cells (MSCs) with high survival rates[177]. Fabien Guillemot, the founder of Poietis (France), proposed a high-resolution positioning platform, allowing the exchange of up to six different donors using a carousel holder[179]. Therein, different cell types could be switched on demand using a motorized system to fabricate multi-cellular structures (**Figure 2.9B**). This bioprinter was applied for 3D assembly and patterning of multiple cells and biomaterials. However, due to the complexities of the LIFT method

regarding the required high precision and calibration, the exchange process can affect critical parameters associated with jet-initiation in the deposition procedure. A method that allows well-controlled spatial micropatterning of cell-laden beads has recently been developed. Using this method, multi-cellular embryoid bodies and tumor spheroids were produced with precise control over the size and shape of the beads (**Figure 2.9C-E**)[180]. This method is only limited to self-aggregating and self-assembling cells. Further improvement is needed in the development of affordable and accessible LIFT bioprinters for the fabrication of heterogeneous structures.

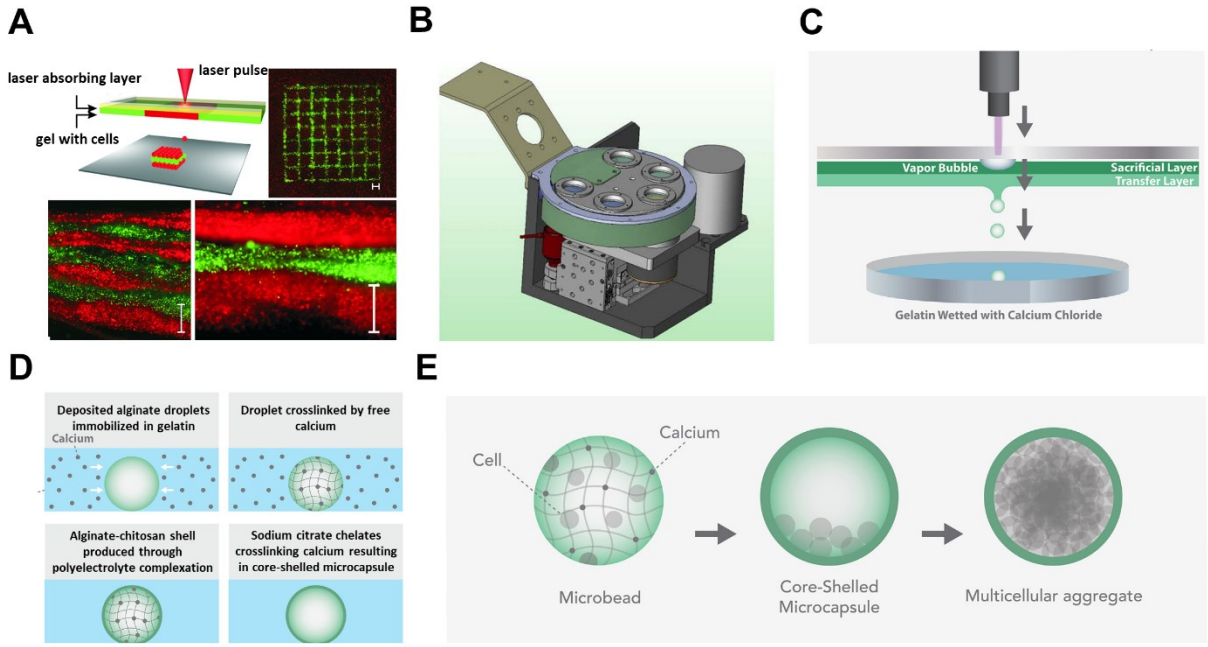

Figure 2.9. LIFT multi-material bioprinting. A) Multi-component LIFT bioprinting using rapid replacement of donor-slides by a carrier (scale bars = 500 mm). Reproduced with permission.[178] Copyright 2012, Wiley-VCH. B) High-resolution ribbon switching system based on a carousel holder with a loading capacity of five different ribbons. Reproduced with permission.[181] Copyright 2010, Elsevier. C-E) Illustration of multi-cellular LIFT mechanism. Reproduced with permission.[180] Copyright 2019, Elsevier. C) alginate bead-deposition; D) conversion of microbeads into a core-shell structure; E) aggregate-formation.

2.4.4 Vat-photopolymerization bioprinting

The past decade has seen increasingly rapid advances in vat-photopolymerization 3D printing, including microstereolithography that enables micron-scale features[182,183], continuous liquid interface production (CLIP) commercialized by Carbon enabling 100 times faster printing compared to conventional vat-photopolymerization 3D printing[184], volumetric 3D printing inspired by computed tomography[185,186], and more recently, xolography 3D printing based on using photoswitchable photoinitiators[187]. However, the majority of existing studies have focused on single-material 3D bioprinting. When compared with other bioprinting methods, the development of multi-material vat-photopolymerization-based 3D bioprinters is still relatively challenging and limited. Different strategies have been applied to overcome this problem, including using multi-vat, sequential injection, sequential deposition, and multi-wavelength.

2.4.4.1 Multi-vat-photopolymerization

The most common multi-material vat-photopolymerization 3D-printing method is based on using a system that automatically alters the resin vat. Choi et al. developed a system with multiple resin containers on a top-down DLP exposure with an automated rotating vat-carousel mechanism[188]. The use of cleaning solutions to wash the uncured resin turned out to be damaging for features smaller than ~300 μm[188]. Similarly, composite structures as small as 30 μm with shape-memory hydrogels were 3D-printed using a downward exposure (**Figure 2.10A, B**)[189]. However, top-down exposure is not considered an efficient and cost-effective method for bioprinting since the resin vat must be completely filled with cell-laden hydrogels. Zhou et al. reported a multi-material 3D printer based on the bottom-up exposure method with a rotating resin container system. To minimize cross-contamination, two different cleaning steps, including rough cleaning using two soft brushes and fine cleaning using ultrasonication along with a dryer, were implemented[190,191]. Likewise, an osteochondral composite scaffold was fabricated using an

efficient washing step with two sponges and consequently sub-merging the printed layer in a cleaning medium[192]. In the same way, Grix et al. developed a liver model with vascular networks for organ-on-a-chip applications[193]. Photopolymerizable degradable PEG-bis-(acryloyloxy acetate) (PEG-bis-AA) and cell-laden GelMA hydrogel-precursor (cell density of ~1×10^8 cell/mL) were 3D-bioprinted and lumens, as small as 200 μm, were formed by degradation of the PEG-bis-AA hydrogel after 3 days in culture (**Figure 2.10C-F**). The 3D-bioprinted liver model showed a higher albumin and gene expressions compared to monolayer controls over 14 days of the post-bioprinting period. The multi-step washing process in these methods significantly increased the fabrication time and might damage the bioprinted parts especially when they are made of soft hydrogels. In addition, several labs fabricated multi-component structures by manually changing the resin vat for different applications, such as fabrication of a porous membrane within a microfluidic device and soft hydrogel-based actuators[194–196].

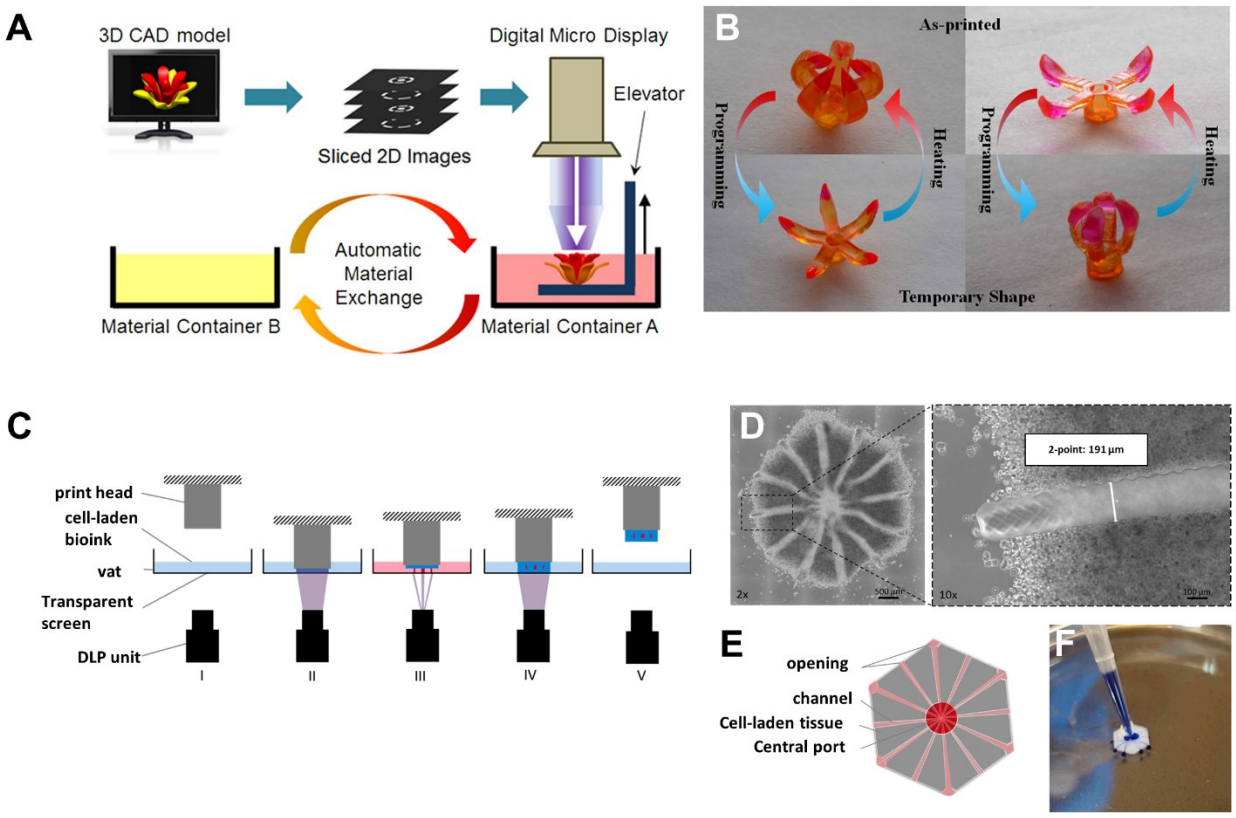

Figure 2.10. Multi-vat photopolymerization. A) Automated material-exchange process based on a top-down exposure system enabled the fabrication of shape memory structures. B) A multi-component thermo-sensitive construct. Reproduced under the terms of the CC-BY Creative Commons Attribution 4.0 International license (https://creativecommons.org/licenses/by/4.0).[189] Copyright 2016, The Authors, published by Springer Nature. C) Schematic illustration of a multi-vat multi-material bioprinter based on the bottom-up DLP approach. D-F) Vasculature networks 3D-bioprinted with degradable PEG within cell-laden GelMA hydrogel. Reproduced under the terms of the CC-BY Creative Commons Attribution 4.0 International license (https://creativecommons.org/licenses/by/4.0).[193] Copyright 2018, The Authors, published by Multidisciplinary Digital Publishing Institute.

2.4.4.2 Sequential injection

The sequential injection of different (bio)inks is another common multi-material photopolymerization approach to minimize bioink usage. This method was initially introduced by Chen and colleagues, who developed a method based on the delivery of pre-hydrogel solutions into the gap between a hydrophobic glass and a servo-stage that enabled fabrication of heterogeneous scaffolds with features as small as 50 µm. In this top-down DLP 3D printing

mechanism, rapid biomaterial-exchange with minimal material consumption was achieved by injection of 10 µL of a pre-hydrogel solution. Since the inlet of the monomer was placed within the servo stage, this method could only be used for the fabrication of lattice structures such as honeycomb and woodpile microstructures that allow efficient cleaning with free transfer of solvent within the structure. Recently, Han et al. addressed this limitation by placing multiple ink inlets equipped with precise control valves on the side of the servo stage[197]. Complex structures with features as small as 100 µm were 3D-printed using this method (**Figure 2.11A-E**). To achieve an efficient cleaning step with minimal cross-contamination, prolonged pumping time is required, which eventually increases swelling, material-consumption, and printing time that are not desirable for bioprinting.

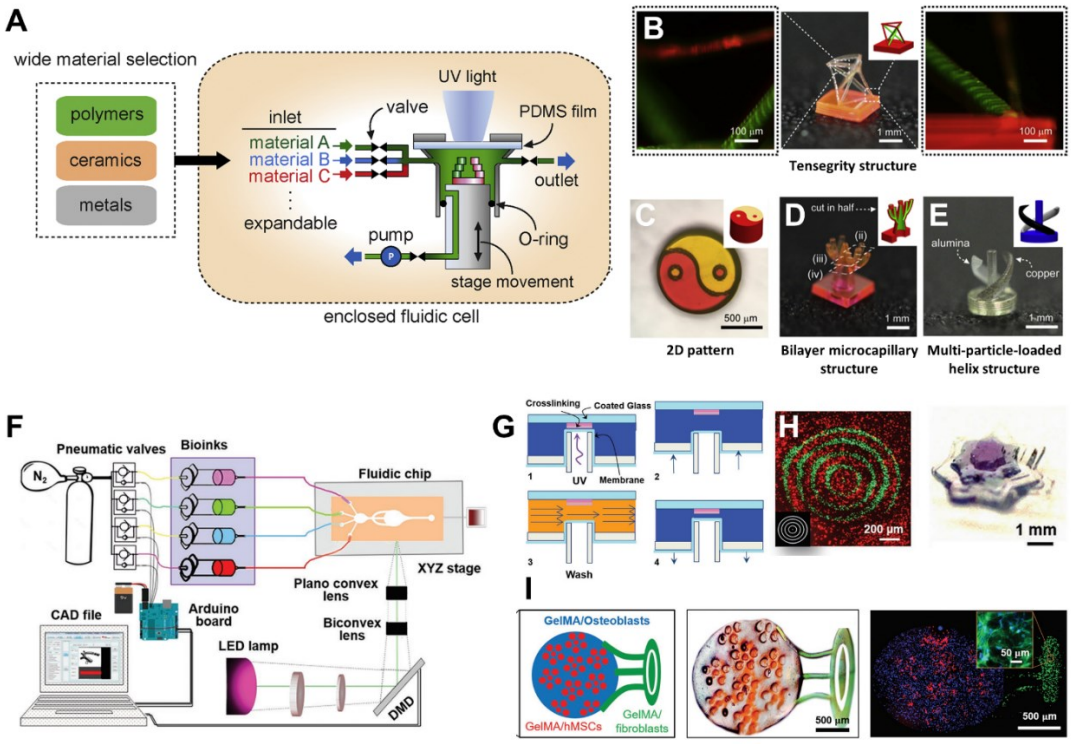

Figure 2.11. Sequential injection multi-material vat-photopolymerization approaches. A) Schematic illustration of dynamic fluidic control-based multi-material 3D printer. B-E) Multi-component structures: (B) two-component tensegrity structure with high aspect ratio beams, (C) Taiji symbol, (D) two-component

bilayer micro-capillary structure, and (E) three-component helix structure. Reproduced with permission.[197] Copyright 2019, Elsevier. F) Schematic illustration of the DLP-based bioprinter based on the sequential injection of different bioinks into a microfluidic chamber. G) the four-step bioprinting process inside the microfluidic chip. H) multi-component constructs: a two-component GelMA structure (left) and a three-component star-shaped pyramid (right). I) A tendon-to-bone model bioprinted with this approach with different cell-laden GelMA hydrogels. Reproduced with permission.[198] Copyright 2018, Wiley-VCH.

Alternatively, a multi-material DLP 3D bioprinter was developed based on the sequential delivery of up to four hydrogels into a custom-designed microfluidic chamber (**Figure 2.11F-H**)[198]. The material-exchange was performed by flushing the microchannel with phosphate-buffered saline (PBS) to wash out the previous bioink. In addition to pneumatic valves for sequential delivery of different bioinks, we implemented an elastomeric polydimethylsiloxane (PDMS) membrane within the microfluidic chip allowing in-chip depth control for constructing 3D objects (**Figure 2.11G-H**). This method was exploited to bioprint multi-component structures using three hydrogels in 20 seconds, which is significantly faster than other multi-material vat-photopolymerization methods. The same technique was successfully employed for the fabrication of multi-cellular structures such as a tumor angiogenesis model and a tendon-to-bone insertion model (**Figure 2.11I**). Satisfactory proliferation and metabolic activities were achieved on day 1 and day 7 after bioprinting. The chance of dehydration during the bioprinting process is significantly lower for this method since the printing is happening in a closed chamber. The main drawback of this method is that the remaining hydrogel precursors in the chamber (~125 μL) will be discarded during the washing step. Furthermore, the printing area is limited to the closed microfluidic chamber space that restricts the height on the Z-axis. In addition to the aforementioned methods, human induced pluripotent stem cell (iPSC)-derived cardiomyocytes and hepatic progenitor cells (hiPSC-HPCs) were 3D-bioprinted by manually pipetting of cell-material solutions between the gap[51,199]. The bioprinting process consists of printing iPSC-derived

cells followed by washing extra prepolymer solution with PBS and patterning of supporting cells that fill in the empty space of the pattern. After 7 days, high maturity marker expressions were observed in 3D-bioprinted multi-cellular liver and cardiac models.

2.4.4.3 Sequential deposition

Another approach in multi-material vat-photopolymerization is the sequential deposition of different precursors, in which no closed chamber is needed for delivering the materials. Wang et al. developed a bottom-up DLP exposure-based multi-material 3D printer by sequentially depositing different material droplets onto a rotating wheel[200]. Using this technique, multi-material structures with negative thermal expansion were successfully fabricated. This method, however, suffers from two main drawbacks in multi-material 3D printing, including the increased risk of contamination and prolonged fabrication time (~6 hours for a structure with a volume of 220 mm^3). More recently, the same group developed a novel minimal-waste material-exchange process using an air jet to remove residual resin attached to the previous layer[201]. They concluded that this method is 58% faster than existing methods that are based on cleaning solutions. However, in the case of resin contamination, the hydrophobic layer must be washed. This step, which is only functional for resins with relatively low viscosities, may disrupt the printing process. In addition, the air jet might dehydrate the printed layer and lead to unexpected deformation of the layer. Recently, the same method has been applied for 3D printing of complex hybrid structures consisting of a covalently bonded elastomer, a rigid polymer, and soft hydrogels (**Figure 2.12A-E**)[111]. Miller's group also developed a 3D bioprinter using a very similar approach capable of utilizing up to four bioinks at a time in a semi-automated way (**Figure 2.12F-H**)[202]. Using this approach, several multimaterial architectures, such as structures consisting of acellular and cellular domains, were bioprinted with a high cell density (2×10^7 cells/mL) in a GelMA bioink. This method requires manual washing and drying of the printing platform during the material-exchange

process, which significantly increases the fabrication time and could lead to reduced cell viability. Another limitation of their technology is the inability to fabricate large constructs since this method is based on the deposition of material droplets. Hohnholz et al. used a top-down exposure system equipped with an aerosol jet mechanism to sequentially deposit different resins[203]. In this approach, various compositions of different materials from one layer to another layer are attainable using the aerosol jet. Due to the complexity of the system and the use of a laser beam instead of a DLP projector, the fabrication time is longer than other multi-material vat-photopolymerization 3D printing methods. Furthermore, by employing the SLA and fused-deposition modeling (FDM) methods, a hybrid 3D printing method was proposed for the fabrication of multi-material scaffolds with soft hydrogels and rigid scaffolds[204].

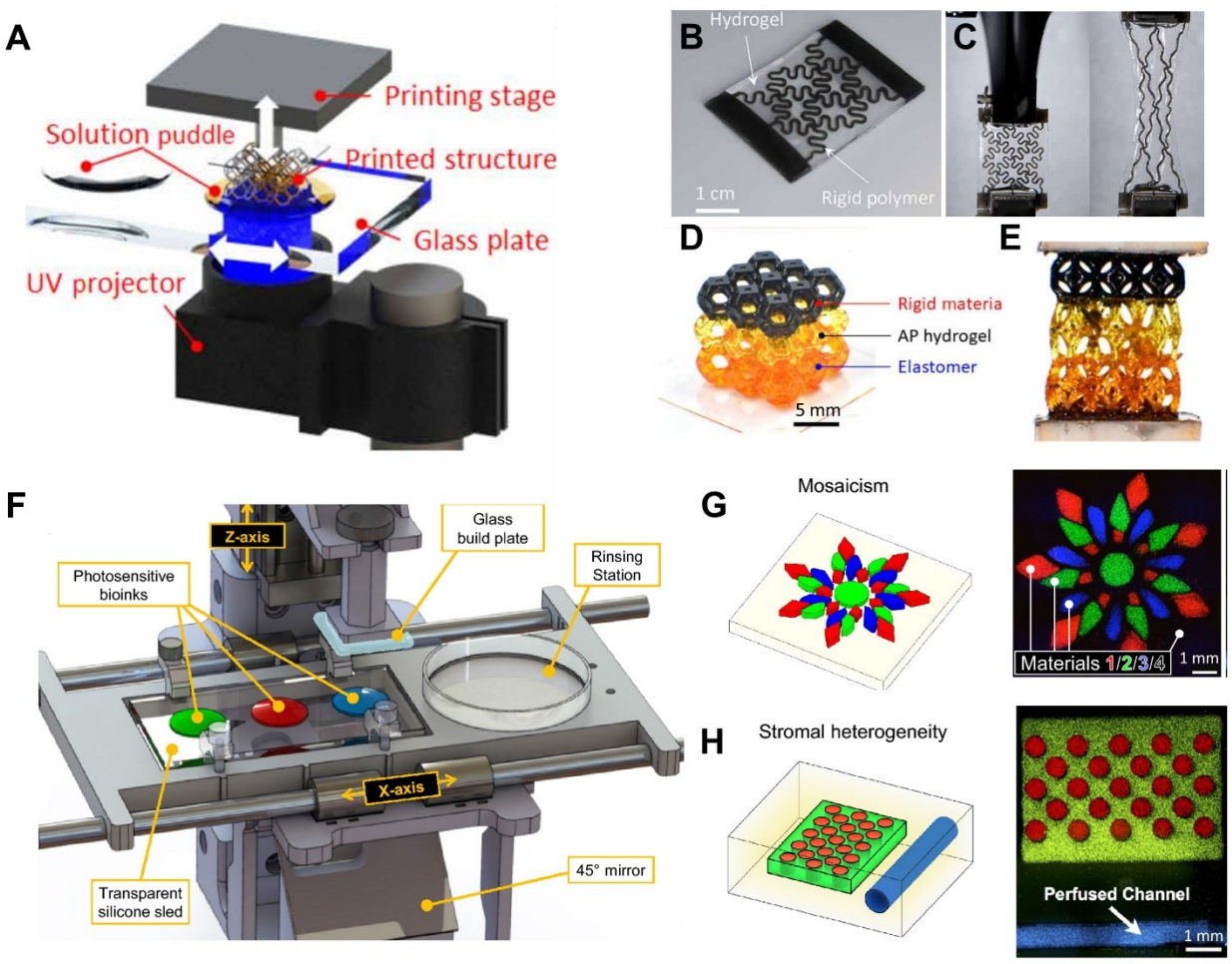

Figure 2.12. Sequential deposition in vat-photopolymerization 3D printing technology. A) High-Efficiency multi-material 3D printer based on the sequential deposition of different liquid puddles. B) Hydrogel composite reinforced by rigid polymer structure. C) Composite structure under tensile test. D) Printed multi-material structure consisting of rigid polymer, elastomer, and PEG-diacrylate (PEGDA) hydrogel. E) High stretchability of the printed structure. Reproduced under the terms of the CC-BY Creative Commons Attribution 4.0 International license (https://creativecommons.org/licenses/by/4.0).[111] Copyright 2021, The Authors, published by American Association for the Advancement of Science. F) Schematic illustration of a multi-material stereolithography bioprinter. G) Printed structure with four different bioinks. H) Heterogeneous construct with an embedded vessel. Reproduced under the terms of the CC-BY Creative Commons Attribution 4.0 International license (https://creativecommons.org/licenses/by/4.0).[202] Copyright 2021, The Authors, published by Springer Nature.

2.4.4.4 Multi-wavelength photopolymerization

In addition to the above-mentioned approaches that are based on different material-exchange mechanisms, more recently, a continuous multi-material technique was introduced based on selective polymerization of ink components using a multi-wavelength strategy[205]. The photocurable ink consisted of acrylate and epoxy monomers with their corresponding photoinitiators with different absorption spectrums. This allowed independent polymerization of various photocurable monomers using different photoinitiators and wavelengths. A soft hydrogel could be achieved by exposing the ink to blue light, whereas a stiff material can be printed under short-wavelength (UV) irradiation (**Figure 2.13A-B**). This strategy enabled the 3D printing of multi-material structures containing soft hydrogels along with hard solid epoxide networks (**Figure 2.13C-D**). Therefore, spatial heterogeneity in 3D-printed parts can be achieved by exposing the resin to different wavelengths (365 and 450 nm) to tailor the mechanical properties of the structure[205,206]. However, due to the toxicity of epoxide monomers, the application of this method is still only limited to non-biological applications. Further investigation in developing biocompatible formulation is, therefore, needed to implement this method for bioprinting.

The printing rate in multi-material vat-photopolymerization is mainly dependent on the model complexity, material-switching, and washing process. 3D printing of structures in which each layer consists of multiple materials is more laborious. The fastest material-exchange rate that has been reported is based on the sequential deposition of inks on a glass plate with the air-jet cleaning process that takes around 3 s[207]. Using this method, structures with different materials side-by-side within the same layer could be 3D-printed with a fabrication time ~2.2 times longer than single-material 3D printing[201]. In methods based on sequential injection, bioinks could be washed within 5-20 s by the subsequent flow of PBS[198]. These methods are more suitable for 3D bioprinting due to using PBS for cleaning that avoids unwanted dehydration of the printed layers. Ink-replacement

rate must be optimized based on the maximum air jet pressure and flow rate of the washing buffer that would not damage the printed layers.

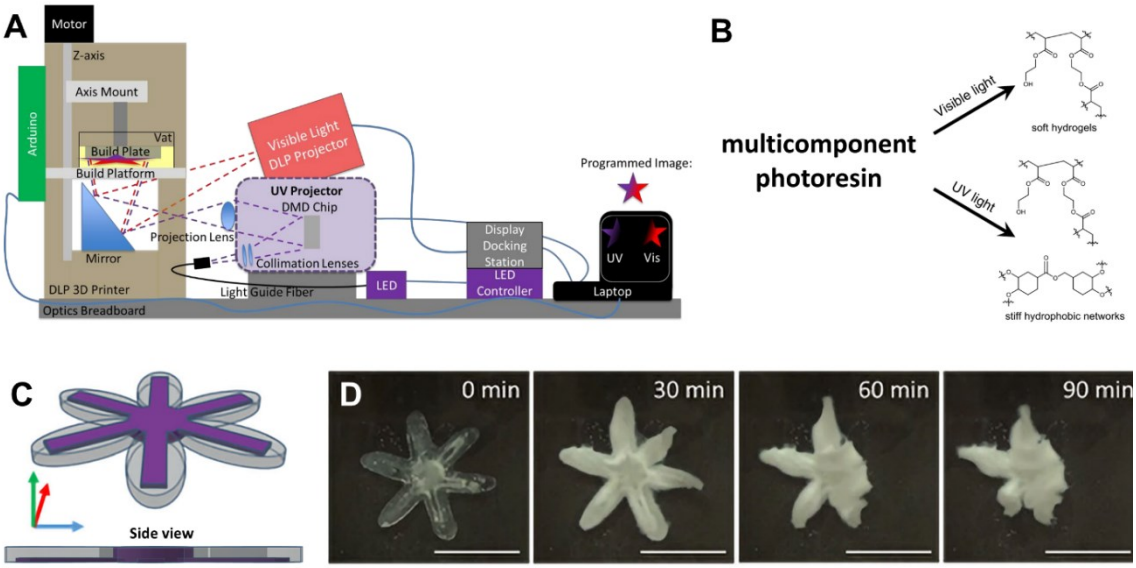

Figure 2.13. Multi-wavelength photopolymerization approach. A) Schematic illustration of the multi-wavelength 3D-printing setup. B) multi-component photoresin consisting of acrylate and epoxy monomers. C) Design of a two-component sea star construct. D) Swelling actuation of the 3D-printed part with soft hydrogels and stiff hydrophobic networks. Scale bars = 25 mm. Reproduced under the terms of the CC-BY Creative Commons Attribution 4.0 International license (https://creativecommons.org/licenses/by/4.0).[205] Copyright 2019, the Authors, published by Springer Nature.

Although outstanding advances in the field of multi-material vat-photopolymerization have been reported, several significant challenges for vat-photopolymerization bioprinting of biomimetic tissue constructs remain. The incapability for continuous printing of hydrogels with clinically relevant dimensions and the inability to fabricate multi-material complex constructs with high efficiency and accuracy are among the major concerns[189,191,195,204,208–210]. The main challenge in using multiple polymers during the polymerization process is cross-contamination while switching between the different bioinks. The washing step might lead to deformation and

dehydration of 3D-bioprinted constructs during the bioprinting process that could limit the application of this method in fabricating small-scale constructs.

In general, multi-vat photopolymerization is more suitable for fabricating organ-sized objects in comparison to other methods since the bioprinting area is not restricted by the material-exchange mechanisms. In contrast, methods based on sequential injections and deposition are more efficient in terms of material-switching, cleaning process, and bioink-consumption. Washing and material-exchange mechanisms are time-consuming and complex steps in all vat-polymerization methods other than multi-wavelength photopolymerization that would elongate the fabrication time for multi-material constructs. This could also affect the cell viability and lead to dehydration of 3D-bioprinted parts. Although many of the aforementioned techniques are used for 3D printing, they can be implemented readily in 3D bioprinting by using biocompatible photocurable bioinks. The reader may refer to other reviews on vat-photopolymerization 3D printing for more technical aspects[47,65,211,212].

2.5 Commercial multi-material bioprinters

The arrival of commercially available 3D bioprinters has enabled access to these technologies for many more research laboratories and industrial utilities. The bioprinting market is expected to reach a value of approximately 4.1 billion US dollars by 2026[213]. There are numerous commercial bioprinters in the market based on different technologies. Commercial bioprinters were initially prohibitively expensive and not accessible to most academic research facilities, making their use largely exclusive to the industry. However, many companies recently have addressed the unmet need for accessible 3D bioprinters by producing modular and affordable bioprinters. Since commercial bioprinters play an important role in the advancement of multi-material bioprinting

technologies, we devoted this section to introducing a number of commercial multi-material 3D bioprinters.

2.5.1 Extrusion bioprinters

Due to the affordability and simplicity of the extrusion-based bioprinting method, most commercial bioprinters are based on this technology with the highest market share[213]. EnvisionTEC, a globally leading 3D printing company, developed the first commercial bioprinter in 2000. The 3D-Bioplotter was initially invented by Mulhapt's group at the University of Freiburg and then commercialized by EnvisionTEC[214]. Since then, several research laboratories around the world have employed the extrusion bioprinting approach for tissue engineering and other fields of biomedical engineering. Another extrusion-based multi-material bioprinter, NovoGen MMX, was developed by Organovo in 2009 and could deliver cells and hydrogels using two syringes[79,215]. However, this company does not market its bioprinter anymore; instead, it only sells this bioprinter mostly to pharmaceutical companies for drug screening[79]. Other than the two pioneering extrusion-based bioprinters, 3D-Bioplotter and NovoGen MMX, many companies have developed bioprinters based on different extrusion bioprinting methods. Several companies such as Allevi, Aether, CELLINK, and REGEMAT use value adds-on to provide more affordable and accessible 3D bioprinters. Allevi and CELLINK, arguably two of the largest bioprinter-providers, have developed several extrusion-based bioprinters with different specifications and price ranges. Allevi 3 bioprinter has three extruders with precise temperature control from 4 °C to 160 °C enabling bioprinting a wide range of bioinks. CELLINK BIO X6 bioprinter consists of six printheads that allow fast and versatile multi-material bioprinting. Aether, another hybrid multi-material bioprinter, is capable of depositing twenty-four materials at a time using eight syringe extruders, two heated nozzles and fourteen droplet jet extruders. Aspect Biosystems, a Canadian bioprinter company, has also developed a microfluidic bioprinter based on its patented Lab-on-a-Printer

(LOP) microfluidic technology[138]. Biological fibers can be deposited with varied diameters by changing the flow rate in the flow-focusing LOP co-axial method. Similar to Organovo, Aspect Biosystem only provides its bioprinters based on partnership programs. In addition to the conventional extrusion-based bioprinters, a scaffold-free bioprinter, based on the Kenzen method, was created by Nakayama at Saga University and commercialized by Cyfuse Biomedical. This approach is capable of 3D assembling and positioning of different spheroids as building blocks of biological constructs using an array of 160-µm-thick stainless-steel microneedles[216,217]. Revotek is another scaffold-free bioprinter based on a proprietary technology named Biosynsphere which makes it suitable for fabrication of scaffold-free vascular structures. Blood vessels with iPSC-laden bioinks were successfully 3D-bioprinted using this technology and implanted into rhesus monkeys[218]. Furthermore, the BioassemblyBot (Advanced Solutions), a six-axis bioprinter, employs a robotic arm for the deposition of different materials in 3D space, enabling multi-material bioprinting[219].

2.5.2 Inkjet bioprinters

In comparison with commercial extrusion-based bioprinters, the number of available inkjet bioprinters on the market is very limited. The RASTRUM 3D inkjet desktop bioprinter by Inventia is equipped with an inbuilt laminar flow hood with a deposition capability of droplets as small as 5 nL. This multi-material bioprinter can rapidly print up to eight different droplets of cells and matrix components simultaneously in a reproducible way[220]. Ricoh, a Japanese imaging and electronics company, has developed a new inkjet head for precise and gentle deposition of different cell types. Ricoh has also partnered with Elixirgen Scientific, a pioneer company in high-speed production of iPSCs, in drug screening and precise positioning of multiple disease-specific iPSC lines[221]. The Jetlab printer, manufactured by MicroFab Technologies, is a high-precision industrial drop-on-demand piezoelectric inkjet printer with a large printing area. This 3D printer is capable

of microdispensing up to four different materials simultaneously. Since this 3D printer is not specifically designed for bioprinting, prior optimization on the viscosities of bioinks and dispensing parameters is essential to eliminate nozzle clogging during cell-laden bioprinting. Another inkjet 3D bioprinter is CellJet, which was developed based on the Digilab inkjet technology. Using sixteen independent channels, this technology ensures high cell viabilities (~95%) through non-invasive dispensing of droplets ranging from 20 nL to 4 μL by preventing cells from the adverse impact of shear forces. In addition, the bioprinter software enables full control over dispensing parameters such as the inkjet speed and the height, which are quite critical for viscous bioinks and delicate cells. This 3D bioprinter can be placed in most biological safety cabinets[222,223]. There is still an unmet need for commercially available, affordable, and on-the-bench inkjet 3D bioprinters.

2.5.3 LIFT bioprinters

Despite the complexity of the LIFT technology, it has been successfully commercialized. NGB-R^{TM} is the first commercially available LIFT 3D bioprinter that has been developed. This 3D hybrid bioprinter uses the laser-assisted bioprinting (LAB) technology along with multiple dispensers, allowing fabrication of heterocellular patterns with a single-cell resolution[57,224,225]. Besides, Poietis partnered with large cosmetic and pharmaceutical companies such as L'Oréal and BASF to assess the efficacy and toxicity of cosmetic products and drug candidates using 3D-bioprinted tissue models, such as hair follicles and human skin[226]. Precise Bio, a North Carolina-based company, is another leading company in LIFT bioprinting. It achieved the first transplantation of a 3D-bioprinted cornea graft into an animal using its innovative laser-assisted four-dimensional (4D) biofabrication technology. This technology allows the fabrication of complex tissues with single-cell resolution and spatial accuracy with high cell viability (>95%)[227].

2.5.4 Vat-photopolymerization bioprinters

Even though vat-photopolymerization is among the high-resolution and cost-effective 3D bioprinting methods, there are only a few commercially available multi-material bioprinters. To the best of our knowledge, Cellbricks is the only commercially available multi-material bioprinter based on vat-photopolymerization. This bioprinter employs rapid material-exchange using multiple vats for bioprinting of heterogeneous constructs with 10-µm accuracy[193,228]. Most of the SLA 3D printers can also be used for bioprinting cell-laden hydrogels. For example, the EnvisionTech 3D printer has been widely used in research labs for bioprinting jobs[229,230]. Lumen X, another commercial SLA 3D bioprinter, was developed by Miller's group and commercialized by CELLINK[231]. Stemaker™ bioprinter (Allegro 3D) is also a DLP-based 3D bioprinter that is capable of direct printing in multi-well plates. In addition, EFL's DLP bioprinter has been used for fabrication of nerve guidance conduits using GelMA hydrogels[232]. Although these bioprinters are not capable of performing multi-material 3D bioprinting jobs, heterogeneous structures can be successfully 3D-bioprinted by manually altering the resin container. The readers may refer to **Table 1** for a list of commercial most common multi-material bioprinters and selected applications of them that have been reported in the literature.

Table 2-1. List of commercial most common multi-material bioprinters and selected applications

Bioprinter	**Company**	**Technology**	**Selected Applications**
3D NovoGen	Organovo (USA)	Extrusion	Liver model, kidney model, intestinal

			model, vascular constructs[233–237]
3D-Bioplotter	EnvisionTEC (Germany)	Extrusion	Tendon-to-bone model, adipose tissue model[238,239]
3D Discovery™ Evolution, BioFactory™	regenHU (Switzerland)	Extrusion (capable of using electrospinning and melt electrowriting technology)	Bone-regeneration, perfusable cardiac patches, meniscus, skin[240–243]
Aether 1	Aether (USA)	Extrusion (capable of depositing twenty-four materials at a time)	Superficial skin cancer therapy[244]
Allevi 1, 2, 3	3D Systems (USA)	Extrusion (with precise temperature control from 4 °C to 160 °C)	Angiogenesis and vascularization model[245,246], Liver model[247], 3D cell culture[247]
BAT Series	nScrypt (USA)	Extrusion	Spheroid-manufacturing[248], knee cartilage[249]
BIO X, BIO X6, INKREDIBLE	CELLINK (USA)	Extrusion (compatible with	Vascularized skin graft[250], bone and

		various modular printheads)	nerve tissues[251], corneal stroma[252]
BioAssemblyBot	Advanced Solutions Life Sciences (USA)	Extrusion (six-axis printhead with a robotic arm)	Vocal fold tissue, tumor modeling[253]
Bio-Architect®-Pro, WS, x, Sparrow	REGENOVO (China)	Extrusion	Cartilage[254], sweat gland[254], skin[255], neuronal tissue[256]
BioScaffolder	GeSiM (Germany)	Extrusion	Multi-cellular tumor spheroid[257,258]
BRINTER 1	BRINTER (Finland)	Extrusion	-
Fabion 1, 2	3D Bioprinting Solutions (Russia)	Extrusion (compatible with various modular printheads)	Vascularized thyroid gland construct[259,260]
FELiX BIOPRINTER	FELIXprinters (The Netherlands)	Extrusion	Bioprinting of human iPSCs[261]
FLUX-1	Frontier Bio (USA)	Extrusion	-
Genesis™ I and II, Reactor™, Octopus™, BioFDM™	3D Biotechnologies Solutions (USA)	Extrusion	-
MedPrin	MedPrin (China)	Extrusion	Lung cancer model[262], brain tumor model[263], artificial dura mater[264]
PCPrinter BC	Particle Cloud (China)	Extrusion	Bone[265]

REG4LIFE, BIO V1	Regemat 3D (Spain)	Extrusion (compatible with various modular printheads)	Articular cartilage[266]
Revotek	Sichuan Revotek (China)	Extrusion (scaffold-free 3D bioprinting of vascular structures)	Blood vessels[267,268]
ROKIT INVIVO	Rokit (South Korea)	Extrusion (with built-in cell incubator)	Cartilage-regeneration[269], vascularized tumor model[149,270]
RX1	Aspect Biosystems (Canada)	Extrusion (Based on Lab-on-a-Printer (LOP) microfluidic technology)	Glioblastoma tumor model[271], neuronal tissue[272], brain tissue model[273], contractile smooth muscle tissue[274]
SUNP BIOMAKER	SunP Biotech International (USA)	Extrusion	Cancer model[275], liver[276]
T&R Biofab	T&R Biofab (South Korea)	Extrusion	Pre-vascularized cardiac patch[23], superficial knee cartilage and subchondral bone[277],

			organoid-manufacturing[278]
WeBio	WeBio (Argentina)	Extrusion	Cartilage regeneration[279]
Autodrop	Microdrop	Inkjet	
RASTRUM™	Inventia (Australia)	Inkjet	Production of multi-cellular spheroids[280]
CellJet	Digilab (USA)	Inkjet	Bioprinting of human MSCs[281]
Hp D300e	Hewlett-Packard (USA)	Inkjet	Skin model[282]
Cellbricks	Cellbricks GmbH (Germany)	Vat-photopolymerization	Liver model[193]
NGB-R	Poietis (France)	LIFT	MSC-patterning[283], skin model
Precise Bio	Precise Bio (USA)	LIFT	Ophthalmology[284]
Regenova, S-PIKE	Cyfuse Biomedical (Japan)	Scaffold-free bioprinting	Liver tissue model[285], glioblastoma invasion model[286]

2.6 Applications of multi-material bioprinting

2.6.1 Tissue fabrication

The current accomplishment in the bioprinting field has opened new arenas for regenerative medicine, tissue modeling, and beyond. However, many existing developments, especially at the beginning of bioprinting technology, have been limited to the creation of monocellular and

homogeneous environments. In contrast, human tissues are multi-cellular constructs with hierarchical structures. They are mechanically anisotropic and intrinsically heterogeneous. It is challenging, or even unrealistic, to use one single material to analog all human tissues. Therefore, advances in materials science and innovations in multi-material bioprinting technologies are critically needed towards the fabrication of more biomimetic tissue and organ constructs.

Multi-material dispensing systems, such as co-axial and microfluidic nozzles, can offer simultaneous deposition of different bioinks to build complex constructs. For example, the co-axial nozzle has been employed to engineer 3D brain-like structures using bioinks comprising peptide-modified gellan gum with primary cortical neurons[109]. The co-extrusion of low-viscosity bioink and crosslinker enabled by the co-axial nozzle allowed the bioprinted filaments to have the mechanical strength to fabricate laminated brain-like structures with a high aspect ratio. In such multi-material constructs, the precise arrangement of material concentration, cell distribution, and height gradients among different layers are important to resemble tissues with layered architectures.

Besides the ability to recreate the structural complexity of various tissues, another salient feature of multi-material technologies is their potential to improve the printing speed (mainly for extrusion-based bioprinters, see Section 2.4.1 for details). Because most existing extrusion bioprinting tasks happen in the ambient environment, the viability of encapsulated cells may be decremented due to the exposure to room temperature and low humidity for a prolonged period. Such a consideration is critical for fabricating large-scale cellular constructs, especially when the direct ink-writing (DIW) methods are used. Therefore, it is preferred to complete the bioprinting tasks in a quick manner. A co-axial printhead has been designed to fabricate complex liver tissue models with a compartmentalized arrangement similar to hepatic lobule structures through single-filament writing[87]. The highly customized design of the nozzle allowed the co-extrusion of

hepatocellular cells, endothelial cells, and a lumen at the same time (**Figure 2.14A-C**). Without employing this multi-material single-nozzle design, bioprinting such a construct would have been a cumbersome job as each compartment of the hepatic lobule would have to be bioprinted separately using a single-material printhead. The technology enabled the buildup of multi-scale functional, heterogeneous, and multi-cellular hepatic structures in a facile and rapid fashion. Other tissue-engineering applications are also achievable with adjustment to the co-axial nozzle design.

So far, single-nozzle technologies have been demonstrated to accommodate the co-extrusion of several different bioinks at the same time[126]. It has been shown that human dermal fibroblasts, human hepatocellular cells, MSCs, and HUVECs could be hierarchically assembled and co-cultured using such a system to form complex tissues. Microfluidic nozzles can also be used in conjunction with co-axial nozzles to fabricate filaments with compartments containing different bioinks. An example of using such a hybrid nozzle is the printing of PEG-fibrinogen/alginate bioinks[85]. The alginate content of this compartmented bioink was ionically crosslinked by a crosslinker solution from the co-axial nozzle, therefore enabling the DIW ability of the low-viscosity bioink. The printed constructs were further stabilized by UV irradiation to initiate free-radical polymerization of the PEG content before the removal of alginate with ethylenediaminetetraacetic acid (EDTA). The co-cultured constructs showed a proper spread of C2C12 and highly aligned long-range multi-nucleated myotubes, with abundant and functional expressions of myosin heavy chain and laminin[85]. The better recapitulation of the whole muscle histoarchitecture in vitro and in vivo by bioprinted multi-cellular hydrogels compared to cast-hydrogels also revealed the advantages of the multi-material bioprinting technology.

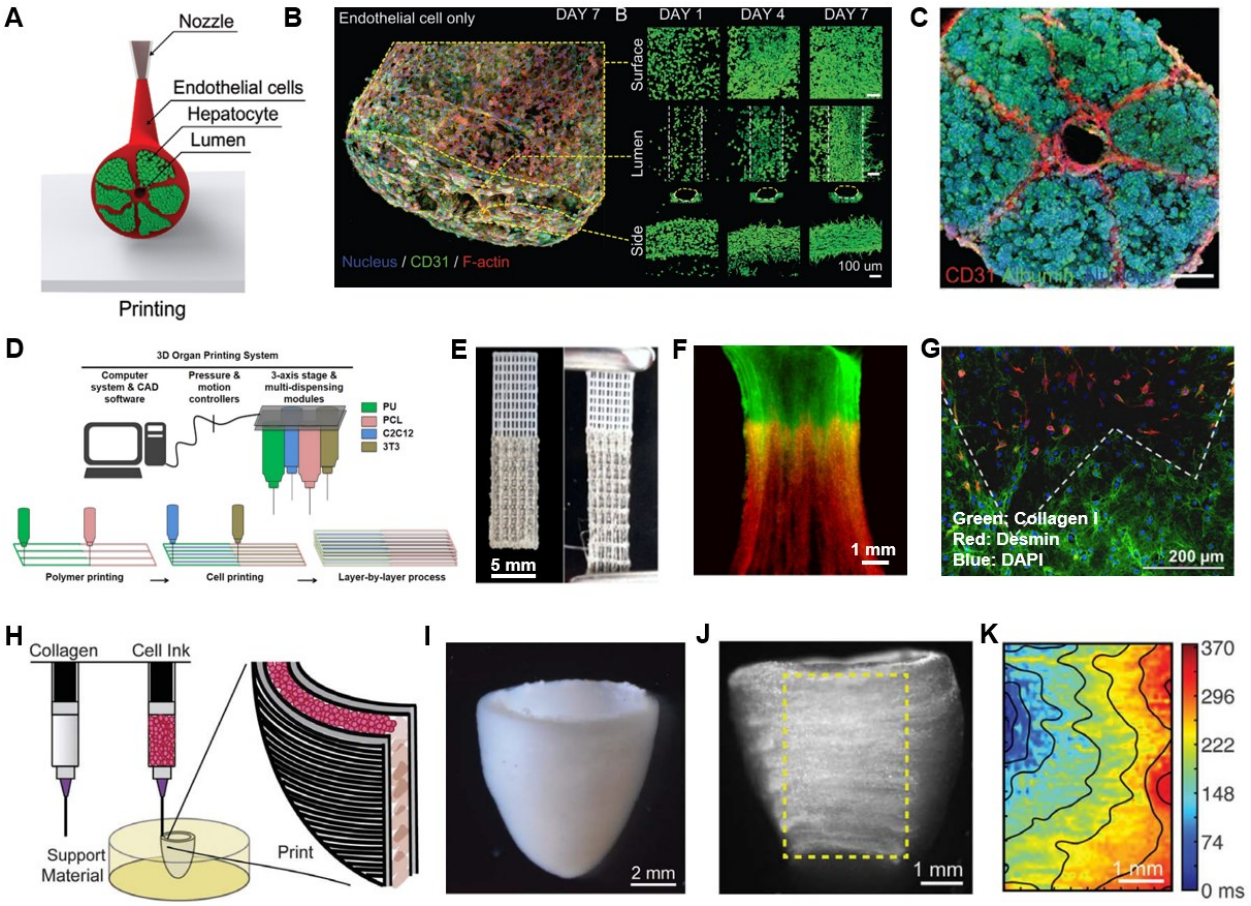

Figure 2.14. Extrusion-based multi-material bioprinting for tissue-fabrication. (A) Schematic illustration of multi-material extrusion printhead design for hepatic lobule printing. (B) Left: Immunostaining of CD31 (green) and f-actin (red) for the bioprinted epithelial cells. Nuclei were counterstained in blue; right: Live (green) and dead (red) staining showing morphological changes and viability. (C) Immunostaining of CD31 (red), albumin (green), and MRP2 (green) for the bioprinted hepatic lobule with hepatocellular cells. Nuclei were counterstained in blue. Reproduced with permission.[87] Copyright 2020, Wiley-VCH. (D) Schematic showing the multi-material bioprinting setup for dual-cell MTU constructs fabrication. (E) Tensile behavior of the bioprinted MTU with both soft and rigid regions. (F) Fluorescence image showing bioprinted MTU after 7-day culture (green: DiO-labeled C2C12 cells; red: DiI-labeled NIH/3T3 cells). (G) Differential expression between the two cell types at the interface region (depicted by the dotted line) is observed. Reproduced with permission.[287] Copyright 2015, Institute of Physics. (H) Schematic of dual-material FRESH printing using collagen ink and a high-concentration cell ink. (I) Micrograph of FRESH-printed multi-component ventricle. (J) Side view of FRESH-printed ventricle stained with calcium-sensitive dye showing uniform cell distribution. (K) Calcium mapping of the

subregion [yellow box in (J)] showing spontaneous, directional calcium wave propagation. Reproduced with permission.[165] Copyright 2015, American Association for the Advancement of Science.

Bioprinters equipped with multiple dispensing modules are helpful in fabricating multiple materials with different processing conditions. For instance, (bio)inks that require different printing temperatures and pressures can be loaded into separate extruders and be printed individually at their own desirable conditions. This is particularly useful when fabricating materials with dissimilar natures, such as thermoplastics and hydrogels. Printing such combinations is important to provide mechanical resemblance while maintaining cellular support. The muscle-tendon unit (MTU), for example, possesses regional differences in cell types and mechanical properties[287]. Muscle is predominately composed of elastic fibrous myofibers, while the tendon is stiff and rich in collagen fibers. It is traditionally challenging to mimic such distinctly different environments with a single material system. However, bioprinters with multi-material dispensing capacities can integrate the two parts seamlessly. A study bioprinted an MTU construct with thermoplastic polyurethane (PU)/C2C12 myoblasts-laden bioink and PCL/NIH-3T3 fibroblasts-laden bioink to mimic the muscle and tendon parts, respectively. The bioprinted MTU comprised of both soft and stiff sides, similar to the real tissue. The excellent viability, highly aligned cell morphologies, and increased MTU-associated gene expressions showed the potential of this multi-material bioprinting strategy for the reconstructions of complex tissues (**Figure 2.14D-G**).

Multi-nozzle bioprinting can also enable the direct writing of bioinks that do not comply with suitable rheological properties for bioprinting. One example is decellularized ECM (dECM)-derived bioinks. They have been proved to provide an optimized microenvironment leading to the growth of cells for specific tissues[288]. However, they are usually too weak (i.e., low yield stresses)

to withstand their weight during fabrication, resulting in poor spatial resolution. An exemplary printing method for providing stable structural support to soft biomaterials is to dispense the low-viscosity bioinks within a stiff printed construct. The bioprinting of dECM bioinks within printed PCL structures has been demonstrated to greatly improve printing fidelity[288]. Similarly, a study employed cell-laden hydrogels, PCL, and Pluronic F-127 to fabricate human-scale tissue constructs, such as ear, bone, and muscle[289]. PCL and sacrificial Pluronic F-127 ensured the stability of the bioprinted structures during and after the fabrication, respectively. The cell-laden hydrogels were found to secrete the corresponding ECM with demonstrated long-term functionalities.

Multi-material bioprinting has been implemented in embedded bioprinting as well. As mentioned before, embedded bioprinting allows the deposition of multiple bioinks within a supportive liquid reservoir. The freeform modeling ability and the compatibility with low-viscosity bioink-writing comply well with the trend of multi-cellular whole-organ fabrication. Cells and microtissues can also be bioprinted directly through this method[290]. A multi-material bioprinting system comprising a collagen ink, a cell-only bioink, and a gelatin-based supporting bath displayed the potential to recreate cardiac ventricles and tri-leaflet valves with high resolution[165]. The bioprinted ventricles containing human cardiomyocytes exhibited synchronized contractions and directional action potential propagation, recapitulating the structural, mechanical, and biological properties of native cardiac tissues (**Figure 2.14H-K**). Another study employed embedded bioprinting to bioprint decellularized cardiac bioinks[291]. The fabricated multi-material, thick, vascularized, and perfusable cardiac patches recapitulated the structural, immunological, and anatomical properties similar to those of human hearts. Cell viability could be well-preserved owing to the mild and all-liquid environment of the supporting reservoirs. This cell-friendly feature

is important for time-consuming multi-material fabrication on a whole-organ scale. Other novel functions such as the erasing of existing filaments by withdrawing the extruded bioinks also offer flexibility to correct errors during a complicated tissue-construction task[36].

2.6.2 Vascularization

Most tissues in the human body require vessels and microvasculature systems to supply oxygen and nutrients and to remove wastes. Although biocompatible hydrogels have been shown to support cellular activities, their pore sizes are typically on the nanometer scale and incapable of enabling sufficient mass transfer when the thickness of the scaffolds is greater than ~800-1,000 μm[166]. Vascularization is critical to ensure the survival and functions of thick scaffolds but is a major challenge in the fabrication process at the same time. The precise positioning of biomaterials opens the opportunities for creating controllable, repeatable, and freeform modeling of engineered vascular channels. An intuitive strategy is to leave spacings between printed filaments as open pores or channels. Such spacings have been proven to effectively support cell survival in relatively large constructs[292]. However, the open pores and channels generated using this strategy may not be reliable. For instance, the swelling, shrinkage, and degradation of printed hydrogels can be significantly affected, or the construct may become structurally unstable, which may clog the spacings. The ECM deposition inside scaffolds by cells can also deteriorate the channels[293].

Multi-material bioprinting can be employed for fabricating physiologically relevant vasculature through co-printing of hydrogel and sacrificial materials. This strategy relies on the removal of sacrificial channels within the bioprinted hydrogels after the scaffold fabrication. Pluronic F-127 is a thermosensitive ink often used as the sacrificial material[294]. This thixotropic material has an excellent shear-thinning property favoring the extrusion bioprinting process but resumes high yield stress quickly when shear stress is removed so that the printing fidelity is

preserved. Cell-laden hydrogels can be bioprinted or cast surrounding the sacrificial channels. Pluronic F-127 is subjected to phase-transition and becomes hydrophilic when the temperature is lowered and therefore can be flushed away at 4 ℃ or lower, resulting in multi-cellular and heterogeneous vascularized tissue constructs[294]. HUVECs can be seeded to the channels to provide long-term perfusion stability. Using this approach, multi-material bioprinting was employed to fabricate vascularized scaffolds with a large thickness (>1 cm)[295]. These constructs have been demonstrated to support long-term cell survival for over 45 days[295]. Programmable cellular heterogeneity and in situ development of MSCs within the bioprinted vascularized scaffolds have also been shown to recapitulate physiologically relevant features.

Other thermosensitive biopolymers have also been explored in conjunction with multi-material bioprinting technologies to create vascularized constructs. Studies on the co-printing of matrix bioinks and gelatin-based sacrificial inks have provided a vascularization solution[296]. Both matrix and sacrificial inks can be printed adjacent with no spacing needed to establish void-free multi-material structures. The matrix phases can be crosslinked during fabrication, while the sacrificial ink can be removed through mild triggers, such as temperature change. The embedded endothelial cells can then be released from the sacrificial bioink to functionalize the channels with a confluent endothelial layer. Such an approach avoids structural collapse and instability during the fabrication of mechanically weak materials (**Figure 2.15A-B**). A similar idea has also been explored on the co-extrusion of collagen and gelatin bioinks, in which HUVEC-laden gelatin was used to print sacrificial vascular channels[297,298]. The functional vascular channels with perfused open lumens were capable of supporting cell viability in scaffolds up to 5-mm-thick. Such a strategy enabled by multi-material bioprinting shows great potential to investigate fundamental mechanisms of vascular functions and maturation under physiological flow conditions.

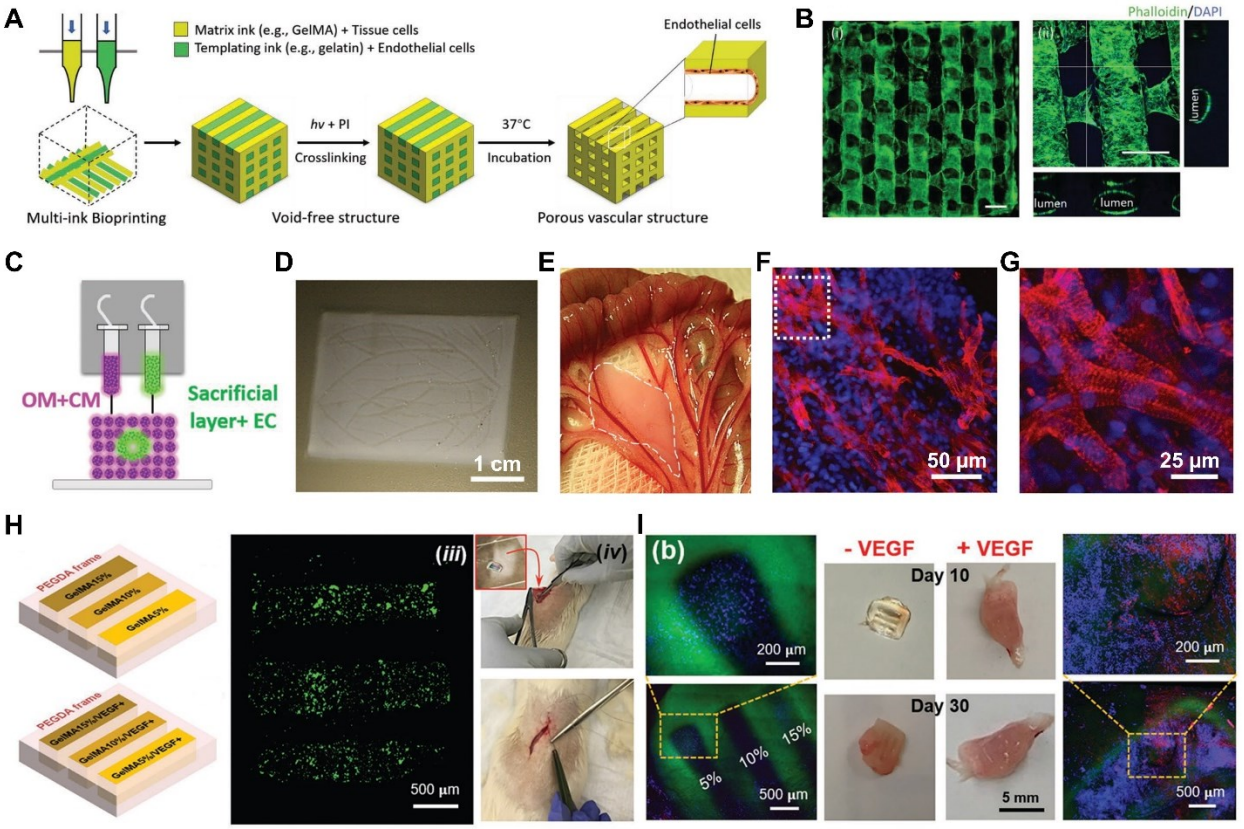

Figure 2.15. Vascularization strategies with multi-material bioprinting. (A) Schematic of the void-free 3D bioprinting process, where a biocompatible templating bioink (green) and a matrix bioink (yellow) are printed side-by-side, followed by photo-crosslinking of the matrix phase and 37 °C incubation to release the templating phase. Preloading endothelial cells in the templating bioink allows in situ endothelialization of the channels. (B) The widespread formation of endothelialized channels after 7 days of culture. Reproduced under the terms of the CC-BY Creative Commons Attribution 4.0 International license (https://creativecommons.org/licenses/by/4.0).[296] Copyright 2020, The Authors, published by Wiley-VCH. (C) Schematic showing the multi-material bioprinting of vascularized constructs with sacrificial materials. (D) A bioprinted vascularized cardiac patch. (E) Transplantation of the printed patch in between two layers of rat omentum. Dashed, white line highlights the borders of the patch. (F-G) Sarcomeric actinin (red) and nuclei (blue) staining of sections from the explanted patch. Reproduced under the terms of the CC-BY Creative Commons Attribution 4.0 International license (https://creativecommons.org/licenses/by/4.0).[291] Copyright 2019, The Authors, published by Wiley-VCH. (H) A concentration-gradient model comprising

PEGDA and GelMA hydrogels generated by multi-vat-photopolymerization bioprinting. (I) Photographs showing retrieved implants with evidence of vascularization within VEGF-laden constructs. Reproduced with permission.[198] Copyright 2018, Wiley-VCH.

Embedded multi-material printing of sacrificial channels has been utilized to vascularize thick scaffolds with biomimetic vasculature structures[161]. A study printed sacrificial gelatin channels inside a supporting matrix composed of patient-specific iPSC-derived spheroids[14]. The rapid building of perfusable vascularized constructs with high cell density ($\sim 1 \times 10^8$ cells/mL) enabled patient- and organ-specific tissues at the therapeutic scales. A similar approach was also adopted to bioprint vascularized cardiac patches[291]. Endothelial cells maintained high viability after bioprinting and formed physically robust vessels after gelatin channel removal. The functionality of the vascularized patches was evaluated by transplanting to rat omentum. The cells inside the patches exhibited elongated and aligned morphology with massive striation, which indicated functional contractility potential (**Figure 2.15C-G**).

Multi-material bioprinting through co-axial nozzles is another prominent advancement towards the reconstructions of vasculatures. This type of printing nozzle accommodates the interior flow of the crosslinker solution surrounded by the exterior flow of (bio)inks, leading to the formation of hollow microchannels that are perfusable. Sodium alginate and $CaCl_2$ ionic crosslinker are one of the most common combinations. Engineered vessels made of other materials, such as GelMA, hyaluronic acid (HA), cellulose, and dECM, have also been explored using this method in conjunction with their associated crosslinking mechanisms[299–301]. Circumferential multi-layered tubular tissues can be created with multi-channel multi-material co-axial bioprinters. For example, cannular urothelial tissue constructs containing human urothelial cells and human bladder smooth muscle cells, or cannular blood vessels containing HUVECs and human vascular

smooth muscle cells, have been bioprinted with such a system[152]. The bioprinted cannular tissues were perfusable with the cell culture medium to promote the growth and proliferation of the embedded cells.

Multi-vat-photopolymerization, as a fast and high-resolution multi-material bioprinting modality, has been explored to (bio)print the vasculature. As a result of its superlative resolution, this method is favorable for bioprinting minuscule vasculatures. Through sequential changing of (bio)inks with and without endothelial cells, prevascularized tissues with complex 3D microarchitectures can be created. A study using anastomosis between grafted prevascularized bioprinted constructs and the host vasculature showed the formation of functional vasculature within the engineered tissues[302]. Heterogeneous PEGDA and GelMA constructs printed by a microfluidics-enabled multi-material vat-photopolymerization bioprinter have also been tested for their neovascularization potential in a rat model. The presence of vascular endothelial growth factor (VEGF) in the bioprinted constructs led to more blood vessel-formation in the implants compared to those without VEGF (**Figure 2.15H, I**)[198]. In terms of the technology itself, the relative ease to scale up in multi-vat-photopolymerization can potentially lead to the creation of large-scale vascularized constructs for tissue repair or even organ transplantations. Gene expression could also be patterned through tuning the channel network architecture, medium temperature, and flow directions, which expands the capacity to regulate cellular development and regeneration through vascularization[303]. However, it should be noted that the generation of bioink wastes associated with vat-photopolymerization may increase the costs and therefore limit the scalability.

2.6.3 Organ-on-a-chip (OoC) models

OoC is a type of microfluidics-based cell culture platform recreating the key elements of biological tissues[304–306]. In the past decade, various OoCs have been developed to mimic different human organs for fundamental biological studies, tissue/disease modeling, and drug screening[307–311]. Traditional OoC fabrications involve a steep learning curve and time-consuming manual operations, which hinder their adoption to biomedical research labs. However, the flexible and automated bioprinting technology can bring more user-friendly fabrication approaches to researchers with rapid prototyping capability. To this end, multi-material bioprinting facilitates the construction of functional OoC models with hierarchical architectures and spatial heterogeneity.

OoC models often require the arrangement of multiple cell types and ECM-mimicking materials in a spatially defined fashion to resemble the physiological environment of individual organs. One advantage of OoC model fabrications using multi-material bioprinting is the design freedom offered by this technology. Cell types, amounts, and spatial arrangements can be controlled with relative ease. The 3D environments provided by the bioprinted constructs, usually composed of polymeric hydrogel networks, have been shown to yield more realistic cellular behavior such as spreading and migration compared to locally 2D cultures in most conventional OoCs. For example, a multi-cellular liver OoC model containing hepatocytes and endothelial cells has been developed (**Figure 2.16A-C**)[312]. The co-culture of these two cell types showed significantly enhanced liver functions, such as higher values of urea and albumin secretions. The OoC model can also be bioprinted in conjunction with conventional 3D printing to yield a complete OoC device to further improve the fabrication and research efficiencies[312].

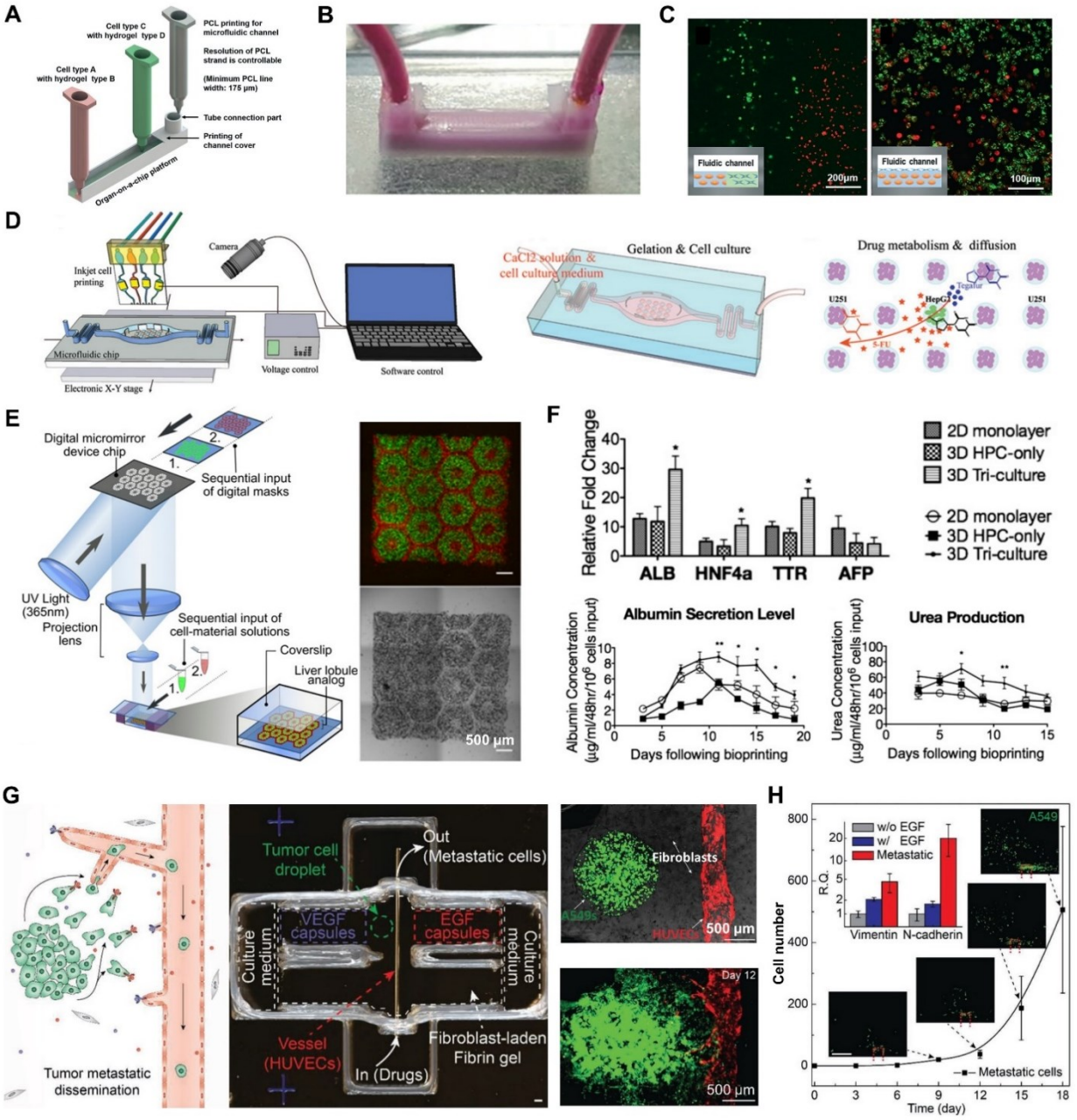

Figure 2.16. OOC and tumor modeling with multi-material bioprinting. (A) Schematic illustration of the 3D bioprinting technology for the OOC applications. (B) Digital image showing a bioprinted liver chip. (C) Various configurations of cells and biomaterials within the printed chips. Reproduced under the terms of the CC-BY Creative Commons Attribution 3.0 International license (https://creativecommons.org/licenses/by/3.0).[312] Copyright 2016, Royal Society of Chemistry. (D) Schematics showing precisely controlled multiple-cell patterning in microfluidic chips by inkjet printing

and the detection of drug metabolism and diffusion. Reproduced with permission.[313]. Copyright 2016, Royal Society of Chemistry. (E) Multi-vat-photopolymerization bioprinting of hydrogel-based hepatic construct. (F) Gene expression profiles and albumin and urea secretion levels of HPCs from 2D, 3D single-cellular, and 3D multi-cellular cell cultures. Reproduced with permission.[51]. Copyright 2016, The Authors, published by National Academy of Sciences. (G) A 3D-bioprinted in vitro tumor model mimicking metastatic dissemination. (H) Plots and micrographs of the population of disseminated A549 lung cancer cells detected in the collection chamber versus time. Reproduced with permission.[314] Copyright 2019, Wiley-VCH.

Multi-material bioprinting can assist microfluidic devices with patterning cellular constructs for high(er)-throughput detection and screening[315]. A study utilized a multi-material inkjet bioprinter to dispense cell-laden alginate hydrogels to form precisely distributed cell arrays in a microfluidic chip (**Figure 2.16D**)[313]. Hepatocellular carcinoma (HepG2) and glioblastoma tumor (U251) cells were co-patterned for drug metabolism and diffusion tests under a biomimetic environment. The efficacy enabled by multi-cellular bioprinting of the cell arrays can significantly reduce the extent of laborious experimental work from fabricating multiple conventional microfluidic devices. In addition to cell-laden hydrogels, the array can also be composed of cell spheroids. The response of multi-cellular OoC models could be comparable to the corresponding animal model, which confirmed the utility of this technology for biological testing and potentially facilitate drug development[316]. With the aid of multi-material bioprinting technologies, the ability to recapitulate human physiology and disease states can potentially exceed the animal models and offer more accurate therapeutic prediction[317]. Multi-material bioprinters with hybrid modules have the potential to further streamline the fabrication steps and decrease costs (both material- and financial-wise). An exemplar is a structurally heterogeneous skin model/device bioprinted with a combination of extrusion and inkjet modules[318]. Reductions of 50-fold in cost and 10-fold in

culture medium-consumption were achieved compared to traditional cell culture platforms. Such migration from traditional cell culture platforms to bioprinted microdevices has great socio-economical implications and could potentially decrease the amount of time and cost for technological translations in a greener way.

Sophisticated miniature biological constructs have also been developed with the assistance of multi-material vat-photopolymerization bioprinting. For example, human-derived hiPSC-HPCs, adipose-derived stem cells, and HUVECs have been demonstrated to pattern into microscale hexagonal architecture, representing the building unit of the hepatic tissue (**Figure 2.16E**). Multiple folds of increases in the morphological organization, higher liver-specific gene-expression levels, increased metabolic product-secretion, and enhanced cytochrome P450-induction were observed from constructs created by multi-material bioprinting (**Figure 2.16F**). The vascularized hepatic model showed both phenotypic and functional enhancements, which is essential for building personalized platforms for in vitro drug screening and disease studies[319]. A similar liver spheroid model with perfusable intrinsic channels has been established with multi-material vat-photopolymerization bioprinting[193]. The strengthened metabolism and gene expressions compared to 2D culture models support long-term drug screening for pharmaceutical developments.

2.6.4 Tumor modeling

Tumors are dynamic 3D ECM networks consisting of stromal, immune, and vascular cells[320]. It is challenging for 2D tumor models to recapitulate these multi-cellular, highly heterogeneous microenvironments, which yield non-physiological cellular behavior, such as altered gene expressions, cell-cell interactions, and drug responses, among others[321]. Multi-material bioprinting can mimic the complicated 3D microenvironments of tumors and therefore has the potential to

create better biomimetic tumor models compared to traditional methods[151,322]. For instance, an in vitro cervical tumor model comprising Hela cells and gelatin/alginate/fibrinogen promoted cell proliferation, matrix metallopeptidase (MMP)-expressions, and chemoresistance when compared with 2D planar models[323]. Therefore, multi-material bioprinting is becoming a standard approach to recapitulating the multi-cellular, hierarchically architectured, and dynamic microenvironments of tumors.

Bioprinted heterogeneous tumor models enable the study of the dynamic tumor progression process. For instance, a few recent studies on triple-negative breast cancer cells are focused on the development of multi-cellular tumor spheroids composed of MDA-MB-231 triple-negative breast cancer cells and IMR-90 cancer-associated fibroblasts with the aid of multi-material bioprinting[257,258]. The flexibility of multi-material bioprinting allowed convenient construction of different tumor microenvironments that involved different bioink compositions, matrix elasticities, and MDA-MB-231 initial cell densities. The developed 3D models were robust and suitable for long-term cultures and probed various parameters of the initial cancer model environment in regulating breast tumor progression and metastasis. 3D-bioprinted mini-brains containing two types of bioinks have also been developed to study the crosstalk between glioblastoma cells and glioma-associated macrophages (GAMs)[324]. The two types of cells were found to actively interact with each other, resulting in changes in macrophage phenotype and cancer progression and invasiveness. Such clinically relevant models are important to improve the understanding of tumor biology for evaluating novel cancer therapeutics. Other types of multi-material bioprinting, such as co-axial technology and DLP-based bioprinting, have also been used for tumor modeling. In a study, self-assembled multi-cellular heterogeneous brain tumor fibers were fabricated with co-axially printed alginate/gelatin hydrogels as the external shell and cell suspension containing

fibrinogen as the core[153]. This biomimetic design improved viability, proliferation, and tumor-stromal interactions, which was benefited from the recapitulation of the dynamic tumor microenvironment using multi-material bioprinters. Other configurations, such as GelMA/alginate (core/sheath), have also been investigated for tumor modeling[122]. In another study, glioblastoma models consisting of a distinct tumor, acellular ECM, and/or endothelial regions were built using a DLP-based bioprinter[325]. The stiffness of different regions corresponding to glioblastoma stroma, healthy or pathological brain parenchyma, and brain capillaries was tuned to recapitulate the biochemical and biophysical heterogeneity of the glioblastoma microenvironment. While the enhancement of hypoxia, stemness, endothelial protruding morphology, and angiogenic potentials related to malignant phenotypes was observed in stiff models, rapid proliferation and expansion of cells with the classical phenotype occurred in soft models. In a similar way, glioblastoma microenvironments containing patient-derived glioblastoma stem cells (GSCs), macrophages, astrocytes, and neural stem cells (NSCs) in an HA-based hydrogel were 3D-bioprinted to investigate the growth of GSCs with or without macrophages[326]. The presence of macrophages yielded transcriptional profiles that were closer to those of patient-derived glioblastoma tissues. The collective findings from these studies suggest that building biomimetic and controllable 3D tumor models can be realized by leveraging the precise spatial programming of matrices and cells with multi-material bioprinting.

Creating biomimetic in vitro 3D tumor models is critical for anticancer drug screening and development[327]. The spatiotemporal control of signaling molecular gradients enabled by multi-material bioprinting has been employed to modulate cellular behaviors of tumors at a local level (**Figure 2.16G, H**)[314]. Vascularized tumor models were created to mimic cancer invasion, intravasation, and angiogenesis. The flexibility to add functional materials and precise placement

of different combinations of tumor-relevant cells and hydrogels enabled programmable tumor microenvironments, which potentially could provide insights to identify the fundamental problems in preclinical settings[314]. Another study proposed a bioprinted tumor-on-a-chip device with co-axially bioprinted blood/lymphatic vessel pair to recapitulate the different levels of drug transport profile[328]. This unique design demonstrated the capacity of simulating the complex transport mechanisms of certain pharmaceutical compounds inside tumors and exhibited great potential to improve cancer drug screening accuracy.

2.6.5 Organoids

Organoids are miniature and simplified model organs derived from self-organization and differentiation of pluripotent stem cells or progenitor cells isolated from tissues. They recapitulate similar gene/protein expressions, metabolic functions, and microscale architectures of the native organs[329]. Owing to the remarkable resemblance, they show significant advantages over some traditional 2D and 3D culture platforms to serve as model tissues and organs for cell therapy, drug screening, and disease modeling[330,331]. Despite much progress in the field, organoids formed with manual techniques face problems such as low throughput and high variability, which hinder the translatability of organoids[329,332]. Besides, the size of organoids is typically restricted on a millimeter-scale due to the lack of nutrient supply, which results in a necrotic inner core when the organoid grows large[329]. This size-limitation precludes the culture of physiologically relevant scales to be used as implantable medicines.

Automated 3D bioprinting techniques have demonstrated outstanding promise to fabricate conformable, scalable, and reproducible organoids in a higher-throughput manner[333]. In a typical procedure for bioprinting organoids, concentrated cell suspension solutions or pastes are dispensed to a location, either on a well plate or within a biochemical- and biophysical-mimicking niche

(such as collagen and Matrigel). The cell numbers and the dispensed locations can be precisely controlled, which can drastically improve the reproducibility of bioprinted organoids. A pioneer work has shown that kidney organoids can be bioprinted within 6- and 96-well plates with high throughput and low individual variation[332]. Such a reproducibility favors the accuracy of drug screening, such as the toxicity screening of doxorubicin and aminoglycoside, compared to the unrepeatable results for organoids from manual culture. Conformation of the organoids can also be controlled by spatially define the location of dispensed cells, which enables the easy programming of the organoid maturation. Furthermore, dispensing different cell densities and geometries can alter the spontaneous cellular self-organization into mesoscopic organoids. Spatiotemporal modulation of morphogenesis of mesenchymal aggregates, intestinal organoids, and vascular organoids was proven successful[334]. Organoids with centimeter-scales were achieved by bioprinting the stem cells in their permissive environments, which hold promise in fabricating physiologically relevant organs for implantable regenerative medicines. Multi-material bioprinting, in principle, can in addition, expand the functionality and integration of various bioprintable organoids within a single system.

Despite several transformative studies mentioned above, the use of bioprinting for organoid-fabrication is still in its infancy. Currently, organoid-bioprinting heavily relies on mechanically actuated extrusion techniques, such as syringe pumps, due to their excellent volume control capability. The employed bioinks are also often comprised of low-viscosity cell-only suspensions or pastes. Pneumatically actuated extrusion bioprinters are intrinsically not suitable to promise repeatability due to their incapability in flow rate control, which is associated with the inconsistency in the cell number. Another intrinsic limitation that hinders the adoption of bioprinting organoids is the high costs of stem cell expansion. Bioprinting organoids often requires

the cell density to reach 1×10^7 cells/mL. To compromise the limited number of cells in practice, specialized hardware, such as gas-tight low-volume syringes (~10-10^2 μL) and small nozzles (10-10^2 μm), are often needed to accommodate the limited volumes of the bioinks. Treatments for the prevention of drying and cell adhesion to the printing nozzle are also important to ensure successful bioprinting. To accommodate the process for organoid-fabrication, development in bioprinting hardware and accessories that are easy to control flow rate and with low ink-consumption is a critical mission. Meanwhile, other bioprinting techniques such as robotic microtissue assembly (the Kenzan method) show potentials in precisely placing spheroids to form complicated biological constructs, which could also be explored for the assembly of organoids[335–337].

2.7 Conclusions and perspectives

Multi-material bioprinters outperform their single-material counterparts in fabricating heterogenous/multi-cellular tissue constructs. Developments in the technology of multi-material bioprinters were discussed, and different modalities were compared. Each of the four primary bioprinting technologies has its own advantages and disadvantages. In **Figure 2.17**, we further compared these technologies in three aspects: bioprinter basics, cost-effectiveness, and functionality. Due to their simplicity and prevalence, nozzle-based techniques provide the basics of a bioprinter in a more cost-effective manner. However, in terms of functionality, the laser/light-based technologies, i.e., LIFT and vat-photopolymerization, are likely more advantageous.

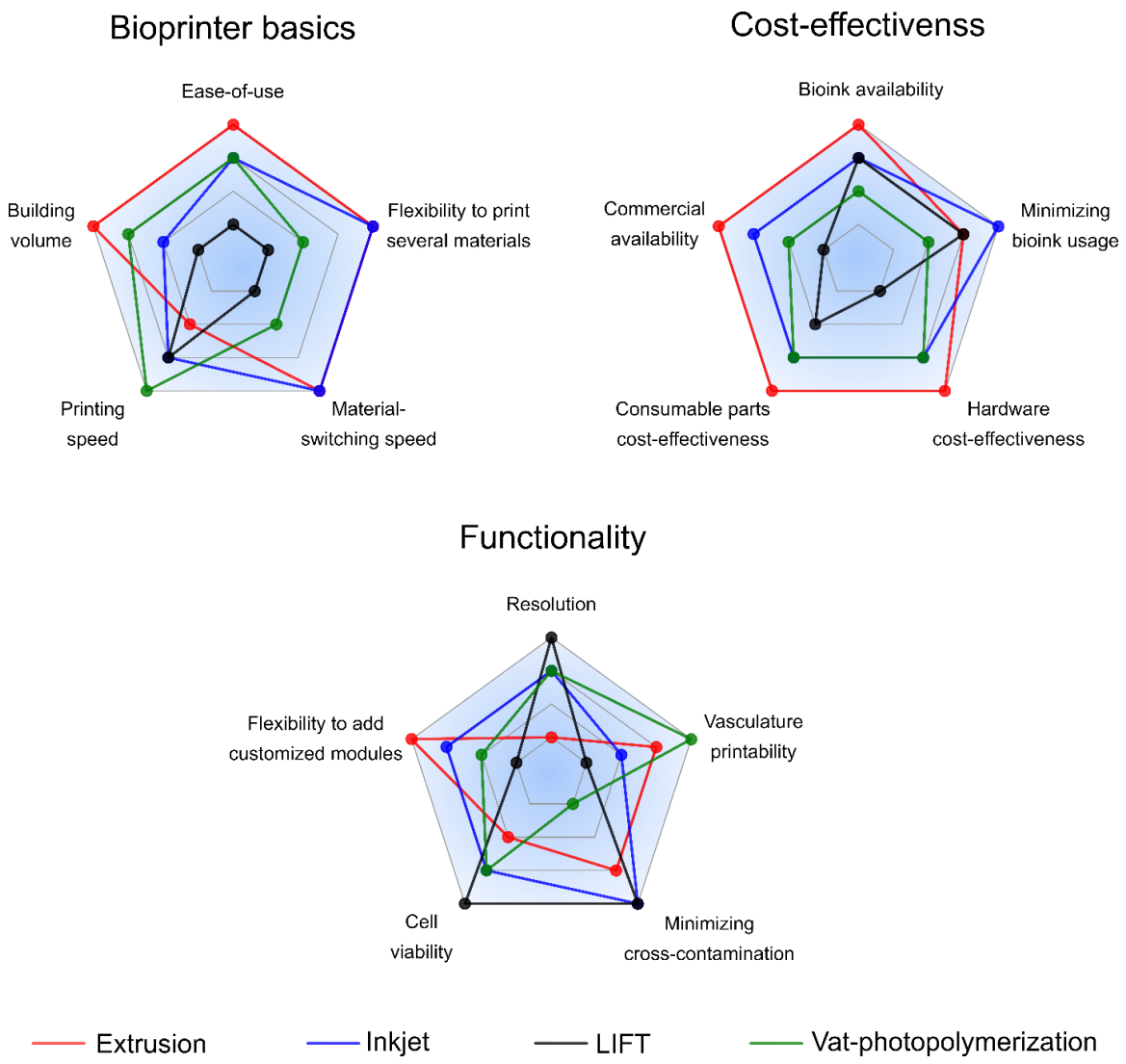

Figure 2.17. Comparison of the four primary bioprinting technologies in different aspects. Features are ranked in four levels, with the outer level presenting the highest score.

Regarding the bioprinter basics, extrusion and inkjet bioprinters are very flexible to be upgraded for bioprinting of more than a single material. There are, however, complications for accommodating this feature in laser/light-based technologies, although not impossible. Another advantage of multi-material nozzle-based techniques is the relatively high material-switching speed, which is missing in laser/light-based methods. LIFT and vat-photopolymerization are excellent in terms of printing speed; however, their building volumes and user-friendliness cannot compete with the extrusion method, at least at this stage of development. In general, nozzle-based

modalities are more commercially available, which results in a lower price for their hardware and consumable parts. Furthermore, the minimal bioink usage due to the intrinsic nature of nozzle-based techniques and the abundance of compatible bioinks make this technique a cost-efficient and accessible method. In the functionality spider chart of **Figure 2.17**, it is evident that there is still room for enhancing the resolution and cell viability of the extrusion technique. Laser/light-based methods deliver excellent resolutions and cell viabilities. Specifically, the most suitable approach for printing multi-scale vascular structures is perhaps vat-photopolymerization. A critical drawback of the current multi-material vat-photopolymerization techniques is the risk of cross-contamination as well as swelling or dehydration during the printing process, which could be a potential direction for future endeavors. The washing buffer during the material-exchange process could lead to deformation of the construct and would affect the 3D-bioprinting resolution, especially for organ-sized constructs. In addition, vascular networks with a physiological dimension have not yet been 3D-bioprinted and studied using cell-laden hydrogels. Fabrication of such constructs is more challenging due to the absorption of light by cells that could affect the penetration depth depending on the cell density and type as well as wavelength of the light source.

As illustrated in **Figure 2.18**, several improvements are envisioned to overcome the current limitations. One challenge faced by most existing multi-material bioprinting technologies is to scale up the printing volume to clinically relevant sizes within a reasonable fabrication time. For instance, with a typical extrusion-based bioprinter, it can take hours to even days to create an entire multi-cellular organ structure with a decent resolution. Such a long fabrication process keeps the cells away from physiological conditions and significantly decreases the cell viability in the fabricated cell-laden constructs. Although this issue can be potentially remedied with a 3D-bioprinting setup within a temperature-, humidity-, and CO_2-controlled environment, such

attempts would inevitably increase the equipment and fabrication costs and hinder the accessibility of the technology. Maintaining the physiological temperature during a fabrication process might also be incompatible with some thermosensitive materials, such as gelatin and collagen. Speeding up the biofabrication process, therefore, still seems to be the most feasible and economical pathway at the current stage. Embedded bioprinting can possibly alleviate this concern for mid-sized organs to some extent since cells stay in a humidified environment. Yet, bioprinted full-sized organs with high cell viability have not been reported so far with embedded bioprinting. Other designs such as multi-nozzle printheads have also been explored[146], but they are mainly suitable for creating repeating patterns.

Large-scale bioprinting has higher chances to introduce defects, such as bubbles and voids. The involvement of multiple materials further impedes the quality control for layer-by-layer methods, leading to a low success rate for production. Such complications are mainly due to the relatively unstable properties of soft bioinks. Although the defects are difficult to avoid or predict, they are usually easy to detect during the printing process. Machine-learning approaches have been recently employed to enhance the printing quality[338]. By introducing artificial intelligence (AI), bioprinting on dynamically moving substrates, such as breathing lungs, has been successfully demonstrated[339–341]. With the assistance of AI in conjunction with computer vision, substrate height, printing pressure, or writing speed can be dynamically adjusted to correct the defects and errors, yielding better printing quality[342].

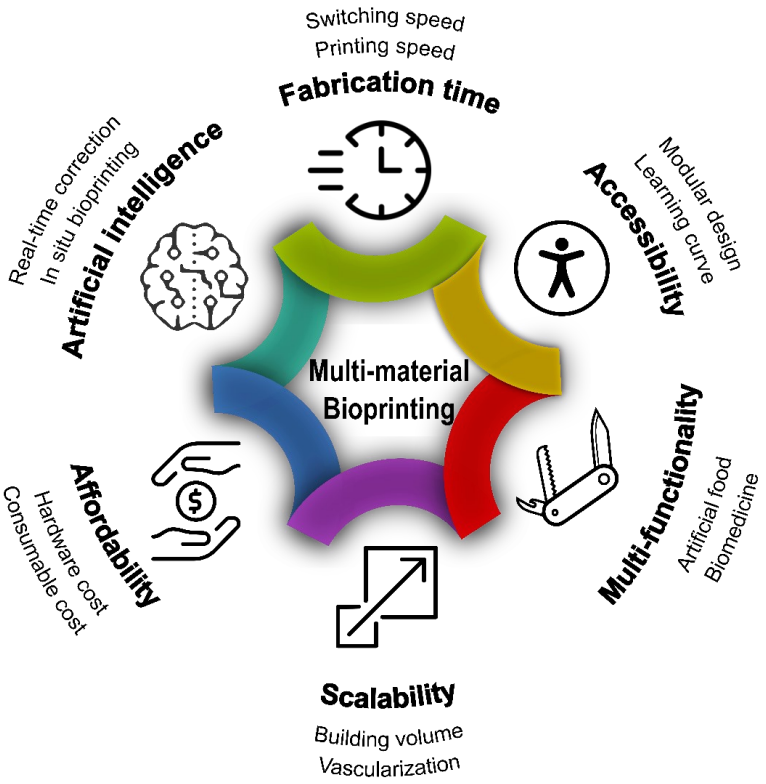

Figure 2.18. Future perspective of potential improvements in multi-material bioprinting.

Although several multi-material vat-photopolymerization methods have been developed, one of the remaining challenges is fabricating large constructs while not compromising printing resolution and speed. The advent of DLP light engines with a higher number of pixels and 3D printers with a dynamic projector could increase the throughput without reducing the print speed or resolution. The throughput of the TPP method can be enhanced by using multiple beams as well as developing highly efficient water-soluble TPP photoinitiators. In addition, further improvement is needed in the rapid bioink-exchange process with minimal bioink cross-contamination and high cleaning efficiency. The LIFT bioprinting method also requires further development to make it more accessible and affordable to fabricate multi-cellular constructs.

Hardware aside, the capacity of multi-material bioprinting can be further broadened through the use of advanced material concepts, such as self-assembling materials[343]. For instance, a self-

assembled collagen-fibrin hydrogel has been shown to improve mechanical strength and stretchability while providing a better ECM-mimetic structure for cell alignment[344] or growth[345]. Self-assembling chitosan bioinks have been shown to generate cell-sized pores within the scaffolds. Their stiffness and viscoelasticity can be modulated over a wide range by controlling the strength of supramolecular interactions[346]. The delivery of bioinks within a Bingham fluid material could enable the freeform fabrication of constructs with geometrical details that are not easily achievable using DIW[162,347]. The combination of a top-down bioprinting approach and bottom-up material self-assembly is desirable to maximize mechanical, structural, and biological functions.

Application-wise, multi-material bioprinting may be employed to further improve the current single-material designs through the use of sacrificial inks. For instance, in a co-axial configuration, where the researchers used HUVEC-laden GelMA as the core and cell-free alginate as the shell, a lumen structure formed around the core fiber[156], as explained in Section 2.4.1.3. However, the microfibers were not hollow, and they cannot essentially resemble a vessel-like structure. Tubular vessel-like constructs may be fabricated using a sacrificial material as the core ink[299]. Generally, the fabrication of vascularized constructs can be fostered by effectively exploiting multi-material bioprinting of bioinks and sacrificial inks. Another unique perspective in bioprinting is integrating multi-material technologies in 4D bioprinting, a method to use stimuli-responsive materials as the bioink[348–350]. Multi-material bioprinters can accommodate the use of multiple smart bioinks to fabricate multi-functional stimuli-responsive constructs.

The accessibility of commercial multi-material bioprinters has motivated many researchers from different fields to leverage this technology for desirable tissue engineering applications without spending time and resources on the production of bioprinters. Previously, multi-material technologies were mostly limited to biomedical engineering labs with essential engineering

backgrounds for its development. Most commercial bioprinters are based on the extrusion technique due to its accessibility, affordability, and easy-to-use platform. There is still an unmet need for commercial multi-material LIFT and vat-photopolymerization bioprinters to make these technologies accessible and available to more research labs, where they can be used for cutting-edge applications. The cost barrier and the complexity of the LIFT bioprinting method are the main challenges in commercializing this method.

Looking into the future, we envision hybrid bioprinters comprising multi-material modules to be developed. With the aid of various parallel modules, different tissue parts can be fabricated and assembled to form a complete and functional whole-size organ. An exploratory 3D printer combining an aerosol jet head, a photonic cure head, extrusion modules, and inkjet heads has been recently reported to create complex structures with high precision[351]. Hybrid bioprinters comprising molten material-extrusion and DLP/SLA modules have also been used to print soft hydrogels and thermoplastics simultaneously[352]. Such a combination is favorable to fabricate cell-laden constructs with gradients and high mechanical strength. Acoustic-based technologies have recently been utilized for the spatial assembly and patterning of cells or organoids into complex microtissues[353–355]. Ultrasound acoustic waves could potentially be used as a contact-free and cell-friendly approach to align multi-cellular 3D constructs within layers to recapitulate the intrinsic microarchitectural organization of many native tissues. For instance, hybrid bioprinters capable of preferentially organize cellular arrays within bioprinted constructs have pioneered the integration of acoustophoresis with nozzle-based bioprinting methods[356,357]. Other works such as manual[358] or robotic[337] mini-tissue assemblies also prove the feasibility of modular tissue fabrication.

Significant advances in multi-material bioprinting technologies have been achieved over the last two decades. However, synergetic efforts on developing bioprinting techniques, bioinks, and

gantries are still needed to realize the full potential of these technologies. This review focused on the technologies developed for multi-material bioprinting and provided a comprehensive overview of their design, standard techniques, commercialization progress, and biomedical applications. Multi-disciplinary research and collaborations between academic research and industries will be crucial to bringing this technology into clinical use.

Acknowledgments

H.R., V.K., and G.B. contributed equally. H.R., G.B., and L.M. were supported by the National Institutes of Health under awards number R01DC018577, R01DC005788, and R01DC014461. H.R. acknowledges the FRQNT's postdoctoral fellowship (296447), the FRQNT's International Internship Award (279390), MITACS Globalink Research Award (IT14553), McGill's Graduate Mobility Award, and McGill's Doctoral Internship Award. V.K. acknowledges FRQNT for the doctoral scholarship. D.J. acknowledges a Canada Research Chair in Bioengineering. V.K. and D.J. acknowledge the support by NSERC Discovery Grant (RGPIN-2016-06723) and Strategic Grant (STPGP 506689-17). Y.S.Z. acknowledges the support by the National Institutes of Health (R21EB025270, R21EB026175, R00CA201603, R01EB028143, R01HL153857, R21EB030257), National Science Foundation (CBET-EBMS-1936105), and Brigham Research Institute.

Conflict of interest

Y.S.Z. sits on the Scientific Advisory Board of Allevi, Inc., which however, did not support or bias this work. The other authors declare no competing financial/commercial interest.

2.8 References

1. Zhang, Y. S., Oklu, R., Dokmeci, M. R. & Khademhosseini, A. Three-dimensional bioprinting strategies for tissue engineering. *Cold Spring Harb. Perspect. Med.* **8**, (2018).

2. Bernal, P. N. *et al.* Volumetric Bioprinting of Complex Living-Tissue Constructs within Seconds. *Adv. Mater.* **31**, 1904209 (2019).

3. Li, J., Wu, C., Chu, P. K. & Gelinsky, M. 3D printing of hydrogels: Rational design strategies and emerging biomedical applications. *Materials Science and Engineering R: Reports* vol. 140 100543 (2020).

4. Sydney Gladman, A., Matsumoto, E. A., Nuzzo, R. G., Mahadevan, L. & Lewis, J. A. Biomimetic 4D printing. *Nat. Mater.* **15**, 413–419 (2016).

5. Van Belleghem, S. *et al.* Hybrid 3D Printing of Synthetic and Cell-Laden Bioinks for Shape Retaining Soft Tissue Grafts. *Adv. Funct. Mater.* **30**, 1907145 (2020).

6. You, S. *et al.* Nanoscale 3D printing of hydrogels for cellular tissue engineering. *J. Mater. Chem. B* **6**, 2187–2197 (2018).

7. Correia Carreira, S., Begum, R. & Perriman, A. W. 3D Bioprinting: The Emergence of Programmable Biodesign. *Adv. Healthc. Mater.* 1900554 (2019) doi:10.1002/adhm.201900554.

8. Lee, J. M. & Yeong, W. Y. Design and Printing Strategies in 3D Bioprinting of Cell-Hydrogels: A Review. *Advanced Healthcare Materials* vol. 5 2856–2865 (2016).

9. Groll, J. *et al.* A definition of bioinks and their distinction from biomaterial inks. *Biofabrication* vol. 11 013001 (2019).

10. Groll, J. *et al.* Biofabrication: Reappraising the definition of an evolving field. *Biofabrication* vol. 8 013001 (2016).

11. Freeman, S. *et al.* A bioink blend for rotary 3D bioprinting tissue engineered small-diameter vascular constructs. *Acta Biomater.* **95**, 152–164 (2019).

12. Derakhshanfar, S. *et al.* 3D bioprinting for biomedical devices and tissue engineering: A review of recent trends and advances. *Bioactive Materials* vol. 3 144–156 (2018).

13. Poldervaart, M. T. *et al.* 3D bioprinting of methacrylated hyaluronic acid (MeHA) hydrogel with intrinsic osteogenicity. *PLoS One* **12**, (2017).

14. Skylar-Scott, M. A. *et al.* Biomanufacturing of organ-specific tissues with high cellular density and embedded vascular channels. *Sci. Adv.* **5**, (2019).

15. Kesti, M. *et al.* Bioprinting Complex Cartilaginous Structures with Clinically Compliant Biomaterials. *Adv. Funct. Mater.* **25**, (2015).

16. Zhang, Y. S. *et al.* 3D Bioprinting for Tissue and Organ Fabrication. *Ann. Biomed. Eng.* **45**, 148–163 (2017).

17. Ma, X. *et al.* 3D bioprinting of functional tissue models for personalized drug screening and in vitro disease modeling. *Adv. Drug Deliv. Rev.* **132**, 235–251 (2018).

18. Jiang, T., Munguia-Lopez, J. G., Flores-Torres, S., Kort-Mascort, J. & Kinsella, J. M. Extrusion bioprinting of soft materials: An emerging technique for biological model fabrication. *Appl. Phys. Rev.* **6**, 011310 (2019).

19. Li, X. *et al.* Inkjet Printing for Biofabrication. in *3D Printing and Biofabrication* 283–301 (2018). doi:10.1007/978-3-319-45444-3_26.

20. Serra, P. & Piqué, A. Laser-Induced Forward Transfer: Fundamentals and Applications. *Advanced Materials Technologies* vol. 4 1800099 (2019).

21. Kumar, H. & Kim, K. Stereolithography 3D Bioprinting. in *Methods in Molecular Biology* vol. 2140 93–108 (Humana Press Inc., 2020).

22. Leijten, J. *et al.* Spatially and temporally controlled hydrogels for tissue engineering. *Materials Science and Engineering R: Reports* vol. 119 1–35 (2017).

23. Jang, J. *et al.* 3D printed complex tissue construct using stem cell-laden decellularized extracellular matrix bioinks for cardiac repair. *Biomaterials* **112**, 264–274 (2017).

24. Ashammakhi, N. *et al.* Bioinks and bioprinting technologies to make heterogeneous and biomimetic tissue constructs. *Materials Today Bio* vol. 1 100008 (2019).

25. Ying, G. *et al.* An Open-Source Handheld Extruder Loaded with Pore-Forming Bioink for in situ Wound Dressing. *Mater. Today Bio* 100074 (2020) doi:10.1016/j.mtbio.2020.100074.

26. Lozano, R. *et al.* 3D printing of layered brain-like structures using peptide modified gellan gum substrates. *Biomaterials* **67**, 264–273 (2015).

27. Hakimi, N. *et al.* Handheld skin printer: In situ formation of planar biomaterials and tissues. *Lab Chip* **18**, 1440–1451 (2018).

28. Di Bella, C. *et al.* In situ handheld three-dimensional bioprinting for cartilage regeneration. *J. Tissue Eng. Regen. Med.* **12**, 611–621 (2018).

29. Alarçin, E. *et al.* Injectable shear-thinning hydrogels for delivering osteogenic and angiogenic cells and growth factors. *Biomater. Sci.* **6**, 1604–1615 (2018).

30. Ozbolat, I. T. & Hospodiuk, M. Current advances and future perspectives in extrusion-based bioprinting. *Biomaterials* vol. 76 321–343 (2016).

31. Liu, W. *et al.* Extrusion Bioprinting of Shear-Thinning Gelatin Methacryloyl Bioinks. *Adv. Healthc. Mater.* **6**, 1601451 (2017).

32. Wang, Z. *et al.* A Novel, Well-Resolved Direct Laser Bioprinting System for Rapid Cell Encapsulation and Microwell Fabrication. *Adv. Healthc. Mater.* **7**, 1701249 (2018).

33. Shi, L. *et al.* Cryogenic free-form extrusion bioprinting of decellularized small intestinal submucosa for potential applications in skin tissue engineering. *Biofabrication* **11**, (2019).

34. O'Connell, C. D. *et al.* Free-form co-axial bioprinting of a gelatin methacryloyl bio-ink by direct in situ photo-crosslinking during extrusion. *Bioprinting* **19**, e00087 (2020).

35. Shao, L. *et al.* Directly coaxial 3D bioprinting of large-scale vascularized tissue constructs. *Biofabrication* **12**, 35014 (2020).

36. Luo, G. *et al.* Freeform, reconfigurable embedded printing of all-aqueous 3D architectures. *Adv. Mater.* **1904631**, 1–7 (2019).

37. Bader, C. *et al.* Making data matter: Voxel printing for the digital fabrication of data across scales and domains. *Sci. Adv.* **4**, eaas8652 (2018).

38. Murphy, S. V & Atala, A. 3D bioprinting of tissues and organs. *Nat. Biotechnol.* **32**, 773–785

(2014).

39. Solis, L. H. *et al.* Thermal inkjet bioprinting triggers the activation of the VEGF pathway in human microvascular endothelial cells in vitro. *Biofabrication* **11**, (2019).

40. Masaeli, E. *et al.* Tissue engineering of retina through high resolution 3-dimensional inkjet bioprinting. *Biofabrication* **12**, 25006 (2020).

41. Angelopoulos, I., Allenby, M. C., Lim, M. & Zamorano, M. Engineering inkjet bioprinting processes toward translational therapies. *Biotechnology and Bioengineering* vol. 117 272–284 (2020).

42. Zhang, Z. *et al.* Evaluation of bioink printability for bioprinting applications. *Appl. Phys. Rev.* **5**, (2018).

43. Pedde, R. D. *et al.* Emerging biofabrication strategies for engineering complex tissue constructs. *Adv. Mater.* **29**, (2017).

44. Davoodi, E. *et al.* Extrusion and Microfluidic-Based Bioprinting to Fabricate Biomimetic Tissues and Organs. *Advanced Materials Technologies* 1901044 (2020) doi:10.1002/admt.201901044.

45. Lim, K. S. *et al.* Visible Light Cross-Linking of Gelatin Hydrogels Offers an Enhanced Cell Microenvironment with Improved Light Penetration Depth. *Macromol. Biosci.* **19**, 1900098 (2019).

46. Chen, Y. *et al.* Noninvasive in vivo 3D bioprinting. *Sci. Adv.* **6**, eaba7406 (2020).

47. Li, W. *et al.* Recent Advances in Formulating and Processing Biomaterial Inks for Vat Polymerization-Based 3D Printing. *Adv. Healthc. Mater.* 2000156 (2020) doi:10.1002/adhm.202000156.

48. Yu, C. *et al.* Photopolymerizable Biomaterials and Light-Based 3D Printing Strategies for Biomedical Applications. *Chemical Reviews* (2020) doi:10.1021/acs.chemrev.9b00810.

49. Miri, A. K. *et al.* Effective bioprinting resolution in tissue model fabrication. *Lab Chip* **19**, 2019–2037 (2019).

50. Mao, Q. *et al.* Fabrication of liver microtissue with liver decellularized extracellular matrix (dECM) bioink by digital light processing (DLP) bioprinting. *Mater. Sci. Eng. C* **109**, 110625 (2020).

51. Ma, X. *et al.* Deterministically patterned biomimetic human iPSC-derived hepatic model via rapid 3D bioprinting. *Proc. Natl. Acad. Sci. U. S. A.* **113**, 2206–2211 (2016).

52. Gong, H., Bickham, B. P., Woolley, A. T. & Nordin, G. P. Custom 3D printer and resin for 18 μm × 20 μm microfluidic flow channels. *Lab Chip* **17**, 2899–2909 (2017).

53. Kuo, A. P. *et al.* High-Precision Stereolithography of Biomicrofluidic Devices. *Adv. Mater. Technol.* **4**, 1–11 (2019).

54. Leberfinger, A. N. *et al.* Bioprinting functional tissues. *Acta Biomaterialia* vol. 95 32–49 (2019).

55. Grigoryan, B. *et al.* Multivascular networks and functional intravascular topologies within biocompatible hydrogels. *Science (80-.).* **364**, 458–464 (2019).

56. Yu, C. *et al.* Scanningless and continuous 3D bioprinting of human tissues with decellularized extracellular matrix. *Biomaterials* **194**, 1–13 (2019).

57. Guillotin, B. *et al.* Laser assisted bioprinting of engineered tissue with high cell density and microscale organization. *Biomaterials* **31**, 7250–7256 (2010).

58. Shen, Y. *et al.* DLP printing photocurable chitosan to build bio-constructs for tissue engineering. *Carbohydr. Polym.* **235**, 115970 (2020).

59. Lee, J. M., Ng, W. L. & Yeong, W. Y. Resolution and shape in bioprinting: Strategizing towards complex tissue and organ printing. *Appl. Phys. Rev.* **6**, 011307 (2019).

60. Gao, G., Yonezawa, T., Hubbell, K., Dai, G. & Cui, X. Inkjet-bioprinted acrylated peptides and PEG hydrogel with human mesenchymal stem cells promote robust bone and cartilage formation with minimal printhead clogging. *Biotechnol. J.* **10**, 1568–1577 (2015).

61. Zhang, Y. S. *et al.* Bioprinted thrombosis-on-a-chip. *Lab Chip* **16**, 4097–4105 (2016).

62. Wang, X., Wei, Z., Baysah, C. Z., Zheng, M. & Xing, J. Biomaterial-based microstructures fabricated by two-photon polymerization microfabrication technology. *RSC Advances* vol. 9 34472–34480 (2019).

63. Ovsianikov, A. *et al.* Laser photofabrication of cell-containing hydrogel constructs. *Langmuir* **30**, 3787–3794 (2014).

64. Dobos, A. *et al.* Thiol–Gelatin–Norbornene Bioink for Laser-Based High-Definition Bioprinting. *Adv. Healthc. Mater.* 1900752 (2019).

65. Lim, K. S. *et al.* Fundamentals and Applications of Photo-Cross-Linking in Bioprinting. *Chem. Rev.* (2020) doi:10.1021/acs.chemrev.9b00812.

66. Xing, J.-F., Zheng, M.-L. & Duan, X.-M. Two-photon polymerization microfabrication of hydrogels: an advanced 3D printing technology for tissue engineering and drug delivery. *Chem. Soc. Rev.* **44**, 5031–5039 (2015).

67. Blaeser, A. *et al.* Controlling Shear Stress in 3D Bioprinting is a Key Factor to Balance Printing Resolution and Stem Cell Integrity. *Adv. Healthc. Mater.* **5**, 326–333 (2016).

68. Gudapati, H., Dey, M. & Ozbolat, I. A comprehensive review on droplet-based bioprinting: Past, present and future. *Biomaterials* **102**, 20–42 (2016).

69. Jentsch, S. *et al.* Multiscale 3D Bioprinting by Nozzle-Free Acoustic Droplet Ejection. *Small Methods* **5**, (2021).

70. Kim, J. D., Choi, J. S., Kim, B. S., Choi, Y. C. & Cho, Y. W. Piezoelectric inkjet printing of polymers: Stem cell patterning on polymer substrates. *Polymer (Guildf).* **51**, 2147–2154 (2010).

71. Yuk, H. & Zhao, X. A New 3D Printing Strategy by Harnessing Deformation, Instability, and Fracture of Viscoelastic Inks. *Adv. Mater.* **30**, 1704028 (2018).

72. Jiang, T., Munguia-Lopez, J. G., Flores-Torres, S., Kort-Mascort, J. & Kinsella, J. M. Extrusion bioprinting of soft materials: An emerging technique for biological model fabrication. *Appl. Phys. Rev.* **6**, (2019).

73. Regehly, M. *et al.* Xolography for linear volumetric 3D printing. *Nature* **588**, 620–624 (2020).

74. Armstrong, J. P. K. *et al.* Engineering Anisotropic Muscle Tissue using Acoustic Cell Patterning. *Adv. Mater.* **30**, 1–7 (2018).

75. Ren, T., Steiger, W., Chen, P., Ovsianikov, A. & Demirci, U. Enhancing cell packing in

buckyballs by acoustofluidic activation. *Biofabrication* **12**, (2020).

76. Chansoria, P. & Shirwaiker, R. Characterizing the Process Physics of Ultrasound-Assisted Bioprinting. *Sci. Rep.* **9**, 1–17 (2019).

77. Shapiro, J. M., Drinkwater, B. W., Perriman, A. W. & Fraser, M. Sonolithography: In-Air Ultrasonic Particulate and Droplet Manipulation for Multiscale Surface Patterning. *Adv. Mater. Technol.* **6**, 2000689 (2021).

78. Lee, J., Kim, K. E., Bang, S., Noh, I. & Lee, C. A desktop multi-material 3D bio-printing system with open-source hardware and software. *Int. J. Precis. Eng. Manuf.* **18**, 605–612 (2017).

79. Choudhury, D., Anand, S. & Naing, M. W. The arrival of commercial bioprinters - Towards 3D bioprinting revolution! *International Journal of Bioprinting* vol. 4 (2018).

80. Rafiee, M., Farahani, R. D. & Therriault, D. Multi-Material 3D and 4D Printing: A Survey. *Adv. Sci.* 1902307 (2020) doi:10.1002/advs.201902307.

81. Khare, V., Sonkaria, S., Lee, G. Y., Ahn, S. H. & Chu, W. S. From 3D to 4D printing – design, material and fabrication for multi-functional multi-materials. *Int. J. Precis. Eng. Manuf. - Green Technol.* **4**, 291–299 (2017).

82. Tetsuka, H. & Shin, S. R. Materials and technical innovations in 3D printing in biomedical applications. *Journal of Materials Chemistry B* vol. 8 2930–2950 (2020).

83. Heinrich, M. A. *et al.* 3D Bioprinting: from Benches to Translational Applications. *Small* vol. 15 1805510 (2019).

84. Richard, C., Neild, A. & Cadarso, V. The Emerging Role of Microfluidics in Multi-Material 3D Bioprinting. *Lab Chip* (2020) doi:10.1039/c9lc01184f.

85. Costantini, M. *et al.* Microfluidic-enhanced 3D bioprinting of aligned myoblast-laden hydrogels leads to functionally organized myofibers in vitro and in vivo. *Biomaterials* **131**, 98–110 (2017).

86. Prendergast, M. E. & Burdick, J. A. Recent Advances in Enabling Technologies in 3D Printing for Precision Medicine. *Advanced Materials* vol. 32 1902516 (2020).

87. Kang, D. *et al.* Bioprinting of Multiscaled Hepatic Lobules within a Highly Vascularized Construct. *Small* **16**, 1905505 (2020).

88. Zhou, L., Fu, J. & He, Y. A Review of 3D Printing Technologies for Soft Polymer Materials. *Adv. Funct. Mater.* **2000187**, 1–38 (2020).

89. Bandyopadhyay, A. & Heer, B. Additive manufacturing of multi-material structures. *Materials Science and Engineering R: Reports* vol. 129 1–16 (2018).

90. Sinha, R. *et al.* A hybrid additive manufacturing platform to create bulk and surface composition gradients on scaffolds for tissue regeneration. *Nat. Commun.* **12**, 500 (2021).

91. Yang, S., Tang, H., Feng, C., Shi, J. & Yang, J. The research on multi-material 3D vascularized network integrated printing technology. *Micromachines* **11**, 237 (2020).

92. Ligon, S. C., Liska, R., Stampfl, J., Gurr, M. & Mülhaupt, R. Polymers for 3D Printing and Customized Additive Manufacturing. *Chemical Reviews* vol. 117 10212–10290 (2017).

93. Ouyang, L., Armstrong, J. P. K., Chen, Q., Lin, Y. & Stevens, M. M. Void-Free 3D Bioprinting for In Situ Endothelialization and Microfluidic Perfusion. *Adv. Funct. Mater.* **30**, 1908349 (2020).

94. Rutz, A. L., Hyland, K. E., Jakus, A. E., Burghardt, W. R. & Shah, R. N. A multimaterial bioink method for 3D printing tunable, cell-compatible hydrogels. *Adv. Mater.* **27**, 1607–1614 (2015).

95. Zhao, H. *et al.* Spatiotemporal control of polymer brush formation through photoinduced radical polymerization regulated by DMD light modulation. *Lab Chip* **19**, 2651–2662 (2019).

96. Cui, X. *et al.* Advances in Extrusion 3D Bioprinting: A Focus on Multicomponent Hydrogel-Based Bioinks. *Advanced Healthcare Materials* vol. 1901648 1–27 (2020).

97. Ravanbakhsh, H., Bao, G., Luo, Z., Mongeau, L. G. & Zhang, Y. S. Composite Inks for Extrusion Printing of Biological and Biomedical Constructs. *ACS Biomater. Sci. Eng.* acsbiomaterials.0c01158 (2020) doi:10.1021/acsbiomaterials.0c01158.

98. Lakes, R. S. Composite biomaterials. in *Biomaterials: Principles and Applications* 79–94 (Springer, Cham, 2002). doi:10.1201/b15739-10.

99. Mobaraki, M., Ghaffari, M., Yazdanpanah, A., Luo, Y. & Mills, D. K. Bioinks and bioprinting: A focused review. *Bioprinting* vol. 18 e00080 (2020).

100. Ravanbakhsh, H., Bao, G., Latifi, N. & Mongeau, L. G. Carbon nanotube composite hydrogels for vocal fold tissue engineering: Biocompatibility, rheology, and porosity. *Mater. Sci. Eng. C* **103**, 109861 (2019).

101. Ravanbakhsh, H., Bao, G. & Mongeau, L. Carbon nanotubes promote cell migration in hydrogels. *Sci. Rep.* **10**, 1–10 (2020).

102. Levato, R. *et al.* From Shape to Function: The Next Step in Bioprinting. *Advanced Materials* vol. 32 1906423 (2020).

103. Velasco- Rodriguez, B. *et al.* Hybrid methacrylated gelatin and hyaluronic acid hydrogel scaffolds. Preparation and systematic characterization for prospective tissue engineering applications. *Int. J. Mol. Sci.* **22**, (2021).

104. Thomas, A. *et al.* Vascular bioprinting with enzymatically degradable bioinks via multi-material projection-based stereolithography. *Acta Biomater.* **117**, 121–132 (2020).

105. Parak, A. *et al.* Functionalizing bioinks for 3D bioprinting applications. *Drug Discovery Today* vol. 24 198–205 (2019).

106. Park, J. *et al.* Cell-laden 3D bioprinting hydrogel matrix depending on different compositions for soft tissue engineering: Characterization and evaluation. *Mater. Sci. Eng. C* **71**, 678–684 (2017).

107. Cui, X. *et al.* Advances in Extrusion 3D Bioprinting: A Focus on Multicomponent Hydrogel-Based Bioinks. *Adv. Healthc. Mater.* **1901648**, 1–27 (2020).

108. Yang, H. *et al.* Fabricating hydrogels to mimic biological tissues of complex shapes and high fatigue resistance. *Matter* **4**, 1935–1946 (2021).

109. Lozano, R. *et al.* 3D printing of layered brain-like structures using peptide modified gellan gum substrates. *Biomaterials* **67**, 264–273 (2015).

110. Rodell, C. B., Dusaj, N. N., Highley, C. B. & Burdick, J. A. Injectable and Cytocompatible Tough Double-Network Hydrogels through Tandem Supramolecular and Covalent Crosslinking. *Adv. Mater.* **28**, 8419–8424 (2016).

111. Ge, Q. *et al.* 3D printing of highly stretchable hydrogel with diverse UV curable polymers. *Sci. Adv.* **7**, eaba4261 (2021).

112. Yang, J. *et al.* Design Molecular Topology for Wet-Dry Adhesion. *ACS Appl. Mater. Interfaces* **11**, 24802–24811 (2019).

113. Bao, G. *et al.* Ionotronic Tough Adhesives with Intrinsic Multifunctionality. *ACS Appl. Mater. Interfaces* (2021) doi:10.1021/acsami.1c09231.

114. Zhang, W. *et al.* Catechol-functionalized hydrogels: biomimetic design, adhesion mechanism, and biomedical applications. *Chem. Soc. Rev.* **49**, 433–464 (2020).

115. Ma, Z. *et al.* Bioinspired tough gel sheath for robust and versatile surface functionalization. *Sci. Adv.* **7**, eabc3012 (2021).

116. Contessi Negrini, N., Angelova Volponi, A., Sharpe, P. T. & Celiz, A. D. Tunable Cross-Linking and Adhesion of Gelatin Hydrogels via Bioorthogonal Click Chemistry. *ACS Biomater. Sci. Eng.* (2021) doi:10.1021/acsbiomaterials.1c00136.

117. Ma, Z., Bao, G. & Li, J. Multifaceted Design and Emerging Applications of Tissue Adhesives. *Adv. Mater.* 2007663 (2021) doi:10.1002/adma.202007663.

118. Yang, J., Bai, R., Chen, B. & Suo, Z. Hydrogel Adhesion: A Supramolecular Synergy of Chemistry, Topology, and Mechanics. *Adv. Funct. Mater.* **30**, 1–27 (2020).

119. Nam, S. & Mooney, D. Polymeric Tissue Adhesives. *Chem. Rev.* (2021) doi:10.1021/acs.chemrev.0c00798.

120. Joung, D. *et al.* 3D Printed Stem-Cell Derived Neural Progenitors Generate Spinal Cord Scaffolds. *Adv. Funct. Mater.* **28**, 1801850 (2018).

121. Chen, M. *et al.* Parallel, Multi-Material Electrohydrodynamic 3D Nanoprinting. *Small* **16**, 1906402 (2020).

122. Liu, W. *et al.* Coaxial extrusion bioprinting of 3D microfibrous constructs with cell-favorable gelatin methacryloyl microenvironments. *Biofabrication* **10**, (2018).

123. du Chatinier, D. N., Figler, K. P., Agrawal, P., Liu, W. & Zhang, Y. S. The potential of microfluidics-enhanced extrusion bioprinting. *Biomicrofluidics* **15**, 041304 (2021).

124. Costantini, M., Colosi, C., Święszkowski, W. & Barbetta, A. Co-axial wet-spinning in 3D bioprinting: State of the art and future perspective of microfluidic integration. *Biofabrication* **11**, (2019).

125. Rocca, M., Fragasso, A., Liu, W., Heinrich, M. A. & Zhang, Y. S. Embedded Multimaterial Extrusion Bioprinting. *SLAS Technol.* **23**, 154–163 (2018).

126. Liu, W. *et al.* Rapid Continuous Multimaterial Extrusion Bioprinting. *Adv. Mater.* **29**, 1604630 (2017).

127. Cameron, T., Naseri, E., MacCallum, B. & Ahmadi, A. Development of a disposable single-nozzle printhead for 3D bioprinting of continuous multi-material constructs. *Micromachines* **11**, 459 (2020).

128. Feng, F., He, J., Li, J., Mao, M. & Li, D. Multicomponent bioprinting of heterogeneous hydrogel constructs based on microfluidic printheads. *Int. J. Bioprinting* **5**, 39–48 (2019).

129. Serex, L., Bertsch, A. & Renaud, P. Microfluidics: A new layer of control for extrusion-based 3D printing. *Micromachines* **9**, (2018).

130. Hardin, J. O., Ober, T. J., Valentine, A. D. & Lewis, J. A. Microfluidic printheads for multimaterial 3D printing of viscoelastic inks. *Adv. Mater.* **27**, 3279–3284 (2015).

131. Colosi, C. *et al.* Microfluidic Bioprinting of Heterogeneous 3D Tissue Constructs Using Low-Viscosity Bioink. *Adv. Mater.* **28**, 677-684a (2016).

132. Ward, K. & Fan, Z. H. Mixing in microfluidic devices and enhancement methods. *J. Micromechanics Microengineering* **25**, 94001 (2015).

133. Ober, T. J., Foresti, D. & Lewis, J. A. Active mixing of complex fluids at the microscale. *Proc. Natl. Acad. Sci. U. S. A.* **112**, 12293–12298 (2015).

134. Bachman, H. *et al.* An acoustofluidic device for efficient mixing over a wide range of flow rates. *Lab Chip* **20**, 1238–1248 (2020).

135. Golobic, A. M. *et al.* Active Mixing of Reactive Materials for 3D Printing. *Adv. Eng. Mater.* **21**, 1900147 (2019).

136. Ortega, J. M. *et al.* Active Mixing of Disparate Inks for Multimaterial 3D Printing. *Adv. Mater. Technol.* **4**, 1800717 (2019).

137. Idaszek, J. *et al.* 3D bioprinting of hydrogel constructs with cell and material gradients for the regeneration of full-thickness chondral defect using a microfluidic printing head. *Biofabrication* **11**, (2019).

138. Bsoul, A., Pan, S., Cretu, E., Stoeber, B. & Walus, K. Design, microfabrication, and characterization of a moulded PDMS/SU-8 inkjet dispenser for a Lab-on-a-Printer platform technology with disposable microfluidic chip. *Lab Chip* **16**, 3351–3361 (2016).

139. Wang, J. *et al.* Finding the optimal design of a passive microfluidic mixer. *Lab Chip* **19**, 3618–3627 (2019).

140. Chávez-Madero, C. *et al.* Using chaotic advection for facile high-throughput fabrication of ordered multilayer micro- and nanostructures: continuous chaotic printing. *Biofabrication* **12**, 035023 (2020).

141. Trujillo-de, G. & Tamayol, A. Controlling cellular organization in bioprinting through designed 3D microcompartmentalization Controlling cellular organization in bioprinting through designed 3D microcompartmentalization. **021404**, (2021).

142. Ceballos-González, C. F. *et al.* High-Throughput and Continuous Chaotic Bioprinting of Spatially Controlled Bacterial Microcosms. *ACS Biomater. Sci. Eng.* (2021) doi:10.1021/acsbiomaterials.0c01646.

143. Liu, H., Zhou, H., Lan, H., Liu, F. & Wang, X. Multinozzle Multichannel Temperature Deposition System for Construction of a Blood Vessel. *SLAS Technol.* **23**, 64–69 (2018).

144. Kolesky, D. B. *et al.* 3D Bioprinting of Vascularized, Heterogeneous Cell-Laden Tissue Constructs. *Adv. Mater.* **26**, 3124–3130 (2014).

145. Kang, H. W. *et al.* A 3D bioprinting system to produce human-scale tissue constructs with structural integrity. *Nat. Biotechnol.* **34**, 312–319 (2016).

146. Skylar-Scott, M. A., Mueller, J., Visser, C. W. & Lewis, J. A. Voxelated soft matter via multimaterial multinozzle 3D printing. *Nature* **575**, 330–335 (2019).

147. Dai, X. *et al.* Coaxial 3D bioprinting of self-assembled multicellular heterogeneous tumor fibers.

Sci. Rep. **7**, 1–11 (2017).

148. Ouyang, L., Highley, C. B., Sun, W. & Burdick, J. A. A Generalizable Strategy for the 3D Bioprinting of Hydrogels from Nonviscous Photo-crosslinkable Inks. *Adv. Mater.* **29**, (2017).

149. Hong, S., Kim, J. S., Jung, B., Won, C. & Hwang, C. Coaxial bioprinting of cell-laden vascular constructs using a gelatin-tyramine bioink. *Biomater. Sci.* **7**, 4578–4587 (2019).

150. Wang, X. *et al.* Coaxial extrusion bioprinted shell-core hydrogel microfibers mimic glioma microenvironment and enhance the drug resistance of cancer cells. *Colloids Surfaces B Biointerfaces* **171**, 291–299 (2018).

151. Zhang, Y. S. *et al.* Bioprinting the Cancer Microenvironment. *ACS Biomaterials Science and Engineering* vol. 2 1710–1721 (2016).

152. Pi, Q. *et al.* Digitally Tunable Microfluidic Bioprinting of Multilayered Cannular Tissues. *Adv. Mater.* **30**, 1706913 (2018).

153. Dai, X. *et al.* Coaxial 3D bioprinting of self-assembled multicellular heterogeneous tumor fibers. *Sci. Rep.* **7**, 1–12 (2017).

154. Gao, Q. *et al.* 3D Bioprinting of Vessel-like Structures with Multilevel Fluidic Channels. *ACS Biomater. Sci. Eng.* **3**, 399–408 (2017).

155. Yu, Y., Shang, L., Guo, J., Wang, J. & Zhao, Y. Design of capillary microfluidics for spinning cell-laden microfibers. *Nat. Protoc.* **13**, 2557–2579 (2018).

156. Shao, L. *et al.* Fiber-Based Mini Tissue with Morphology-Controllable GelMA Microfibers. *Small* **14**, 1802187 (2018).

157. Xie, R. *et al.* Composable microfluidic spinning platforms for facile production of biomimetic perfusable hydrogel microtubes. *Nat. Protoc.* (2020) doi:10.1038/s41596-020-00442-9.

158. Xu, P. *et al.* Bioinspired Microfibers with Embedded Perfusable Helical Channels. *Adv. Mater.* **29**, 1–7 (2017).

159. Chao, Y. & Shum, H. C. Emerging aqueous two-phase systems: From fundamentals of interfaces to biomedical applications. *Chemical Society Reviews* vol. 49 114–142 (2020).

160. Leung, B. M., Labuz, J. M., Moraes, C. & Takayama, S. Bioprinting using aqueous two-phase system. in *Essentials of 3D Biofabrication and Translation* 165–178 (Elsevier Inc., 2015). doi:10.1016/B978-0-12-800972-7.00009-8.

161. Wu, W., Deconinck, A. & Lewis, J. A. Omnidirectional printing of 3D microvascular networks. *Adv. Mater.* **23**, 178–183 (2011).

162. Highley, C. B., Rodell, C. B. & Burdick, J. A. Direct 3D Printing of Shear-Thinning Hydrogels into Self-Healing Hydrogels. *Adv. Mater.* **27**, 5075–5079 (2015).

163. Bhattacharjee, T. *et al.* Writing in the granular gel medium. *Sci. Adv.* **1**, e1500655 25 (2015).

164. Hinton, T. J. *et al.* Three-dimensional printing of complex biological structures by freeform reversible embedding of suspended hydrogels. *Sci. Adv.* **1**, e1500758 (2015).

165. Lee, A. *et al.* 3D bioprinting of collagen to rebuild components of the human heart. *Science (80-.).* **365**, 482–487 (2019).

166. Bao, G. Biofabrication in Tissue Engineering. in *Racing for the Surface: Antimicrobial and*

Interface Tissue Engineering 289–312 (Springer, Cham, 2020). doi:10.1007/978-3-030-34471-9_12.

167. Foresti, D. *et al.* Acoustophoretic printing. *Sci. Adv.* **4**, 1–10 (2018).

168. Xu, T. *et al.* Complex heterogeneous tissue constructs containing multiple cell types prepared by inkjet printing technology. *Biomaterials* **34**, 130–139 (2013).

169. Sakai, S., Ueda, K., Gantumur, E., Taya, M. & Nakamura, M. Drop-On-Drop Multimaterial 3D Bioprinting Realized by Peroxidase-Mediated Cross-Linking. *Macromol. Rapid Commun.* **39**, 1–6 (2018).

170. Wilson, W. C. & Boland, T. Cell and organ printing 1: Protein and cell printers. *Anat. Rec. - Part A Discov. Mol. Cell. Evol. Biol.* **272**, 491–496 (2003).

171. Boland, T., Mironov, V., Gutowska, A., Roth, E. A. & Markwald, R. R. Cell and organ printing 2: Fusion of cell aggregates in three-dimensional gels. *Anat. Rec. - Part A Discov. Mol. Cell. Evol. Biol.* **272**, 497–502 (2003).

172. Jones, R. E., Zheng, W., McKew, J. C. & Chen, C. Z. An Alternative Direct Compound Dispensing Method Using the HP D300 Digital Dispenser. *J. Lab. Autom.* **18**, 367–374 (2013).

173. Compaan, A. M., Christensen, K. & Huang, Y. Inkjet Bioprinting of 3D Silk Fibroin Cellular Constructs Using Sacrificial Alginate. *ACS Biomater. Sci. Eng.* **3**, 1519–1526 (2017).

174. Moroni, L. *et al.* Biofabrication: A Guide to Technology and Terminology. *Trends Biotechnol.* **36**, 384–402 (2018).

175. Bohandy, J., Kim, B. F. & Adrian, F. J. Metal deposition from a supported metal film using an excimer laser. *J. Appl. Phys.* **60**, 1538–1539 (1986).

176. Antoshin, A. A. *et al.* LIFT-bioprinting, is it worth it? *Bioprinting* vol. 15 e00052 (2019).

177. Koch, L. *et al.* Laser printing of skin cells and human stem cells. *Tissue Eng. - Part C Methods* **16**, 847–854 (2010).

178. Koch, L. *et al.* Skin tissue generation by laser cell printing. *Biotechnol. Bioeng.* **109**, 1855–1863 (2012).

179. Guillotin, B. *et al. Rapid prototyping of complex tissues with laser-assisted bioprinting (LAB)*. *Rapid Prototyping of Biomaterials: Techniques in Additive Manufacturing* (Elsevier Ltd., 2019). doi:10.1016/B978-0-08-102663-2.00007-1.

180. Kingsley, D. M. *et al.* Laser-based 3D bioprinting for spatial and size control of tumor spheroids and embryoid bodies. *Acta Biomater.* **95**, 357–370 (2019).

181. Guillemot, F. *et al.* High-throughput laser printing of cells and biomaterials for tissue engineering. *Acta Biomater.* **6**, 2494–2500 (2010).

182. Zheng, X. *et al.* Ultralight, ultrastiff mechanical metamaterials. *Science (80-.).* **344**, 1373–1377 (2014).

183. Raman, R. *et al.* High-resolution projection microstereolithography for patterning of neovasculature. *Adv. Healthc. Mater.* **5**, 610–619 (2016).

184. Tumbleston, J. R. *et al.* Continuous liquid interface production of 3D objects. *Science (80-.).* **347**, 1349–1352 (2015).

185. Bernal, P. N. *et al.* Volumetric Bioprinting of Complex Living-Tissue Constructs within Seconds. *Adv. Mater.* **1904209**, 1904209 (2019).

186. Kelly, B. E. *et al.* Volumetric additive manufacturing via tomographic reconstruction. *Science (80-.).* **363**, 1075–1079 (2019).

187. Regehly, M. *et al.* Xolography for linear volumetric 3D printing. *Nature* **588**, 620–624 (2020).

188. Choi, J. W., Kim, H. C. & Wicker, R. Multi-material stereolithography. *J. Mater. Process. Technol.* **211**, 318–328 (2011).

189. Ge, Q. *et al.* Multimaterial 4D Printing with Tailorable Shape Memory Polymers. *Sci. Rep.* **6**, 1–11 (2016).

190. Zhou, C., Chen, Y., Yang, Z. G. & Khoshnevis, B. Development of a Multi-material Mask-Image-Projection-based Stereolithography for the Fabrication of Digital Materials. *Annu. Solid Free. Fabr. Symp.* 65–80 (2011).

191. Zhou, C., Chen, Y., Yang, Z. & Khoshnevis, B. Digital material fabrication using mask-image-projection-based stereolithography. *Rapid Prototyp. J.* **19**, 153–165 (2013).

192. Wu, X., Lian, Q., Li, D. & Jin, Z. Biphasic osteochondral scaffold fabrication using multi-material mask projection stereolithography. *Rapid Prototyp. J.* **25**, 277–288 (2019).

193. Grix, T. *et al.* Bioprinting perfusion-enabled liver equivalents for advanced organ-on-a-chip applications. *Genes (Basel).* **9**, (2018).

194. Mishra, A. K. *et al.* Autonomic perspiration in 3D-printed hydrogel actuators. *Sci. Robot.* **5**, 1–10 (2020).

195. Kim, Y. T., Castro, K., Bhattacharjee, N. & Folch, A. Digital manufacturing of selective porous barriers in microchannels using multi-material stereolithography. *Micromachines* **9**, (2018).

196. Chan, V. *et al.* Multi-material bio-fabrication of hydrogel cantilevers and actuators with stereolithography. *Lab Chip* **12**, 88–98 (2012).

197. Han, D., Yang, C., Fang, N. X. & Lee, H. Rapid multi-material 3D printing with projection micro-stereolithography using dynamic fluidic control. *Addit. Manuf.* **27**, 606–615 (2019).

198. Miri, A. K. *et al.* Microfluidics-Enabled Multimaterial Maskless Stereolithographic Bioprinting. *Adv. Mater.* **30**, 1–9 (2018).

199. Miller, K. L. *et al.* Rapid 3D BioPrinting of a human iPSC-derived cardiac micro-tissue for high-throughput drug testing. *Organs-on-a-Chip* **3**, 100007 (2021).

200. Wang, Q. *et al.* Lightweight Mechanical Metamaterials with Tunable Negative Thermal Expansion. *Phys. Rev. Lett.* **117**, 1–6 (2016).

201. Kowsari, K., Akbari, S., Wang, D., Fang, N. X. & Ge, Q. High-Efficiency High-Resolution Multimaterial Fabrication for Digital Light Processing-Based Three-Dimensional Printing. *3D Print. Addit. Manuf.* **5**, 185–193 (2018).

202. Bhattacharjee, N., Parra-Cabrera, C., Kim, Y. T., Kuo, A. P. & Folch, A. Desktop-Stereolithography 3D-Printing of a Poly(dimethylsiloxane)-Based Material with Sylgard-184 Properties. *Adv. Mater.* **30**, (2018).

203. Hohnholz, A. *et al.* Multimaterial bathless stereolithography using aerosol jet printing and UV

laser based polymerization. *J. Laser Appl.* **31**, 022301 (2019).

204. Shanjani, Y., Pan, C. C., Elomaa, L. & Yang, Y. A novel bioprinting method and system for forming hybrid tissue engineering constructs. *Biofabrication* **7**, (2015).

205. Schwartz, J. J. & Boydston, A. J. Multimaterial actinic spatial control 3D and 4D printing. *Nat. Commun.* **10**, 1–10 (2019).

206. Larsen, E. K. U. *et al.* Multimaterial hydrogel with widely tunable elasticity by selective photopolymerization of PEG diacrylate and epoxy monomers. *J. Polym. Sci. Part B Polym. Phys.* **54**, 1195–1201 (2016).

207. Folch, A. Lab on a Chip. *Lab Chip* **16**, 1720–1742 (2016).

208. Arcaute, K., Mann, B. K. & Wicker, R. B. Stereolithography of three-dimensional bioactive poly(ethylene glycol) constructs with encapsulated cells. *Ann. Biomed. Eng.* **34**, 1429–1441 (2006).

209. Arcaute, K., Mann, B. & Wicker, R. Stereolithography of spatially controlled multi-material bioactive poly(ethylene glycol) scaffolds. *Acta Biomater.* **6**, 1047–1054 (2010).

210. Huang, T. Q., Qu, X., Liu, J. & Chen, S. 3D printing of biomimetic microstructures for cancer cell migration. *Biomed. Microdevices* **16**, 127–132 (2014).

211. Hwang, H. H., Zhu, W., Victorine, G., Lawrence, N. & Chen, S. 3d Printing: 3D-Printing of Functional Biomedical Microdevices via Light- and Extrusion-Based Approaches (Small Methods 2/2018). *Small Methods* **2**, 1870021 (2018).

212. Ge, Q. *et al.* Projection Micro Stereolithography Based 3D Printing and Its Applications. *Int. J. Extrem. Manuf.* **2**, 022004 (2020).

213. 3D Bioprinting Market Size, Share | Industry Analysis Report, 2019-2026. https://www.grandviewresearch.com/industry-analysis/3d-bioprinting-market.

214. Pereira, F. D. A. S., Parfenov, V., Khesuani, Y. D., Ovsianikov, A. & Mironov, V. Commercial 3D Bioprinters. in *3D Printing and Biofabrication* 535–549 (Springer International Publishing, 2018). doi:10.1007/978-3-319-45444-3_12.

215. Thazhathukunnel, T., Chow, A. & Amirfar, V. A. Is 3D printing the future of health care? *Pharm. Today* **21**, 56 (2015).

216. Moldovan, N. I., Hibino, N. & Nakayama, K. Principles of the kenzan method for robotic cell spheroid-based three-dimensional bioprinting. *Tissue Eng. - Part B Rev.* **23**, 237–244 (2017).

217. Kizawa, H., Nagao, E., Shimamura, M., Zhang, G. & Torii, H. Scaffold-free 3D bio-printed human liver tissue stably maintains metabolic functions useful for drug discovery. *Biochem. Biophys. Reports* **10**, 186–191 (2017).

218. Reeser, K. & Doiron, A. L. Three-Dimensional Printing on a Rotating Cylindrical Mandrel: A Review of Additive-Lathe 3D Printing Technology. *3D Print. Addit. Manuf.* **6**, 293–307 (2019).

219. Burdis, R. & Kelly, D. J. 3D Bioprinting Hardware. in *Polymer-Based Additive Manufacturing* 161–186 (Springer International Publishing, 2019). doi:10.1007/978-3-030-24532-0_8.

220. High-throughput production of GrowInk™-T models by drop-on-demand 3D bioprinting | UPM Biomedicals. https://www.upmbiomedicals.com/resource-center/application-notes/high-throughput-production-of-growink-t-models-by-drop-on-demand-3d-bioprinting/.

221. 3D Bioprinter | Global | Ricoh. https://www.ricoh.com/technology/institute/research/tech_3d_bio_printer.html.

222. Chua, C. K. & Yeong, W. Y. *Bioprinting: Principles and applications*. *Bioprinting: Principles and Applications* (World Scientific Publishing Co. Pte. Ltd., 2015). doi:10.1142/9193.

223. Digilab; Precision towards Perfection CELLJET. https://www.digilabglobal.com/products-celljet.

224. Piqué, A. & Serra, P. *Laser printing of functional materials: 3D microfabrication, Electronics and Biomedicine*. (John Wiley & Sons, 2018).

225. Keriquel, V. *et al.* In situ printing of mesenchymal stromal cells, by laser-assisted bioprinting, for in vivo bone regeneration applications. *Sci. Rep.* **7**, 1–10 (2017).

226. Poietis Announces the First Commercial Launch of a Tissue Model Manufactured by Bioprinting | BioSpace. https://www.biospace.com/article/releases/poietis-announces-the-first-commercial-launch-of-a-tissue-model-manufactured-by-bioprinting/.

227. Precise Bio Platform - Bio-fabricated organs made available. https://www.precise-bio.com/precise-bio-platform/.

228. Cellbricks Bioprinting. https://cellbricks.com/.

229. Lim, K. S. *et al.* Bio-resin for high resolution lithography-based biofabrication of complex cell-laden constructs. *Biofabrication* **10**, (2018).

230. Gao, Q. *et al.* 3D printing of complex GelMA-based scaffolds with nanoclay. *Biofabrication* (2019) doi:10.1088/1758-5090/ab0cf6.

231. Lumen X™ - CELLINK. https://www.cellink.com/bioprinting/lumen-x/.

232. Ye, W. *et al.* 3D printing of gelatin methacrylate-based nerve guidance conduits with multiple channels. *Mater. Des.* **192**, 108757 (2020).

233. Madden, L. R. *et al.* Bioprinted 3D Primary Human Intestinal Tissues Model Aspects of Native Physiology and ADME/Tox Functions. *iScience* **2**, 156–167 (2018).

234. Jia, W. *et al.* Direct 3D bioprinting of perfusable vascular constructs using a blend bioink. *Biomaterials* **106**, 58–68 (2016).

235. King, S. M. *et al.* 3D proximal tubule tissues recapitulate key aspects of renal physiology to enable nephrotoxicity testing. *Front. Physiol.* (2017) doi:10.3389/fphys.2017.00123.

236. Nguyen, D. G. *et al.* Bioprinted 3D primary liver tissues allow assessment of organ-level response to clinical drug induced toxicity in vitro. *PLoS One* (2016) doi:10.1371/journal.pone.0158674.

237. Norona, L. M., Nguyen, D. G., Gerber, D. A., Presnell, S. C. & LeCluyse, E. L. Modeling compound-induced fibrogenesis in vitro using three-dimensional bioprinted human liver tissues. *Toxicol. Sci.* (2016) doi:10.1093/TOXSCI/KFW169.

238. Cao, Y. *et al.* Three-dimensional printed multiphasic scaffolds with stratified cell-laden gelatin methacrylate hydrogels for biomimetic tendon-to-bone interface engineering. *J. Orthop. Transl.* **23**, 89–100 (2020).

239. Qi, D. *et al.* Mechanically robust cryogels with injectability and bioprinting supportability for adipose tissue engineering. *Acta Biomater.* **74**, 131–142 (2018).

240. Noor, N. *et al.* 3D Printing of Personalized Thick and Perfusable Cardiac Patches and Hearts. *Adv.*

Sci. **6**, 1900344 (2019).

241. Filardo, G. *et al.* Patient-specific meniscus prototype based on 3D bioprinting of human cell-laden scaffold. *Bone Joint Res.* **8**, 101–106 (2019).

242. Huang, B. *et al.* Fabrication and characterisation of 3D printed MWCNT composite porous scaffolds for bone regeneration. *Mater. Sci. Eng. C* **98**, 266–278 (2019).

243. Ng, W. L., Qi, J. T. Z., Yeong, W. Y. & Naing, M. W. Proof-of-concept: 3D bioprinting of pigmented human skin constructs. *Biofabrication* **10**, 25005 (2018).

244. Pashazadeh, A. *et al.* Feasibility of 3D printing for customized radiotherapeutic models to be used in superficial skin cancer therapy. *Trans. Addit. Manuf. Meets Med.* **1**, (2019).

245. Ji, S., Almeida, E. & Guvendiren, M. 3D bioprinting of complex channels within cell-laden hydrogels. *Acta Biomater.* **95**, 214–224 (2019).

246. Dikici, S., Claeyssens, F. & MacNeil, S. Bioengineering Vascular Networks to Study Angiogenesis and Vascularization of Physiologically Relevant Tissue Models in Vitro . *ACS Biomater. Sci. Eng.* (2020) doi:10.1021/acsbiomaterials.0c00191.

247. Mazzocchi, A., Devarasetty, M., Huntwork, R., Soker, S. & Skardal, A. Optimization of collagen type I-hyaluronan hybrid bioink for 3D bioprinted liver microenvironments. *Biofabrication* **11**, 15003 (2018).

248. Gettler, B. C., Zakhari, J. S., Gandhi, P. S. & Williams, S. K. Formation of Adipose Stromal Vascular Fraction Cell-Laden Spheroids Using a Three-Dimensional Bioprinter and Superhydrophobic Surfaces. *Tissue Eng. - Part C Methods* **23**, 516–524 (2017).

249. Techshot Successfully Completes Knee Cartilage Test Prints in Space. https://techshot.com/techshot-successfully-completes-knee-cartilage-test-prints-in-space/.

250. Baltazar, T. *et al.* Three Dimensional Bioprinting of a Vascularized and Perfusable Skin Graft Using Human Keratinocytes, Fibroblasts, Pericytes, and Endothelial Cells. *Tissue Eng. - Part A* **26**, 227–238 (2020).

251. Liu, X. *et al.* 3D Bioprinting of Oligo (Poly (Ethylene Glycol) Fumarate) for Bone and Nerve Tissue Engineering. *J. Biomed. Mater. Res. Part A* **109**, 6–17 (2021).

252. Kutlehria, S. *et al.* High-throughput 3D bioprinting of corneal stromal equivalents. *J. Biomed. Mater. Res. Part B Appl. Biomater.* (2020).

253. Bao, G. *et al.* Triggered micropore-forming bioprinting of porous viscoelastic hydrogels. *Mater. Horizons* **7**, 2336–2347 (2020).

254. Yipeng, J. *et al.* Microtissues enhance smooth muscle differentiation and cell viability of hADSCs for three dimensional bioprinting. *Front. Physiol.* **8**, 534 (2017).

255. Lei, Z., Wang, Q. & Wu, P. A multifunctional skin-like sensor based on a 3D printed thermo-responsive hydrogel. *Mater. Horizons* **4**, 694–700 (2017).

256. Hsiao, S.-H. & Hsu, S. Synthesis and characterization of dual stimuli-sensitive biodegradable polyurethane soft hydrogels for 3D cell-laden bioprinting. *ACS Appl. Mater. Interfaces* **10**, 29273–29287 (2018).

257. Jiang, T. *et al.* Directing the self-assembly of tumour spheroids by bioprinting cellular heterogeneous models within alginate / gelatin hydrogels. *Sci. Rep.* **7**, 4575 (2017).

258. Jiang, T. *et al.* Engineering bioprintable alginate/gelatin composite hydrogels with tunable mechanical and cell adhesive properties to modulate tumor spheroid growth kinetics. *Biofabrication* **12**, 15024 (2020).

259. Bulanova, E. A. *et al.* Bioprinting of a functional vascularized mouse thyroid gland construct. *Biofabrication* **9**, 34105 (2017).

260. Hesuani, Y. D. *et al.* Design and Implementation of Novel Multifunctional 3D Bioprinter. *3D Print. Addit. Manuf.* **3**, 64–68 (2016).

261. Reid, J. A. *et al.* Accessible bioprinting: adaptation of a low-cost 3D-printer for precise cell placement and stem cell differentiation. *Biofabrication* **8**, 25017 (2016).

262. Wang, X. *et al.* Tumor-like lung cancer model based on 3D bioprinting. *3 Biotech* **8**, 1–9 (2018).

263. Dai, X., Ma, C., Lan, Q. & Xu, T. 3D bioprinted glioma stem cells for brain tumor model and applications of drug susceptibility. *Biofabrication* **8**, 45005 (2016).

264. Xu, T. & Yuan, Y. Artificial dura mater and manufacturing method thereof. (2012).

265. Liu, B. *et al.* 3D-bioprinted functional and biomimetic hydrogel scaffolds incorporated with nanosilicates to promote bone healing in rat calvarial defect model. *Mater. Sci. Eng. C* 110905 (2020).

266. Jiménez, G. *et al.* Design of 3D bioprinted articular cartilage of MSCs-loaded for osteochondral injuries. *Cytotherapy* **19**, S27–S28 (2017).

267. Kang, Y. J., & Huixing, Z. H. O. U. (2018). U.S. Patent Application No. 15/562,560. (2019).

268. Kang, Yujian James, and Z. H. O. U. Huixing. 'Rotary device for bio-printing and method for using the same.' U.S. Patent Application No. 15/562,560. (2018).

269. Kim, S. W. *et al.* Three-Dimensional Bioprinting of Cell-Laden Constructs Using Polysaccharide-Based Self-Healing Hydrogels. *Biomacromolecules* **20**, 1860–1866 (2019).

270. Han, S. *et al.* 3D Bioprinted Vascularized Tumour for Drug Testing. *Int. J. Mol. Sci.* **21**, 2993 (2020).

271. Lee, C., Abelseth, E., de la Vega, L. & Willerth, S. M. Bioprinting a novel glioblastoma tumor model using a fibrin-based bioink for drug screening. *Mater. Today Chem.* **12**, 78–84 (2019).

272. de la Vega, L. *et al.* 3D Bioprinting Human Induced Pluripotent Stem Cell-Derived Neural Tissues Using a Novel Lab-on-a-Printer Technology. *Appl. Sci.* **8**, 2414 (2018).

273. Walus, K., Beyer, S. & Willerth, S. M. Three-dimensional bioprinting healthy and diseased models of the brain tissue using stem cells. *Current Opinion in Biomedical Engineering* vol. 14 25–33 (2020).

274. Dickman, C. T. D. *et al.* Functional characterization of 3D contractile smooth muscle tissues generated using a unique microfluidic 3D bioprinting technology. *FASEB J.* **34**, 1652–1664 (2020).

275. Swaminathan, S., Hamid, Q., Sun, W. & Clyne, A. M. Bioprinting of 3D breast epithelial spheroids for human cancer models. *Biofabrication* **11**, 25003 (2019).

276. Sun, L. *et al.* Application of a 3D Bioprinted Hepatocellular Carcinoma Cell Model in Antitumor Drug Research. *Front. Oncol.* **10**, 878 (2020).

277. Shim, J.-H. *et al.* Three-dimensional bioprinting of multilayered constructs containing human mesenchymal stromal cells for osteochondral tissue regeneration in the rabbit knee joint. *Biofabrication* **8**, 14102 (2016).

278. Kang, D. *et al.* Pre-set extrusion bioprinting for multiscale heterogeneous tissue structure fabrication. *Biofabrication* **10**, 35008 (2018).

279. WeBio - BioPrinting. https://www.webio.tech/#Investigations.

280. Utama, R. H. *et al.* Precise, high-throughput production of multicellular spheroids with a bespoke 3D bioprinter. *bioRxiv* (2020).

281. Stem, I. A. *et al.* Bioprinting Human Mesenchymal Stem Cells using the CellJet without loss in cell viability. 1–3.

282. Ng, W. L. & Yeong, W. Y. The future of skin toxicology testing--Three-dimensional bioprinting meets microfluidics. *Int. J. Bioprinting* **5**, 237 (2019).

283. Pagès, E. *et al.* Creation of Highly Defined Mesenchymal Stem Cell Patterns in Three Dimensions by Laser-Assisted Bioprinting. *J. Nanotechnol. Eng. Med.* **6**, (2015).

284. Precise Bio Ophthalmology - Bio-fabricated organs made available. https://www.precise-bio.com/precise-bio-ophthalmology/#precise-bio-ophthalmology-pipeline.

285. Yanagi, Y. *et al.* In vivo and ex vivo methods of growing a liver bud through tissue connection. *Sci. Rep.* **7**, 1–15 (2017).

286. van Pel, D. M., Harada, K., Song, D., Naus, C. C. & Sin, W. C. Modelling glioma invasion using 3D bioprinting and scaffold-free 3D culture. *J. Cell Commun. Signal.* **12**, 723–730 (2018).

287. Merceron, T. K. *et al.* A 3D bioprinted complex structure for engineering the muscle-tendon unit. *Biofabrication* **7**, 35003 (2015).

288. Pati, F. *et al.* Printing three-dimensional tissue analogues with decellularized extracellular matrix bioink. *Nat. Commun.* **5**, 3935 (2014).

289. Kang, H. *et al.* A 3D bioprinting system to produce human-scale tissue constructs with structural integrity. *Nat. Biotechnol.* **34**, 312–319 (2016).

290. Jeon, O. *et al.* Individual cell-only bioink and photocurable supporting medium for 3D printing and generation of engineered tissues with complex geometries. *Mater. Horizons* **6**, 1625–1631 (2019).

291. Noor, N. *et al.* 3D Printing of Personalized Thick and Perfusable Cardiac Patches and Hearts. *Adv. Sci.* **1900344**, 1900344 (2019).

292. Kang, H. W. *et al.* A 3D bioprinting system to produce human-scale tissue constructs with structural integrity. *Nat. Biotechnol.* **34**, 312–319 (2016).

293. Buenzli, P. R. *et al.* Cell proliferation and migration explain pore bridging dynamics in 3D printed scaffolds of different pore size. *Acta Biomater.* **114**, 285–295 (2020).

294. Kolesky, D. B. *et al.* 3D Bioprinting of Vascularized , Heterogeneous Cell-Laden Tissue Constructs. *Adv. Mater.* **26**, 3124–3130 (2014).

295. Kolesky, D. B., Homan, K. A., Skylar-scott, M. A. & Lewis, J. A. Three-dimensional bioprinting of thick vascularized tissues. *PNAS* **113**, 3179–3184 (2016).

296. Ouyang, L., Armstrong, J. P. K., Chen, Q., Lin, Y. & Stevens, M. M. Void-Free 3D Bioprinting for In Situ Endothelialization and Microfluidic Perfusion. *Adv. Funct. Mater.* **30**, (2020).

297. Lee, V. K. *et al.* Generation of multi-scale vascular network system within 3D hydrogel using 3D bio-printing technology. *Cell. Mol. Bioeng.* **7**, 460–472 (2014).

298. Lee, V. K. *et al.* Creating perfused functional vascular channels using 3D bio-printing technology. *Biomaterials* **35**, 8092–8102 (2014).

299. Wang, Y. *et al.* Coaxial Extrusion of Tubular Tissue Constructs Using a Gelatin/GelMA Blend Bioink. *ACS Biomater. Sci. Eng.* **5**, 5514–5524 (2019).

300. Gao, G. *et al.* Tissue Engineered Bio-Blood-Vessels Constructed Using a Tissue-Specific Bioink and 3D Coaxial Cell Printing Technique: A Novel Therapy for Ischemic Disease. *Adv. Funct. Mater.* **27**, 1700798 (2017).

301. Nam, H. *et al.* Multi-layered Free-form 3D Cell-printed Tubular Construct with Decellularized Inner and Outer Esophageal Tissue-derived Bioinks. *Sci. Rep.* **10**, 1–14 (2020).

302. Zhu, W. *et al.* Direct 3D bioprinting of prevascularized tissue constructs with complex microarchitecture. *Biomaterials* **124**, 106–115 (2017).

303. Corbett, D. C. *et al.* Thermofluidic heat exchangers for actuation of transcription in artificial tissues. *Sci. Adv.* **6**, 1–14 (2020).

304. Bhatia, S. N. & Ingber, D. E. Microfluidic organs-on-chips. *Nat. Biotechnol.* **32**, 760–772 (2014).

305. Zhang, Y. S. The ultimate in personalized medicine: your body on a chip. *IEEE spectrum, IEEE* (2019).

306. Maharjan, S., Cecen, B. & Zhang, Y. S. 3D Immunocompetent Organ-on-a-Chip Models. *Small Methods* **4**, 2000235 (2020).

307. Huh, D., Hamilton, G. A. & Ingber, D. E. From 3D cell culture to organs-on-chips. *Trends Cell Biol.* **21**, 745–754 (2011).

308. Bhise, N. S. *et al.* Organ-on-a-chip platforms for studying drug delivery systems. *J. Control. Release* **190**, 82–93 (2014).

309. Ingber, D. E. Reverse Engineering Human Pathophysiology with Organs-on-Chips. *Cell* **164**, 1105–1109 (2016).

310. Yesil-Celiktas, O. *et al.* Mimicking Human Pathophysiology in Organ-on-Chip Devices. *Adv. Biosyst.* **2**, 1800109 (2018).

311. Zhang, Y. S. & Khademhosseini, A. Engineering in vitro human tissue models through bio-design and manufacturing. *Bio-Design Manuf.* **3**, 155–159 (2020).

312. Lee, H. & Cho, D. W. One-step fabrication of an organ-on-a-chip with spatial heterogeneity using a 3D bioprinting technology. *Lab Chip* **16**, 2618–2625 (2016).

313. Zhang, J. *et al.* A novel approach for precisely controlled multiple cell patterning in microfluidic chips by inkjet printing and the detection of drug metabolism and diffusion. *Analyst* **141**, 2940–2947 (2016).

314. Meng, F. *et al.* 3D Bioprinted In Vitro Metastatic Models via Reconstruction of Tumor Microenvironments. *Adv. Mater.* **31**, 1–10 (2019).

315. Yu, F. & Choudhury, D. Microfluidic bioprinting for organ-on-a-chip models. *Drug Discov. Today* **24**, 1248–1257 (2019).

316. Bhise, N. S. *et al.* A liver-on-a-chip platform with bioprinted hepatic spheroids. *Biofabrication* **8**, (2016).

317. Ingber, D. E. Is it Time for Reviewer 3 to Request Human Organ Chip Experiments Instead of Animal Validation Studies? *Adv. Sci.* **7**, 2002030 (2020).

318. Kim, B. S., Lee, J. S., Gao, G. & Cho, D. W. Direct 3D cell-printing of human skin with functional transwell system. *Biofabrication* **9**, (2017).

319. Ma, X. *et al.* Deterministically patterned biomimetic human iPSC-derived hepatic model via rapid 3D bioprinting. *Proc. Natl. Acad. Sci. U. S. A.* **113**, 2206–2211 (2016).

320. Fong, E. L. S., Harrington, D. A., Farach-Carson, M. C. & Yu, H. Heralding a new paradigm in 3D tumor modeling. *Biomaterials* **108**, 197–213 (2016).

321. Knowlton, S., Onal, S., Yu, C. H., Zhao, J. J. & Tasoglu, S. Bioprinting for cancer research. *Trends Biotechnol.* **33**, 504–513 (2015).

322. Li, J., Parra-Cantu, C., Wang, Z. & Zhang, Y. S. Improving Bioprinted Volumetric Tumor Microenvironments In Vitro. *Trends in Cancer* 1–12 (2020) doi:10.1016/j.trecan.2020.06.002.

323. Zhao, Y. *et al.* Three-dimensional printing of Hela cells for cervical tumor model in vitro. *Biofabrication* **6**, (2014).

324. Heinrich, M. A. *et al.* 3D-Bioprinted Mini-Brain: A Glioblastoma Model to Study Cellular Interactions and Therapeutics. *Adv. Mater.* **31**, 1–9 (2019).

325. Tang, M. *et al.* Rapid 3D Bioprinting of Glioblastoma Model Mimicking Native Biophysical Heterogeneity. *Small* **17**, 2006050 (2021).

326. Tang, M. *et al.* Three-dimensional bioprinted glioblastoma microenvironments model cellular dependencies and immune interactions. *Cell Res.* **30**, 833–853 (2020).

327. Qu, Q. *et al.* Triggered Release from Cellulose Microparticles Inspired by Wood Degradation by Fungi. *ACS Sustain. Chem. Eng.* **9**, 387–397 (2021).

328. Cao, X. *et al.* A Tumor-on-a-Chip System with Bioprinted Blood and Lymphatic Vessel Pair. *Adv. Funct. Mater.* **29**, 1–13 (2019).

329. Hofer, M. & Lutolf, M. P. Engineering organoids. *Nat. Rev. Mater.* **6**, 402–420 (2021).

330. Clevers, H. Modeling Development and Disease with Organoids. *Cell* **165**, 1586–1597 (2016).

331. Takebe, T. & Wells, J. M. Organoids by design. *Science (80-.).* **364**, 956–959 (2019).

332. Lawlor, K. T. *et al.* Cellular extrusion bioprinting improves kidney organoid reproducibility and conformation. *Nat. Mater.* **20**, 260–271 (2021).

333. Rawal, P., Tripathi, D. M., Ramakrishna, S. & Kaur, S. Prospects for 3D bioprinting of organoids. *Bio-Design Manuf.* (2021) doi:10.1007/s42242-020-00124-1.

334. Brassard, J. A., Nikolaev, M., Hübscher, T., Hofer, M. & Lutolf, M. P. Recapitulating macro-scale tissue self-organization through organoid bioprinting. *Nat. Mater.* **20**, 22–29 (2021).

335. Moldovan, N. I., Hibino, N. & Nakayama, K. Principles of the kenzan method for robotic cell

spheroid-based three-dimensional bioprinting. *Tissue Eng. - Part B Rev.* **23**, 237–244 (2017).

336. Daly, A. C., Davidson, M. D. & Burdick, J. A. 3D bioprinting of high cell-density heterogeneous tissue models through spheroid fusion within self-healing hydrogels. *Nat. Commun.* **12**, 1–13 (2021).

337. Ayan, B. *et al.* Aspiration-assisted bioprinting for precise positioning of biologics. *Sci. Adv.* **6**, 1–17 (2020).

338. Conev, A. *et al.* Machine Learning-Guided Three-Dimensional Printing of Tissue Engineering Scaffolds. *Tissue Eng. Part A* ten.tea.2020.0191 (2020) doi:10.1089/ten.tea.2020.0191.

339. Zhu, Z., Park, H. S. & McAlpine, M. C. 3D printed deformable sensors. *Sci. Adv.* **6**, 1–11 (2020).

340. Zhu, Z., Ng, D. W. H., Park, H. S. & McAlpine, M. C. 3D-printed multifunctional materials enabled by artificial-intelligence-assisted fabrication technologies. *Nat. Rev. Mater.* **6**, 27–47 (2021).

341. Zhu, Z. *et al.* 3D Printed Functional and Biological Materials on Moving Freeform Surfaces. *Adv. Mater.* **30**, 1707495 (2018).

342. Conev, A. *et al.* Machine learning-guided three-dimensional printing of tissue engineering scaffolds. *Tissue Eng. - Part A* **26**, 1359–1368 (2020).

343. Hedegaard, C. L. *et al.* Integrating self-assembly and biofabrication for the development of structures with enhanced complexity and hierarchical control. *Biofabrication* **12**, (2020).

344. Schwab, A. *et al.* Tissue mimetic hyaluronan bioink containing collagen fibers with controlled orientation modulating cell migration and alignment. *Mater. Today Bio* **7**, 100058 (2020).

345. Patel, B., Xu, Z., Pinnock, C. B., Kabbani, L. S. & Lam, M. T. Self-assembled collagen-fibrin hydrogel reinforces tissue engineered adventitia vessels seeded with human fibroblasts. *Sci. Rep.* **8**, 1–13 (2018).

346. Bao, G. *et al.* Triggered micropore-forming bioprinting of porous viscoelastic hydrogels. *Mater. Horizons* (2020) doi:10.1039/d0mh00813c.

347. Soitu, C. *et al.* Jet-Printing Microfluidic Devices on Demand. *Adv. Sci.* **7**, 2001854 (2020).

348. Ashammakhi, N. *et al.* Advances and Future Perspectives in 4D Bioprinting. *Biotechnol. J.* **13**, 1800148 (2018).

349. Li, Y. C., Zhang, Y. S., Akpek, A., Shin, S. R. & Khademhosseini, A. 4D bioprinting: The next-generation technology for biofabrication enabled by stimuli-responsive materials. *Biofabrication* vol. 9 012001 (2017).

350. Gao, B. *et al.* 4D Bioprinting for Biomedical Applications. *Trends in Biotechnology* vol. 34 746–756 (2016).

351. Roach, D. J. *et al.* The m4 3D printer: A multi-material multi-method additive manufacturing platform for future 3D printed structures. *Addit. Manuf.* **29**, 100819 (2019).

352. Shanjani, Y., Pan, C. C., Elomaa, L. & Yang, Y. A novel bioprinting method and system for forming hybrid tissue engineering constructs A novel bioprinting method and system for forming hybrid tissue engineering constructs. *Biofabrication* **7**, 45008 (2015).

353. Guex, A. G., Di Marzio, N., Eglin, D., Alini, M. & Serra, T. The waves that make the pattern: a

review on acoustic manipulation in biomedical research. *Mater. Today Bio* 100110 (2021).

354. Ma, Z. *et al.* Acoustic holographic cell patterning in a biocompatible hydrogel. *Adv. Mater.* **32**, 1904181 (2020).

355. Petta, D. *et al.* Sound-induced morphogenesis of multicellular systems for rapid orchestration of vascular networks. *Biofabrication* **13**, 15004 (2020).

356. Chansoria, P. & Shirwaiker, R. Characterizing the Process Physics of Ultrasound-Assisted Bioprinting. *Sci. Rep.* **9**, 1–17 (2019).

357. Chansoria, P., Narayanan, L. K., Schuchard, K. & Shirwaiker, R. Ultrasound-assisted biofabrication and bioprinting of preferentially aligned three-dimensional cellular constructs. *Biofabrication* **11**, 35015 (2019).

358. Daly, A. C., Davidson, M. D. & Burdick, J. A. 3D bioprinting of high cell-density heterogeneous tissue models through spheroid fusion within self-healing hydrogels. *Nat. Commun.* **12**, 1–13 (2021).

Chapter 3

3. Chapter 3: Introduction update

3.1 Microfluidics

Microfluidics is a rapidly growing interdisciplinary field that focuses on manipulating and controlling fluids at sub-millimeter scales in microfabricated devices. The discipline is now well-established, with numerous advancements focused on utilizing microfluidics in biomedical research and point-of-care diagnostics[1,2]. Microfluidic devices can be classified into two main categories based on their liquid actuation mechanisms: actively-powered systems that require external power sources for liquid manipulation, and self-powered systems that rely solely on forces defined by the geometry and material properties of the microfluidic device for liquid manipulation.

Actively-powered microfluidic devices, which include pneumatic, centrifugal, electroosmotic, and acoustic methods, offer precise control over fluid flow. These devices often necessitate peripheral equipment and lab facilities, making them more akin to "lab-around-a-chip" devices rather than "lab-on-a-chip" devices, and subsequently limiting their point-of-need applications. Pneumatic actuation uses air and vacuum lines for precise liquid manipulation in microchannels[3]. It offers robust flow control but relies on connections, limiting point-of-care use. Centrifugal microfluidics, also known as lab-on-a-disk, leverages spinning disk-shaped devices at high speeds to generate centrifugal forces for fluid handling[4,5]. While it is disposable and mass-producible, the motor/ spinner size restricts its portability. Electroosmotic actuation applies electric fields to generate flow within microfabricated channels, allowing for high-precision flow control;

however, its operation is sensitive to changes in buffer composition and surface properties, and the requirement for high-voltage power supplies restricts its application[6]. Acoustic actuation employs acoustic fields for fluid manipulation, offering contactless, non-invasive, and precise control, though its applicability in remote settings may be limited due to the need for complex equipment[7]. Although actively-powered microfluidic devices provide versatility and precision, their reliance on peripheral equipment and lab facilities restricts their use in point-of-care or minimally instrumented operation. On the other hand, self-powered microfluidic devices, such as capillary-driven or capillary microfluidics, leverage capillary effects for fluid flow control without the need for external power sources[8,9]. Due to their low cost, disposability, and potential for automation, they hold great promise for advancing point-of-care diagnostics and other biomedical applications. By addressing the limitations of "lab-around-a-chip" devices, capillary-driven microfluidics can provide more accessible and portable solutions for a wide range of applications.

3.2 Microchannel-Based Capillary Microfluidics

Capillary microfluidics, a subfield of microfluidics, relies on surface tension effects to manipulate liquids without the need for external peripherals or power supplies. Microchannel-based capillary microfluidics is a versatile platform for developing innovative lab-on-a-chip systems by precisely designing and engineering microchannels for self-powered fluid control. Capillaric circuits (CCs) are advanced capillary microfluidic devices that make use of capillary forces to perform complex flow-control operations[9]. CCs are assembled from individual capillaric elements to program multistep processes with minimal user-dependent steps[9,10]. Unlike pressure-driven microfluidics that require peripherals, connections, and computers for automation, CCs can autonomously perform various liquid handling algorithms step-by-step. This makes CCs a versatile platform for developing autonomous and pre-programmed sequential delivery of different

liquids on a single chip. This capability allows CCs to serve as a versatile platform for developing autonomous and pre-programmed sequential delivery of different liquids on a single chip, making them particularly attractive for applications requiring minimal user intervention.

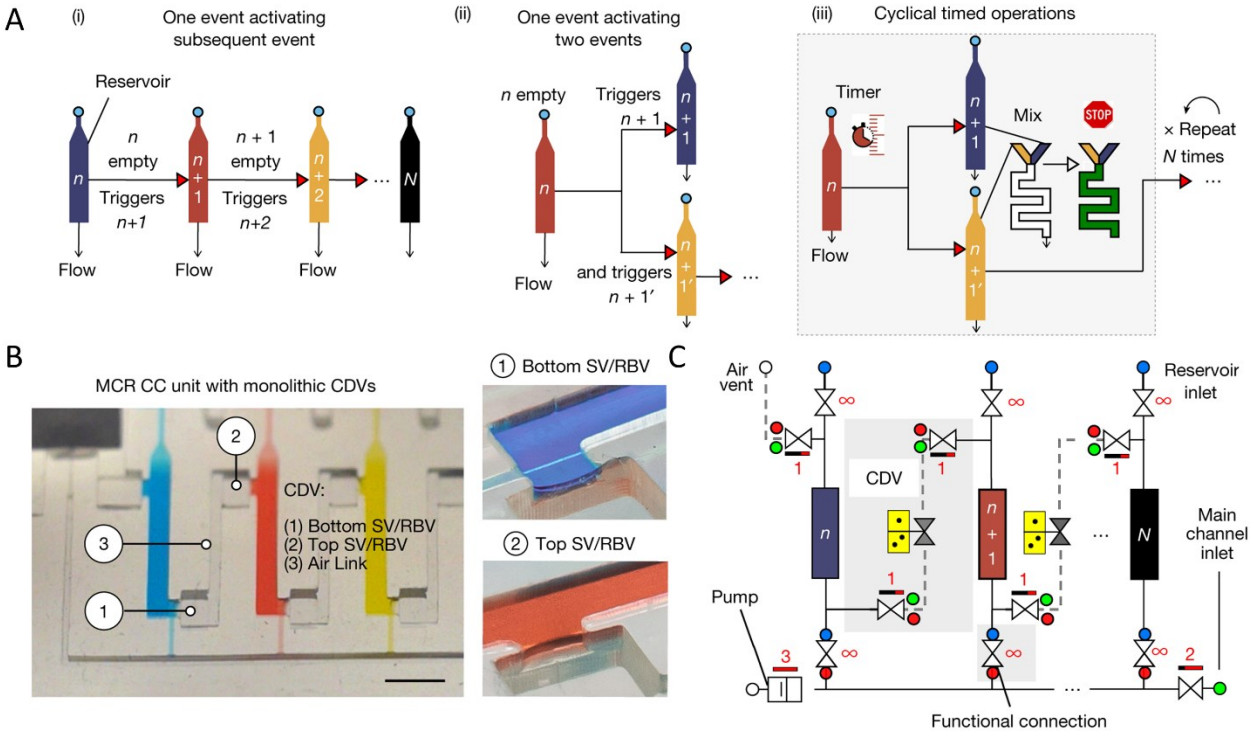

Figure 3.1. Microfluidic chain reaction (MCR) and the capillary domino valve (CDV). A) Serial (i), branching (ii), and timed, cascaded (iii) MCRs. (b) A 3D-printed CC chip with embedded CDVs. A CDV consists of a bottom RBV, top RBV, and an air channel. (c) The schematic representation of the CC shown in panel b[11]. Copyright 2022 Springer Nature Limited.

To further improve capillary microfluidics functionality, ongoing research is dedicated to introducing new elements that enhance the performance of CCs. For instance, recently, our lab introduced a novel concept called microfluidic chain reaction (MCR) for executing autonomous liquid handling algorithms by structurally programming capillary flow events in a CC. MCR operates on the principle that the activation of one event occurs only after the completion of the preceding event[11] (**Figure 3.1**). This is achieved through a specific capillaric element known as

the capillary domino valve (CDV). In essence, a CDV consists of two retention burst valves (RBVs) located at the top and bottom, connected by an air link. When the bottom RBV drains, it terminates the ongoing capillary flow event and exposes the top RBV to atmospheric pressure, initiating the subsequent capillary flow event. Using MCR, Yafia et al. showed automated sequential release of 300 aliquots across 3D-printed connected chips.

To fabricate molds and replicate polymeric CCs devices, silicon wafers and cleanroom techniques were initially used[9]. While this approach offers high-resolution fabrication and works well for a limited set of biocompatible materials in a lab setting, the cost, time, design, and post-processing assembly and functionalization constraints have restricted the applications of CCs.

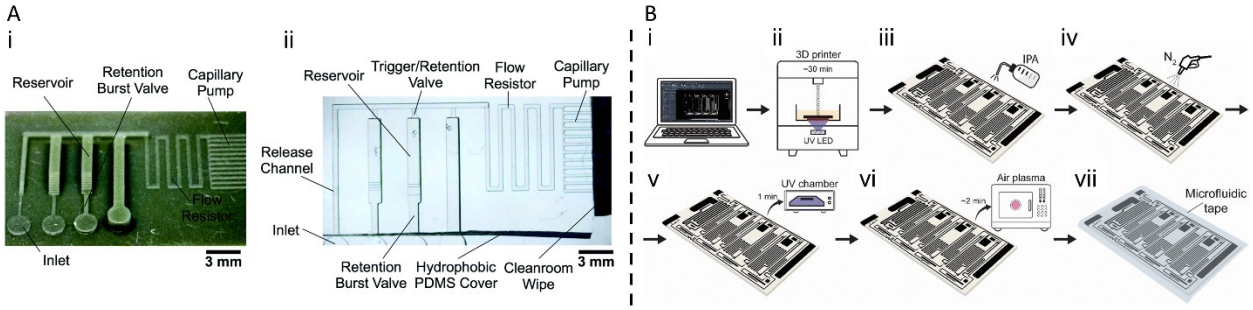

Figure 3.2. CCs fabricated using 3D printing. A) Fabrication of CCs based on 3D-pritned mold[12]. (i) 3D-printed mold of the CC, (ii) PDMS replica with transparent cover. Copyright 2016, Royal Society of Chemistry. B) Mold-less fabrication of CCs[13]. (i) design of the chip in a computer-aided design software, (ii) DLP-based 3D printing of open channels, (iii) rinsing with isopropanol (IPA) to remove uncured resin, (iv) drying the chip, (v) post-UV curing for 1 min, (vi) plasma treatment for surface functionalization, (vii) sealing the chip with a hydrophobic tape. Copyright 2023, Royal Society of Chemistry.

In recent years, additive manufacturing has garnered increasing attention as a means of integrating 3D digital designs and automated fabrication to address the limitations of conventional fabrication processes and improve efficiency[14]. Specifically, 3D printing reduces the resources and skills required to fabricate microfluidic devices, including CCs, enabling the dissemination of

microfluidic technology quickly. In one of our previous studies, we demonstrated the feasibility of using a benchtop DLP-based 3D printer to quickly and inexpensively manufacture reliable circuits by replicating Polydimethylsiloxane (PDMS) from 3D-printed molds[12] (**Figure 3.2A**). With 3D-printed molds, multi-sized height features could be fabricated in one run, addressing one of the key challenges in the classical photolithography method, where each different depth requires a new processing step and precise layer alignment. However, even with these advancements, designs are still limited to two-dimensional planar microchannels, and additional assembly steps and surface modifications are necessary to tune the wettability of channels and make CCs functional.

Our recent works took a step further in making the fabrication procedure of CCs easier, faster, and achievable for users with minimal fabrication skills[11,13]. We demonstrated the mold-less fabrication of capillaric circuits by sealing 3D-printed and plasma-treated open and planar capillaric elements with a hydrophobic plain cover (**Figure 3.2B**). This mold-less method significantly reduces the prototyping time and cost of CCs, enabling the quick execution of multiple rounds of iterations for the early stages of CCs designs. Although recent advancements in mold-less fabrication methods have made CCs prototyping easier, faster, and achievable for users with minimal fabrication skills, the need for surface modification, post-print assembly, and planar 2D design restrictions continue to be significant barriers to designing geometrically complex CCs and fabricating them in non-technical settings.

3.3 Digital Manufacturing Approaches for Microfluidic Applications

Digital manufacturing (DM), an emerging paradigm in the field of engineering and fabrication, has revolutionized the way we design, manufacture, and assemble products[15]. It encompasses a broad range of computer-based technologies, such as 3D printing, computer

numerical control (CNC) machining, and laser-based manufacturing techniques, that enable rapid, precise, controlled, and customizable production of complex components. One of the most notable aspects of DM is the ability to print objects in a manner similar to printing a document from a PDF file. In this case, instead of a 2D document, a 3D design file is used to directly produce physical objects through 3D printing. Over the last few years, the rapid technological progress, low capital costs, and minimal skill requirements associated with DM have resulted in its widespread adoption across various sectors[16]. In the context of microfluidics, digital manufacturing has the potential to overcome the limitations of traditional clean room microfabrication and replication methods by employing both subtractive and additive processes, such as micromilling, laser cutting, and 3D printing.

The integration of DM techniques into microfluidics offers numerous advantages, including rapid and cost-effective prototyping, which allows researchers to iterate, optimize, and share their designs quickly, democratizing microfluidics and streamlining the development process[14]. Moreover, DM can facilitate the production of intricate structures that would otherwise be challenging or impossible to create using traditional fabrication techniques like soft lithography or injection molding.

However, several challenges hinder the full realization of DM's potential in the microfluidics field. For instance, most microfluidic systems require peripherals that can be costly and bulky, limiting their wider adoption and the number of users who could benefit. These active microfluidic systems often consist of a chip actuated by peripherals using a computer program. Additionally, many microfluidic systems are too complex for digital manufacturing, either requiring a multitude of different materials or relying on microscopic features that are too small for typical additive and subtractive manufacturing processes. One promising approach to

circumventing the challenges associated with peripherals in microfluidics is capillary microfluidics, which can operate without requiring any bulky peripherals by utilizing capillary phenomena dictated by the geometry and surface chemistry of microchannels to control fluid flow.

By utilizing digital design files, researchers and manufacturers can easily share, modify, and collaborate on capillary microfluidic device designs. These files can then be sent to a 3D printer or other DM equipment to rapidly produce the devices, thus eliminating the need for complex and expensive traditional fabrication methods. This process not only reduces the time and cost associated with microfluidic device development but also fosters open-source collaboration and innovation within the field. Moreover, the accessibility of DM enables researchers and industries with limited resources to engage in the development and production of microfluidic devices. By leveraging the power of 3D printing, DM reduces the barriers to entry and encourages the widespread adoption of microfluidic technologies across various sectors. For more information on digital manufacturing of microfluidic devices, readers are referred to the published review paper titled 'Digital manufacturing for microfluidics' by Naderi et al.[14].

3.4 Overview of photocurable biocompatible inks for VP

While the photoinitiator also contributes to the reduction of light penetration depth, the photoabsorber has a more significant influence in this regard. Therefore, the photoabsorber has been added specifically to control and reduce the penetration depth of light. Biomaterials compatible with SLA 3D printing method are materials functionalized with acrylate, methacrylate, alkyne, and acrylamide groups, including hyaluronic acid-methacrylate, gelatin-methacrylate, polyethylene glycol diacrylate (PEGDA), polyethylene glycol dimethacrylate (PEGDMA), and polyethylene glycol diacrylamide.

VP printing in biomedical science has been made possible due to significant progress in development of photocurable biomaterials. Implants, biomedical and microfluidics devices can be fabricated using resins and elastomers, while photocrosslinkable hydrogels can encapsulate cells, and being used for bioprinting. To create implantable devices, some recent commercially available resins can meet the necessary requirements for printability, mechanical strength, and biocompatibility. Biodegradable polymers, such as poly (octamethylene maleate [anhydride] citrate) (POMaC), poly(ε-caprolactone) (PCL) and poly(α-hydroxy acids), have been utilized for clinical and tissue engineering applications[17–19]. By using acrylated trimethylene glycol (TMG) or poly(ethylene glycol) (PEG) as the linker, acrylate-endcapped poly(ε-caprolactone-co-trimethylene carbonate) resins have been developed for use in VP 3D printing. This method has been successful in producing microneedles[20]. In addition, there are newly available commercial resins in the market, including those offered by Formlabs and 3D Systems[21]. These resins are classified as biocompatible, falling under categories I to IIa, and are suitable for use in dental applications, surgical, and implant parts for a limited duration.

Although biocompatible resins, hydrogels and elastomer inks have been successfully developed for VP printing, there remains a lack of suitable biomaterials that can fulfill the necessary requirements for both biological and mechanical compatibility and printability. This has limited the applicability of VP printing for biomedical applications.

3.4.1 Synthetic photocurable inks

3.4.1.1 Poly(ethylene glycol) diacrylate (PEGDA)

In tissue engineering and pharmaceutical applications, PEG is a commonly used biomaterial due to its biocompatibility and hydrophilicity. Incorporating acrylate or methacrylate groups into PEG is advantageous since it makes photocurable. The properties of PEGDA vary depending on its molecular weight (Mw). For example, networks formed with an Mw of 8000 Da or less do not

allow the diffusion of myoglobin. However, PEGDA with an Mw of 20,000 Da or higher permits the transport of larger proteins such as ovoalbumin with an Mw of up to 45,000 Da[22–24]. In addition, the lower molecular weight PEGDA exhibited a better printability due to it lower viscosity and faster reaction.

Miller group has utilized PEGDA with an Mw of 6000 Da and 3400 Da as well as food dye as a photoabsorber in the fabrication of intricate volumetric structures using DLP printing, such as a noncellular vascularized alveolar unit capable of ventilation**(Figure 3.3A-B)**[24,25]. Nonetheless, certain factors, such as its nondegradability and solubility, as well as its lack of binding sites for cells, limit the suitability of PEGDA for use in bioprinting in certain circumstances. In addition, it is possible to modify PEGDA to simulate the components of the extracellular matrix (ECM) and improve cell adhesion. As an example, RGDS has been used as a modification to PEGDA, as it is a cell-adhesive peptide that specifically interacts with integrin receptors on the surface of cells[26]. This allows for the creation of ECM-like hydrogels which significantly improve cell adhesion and biocompatibility.

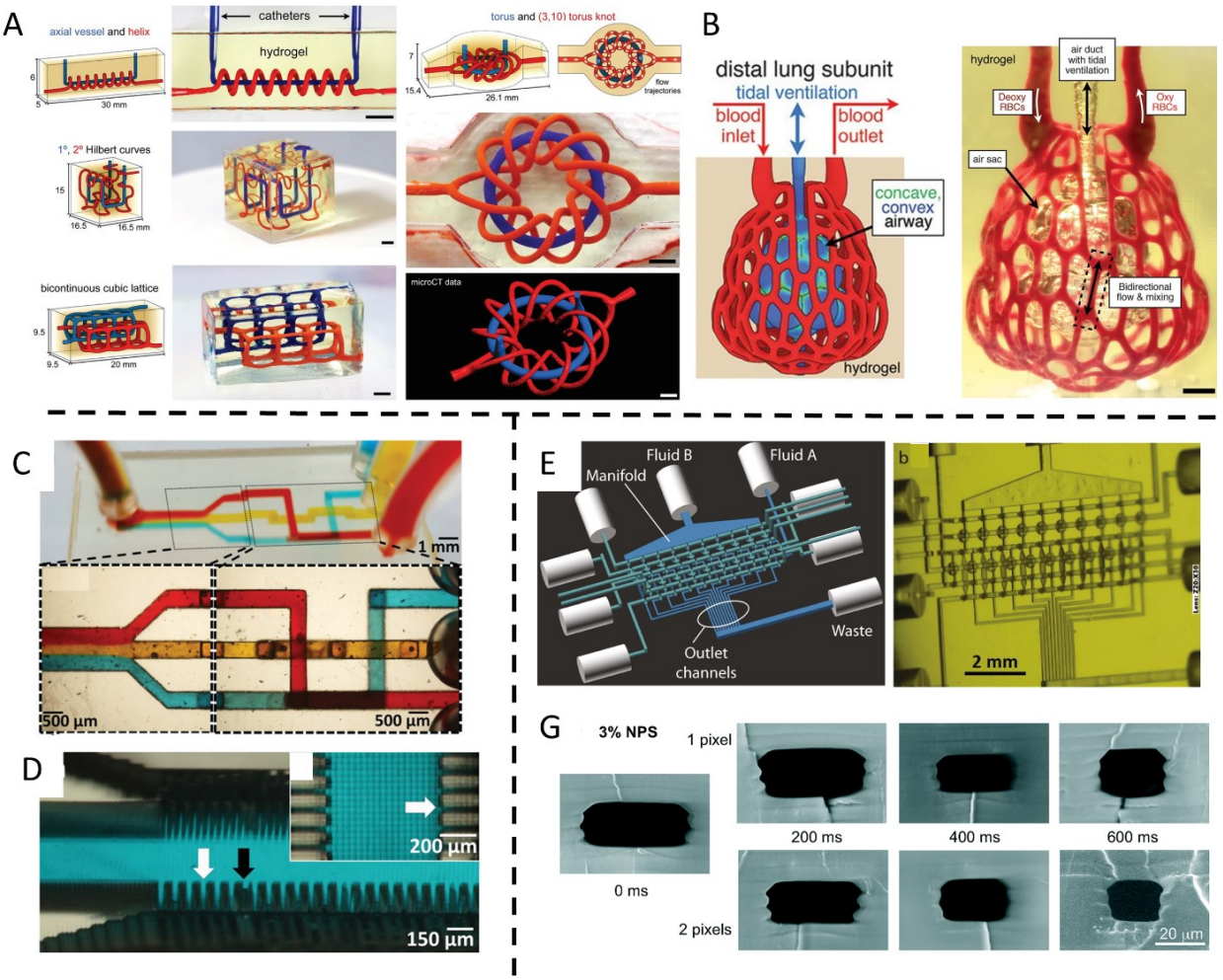

Figure 3.3 Examples of VP 3D-printed constructs using PEGDA. A) Entangled vascular networks 3D-printed with PEGDA with molecular weight 6000, food dye as the photoabsorber. B) 3D printed alveolar model during ventilation[24]. Copyright 2019, The American Association for the Advancement of Science Publishing. C) 3D-printed microfluidic channels using PEGDA-258 and ITX photoabsorber. D) High resolution and high aspect ration channels with a 1 pixel wide and 1 mm height[27]. Copyright 2019 WILEY-VCH Verlag GmbH & Co. KGaA, Weinhei. E) 3D model and microscope image of membrane valve-based diluter 3D-printed with PEGDA-258 and NPS photoabsorber[28]. Copyright 2021 Springer Nature Limited. G) 3D-printed 18 µm height channels with a layer thickness of 6 µm using 3% NPS[29]. Copyright The Royal Society of Chemistry 2017.

PEGDA at a low molecular weight has caught the attention of researchers searching for alternative materials to PDMS that are more amenable to manufacturing microfluidic devices. PEGDA-258 is transparent, biocompatible, and impermeable to water due to its low molecular

weight[30,31]. Furthermore, it can be modified to introduce functionalities that make it more amenable to biological applications. To make it more suitable for 3D printing microfluidic devices, the resin mixture is combined with a photoinitiator, such as BAPO, and a photoabsorber, such as isopropyl thioxanthone (ITX) or 2-nitrophenyl phenyl sulfide (NPS), to reduce the penetration depth of light[27,29]. The Folch group has demonstrated the ability to 3D-print microchannels with a cross-section of one-pixel-wide and 1-mm-tall using PEG-DA-258 with ITX photoabsorber, while the Nordin group has printed microchannels with a smaller cross-section using NPS photoabsorber due to using a 3D printer with a smaller pixel size (**Figure 3.3C-G**). Compared to ITX, NPS is a photoabsorber that is more toxic to cells. Samples printed with NPS require thorough washing before they can be used in cell culture applications[32]. PEGDA-258 is not only easier and less expensive to manufacture than PDMS but also more beneficial in applications that require drug testing[14]. While PEGDA is highly printable and biocompatible, it lacks the oxygen permeability that PDMS possesses.

3.4.1.2 Poly(vinyl alcohol) (PVA)

The use of PVA has been reported as a suitable bioink in the development of cartilage and bone tissue engineering. PVA methacrylate, also known as PVA-MA, exhibits excellent biocompatibility, hydrophilicity, adjustable mechanical properties and modifiable functional groups, giving rise to modifications with methacrylates and tyramines[33,34]. VP printing of tissue-like constructs with high resolutions has been made possible using PVA-MA, either alone or in combination with GelMA, through a visible light illumination. Tissue-like constructs printed with a combination of PVA-MA and GelMA have shown potential for the development of osteogenic and chondrogenic tissues, as well as for the growth of endothelial cells on their surfaces[35]. Nevertheless, unmodified synthetic materials usually lag behind natural polymers in terms of

bioactivity (as they commonly lack innate cell binding sites) and their ability to properly support cell differentiation. To overcome this limitation, studies often apply specific modifications, such as incorporation of adhesive motifs (e.g. RGD) which promote the cell-instructive capability of synthetic materials[36]. To replicate the externally controllable remodelling or degradation of natural materials, proteinase-sensitive crosslinkers have also been integrated into synthetic scaffolds[37]. This suggests that PVA-MA/GelMA could be a promising bioink for VP-based bioprinting.

3.4.1.3 Poly(octamethylene maleate (anhydride) citrate) (POMaC)

Printable materials with high elasticity and stretchability are not only useful for tissue engineering applications, but also, for example, for microfluidic chips, and soft robotic systems. POMaC is a citric acid-based and biodegradable elastomer that can be used for scaffold fabrication[38] **(Figure 3.4C)**. This material is a photo-curable elastomer that allows for fast fabrication under mild conditions. It degrades through hydrolysis reactions in aqueous solutions and is synthesized from non-toxic monomers. POMaC is a biodegradable, soft, and elastic material that can be adjusted to mimic the mechanical properties of a wide range of soft biological tissues, making it of great interest[18,39]. POMaC has recently been successfully used as a crucial component of implantable pressure/strain sensors for tendons and pulse sensors for blood vessels, chosen and validated for its biocompatibility, biodegradability, and mechanical properties[40–42]. In a recent study on the development of a pressure sensor for orthopedic tendon applications, Boutry et al. studied the biodegradability and resistance of POMaC to cycling stress(**Figure 3.4B**)[41]. They defined the required material properties for POMaC as a packaging layer of the overall sensor device, which included a low tensile modulus to prevent the restriction of motion or the healing process of the injured tendon and the ability to resist deformation (to avoid breaking) upon repeated physiological stress. These properties were essential to facilitate the necessary rehabilitation

exercises of the injured individual. Due to their limited printability, POMaC has not been readily used for the manufacturing of complex and intricate structures.

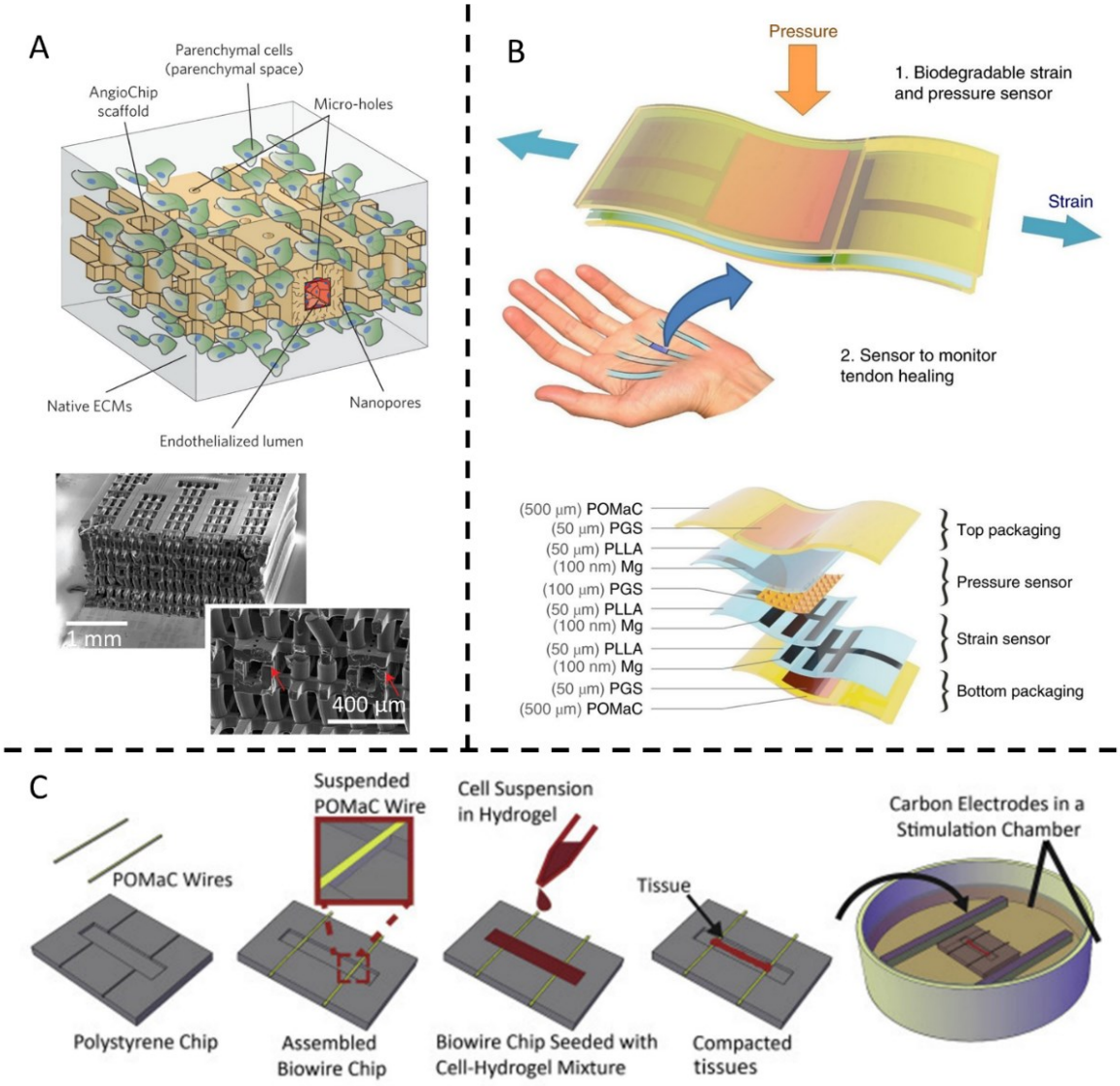

Figure 3.4. Various applications of POMaC. A) Angiochip, a scaffold that supports the culture of cells on a mechanically tunable matrix (POMaC) that incorporates a perfusable, branched microchannel network coated with endothelial cells. Scale bars 1 mm (left) and 400 µm (right)[43]. Copyright 2016, the Authors, published by Springer Nature. B) A stretchable, biodegradable tendon strain and pressure sensor; POMaC was used as a packaging material, coming in direct contact with host tissue[42]. Copyright 2018, the Authors, published by Springer Nature. C) A cultivation platform for the generation of cardiac microtissues to model disease. POMaC wires are placed perpendicularly to the microtissues, which attach onto the POMaC wires;

the displacement of the wires upon contraction of the microtissues can be monitored to deduct the force dynamics of the microtissues in various conditions[44]. Copyright 2018, the Authors, published by Cell Press.

3.5 Tumor-on-a-chip models

As 3D tumor models closely mimic tumor behavior with high precision and are considered ethical and safe, they are ideal for testing drugs before moving onto clinical trials[45]. Tumor spheroids are highly suitable for high-throughput generation and assaying, and closely replicate the in vivo tumor microenvironment[46,47]. Microfluidics technology allows the inclusion of perfusable vasculature, making it an effective tool for drug screening to study the interactions between tumors and blood vessels[48,49].

Chen group utilized a sequential ink delivery approach with DLP technology to create a biomimetic tri-regional model of glioblastoma multiforme (GBM) using multiple bioinks in sequence[50]. This model was made up of a tumor region, an acellular extracellular matrix (ECM) region, and an endothelial region with stiffness patterns designed to mimic the Glioblastoma (GBM), brain parenchyma, and surrounding capillaries (**Figure 3.5A-B**). To achieve regionally varied biophysical properties, the GBM tumor region was printed using different concentrations of HAMA and GelMA. The two ECM formulations with different stiffnesses were designed to replicate the conditions of healthy brain tissue or GBM-remodeled stroma. Results showed that cell proliferation and expansion were increased in the soft ECM, while the stiff model promoted malignant phenotypes such as hypoxia, stemness, and angiogenic potential (**Figure 3.5C-D**). This study demonstrated that the VP bioprinting platform allowed for the fabrication of GBM models with mechanical heterogeneity in a rapid, flexible, and reproducible manner, which could potentially be used as a system for patient-specific GBM modeling and drug screening.

Hu et al. recently developed a chip design for evaluating the efficacy of anticancer drugs using a perfusable, vascularized tumor spheroid-on-a-chip model (**Figure 3.5E-F**)[51]. The chip included a chamber with a depth of 700 μm containing human HUVECs to allow for the development of a thicker layer of vessels with a distinct morphology, while the side channels containing fibroblasts enhanced vascular maturation. They utilized the PHD inhibitor DMOG to prevent the degradation of normal blood vessels while enhancing the effectiveness of the anticancer drugs paclitaxel and cisplatin in human esophageal carcinoma spheroids. This platform can be used for functional drug evaluation to improve chemotherapy treatments, with potential clinical translation in personalized medicine. The study highlights the need for further research to understand the molecular mechanisms underlying the effects of DMOG.

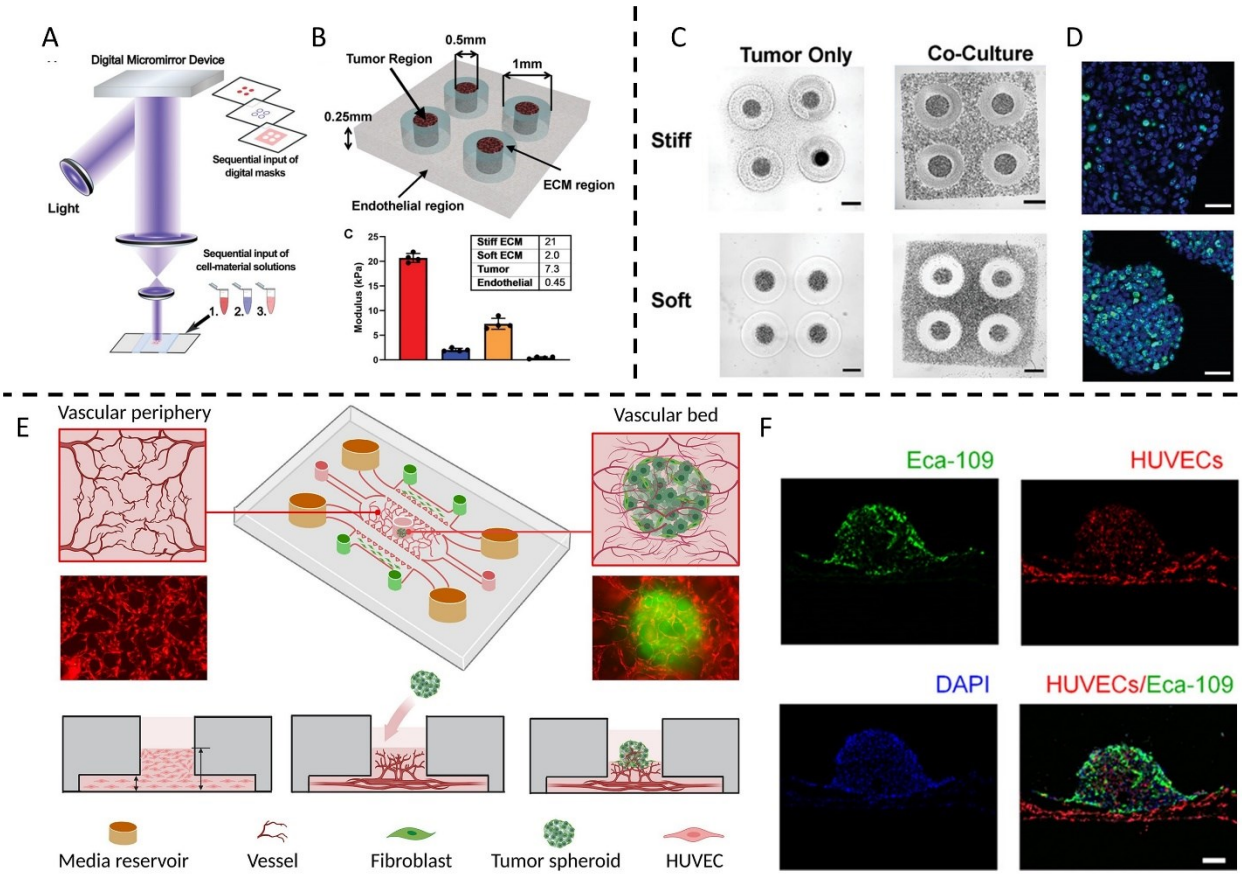

Figure 3.5 OoC devices. A-B) 3D-bioprinted Glioblastoma models with locally varied mechanical properties[50]. A) The VP 3D printing approach. B) the model dimensions and stiffness of each region in the 3D-printed model. Copyright 2021, Wiley-VCH. C) Bright field images of 3D printed models with stiff and soft environment. D) Comparing the 3D tumor-only stiff condition with the 3D tumor-only soft condition. E-F) Vascularized Tumor Spheroid-on-a-Chip Model. E) Schematic of the vascularized tumor spheroid-on-a-chip. F) Fluorescence images display a representative cryosection that demonstrates the vascularization of a tumor spheroid following 10 days of culture[51]. Copyright 2022, American Chemical Society.

3.6 Conclusion

In conclusion, in this chapter, we focused on reviewing capillary microfluidics, DM, and photocurable bioinks for vat-photopolymerization, specifically synthetic ink, including PEGDA and POMaC. This chapter aims to fill the gaps in background knowledge not addressed in the previous chapter and provides a foundation for the forthcoming sections of the thesis. This chapter

serves as a foundation for the subsequent sections of the thesis, which will delve deeper into the topics covered and contribute to advancing the field of biofabrication.

3.7 References

1. Liu, Y., Sun, L., Zhang, H., Shang, L. & Zhao, Y. Microfluidics for drug development: From synthesis to evaluation. *Chem. Rev.* **121**, 7468–7529 (2021).

2. Ayuso, J. M., Virumbrales-Muñoz, M., Lang, J. M. & Beebe, D. J. A role for microfluidic systems in precision medicine. *Nat. Commun.* **13**, 3086 (2022).

3. Sivaramakrishnan, M., Kothandan, R., Govindarajan, D. K., Meganathan, Y. & Kandaswamy, K. Active microfluidic systems for cell sorting and separation. *Curr. Opin. Biomed. Eng.* **13**, 60–68 (2020).

4. Hess, J. F. *et al.* Review on pneumatic operations in centrifugal microfluidics. *Lab Chip* **19**, 3745–3770 (2019).

5. Shi, Y. *et al.* Application of centrifugal microfluidics in immunoassay, biochemical analysis and molecular diagnosis. *Analyst* **146**, 5800–5821 (2021).

6. Alizadeh, A., Hsu, W., Wang, M. & Daiguji, H. Electroosmotic flow: From microfluidics to nanofluidics. *Electrophoresis* **42**, 834–868 (2021).

7. Rasouli, R., Villegas, K. M. & Tabrizian, M. Acoustofluidics–changing paradigm in tissue engineering, therapeutics development, and biosensing. *Lab Chip* **23**, 1300–1338 (2023).

8. Safavieh, R. & Juncker, D. Capillarics: pre-programmed, self-powered microfluidic circuits built from capillary elements. *Lab Chip* **13**, 4180 (2013).

9. Olanrewaju, A., Beaugrand, M., Yafia, M. & Juncker, D. Capillary microfluidics in microchannels: from microfluidic networks to capillaric circuits. *Lab Chip* **18**, 2323–2347 (2018).

10. Yafia, M. *et al.* Microfluidic chain reaction of structurally programmed capillary flow events. *Nature* **605**, 464–469 (2022).

11. Yafia, M. *et al.* Microfluidic chain reaction of structurally programmed capillary flow events. *Nature* **605**, 464–469 (2022).

12. Olanrewaju, A. O., Robillard, A., Dagher, M. & Juncker, D. Autonomous microfluidic capillaric circuits replicated from 3D-printed molds. *Lab Chip* **16**, 3804–3814 (2016).

13. Parandakh, A. *et al.* 3D-printed capillaric ELISA-on-a-chip with aliquoting. *Lab Chip* (2023).

14. Naderi, A., Bhattacharjee, N. & Folch, A. Digital Manufacturing for Microfluidics. *Annu. Rev. Biomed. Eng.* **21**, 325–364 (2019).

15. Paritala, P. K., Manchikatla, S. & Yarlagadda, P. K. D. V. Digital manufacturing-applications past, current, and future trends. *Procedia Eng.* **174**, 982–991 (2017).

16. Rayna, T. & Striukova, L. From rapid prototyping to home fabrication: How 3D printing is changing business model innovation. *Technol. Forecast. Soc. Change* **102**, 214–224 (2016).

17. Melchels, F. P. W., Feijen, J. & Grijpma, D. W. A review on stereolithography and its applications in biomedical engineering. *Biomaterials* **31**, 6121–6130 (2010).

18. Zhang, B. *et al.* Microfabrication of AngioChip, a biodegradable polymer scaffold with microfluidic vasculature Microengineered biomimetic systems for organ-on-a. *Nat. Protoc.* **13**, (2018).

19. Zhang, B., Korolj, A., Lai, B. F. L. & Radisic, M. Advances in organ-on-a-chip engineering. *Nat.*

Rev. Mater. **3**, 257–278 (2018).

20. Mizutani, M. & Matsuda, T. Liquid acrylate-endcapped biodegradable poly (ϵ-caprolactone-co-trimethylene carbonate). I. Preparation and visible light-induced photocuring characteristics. *J. Biomed. Mater. Res. An Off. J. Soc. Biomater. Japanese Soc. Biomater. Aust. Soc. Biomater. Korean Soc. Biomater.* **62**, 387–394 (2002).

21. Guttridge, C., Shannon, A., O'Sullivan, A., O'Sullivan, K. J. & O'Sullivan, L. W. Biocompatible 3D printing resins for medical applications: A review of marketed intended use, biocompatibility certification, and post-processing guidance. *Ann. 3D Print. Med.* **5**, 100044 (2022).

22. Cavallo, A., Madaghiele, M., Masullo, U., Lionetto, M. G. & Sannino, A. Photo-crosslinked poly (ethylene glycol) diacrylate (PEGDA) hydrogels from low molecular weight prepolymer: swelling and permeation studies. *J. Appl. Polym. Sci.* **134**, (2017).

23. Ligon, S. C., Liska, R., Stampfl, J., Gurr, M. & Mülhaupt, R. Polymers for 3D printing and customized additive manufacturing. *Chem. Rev.* **117**, 10212–10290 (2017).

24. Grigoryan, B. *et al.* Functional intravascular topologies and multivascular networks within biocompatible hydrogels. *Science (80-.).* **464**, 458–464 (2019).

25. Grigoryan, B. *et al.* Development, characterization, and applications of multi-material stereolithography bioprinting. *Sci. Rep.* **11**, 3171 (2021).

26. Chan, V., Zorlutuna, P., Jeong, J. H., Kong, H. & Bashir, R. Three-dimensional photopatterning of hydrogels using stereolithography for long-term cell encapsulation. *Lab Chip* **10**, 2062–2070 (2010).

27. Kuo, A. P. *et al.* High-Precision Stereolithography of Biomicrofluidic Devices. *Adv. Mater. Technol.* **4**, 1–11 (2019).

28. Sanchez Noriega, J. L. *et al.* Spatially and optically tailored 3D printing for highly miniaturized and integrated microfluidics. *Nat. Commun. 2021 121* **12**, 1–13 (2021).

29. Gong, H., Bickham, B. P., Woolley, A. T. & Nordin, G. P. Custom 3D printer and resin for 18 μm × 20 μm microfluidic flow channels. *Lab Chip* **17**, 2899–2909 (2017).

30. Urrios, A. *et al.* 3D-printing of transparent bio-microfluidic devices in PEG-DA. *Lab Chip* **16**, 2287–2294 (2016).

31. Tasoglu, S. & Folch, A. *3D Printed Microfluidic Devices*. *3D Printed Microfluidic Devices* (2019). doi:10.3390/books978-3-03897-468-0.

32. Warr, C. *et al.* Biocompatible PEGDA Resin for 3D Printing. (2020) doi:10.1021/acsabm.0c00055.

33. Lim, K. S. *et al.* Fundamentals and applications of photo-cross-linking in bioprinting. *Chem. Rev.* **120**, 10662–10694 (2020).

34. Lim, K. S., Alves, M. H., Poole-Warren, L. A. & Martens, P. J. Covalent incorporation of non-chemically modified gelatin into degradable PVA-tyramine hydrogels. *Biomaterials* **34**, 7097–7105 (2013).

35. Lim, K. S. *et al.* Bio-resin for high resolution lithography-based biofabrication of complex cell-laden constructs. *Biofabrication* **10**, 34101 (2018).

36. Murphy, W. L., McDevitt, T. C. & Engler, A. J. Materials as stem cell regulators. *Nat. Mater.* **13**,

547–557 (2014).

37. Lutolf, M. P. *et al.* Synthetic matrix metalloproteinase-sensitive hydrogels for the conduction of tissue regeneration: engineering cell-invasion characteristics. *Proc. Natl. Acad. Sci.* **100**, 5413–5418 (2003).

38. Tran, R. T. *et al.* Synthesis and characterization of a biodegradable elastomer featuring a dual crosslinking mechanism. *Soft Matter* **6**, 2449–2461 (2010).

39. Montgomery, M. *et al.* Method for the Fabrication of Elastomeric Polyester Scaffolds for Tissue Engineering and Minimally Invasive Delivery. *ACS Biomater. Sci. Eng.* **4**, 3691–3703 (2018).

40. Boutry, C. M. *et al.* for the wireless monitoring of blood flow. *Nat. Biomed. Eng.* **3**, (2019).

41. Boutry, C. M. *et al.* pressure sensor for orthopaedic application. *Nat. Electron.* **1**, (2018).

42. Boutry, C. M., Kaizawa, Y., Schroeder, B. C., Chortos, A. & Legrand, A. A stretchable and biodegradable strain and pressure sensor for orthopaedic application. (2018).

43. Zhang, B. *et al.* Biodegradable scaffold with built-in vasculature for organ-on-a-chip engineering and direct surgical anastomosis. *Nat. Mater.* **15**, 669 (2016).

44. Zhao, Y. *et al.* A Platform for Generation of Chamber-Specific Cardiac Tissues and Disease Modeling. *Cell* **176**, 913-927.e18 (2019).

45. Boucherit, N., Gorvel, L. & Olive, D. 3D tumor models and their use for the testing of immunotherapies. *Front. Immunol.* **11**, 603640 (2020).

46. Ivanov, D. P. *et al.* Multiplexing spheroid volume, resazurin and acid phosphatase viability assays for high-throughput screening of tumour spheroids and stem cell neurospheres. *PLoS One* **9**, e103817 (2014).

47. Schuster, B. *et al.* Automated microfluidic platform for dynamic and combinatorial drug screening of tumor organoids. *Nat. Commun.* **11**, 5271 (2020).

48. Nie, J. *et al.* Construction of multi-scale vascular chips and modelling of the interaction between tumours and blood vessels. *Mater. Horizons* **7**, 82–92 (2020).

49. Lai, B. F. L. *et al.* A well plate–based multiplexed platform for incorporation of organoids into an organ-on-a-chip system with a perfusable vasculature. *Nat. Protoc.* **16**, 2158–2189 (2021).

50. Tang, M. *et al.* Rapid 3D Bioprinting of Glioblastoma Model Mimicking Native Biophysical Heterogeneity. *Small* **17**, 2006050 (2021).

51. Hu, Z. *et al.* Vascularized Tumor Spheroid-on-a-Chip Model Verifies Synergistic Vasoprotective and Chemotherapeutic Effects. *ACS Biomater. Sci. Eng.* **8**, 1215–1225 (2022).

Chapter 4

4. Chapter 4: Digital Manufacturing of Functional Ready-to-Use Microfluidic Systems

4.1 Preface

Our research group recently developed multiple capillary microfluidic systems using 3D printing of open channels for automating an ELISA-on-a-chip for COVID19 antibody and antigen assays, and for the first microfluidic thrombin generation assay based on microfluidic chain reaction (MCR). Capillary flow depends on controlled hydrophilicity, which previously required a plasma chamber for post-processing. Here we introduce a new hydrophilic ink formulation, for simplifying the fabrication process. These advances open the door for distributed and digital manufacturing of functional microfluidic CCs and systems by anyone, anywhere, anytime.

This chapter is a manuscript of a research article under review in the journal of Advanced Materials: “Digital Manufacturing of Functional Ready-to-Use Microfluidic Systems”, **V. Karamzadeh***, A. Sohrabi*, M. Shen, and D. Juncker.

4.2 Abstract

Digital manufacturing (DM) strives for the seamless manufacture of a functional device from a digital file. DM holds great potential for microfluidics, but requirements for embedded conduits and high resolution beyond the capability of common manufacturing equipment, and microfluidic systems' dependence on peripherals (e.g. connections, power supply, computer), have limited its adoption. Microfluidic capillaric circuits (CCs) are structurally-encoded, self-contained microfluidic systems that operate and self-fill thanks to precisely tailored hydrophilicity. CCs were heretofore hydrophilized in a plasma chamber, but which only produces transient hydrophilicity, lacks reproducibility, and limits CC design to open surface channels sealed with a tape. Here we introduce the additive DM of monolithic, fully functional and intrinsically hydrophilic CCs. CCs were 3D printed with commonly available light engine-based 3D printers using polyethylene(glycol)diacrylate-based ink co-polymerized with hydrophilic acrylic acid crosslinkers and optimized for hydrophilicity and printability. A new, robust capillary valve design and embedded conduits with circular cross-sections that prevent bubble trapping are presented, and complex interwoven circuit architectures created, and their use illustrated with an immunoassay. Finally, the need for external paper capillary pumps is eliminated by directly embedding the capillary pump in the chip as a porous gyroid structure, realizing fully functional, monolithic CCs. Thence, a computer-aided design file can be made into a CC by commonly available 3D printers in less than 30 minutes enabling low-cost, distributed, DM of fully functional ready-to-use microfluidic systems.

Keywords: Hydrophilic ink, 3D Printing, Capillaric Circuits, diagnostics, functional microfluidics, digital manufacturing

4.3 Introduction

Digital manufacturing (DM) implies the largely automated, computer-centric fabrication of customizable products from a digital file to a final product. Widespread adoption of DM requires both widely available manufacturing equipment, and designs that can be directly manufactured by these equipment. Microfluidic systems have traditionally been made by clean room microfabrication and replication methods[1], but the adoption of classical and emerging subtractive and additive manufacturing processes for microfluidics fabrication makes it a candidate for DM.[2] Subtractive processes include CNC milling[3] and laser cutting[4] while additive processes include 3D printing using filament-based printing[5,6] and light-based photopolymerization[7–9] have become popular over the last few years owing to rapid technological progress, low capital costs, and low skill requirements[10]. In particular, application-specific microfluidic chips would benefit from on-demand and on-the-fly design and manufacturing. DM could drive a broader adoption of microfluidics if one could print functional microfluidic systems similar to the way one can print out a digital text and art, such as this manuscript, on one's own printer at the office or at home in a matter of minutes.

There are several challenges that prevent the rapid adoption of DM for microfluidics. Firstly, most microfluidic systems are computer controlled, and require peripherals that can be costly and bulky, and are application specific, and are thus not universally available. This requirement doubly impacts the adoption of DM because it is conditional on users pre-owning peripheral control systems and will limit the use of DM to making microfluidic chips. Moreover, the very use of computers and peripherals means that what is commonly referred to as active microfluidics[11] is in actuality based on generic, passive chips that can be used for a variety of microfluidic applications by reprogramming the computer without the need for physically

reconfiguring the chip itself. As mass production of generic chips is cheaper than DM, it remains advantageous relative to DM. Secondly, many microfluidic systems cannot be made via DM because DM-compatible manufacturing processes lack versatility. Indeed, if the chip architecture is very complex, or the chips require special materials, or different materials, or if they require microscopic features, or a combination of both microscopic and macroscopic features, or special surface chemical properties, then they may not be compatible with current DM processes.

Capillary microfluidics can operate without requiring any bulky peripherals by making use of capillary phenomena defined by the geometry and surface chemistry of microchannels to control fluid flow[12,13]. Additive manufacturing of monolithic, functional capillary microfluidics using a porous material with different powders of variable hydrophilicity to create microfluidic 'channels' was recently demonstrated using a customized binder jet 3D printer[14]. However, powder printing and this design were dependent on a custom printer design, thus preventing broader adoption. Stereolithography and digital light processor (DLP) have become widely available, and over the last few years, multiple groups[15,16] have developed systems and processes for making microfluidic devices with high resolution and advanced functionality. Polyethylene(glycol)diacrylate (PEGDA) with a molecular weight of 258 (PEGDA-258) has emerged as a popular material for additive 3D printing of microfluidics devices[17,18]. Whereas the initial use of PEGDA was making 'active' microfluidics that use passive chips dependent on peripherals,[17,18] more recently, DLP printing has been used to make so-called capillaric circuits (CCs)[12,19].

CCs are capillary microfluidics assembled from individual capillaric elements that structurally encode liquid handling algorithms. An initial study using replica molded CCs from DLP printed molds established the feasibility DLP printing despite a lower resolution than clean room fabricated CCs[20], and alleviated initials concerns on whether capillary flow functions such

as filling and flow stop could be realized.[20] More recently, application-specific CCs were directly printed on-demand and used to execute structurally pre-programmed liquid handling algorithms with as many as several hundred operations, thanks to the microfluidic chain reaction (MCR), and for applications in various assays.[12,19,21] CCs operate thanks to precisely controlled hydrophilicity with a water contact angle between ~30-60º to meet the dual requirements of self-filling by capillary flow, and flow stoppage at capillary stop valves (SVs)[21]. Currently, 3D printed CCs require plasma post-processing for achieving the required hydrophilicity, which necessitates a plasma chamber, an equipment that is not readily available[12]. Moreover, this post-processing entails two additional limitations: hydrophilicity is fleeting and prevents CC storage and field usage, and only open, surface channels can be plasma activated, and hence CCs are printed as open surface structures enclosed with a hydrophobic cover – hydrophobicity is indeed required to preserve SV function. The cover also needs to be cut-out for sample delivery. In short, there remained multiple impediments that prevented direct DM of CCs.

Here, we introduce a modified PEGDA-258 ink that is intrinsically hydrophilic for DM of monolithic, fully functional CCs with embedded conduits. We further introduce new designs for SVs and non-rectangular cross-sections that both improve functionality and reliability of 3D-printed CCs. CCs with embedded interwoven conduits were used for serial delivery of reagents using the MCR and capillary retention burst valves (RBVs)[22], and validated their use in immunoassays using SARS-CoV-2 protein. Finally, capillary pumps made from high-resolution, mathematically-generated geometries were directly integrated into the CCs, circumventing the need for external paper pumps. Thanks to these advances, fully functional CCs were printed within a few minutes on a commercial DLP 3D printer, paving the way for distributed DM of functional microfluidic systems.

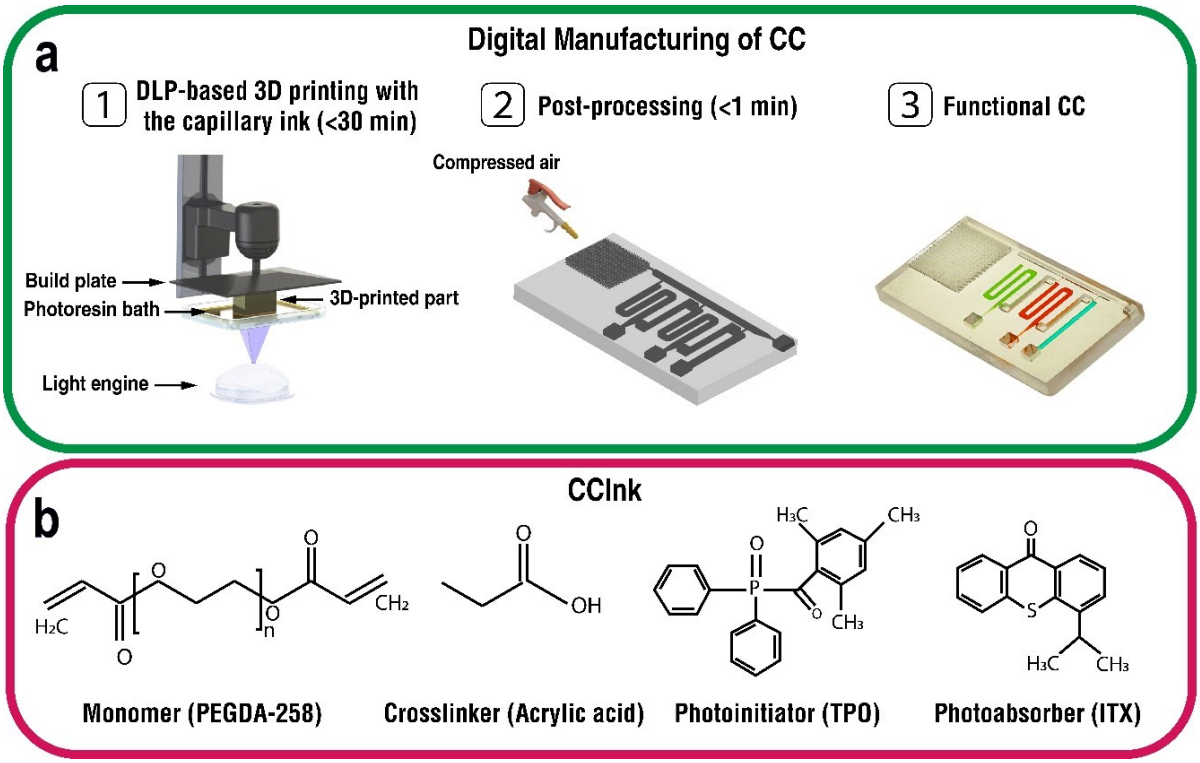

Figure 4.1 Digital manufacturing (DM) of functional capillaric circuits (CCs) using an intrinsically hydrophilic ink (CCInk). (**a**) 1) Additive manufacturing of a CCs from a digital design file using a light engine and layer-by-layer vat photopolymerization (VP). 2) Removal of uncured CCInk under a stream of compressed air (<1 min). 3) Functional CC loaded with reagents and primed to execute the structurally encoded (i.e. pre-programmed) capillary flow events following the addition of the triggering solution. (**b**) Hydrophilic CCInk composition including polyethyleneglycol diacrylate (PEGDA-258) monomer, acrylic acid additive to tune hydrophilicity, a photoinitiator (TPO) and a photoabsorber (ITX).

4.4 Results and Discussions

Figure 4.1 illustrates the streamlined, rapid DM of monolithic CCs with an intrinsically hydrophilic, photopatternable ink (CCInk) comprising four main constituents, namely a monomer (PEGDA-258), a photoinitiator (diphenyl(2,4,6-trimethylbenzoyl) phosphine oxide, TPO), a photoabsorber (isopropylthioxanthone, ITX), and a hydrophilic agent and cross-linker (acrylic acid, AA).

4.4.1 Formulation and characterization of CCInk

CCs made of native PEGDA-258 have a contact angle of ~65°, which albeit considered hydrophilic, is too hydrophobic for reliable self-filling of microchannels by aqueous solutions, especially in the presence of hydrophobic cover. While it is also possible to plasma treat PEGDA-258 and increase hydrophilicity the surface gradually returns to its original, low hydrophilicity state over the course of 4h (**Figure S1, Supporting Information).**

To permanently increase the hydrophilicity of CCs towards supporting reliable self-filling, we incorporated acrylic acid (AA) and methacrylic acid (MA) into the PEGDA ink[23,2424]. AA and MA both have a vinyl group and can thus be co-polymerized with PEGDA by photopolymerization. The acidic groups of AA and MA can form hydrogen bonds with water, and thus lower the contact angle and increase hydrophilicity.[23,24] We reasoned that by adjusting the ratio of PEGDA:Additive, the hydrophilicity could be adjusted to fall within the optimal range for autonomous, structurally encoded flow operations by CCs.

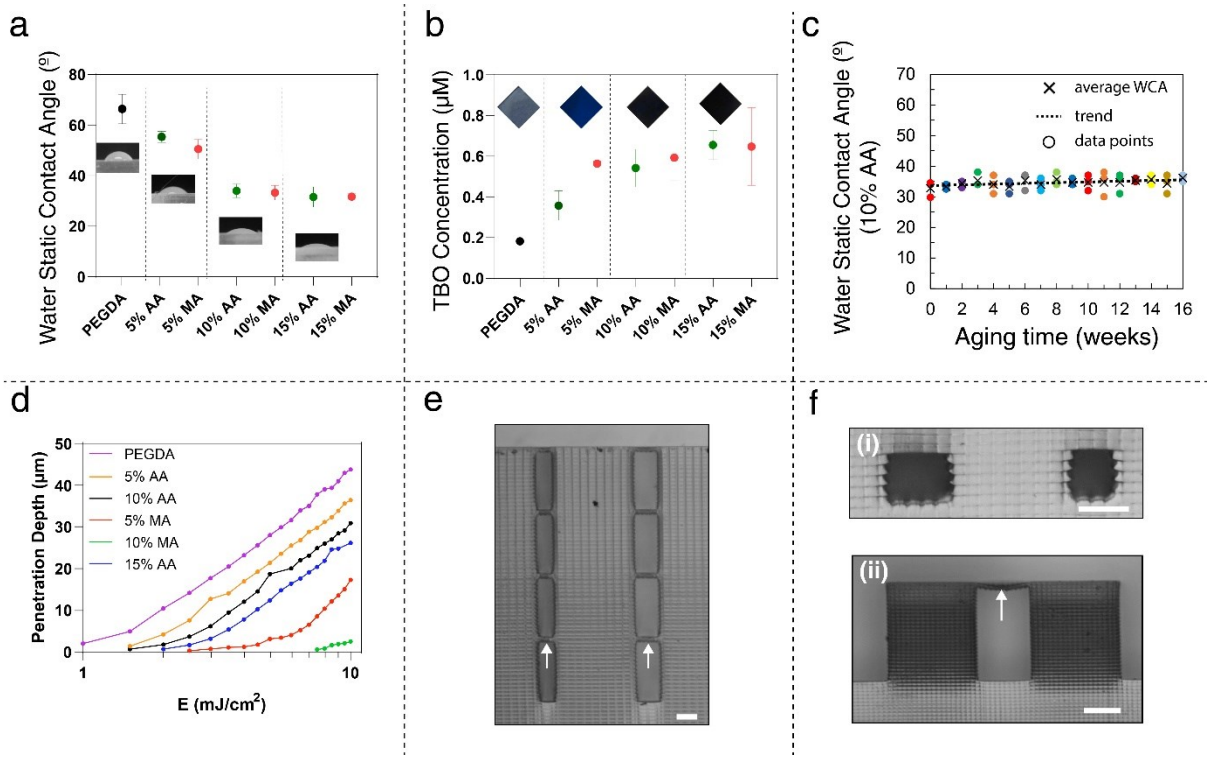

Figure 4.2. Photocurable ink design, optimization, and 3D printability (**a)** Static water contact angle for PEGDA-258 with different AA and MA concentrations (**b)** Toluidine blue assay (TBO) quantification of carboxyl group density on 3D-printed samples. (**c)** serial contact angle measurements over a period of >16 weeks illustrating surface stability (the dashed line shows the linear trend of the average WCA). **(d)** Penetration depth characterization of the hydrophilic formulation with different co-monomer concentrations. **(e)** 3D printed stacked microchannels separated with 25 µm membranes (white arrow) using a formulation with 10% AA. **(f)** (i) embedded rectangular channels, and (ii) 3D printed membrane with single layer roof membrane (white arrow) using a formulation with 10% AA. Scale bar: 100 µm.

The contact angle of water on 3D printed parts as function of the percentage of AA and MA was measured. **Figure 4.2a** shows that it can be lowered to ~35° for 10% or higher additive concentrations. We tested higher concentrations of additives, but we observed no further changes in the contact angle while printing resolution was compromised as additive-additive cross-linking competes with additive-PEGDA cross-linking (results not shown). Toluidine blue is an acidophilic dye that reversibly binds to acidic molecules in a pH-dependent manner and was previously used to characterize carboxyl groups. We utilized toluidine blue assay (TBO) to quantify the density of

carboxyl groups in 3D printed structures (**Figure 4.2b)**. The density of COOH as a function of AA and AM concentration in the ink shows saturation once the concentration reaches 10%. Based on these results, CCInk was formulated with 10% of AA because a contact angle of 35° meets the opposing requirement of self-filling by capillary flow and of halting it at a SV To evaluate the potential for storage of CCs made with CCInk, we assessed the long-term stability of CCInk by measuring the contact angle with water over time on 3D printed chips storted at room temperature over a period of 16 weeks, **Figure 4.2c**. We found the contact angle to be stable throughout, thus confirming the possibility of printing CCs, and use them at a later time.

The photoabsorber and ink exhibit high efficiency at a wavelength of 385 nm, which matches the UV spectrum of 385 nm DLP light engines (**Figure 4.S2a, Supporting Information)**. The ink's absorbance remains unaffected by variations in AA and MA concentrations (**Figure 4.S2b, Supporting Information).** The manufacture of embedded conduits and thin bottom and ceiling walls depends on controlling the cross-linking depth and adsorption of UV light. The cross-linking depth was determined by applying uncured CCInk to a glass slide and exposing it to various light intensities shined through the glass. Upon removal of uncured ink, the thickness of cured ink can be measured, **Figure 4.2d**. As expected, an increase in additive concentration leads to a reduced cross-linking depth. Furthermore, according to the penetration depth results, PEGDA-AA required a lower exposure time for solidification than PEGDA-AM due to more effective cross-linking between AA and PEGDA. The reduced cross-linking in formulations with higher concentrations of AA and MA could be attributed to the lower molarity of acrylate groups, as the absorbance of the ink remains unaffected by variations in AA and MA concentrations. Hence, CCInk was formulated with PEGDA-AA and is the one used in the subsequent sections.

While the resolution of an open channel mainly depends on the projected pixel size in X and Y, embedded channels must also consider light penetration across the cross-linked membrane closing the channel and inadvertent crosslinking of entrapped ink immediately above it in Z. The ability to 3D print small embedded channels is crucial for fabrication of functional CCs. In addition, we demonstrated the printing of stacked embedded microchannels with 25 μm roof membranes, using a formulation with 10% AA (**Figure 4.2e**). Our ability to 3D print small embedded circular and rectangular channels would enable the seamless fabrication of capillarics.

4.4.2 Embedded Stop Valve Optimization

In order to develop functional fully 3D-printed CCs, the functionality and reliability of trigger valves (TV) and SV that are critical to confine liquids to conduits and reservoirs in the circuits needs to be reconsidered[21]. Previous CCs were printed as open channels at the surface of the chip and were sealed with a hydrophobic cover forming the ceiling. In this scenario, the 3 hydrophilic side walls of the conduit ensured self-filling by capillary force, while the hydrophobic ceiling was needed for stoppage of the incoming liquid at SVs and TVs. In contrast, when the conduits are embedded within the CCInK, the channel ceiling in the closed channel is hydrophilic as well, thus jeopardizing the functionality of the valves, and of the entire circuit. Consequently, it was necessary to characterize and optimize SV designs before developing complex CCs. In the conventional SV/TV, the flow within conduits experiences abrupt geometrical changes at the capillary valve only on three sides (bottom, left, and right), and the leakage from the top is controlled by having a fairly hydrophobic top surface (sealing cover). Hence, the meniscus is pinned at the SV outlet edge. Thanks to embedded channels, in the face-centric TV/SV design, the flow could be pinned at valves by having a sudden change on all sides (including the top surface) by designing valves at the middle of the second (orthogonal) microchannel (main channel). In this fashion, the flow will stop at the SV/TV even if the ceiling is hydrophilic by controlling the

expansion angle from the top, which is not attainable in conventional designs. In this design, the vertical gap plays a significant role in the valve performance, so having a sufficient vertical gap is necessary to hold liquids in reservoirs robustly for a longer time[20]. Error! Reference source not f ound.**4.3a** compares the two TV designs 3D-printed with CCInk. In the case of conventional design, both valves (top and side SVs) burst from the top side immediately after loading, and the liquid started spilling to the main channel and the capillary domino valves (CDVs)[12]. However, the face-centric valves could hold the liquid for a long time without leakage. The possibility of 3D printing embedded capillaric valves allows for controlling the expansion angle (90° or even more) on each side of valves and creating stronger and more robust TVs/SVs.

3D printing enables the construction of vertical channels that are not possible or challenging to fabricate using conventional techniques, allowing to development of vertical SVs/TVs from top or bottom. **Figure 4.3b** further shows a vertical SV connecting the reservoir to the main channel from the top; in MCRs, the conduit connecting the reservoir to the main channel was called a functional connection owing to the multiplicity of functions it fulfils.[12] The vertical valve held liquid in the reservoir for 20 min without leakage and was insensitive to gravity effects. The functionality of the conventional and face-centric SVs was also verified by studying capillary filling within functional connections using the level-set method and COMSOL simulation. As shown in **Figure 4.3a,** the conventional valve failed to stop the flow right after capillary-filling, and the flow spread to the top surface of the expansion chamber, while embedded valve stopped the flow without leakage under the same boundary conditions.

To further characterize the performance of the face-centric SVs, a pressure pump was used to measure bursting pressure at SVs of different sizes. Embedded valves with conduits with different square cross-section areas (from 100 to 1000 μm) were designed and 3D-printed for the

burst pressure test, as shown in **Figure 4.3c**. Each SV was connected to a positive pressure line at the inlet and another line at the outlet to provide an adjustable pressure difference between the upstream and downstream of each SV. The pressure difference was gradually increased by applying a positive inlet pressure until the meniscus bursts on the sides of the SV. As shown in **Figure 4.3c**, the bursting pressure value decreased from ~1200 Pa for the smallest SV to ~350 Pa for the largest tested SV with a size of 1 mm. This suggests that face-centric SVs can withstand a higher pressure than conventional SVs (with a hydrophobic top surface) that were tested in our previous study[12]. Using finite element modelling, the bursting pressure at face-centric SVs with different cross-section areas was simulated and the highest pressure that could be rested by the SV calculated, finding a good concordance between experiments and theory.

As a proof-of-concept, a monolithic CC with embedded conduits, a two-layered CC with a MCR with nine capillary flow events, five on top and four on the bottom layers was manufactured (**Figure 4.3d, Video S1, Supporting Information).** The 5th reservoir in the top fluidic network is connected to the 6th reservoir in the bottom network through a CDV, while the main conduit also bridges the two layers. Upon drainage of the reservoirs in the top layer, the ones in the bottom layer were drained. Manufacturing embedded channels could help integrate more conduits within the working footprint of the 3D printer. Vertical connections could add to the pressure head due to gravity, and interfere with capillary valve functionality, however as the height was low, functional CCs could be readily made.

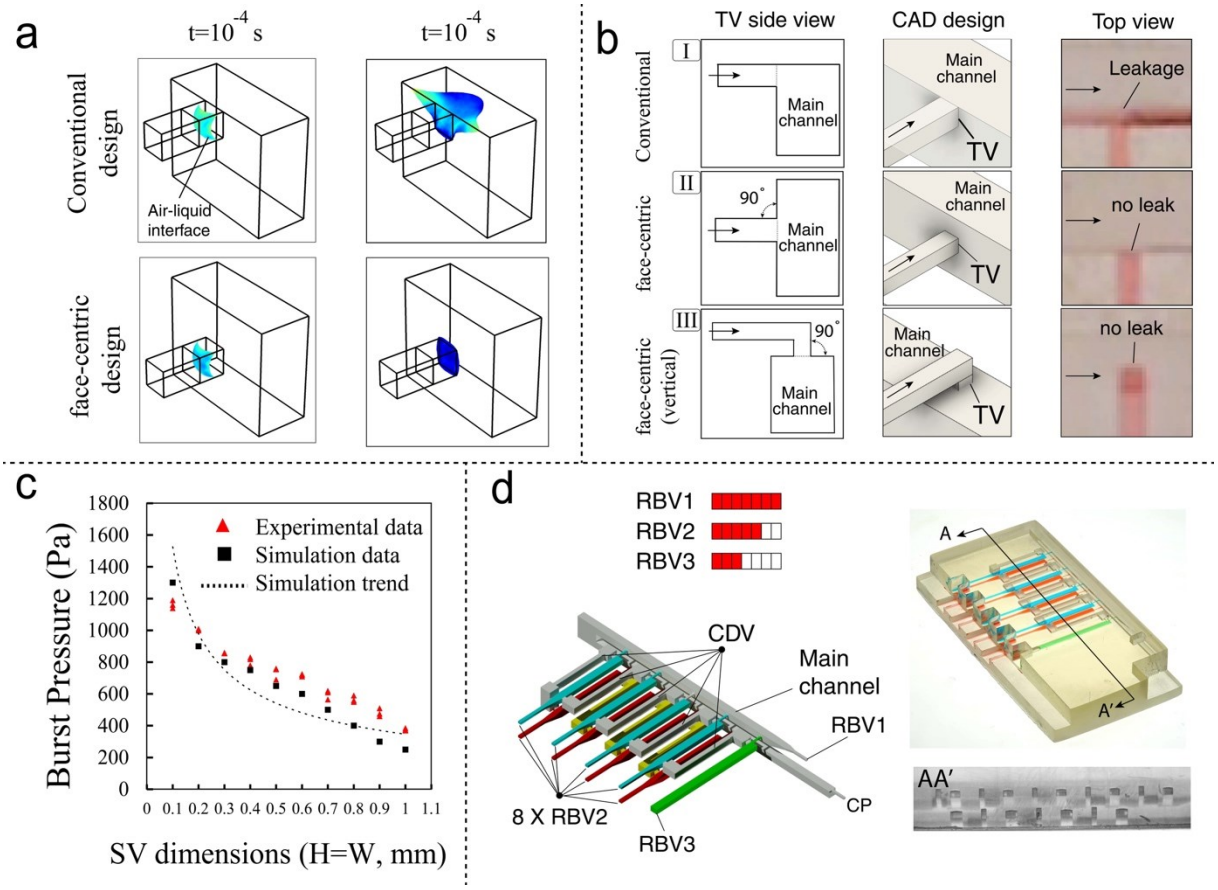

Figure 4.3. Redesigned and improved capillary stop valves. (a) FEM-based simulation of capillary flow reaching a conventional SV with continuous ceiling (0° angle and 3 surfaces with 90° angle relative to flow direction) and of a face-centric SV (four 90° angles). For a CCInk with a water contact angle ~ 35-40°, conventional SV/TV fail immediately while face-centric ones stop the liquid. **(b)** Experimental characterization of (I) conventional, and face-centric SV/TV intersecting the other conduit (II) laterally or (III) from the top; only face centric SV/TV could stop the liquid flow (arrows show the flow direction) **(c)** Comparison between simulation and experimental burst pressure for face-centric SV/TV with different square cross-section areas (from 100 to 1000 µm side) versus fitted values derived from a numerical model. **(d)** 3D printed two-layered CCs with face-centric elements for sequentially draining of 9 reservoirs using MCR (See Video S1, Supporting Information).

4.4.3 3D printing of CCs with embedded conduits with circular cross-sections.

Microfluidic conduits with square and rectangular cross-sections are commonly used as they are easy to manufacture using standard microfabrication methods and 3D printing. However, for liquids where the contact angle falls < 45°, edge flow in the corners arises. Hence liquid filaments

can reach an exit and clog it, thus trapping bubbles. This situation can arise in CCs when using low surface tension solutions, such as buffers including surfactants that are used in assays to prevent non-specific binding. When using a solution containing 0.1 % surfactant, with a water contact angle of 25° with photocured CCInk, we observed corner flow and bubble trapping, **Figure 4.4a.** Therefore, we explored the possibility of printing conduits with circular cross-sections using VP 3D printing while considering the limited resolution of the 3D printer. To improve circularity and minimize artifacts, we utilized anti-aliasing techniques and a low layer thickness of 20 μm. Following optimization, we were able to successfully 3D print circular channels with diameters as small as 160 μm (representing a slight trade-off in diameter compared to rectangular conduits, which were 108×100 μm², **Figure 4.4b**. A serpentine conduit with circular cross-section with varying diameter was also filled with a low surface tension solution, and successfully averted bubble trapping, **Figure 4.4c.** A functional CC with three reservoirs with circular cross-sections each connected to RBVs[21,22] with a different threshold was manufactured, **Figure 4.4d**. Each of the reservoirs was connected to the main conduit via a 200 μm diameter conduit, and upon filling and actuation, the three reservoirs were drained according to the pre-programmed sequence encoded by the RBV thresholds (**Videos S2-S3, Supporting Information**).

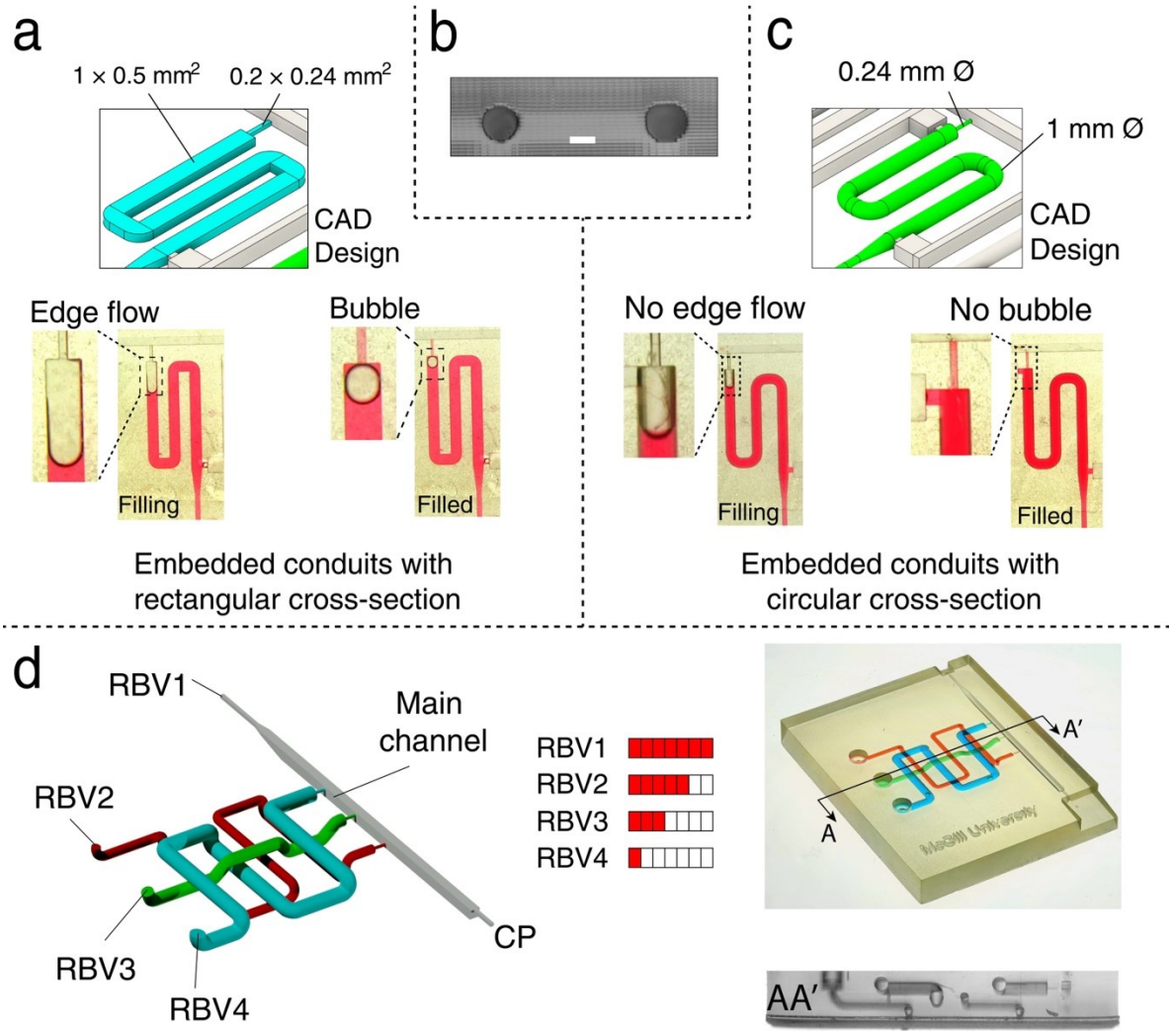

Figure 4.4. Monolithic 3D printed CCs with embedded conduits with circular cross-sections. **(a)** Flow of low surface tension liquid (0.1% Tween 20 in Mili-Q water) in a conduit with a rectangular cross-section is accompanied by edge flow and air bubble trapping. **(b)** cross-section of embedded circular conduits – scale bar is 100 µm. **(c)** Same liquid in a circular conduit without edge flow and without bubble trapping. **(d)** 3D printed CC with circular cross-sections and face-centric SVs/TVs filled with dyed solutions in 3 reservoirs with 4 RBVs with different bursting thresholds for sequential delivery (See Videos S2-S3, Supporting Information).

4.4.4 Immunoassay with a 3D-Printed CC with embedded conduits

To demonstrate the power and compatibility of our 3D printing technique, a proof-of-concept ELISA assay was developed to detect SARS-CoV-2 antibodies. ELISAs require a sequence of steps to amplify the readout signal enzymatically. The designed ELISA protocol for

the colorimetric detection of COVID-19 antibodies consists of three steps. First, the biotinylated antibody (sample) flows over the test zone where we already deposited the Nucleocapsid protein. Second, poly-HRP streptavidin flows over the test zone. Finally, the substrate flows over the test zone to chemically react with poly-HRP and generate a brown precipice visible to the naked eye **(Figure 4.5a**). We performed the ELISA assay manually (off-chip) to optimize the volume and concentration of reagents.

After optimizing capillaric elements and the assay, we designed and 3D-printed a monolithic CC microfluidic device to translate the manual ELISA assay into an autonomous multistep assay, in which sample and reagents are controlled and released sequentially to follow the assay protocol. This design includes three 3D reservoirs, one on the top layer and two on the bottom layer, to deliver the sample and reagents sequentially to the end of the main channel. The device is pre-programmed by designing 3D RBVs upstream of each reservoir, and all three are connected to the main channel through embedded functional connections (3D trigger valves) at their downstream to release the assay components sequentially. CCInk and 3D printing enable the manufacturing of compact devices by designing freeform capillaric elements and channels in three dimensions. Taking advantage of this characteristic, two layers of channels were designed and fabricated in this particular design, as shown in **Figure 4.5a**. A lateral flow module is connected to the end of the main channel. The module comprises a nitrocellulose membrane (test zone) sandwiched between two capillary pumps to ensure the flow throughout the assay. Before running the chip, the functionality of capillaric valves and sequential delivery were verified using dyed solutions, as shown in **Figure 4.5b**. All three reservoirs are first filled, and solutions are stopped into the functional connections. Then the assay starts by adding buffer into the main channel. The flow in each reservoir resumes when the functional connections are triggered by the trigger buffer

in the main channel. Upon contact with the trigger buffer, solutions in reservoirs are released into the main channel and wicked sequentially through the main channel. Error! Reference source not f ound.**b** shows the sequential steps when the main channel is filled and connected to a paper pump (**Video S4, Supporting Information**). The blue solution (sample) in the top layer is released first, followed by releasing green and red solutions representing poly-HRP streptavidin and substrate, respectively, in the bottom layer. The CAD design of the fluidic network shows how channels were connected in 3D. Using a series of chips and samples at six different concentrations (0 to 10000 ng/ml) with three replicates of COVID-19 antibody in buffer, we established a binding curve. The assay results appeared as a line, which was scanned to quantify the signal, **Figure 4.5c**.

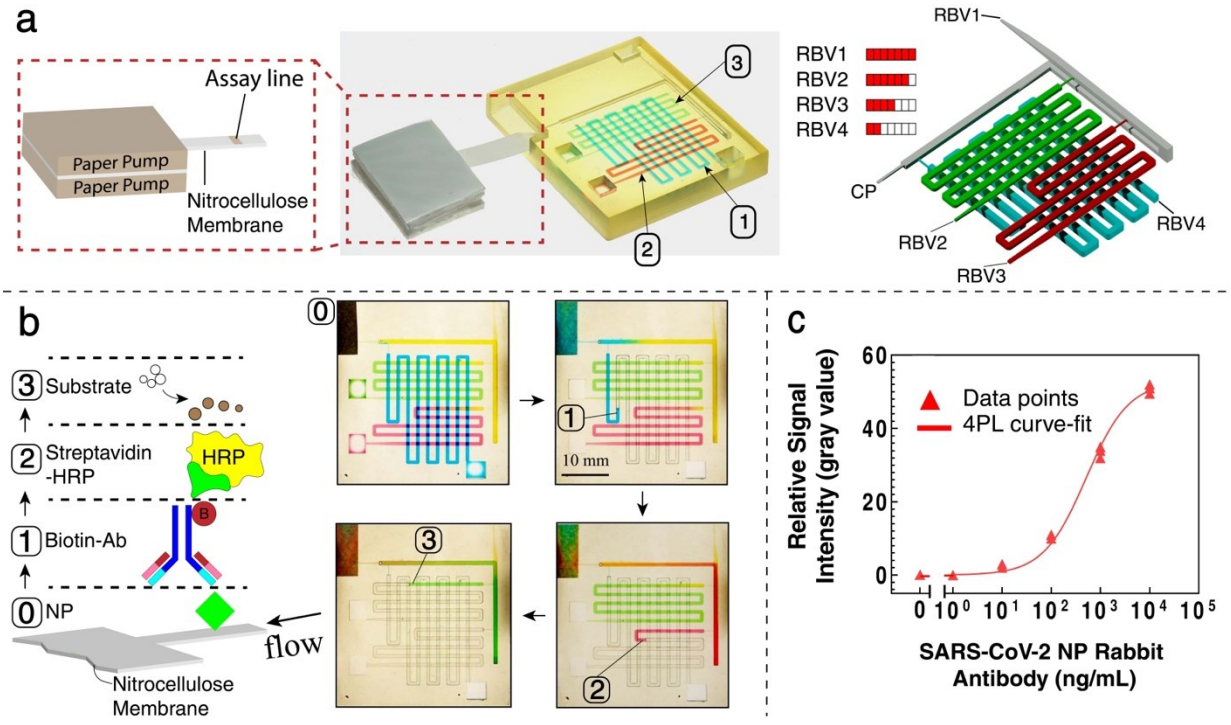

Figure 4.5. An autonomous assay using a 3D-printed monolithic CC. (**a**) A 3D-printed chip to deliver samples and reagents sequentially to the test zone where nucleocapsid protein (NP) is already spotted on the nitrocellulose membrane (NM) to complete the assay workflow. The assay includes three steps; biotinylated rabbit-anti NP (150 µl), Streptavidin-HRP (40 µl), and substrate (DAB, 50 µl) to produce colorimetric signals. (**b**) Sequential and pre-programmed release of colored solutions triggered by

connecting the paper pump (Video S4, Supporting Information). (**c)** Assay results and the binding curve obtained by imaging the test zone with a scanner (fitted with a 4-paramater regression, 3 replicates for each point).

4.4.5 Full Additive Manufacturing of CC with Gyroid Capillaric Pump (GCP)

Using 3D Printing and CCInK, we manufactured fully functional circuits without the need for a paper pump. We adopted a gyroid[25–27] based on triply periodic minimal surfaces (TPMS) as the capillary pump (GCP) (**Figure 4.6a**). The comparative high-resolution of the DLP printers enabled us to make embedded small features and form a capillary pump embedded integrated into the CC. The capillary pump is an essential functional unit of CCs that needs to meet opposing requirements, namely providing a sufficiently high capillary pressure to suck the liquid into the pump, and provide a sufficiently large reservoir for liquids (serving also as the waste), while also not significantly adding to the flow resistance of the circuits. These requirements were thus often met by paper pumps, but which need to be clamped onto the CC. 2D capillary pumps have been made previously, notably by microfabrication, but the volumetric capacity was limited by the 2D geometry. 3D capillary pumps have not been widely explored, in part because the small feature size needed for high capillary pressure and the high open ration were difficult to achieve.

A Gyroid is an infinitely connected TPMS with high and regular porosity, high surface-to-volume ratio, and low flow resistance, which are advantageous for a capillary pump positioned at the outlet of a CC and designed to provide a negative pressure irrespective of the pumped volume. Gyroid units of varying sizes, ranging from 700 μm to 2800 μm can be designed using mathematical models to control the porosity and hydraulic diameter to encode the desired capillary pressure (**Figure 4.6a**). The hydraulic diameter (D_h) for a gyroid structure can be determined using the equation $D_h = 4V/P$, where V represents the unit cell volume, and P is the wetted perimeter of the fluid path. This equation provides a measure of the effective cross-sectional area for fluid flow

through a channel or pore in the structure, and P and V can be obtained through mathematical models. Gyroid structures provide a large volume for draining liquids due to their high porosity. Using our hydrophilic ink, we 3D printed 5×5 mm^2 columns of microstructures with different gyroid sizes and densities to evaluate the capillary rise. As shown in **Figure 4.6b**, the capillary rise increased by increasing the gyroid density and reducing the hydraulic diameter (**Video S5, Supporting Information**). The correlation between the capillary rise and hydraulic diameters of gyroid columns is consistent with Jurin's law, which states that the height of a liquid column is inversely proportional to the tube diameter (**Figure 4.6c**). To show the potential of gyroids as a capillary pump to develop fully functional circuits, we designed, and 3D printed a capillary device consisting of MCR and GCP and successfully achieved sequential delivery of three reagents (**Figure 4.6d, Videos S6-S7, Supporting Information**). The size of the GCP was 15.5 × 14 × 2.3 mm^3, with a porosity of 62 %, and a volumetric capacity of 310 μL. Whereas the capillary pressure of GCP remains comparatively weak relative to paper, which has much smaller pore size, our results show that the GCP, coupled with a capillary circuit, could be used to run the sequential delivery of 3 reagents. Future improvements in resolution will allow making GCPs with higher capillary pressure, while modulation of pore size could be used to tune pressure continuously.

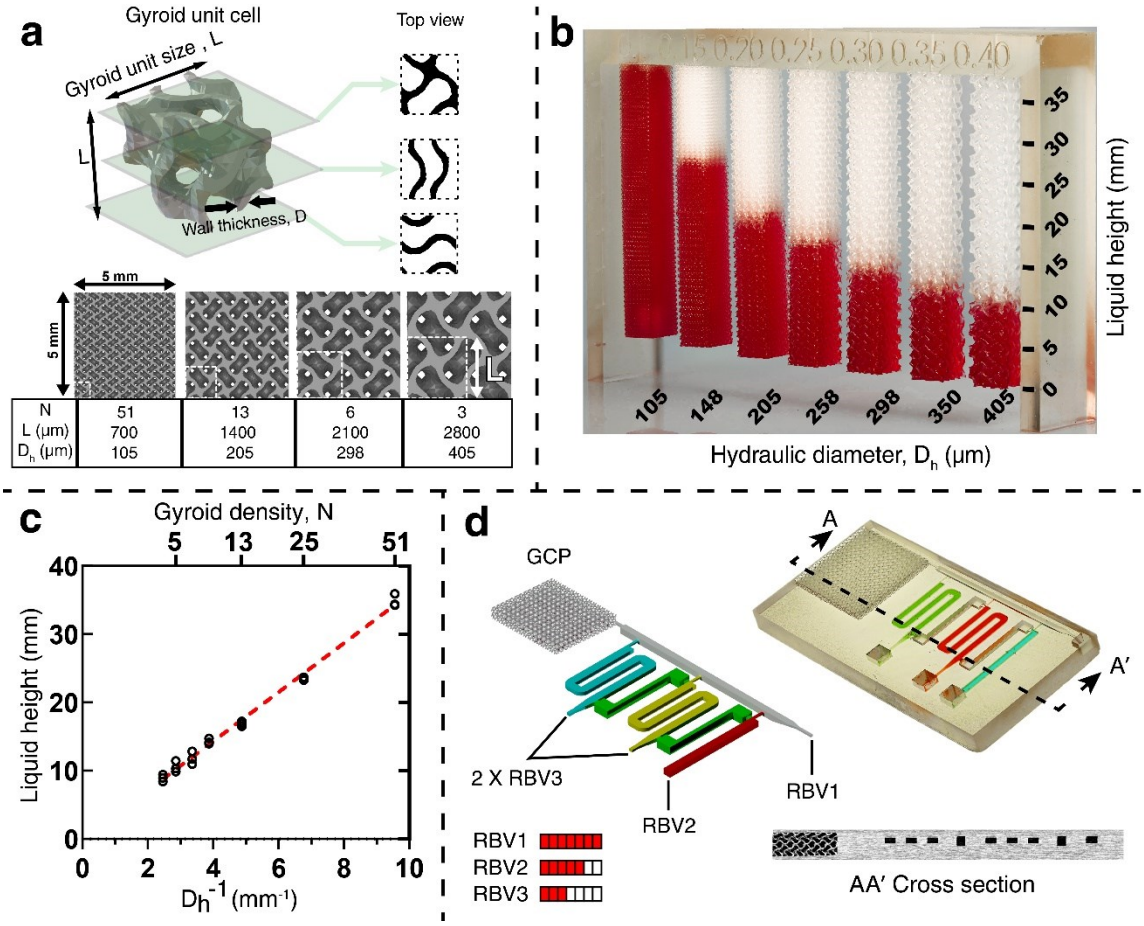

Figure 4.6. Gyroid capillary pump (GCP). (**a)** 3D image of a Gyroid unit cell and top view cross-sections at different planes. Columns of microstructures containing gyroid can be designed to achieve different capillary rise and density. (**b)** Capillary pressure and capillary rise increase with smaller gyroid and smaller hydraulic diameter. See supplementary Video S5 **(c)** Graph of the inverse of hydraulic diameter of the GCP versus the height of capillary rise reveals a linear relationship. **(d)** 3D-printed of functional, ready-to-use CC including GCP and MCR for sequential delivery of solutions in reservoir shown in operation (Video S6, Supporting Information).

4.5 Conclusions and future works

We have introduced DM of functional microfluidic systems as monolithic CCs with embedded conduits thanks to the hydrophilic CCInk made of PEGDA-250 with AA, and that can be 3D printed using common DLP 3D printers. We improved CC reliability and functionality thanks to a new SV/TV design, conduits with circular cross-sections, and embedded GCPs. The functionality of these CCs was demonstrated with a series of multilayer CCs with sequential

delivery by RBV and MCRs, and an immunoassay. Functional CCs can be created by anyone with a DLP printer with a projected pixel size ≲ 50 μm, thus enabling distributed DM thanks to the wide availability and low cost of 3D printers, and the ready-to-use quality of CCs. We foresee that the comparative ease-of-use and low maintenance of DLP printers will facilitate DM of microfluidic as it circumvents the need of advanced skills in neither manufacturing nor microfluidics, given that designs could simply be downloaded from an online repository (e.g. www.printables.com/@JunckerLab_743461), while making it affordable with material costs < 1 US$ per chip (depending on volume) thanks to the low cost of CCInk. We hope that the advances reported here will spur DM of microfluidics and lead to a broader adoption and exploration of microfluidics and CCs in particular, and help catalyse new ideas and applications in synthesis, analysis, assays, and diagnostics and that they will be shared as '3D apps' that can be downloaded from online repositories.

4.6 Material and Methods

CCInk ink Formulation and Preparation

The photocurable inks in this study were made of the monomer poly (ethylene glycol) diacrylate (PEGDA, MW258, no. 475629; Sigma Aldrich), the crosslinkers acrylic acid AA, no. 147230; Sigma Aldrich) and methacrylic acid (MA, no. 155721; Sigma Aldrich), the photoinitiator diphenyl(2,4,6-trimethylbenzoyl) phosphine oxide (TPO, no. 415952; Sigma Aldrich) (0.5 w/w) and the photoabsorber 2-isopropylthioxanthone (ITX, no. TCI0678; VWR International) (0.8 w/w). AA and MA concentration were varied towards identifying the optimal concentrations. The CCInks was prepared by mixing the above-mentioned components using the optimal concentration for 30 min. All inks were stored in amber glass bottles after preparation.

3D printing Microfluidic Devices

All capillaric devices were designed in AutoCAD (Autodesk), exported as "STL" files, and 3D-printed with two different DLP-based 3D printers with 385 nm LED light source, the Asiga MAX X27 (GV Canada Inc., Canada), and Miicraft Prime 110 (Creative CADworks, Concord, Canada) with a projected pixel size of 27 µm and 40 µm, respectively. Unless otherwise noted, all CCs reported in this work are printed with a layer thickness of 20 µm and an exposure time of 950 ms at a light intensity of 5 mW/cm^2. Immediately after printing, to remove unpolymerized ink and clean channels, closed channels were rinsed with isopropanol (Fisher Scientific, Saint-Laurent, Quebec, Canada), and dried under a stream of pressurized nitrogen gas.

Contact angle measurements

2-3 µl of DI water was placed on the top surface of 3D-printed samples and imaged using a Panasonic Lumix DMC-GH3K. The side view images were imported to ImageJ ver. 1.53 (public domain software, NIH, Bethesda, MD, USA) to measure the static contact angle using the contact angle plugin. All measurements were performed on freshly UV-cured samples after cleaning and drying 3D-printed samples. To measure contact angle on plasma-treated surfaces, the above measurements were performed immediately after treating samples for 15 s at 100% power in a plasma chamber (E50 plasma chamber, Plasma Etch, Carson City, USA).

Penetration depth and absorbance measurements

To modulate the surface hydrophilicity properties by adjusting the contact angle, the ink formulation was mixed with different amounts of AA and MA ranging from 5% (w/w) up to 15% (w/w). In order to measure the effect of crosslinker on the penetration depth of light, a drop of the formulation was placed on a glass slide and exposed to different exposure times at a light intensity of 5 mW/cm^2. After rinsing uncured ink with 70% ethanol, we measured the thickness of patterned regions using a stylus profilometer (DektakXT, Bruker Co.). Absorbance measurements of the ink

were performed by triplicate using a NanoDrop@ND-1000 (NanoDrop Technologies, Wilmington, DE, USA.

FTIR, NMR, and XPS

FT-IR and HR-NMR were used to characterize the polymerization reactions by monitoring the transition of functional groups such as carboxyl. The HR-XPS has confirmed the presence of the COOH group in the ink with AA.

Toluidine blue assay to quantify functional groups

Toluidine blue assay (TBO)[28] was used to quantify the density of carboxyl groups of PEGDA co-polymerized with different acrylic and methacrylic acid concentrations. Square-shaped samples ($10\times10\times2$ mm^3) were 3D printed and washed with IPA before using for the assay. PEGDA samples without hydrophilic co-monomers were fabricated under the same conditions and used as controls. To carry out the TBO assay, three samples of each concentration were incubated in 2 mL of a solution containing 1 mM toluidine blue (no. 89640; Sigma Aldrich) in PBS at pH 10 at room temperature on an orbital shaker set at 150 rpm (no. 57018-754VWR; VWR International, Brisbane, CA). After 48 h, samples were rinsed frequently with PBS at pH 10 to remove unbounded dye for 1 day. The samples were then immersed in 2.5 mL of 50% vol. glacial acetic acid in Milli-Q water for 3 h. Finally, NanoDrop@ND-1000 spectrophotometer was used to measure the absorbance at 633 nm to quantify the density of TBO.

COMSOL Simulation

To measure the bursting pressure at SVs, COMOSL Multiphysics v.5.5 (COMSOL AB, Stockholm, Sweden) was used to simulate two-phase capillary flow within embedded channels using the level set method. A free tetrahedral mesh with “fine” size was applied for each simulation. Atmospheric pressure was set for the outlet, and the inlet static pressure was gradually varied (with

50 Pa increments) to determine the pressure of stop valve failure. The contact angle on the channel walls and the interface thickness were set 40° and 8×10^{-8} m, respectively. Each simulation was performed with a time period of 0-0.002 s with a time step of 2.5×10^{-5} s.

Testing capillaric devices

Printed chips were pre-loaded with dyed solutions (2% food dye in Milli-Q water) and connected to filter papers (Whatman CF4, Cytiva, Marlborough, Massachusetts, USA) serving as the paper capillary pump for conducting experiments, except when embedded 3D printed capillary pumps were used. A solution with low surface tension (2% food dye and 0.1%Tween 20 in Milli-Q water) was used to evaluate edge flow and bubble trapping in conduits with either rectangular or cir circular conduits, presented in **Figure 4.4**.

Covid-19 assay test on nitrocellulose membranes

Nitrocellulose lateral flow membranes (vivid™ 120, no. VIV1202503R; Pall Corporation, Port Washington, USA) were cut into 5.2×12 mm^2 rectangles using a Silhouette Portrait cutter (Silhouette, Lindon, USA). SARS-CoV-2 nucleocapsid protein was purchased from Sino Biological, Inc. (no.40588-V08B; Beijing, China) and deposited at the concentration of 1.25 mg/ml as previously described[12,19] on the membranes using a programmable inkjet spotter (sciFLEXARRAYER SX, Scienion, Berlin, Germany). Before running the assay, the strips were immersed in a blocking buffer (1% BSA and 0.05% Tween 20) for one hour on an orbital shaker (no. 57018-754VWR; VWR International, Brisbane, CA) set at 150 rpm and thereafter dried overnight at 4° Celsius. The sample solutions were prepared by spiking biotinylated SARS-CoV-2 N protein rabbit monoclonal antibody (no. 40143-R004-B; Sino Biological, Inc.; Beijing, China) in buffer solution (0.1% BSA and 0.05% Tween 20 in PBS) at the concentrations of 0, 1, 10, 100, 1000 and 10000 ng/ml. Streptavidin poly-HRP (Pierce, no. 21140; ThermoFisher; Ottawa, Canada)

solutions were prepared in the buffer solution with a concentration of 5 µg/mL. SIGMAFAST™ DAB tablets (no. D4293-50SET; Sigma Aldrich; Oakville, Canada) were dissolved in Milli-Q water to prepare substrate solution. The membrane strips were connected to a glass fiber conjugate pad (G041 SureWick, Millipore Sigma, Oakville, Ontario, Canada) on one end and were sandwiched between three absorbent pads (Electrophoresis and Blotting Paper, Grade 320, Ahlstrom-Munksjo Chromatography, Helsinki, Finland) serving as the capillary pump at the other end. Absorbent pads were clamped with a paper clip.

Image Analysis

Nitrocellulose strips were removed from the chip after the assay completion, dried at room temperature, and scanned at 600 DPI (Epson Perfection V600). The images were then imported in Image-J ver. 1.53 (public domain software, W. Rasband, National Institutes of Health, Maryland, USA) to measure the grey value at the test line and top and bottom backgrounds located 1.5 mm below and above the test line. The signal intensity for each strip was calculated by subtracting the average background (of top and bottom) from the grey value at the test line. After that, the average signal intensity of the negative controls (0 ng/ml) was subtracted from the signal intensity, plotted and fitted to generate the normalized standard curve.

Bursting pressure characterization

To evaluate the bursting pressure at face-centric SVs, modules with different cross-sectional areas were 3D printed. Each module consists of an embedded SV connected to an expansion chamber. A conical inlet/outlet was designed, and 3D printed for each SV for tubing connections and avoiding bubble formation. The modules were connected to a pressure pump (MFCS-4C) from both ends and Fluiwell package (Fluigent) with reservoirs containing 2% food dye in Milli-Q water. Once the SV was capillary-filled, MAESFLO v.3.3.1 software (Fluigent)

was used to control positive or negative pressure to calculate the burst pressures of the SV with increments of 10 Pa.

Videos and image stacking

Videos and images of 3D-printed chips were taken using a Panasonic Lumix DMC-GH3K and Sony α7R III. For focus stacking, Imaging Edge Desktop (Sony Imaging Products & Solutions Inc., Japan) was used to take the sequence of images on different focal planes. Then, CombineZP (available at https://combinezp.software.informer.com/) was used to process the images. Micro-computed tomography (Micro-CT) was performed using Skyscan 1172 (Bruker, Kontich, Belgium) at pixel size of 5 μm, and used to confirm the dimensions of embedded channels.

4.7 Supplementary Information

4.7.1 Supplementary Videos

Video S1. Multilayer Microfluidic Chain Reaction (MCR)

Video S2. CC with circular channels

Video S3. Micro-CT of CC with circular channels

Video S4. Autonomous assay using a 3D-printed monolithic CC

Video S5. Capillary rise in gyroid columns

Video S6. CC with GCP and MCR

Video S7. Micro-CT of CC with GCP and MCR

4.7.2 Supplementary Figures

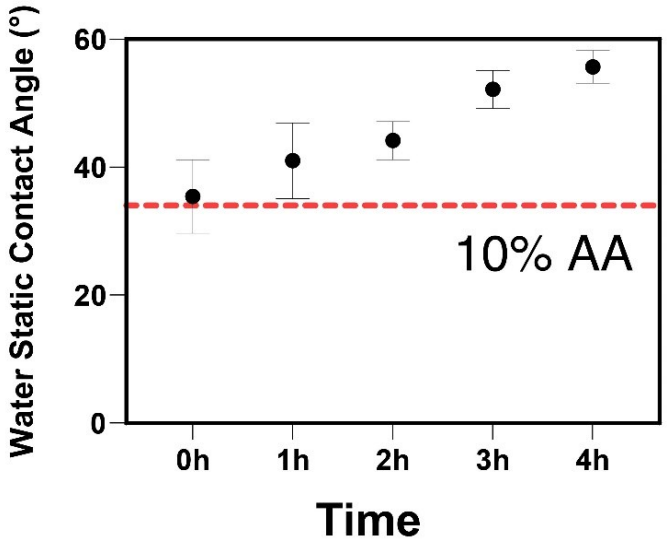

Figure 4.S4.7. Water static contact angle on plasma-treated 3D printed samples over time. The contact angle changes by approximately 20º over a period of 4 h.

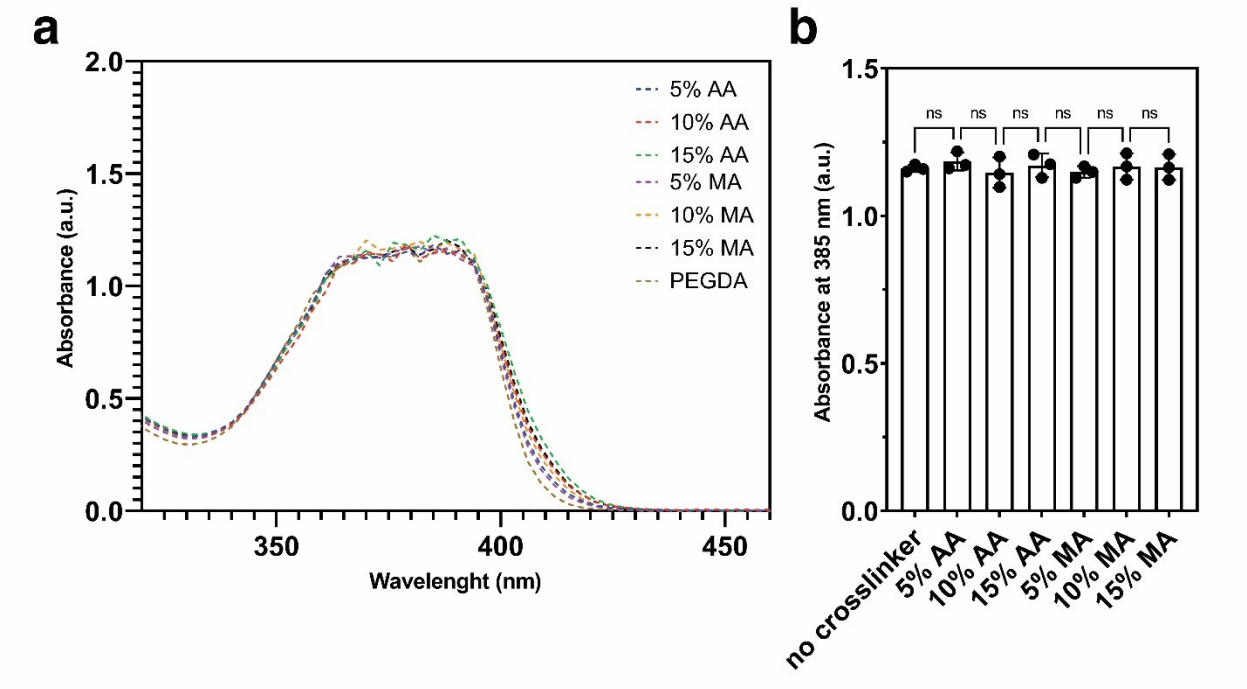

Figure 4.S4.8. Impact of additives on ink absorption at 385 nm illumination wavelength of DLP projector. (a) Absorption of CCInk at 385 nm for different CCInks with varying additive concentrations. **(b)** Absorption of CCInk at 385 nm. Crosslinker concentration does not affect the light absorption of the ink. This is due to low absorption of AA and MA compared to PI and PA.

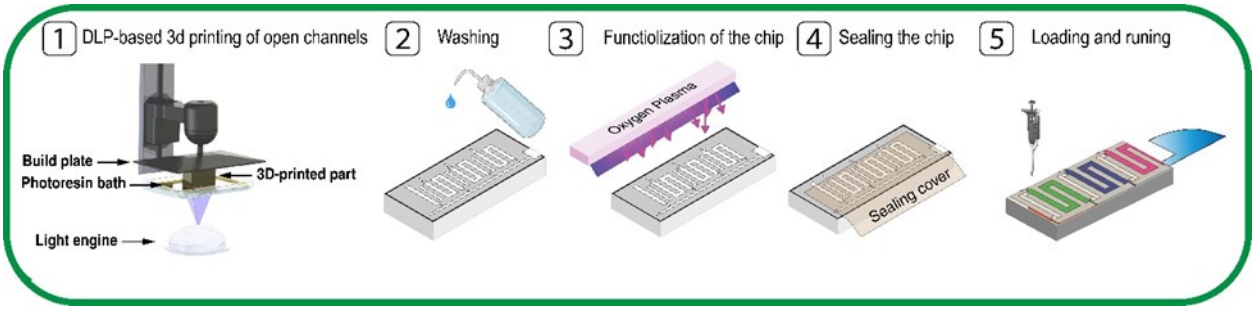

Figure 4.S4.9. Previous fabrication method for capillary microfluidic devices. 1) 3D printing of open channels. 2) Removal of uncured ink. 3) Plasma-treating of the chip. Hydrophilization of CCs using a plasma chamber results in transient hydrophilicity, lacks reproducibility, and limits the design of CCs to open surface channels that are sealed with tape. 4) Sealing the chip with a hydrophobic transparent tape. 5) Loading the chip.

Without crosslinker (98.7%PEGDA+0.5% TPO +0.8% ITX)

Name	Peak BE	FWHM eV	Area (P) CPS.eV	Atomic %
O-C=O (Carboxylic acid)	288.43	0.57	130.23	1.4
C-O-C	285.97	1.06	1902.9	20.45
C-C	284.36	1.4	7280.16	78.15

With crosslinker (93.7%PEGDA+ 0.5% TPO +0.8% ITX+**5%AA**)

Name	Peak BE	FWHM eV	Area (P) CPS.eV	Atomic %
O-C=O (Carboxylic acid)	**288.36**	**0.84**	**522.56**	**5.09**
C-O-C	285.96	1.22	2462.6	23.93
C-C	284.4	1.33	7311.81	70.98

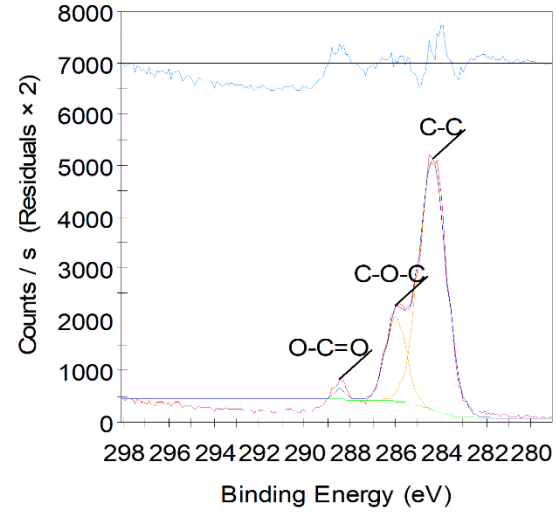

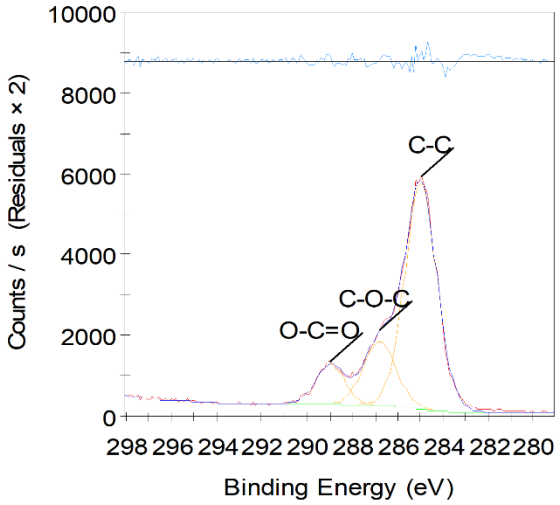

Figure 4.S4.10. X-ray photoelectron spectroscopy (XPS) measurement on the samples with and without AA. The results showed a presence of approximately 5.1% carboxylic acid (COOH) group in the samples with 5% AA, while samples without AA only exhibited approximately 1.4% COOH.

4.8 References

1. McDonald, J. C. *et al.* Fabrication of microfluidic systems in poly(dimethylsiloxane). *Electrophoresis* **21**, 27–40 (2000).

2. Naderi, A., Bhattacharjee, N. & Folch, A. Digital Manufacturing for Microfluidics. *Annu. Rev. Biomed. Eng.* **21**, 325–364 (2019).

3. Choi, S. *et al.* A recyclable CNC-milled microfluidic platform for colorimetric assays and label-free aged-related macular degeneration detection. *Sensors Actuators B Chem.* **290**, 484–492 (2019).

4. Wlodarczyk, K. L., Hand, D. P. & Maroto-Valer, M. M. Maskless, rapid manufacturing of glass microfluidic devices using a picosecond pulsed laser. *Sci. Rep.* **9**, 20215 (2019).

5. Salentijn, G. I. J., Oomen, P. E., Grajewski, M. & Verpoorte, E. Fused Deposition Modeling 3D Printing for (Bio)analytical Device Fabrication: Procedures, Materials, and Applications. *Anal. Chem.* **89**, 7053–7061 (2017).

6. Singh, M. R. & Black, K. Anomalous Dipole-Dipole Interaction in an Ensemble of Quantum Emitters and Metallic Nanoparticle Hybrids. *J. Phys. Chem. C* **122**, 26584–26591 (2018).

7. Melchels, F. P. W., Feijen, J. & Grijpma, D. W. A review on stereolithography and its applications in biomedical engineering. *Biomaterials* **31**, 6121–6130 (2010).

8. Zhao, W. *et al.* Vat Photopolymerization 3D Printing of Advanced Soft Sensors and Actuators: From Architecture to Function. *Adv. Mater. Technol.* **6**, 2001218 (2021).

9. Ravanbakhsh, H. *et al.* Emerging Technologies in Multi-Material Bioprinting. *Adv. Mater.* **33**, 2104730 (2021).

10. Chen, C. *et al.* 3D-printed microfluidic devices: fabrication, advantages and limitations—a mini review. *Anal. Methods* **8**, 6005–6012 (2016).

11. Zhang, Y. *et al.* From passive to active sorting in microfluidics: A review. *Rev. Adv. Mater. Sci.* **60**, 313–324 (2021).

12. Yafia, M. *et al.* Microfluidic chain reaction of structurally programmed capillary flow events. *Nature* **605**, 464–469 (2022).

13. Parra-Cabrera, C. *et al.* Powder-Based 3D Printing of Autonomous Concentration Gradient Generators. *Adv. Eng. Mater.* **25**, 2200824 (2023).

14. Achille, C. *et al.* 3D Printing of Monolithic Capillarity-Driven Microfluidic Devices for Diagnostics. *Adv. Mater.* **33**, 2008712 (2021).

15. Bhattacharjee, N., Parra-Cabrera, C., Kim, Y. T., Kuo, A. P. & Folch, A. Desktop-Stereolithography 3D-Printing of a Poly(dimethylsiloxane)-Based Material with Sylgard-184 Properties. *Adv. Mater.* **30**, (2018).

16. Sanchez Noriega, J. L. *et al.* Spatially and optically tailored 3D printing for highly miniaturized and integrated microfluidics. *Nat. Commun. 2021 121* **12**, 1–13 (2021).

17. Rekowska, N. *et al.* Thermal, Mechanical and Biocompatibility Analyses of Photochemically Polymerized PEGDA250 for Photopolymerization-Based Manufacturing Processes. *Pharmaceutics* **14**, 628 (2022).

18. Warr, C. *et al.* Biocompatible PEGDA Resin for 3D Printing. (2020) doi:10.1021/acsabm.0c00055.

19. Parandakh, A. *et al.* 3D-printed capillaric ELISA-on-a-chip with aliquoting. *Lab Chip* (2023).

20. Olanrewaju, A. O., Robillard, A., Dagher, M. & Juncker, D. Autonomous microfluidic capillaric circuits replicated from 3D-printed molds. *Lab Chip* **16**, 3804–3814 (2016).

21. Olanrewaju, A., Beaugrand, M., Yafia, M. & Juncker, D. Capillary microfluidics in microchannels: from microfluidic networks to capillaric circuits. *Lab Chip* **18**, 2323–2347 (2018).

22. Safavieh, R. & Juncker, D. Capillarics: pre-programmed, self-powered microfluidic circuits built from capillary elements. *Lab Chip* **13**, 4180 (2013).

23. Chiadò, A. *et al.* A modular 3D printed lab-on-a-chip for early cancer detection. *Lab Chip* **20**, 665–674 (2020).

24. Männel, M. J., Weigel, N., Hauck, N., Heida, T. & Thiele, J. Combining Hydrophilic and Hydrophobic Materials in 3D Printing for Fabricating Microfluidic Devices with Spatial Wettability. *Adv. Mater. Technol.* **6**, 2100094 (2021).

25. Silva, C. *et al.* Study on 3D printing of gyroid-based structures for superior structural behaviour. *Prog. Addit. Manuf.* **6**, 689–703 (2021).

26. Dixit, T., Al-Hajri, E., Paul, M. C., Nithiarasu, P. & Kumar, S. High performance, microarchitected, compact heat exchanger enabled by 3D printing. *Appl. Therm. Eng.* **210**, 118339 (2022).

27. Baena-Moreno, F. M. *et al.* Stepping toward Efficient Microreactors for CO2Methanation: 3D-Printed Gyroid Geometry. *ACS Sustain. Chem. Eng.* **9**, 8198–8206 (2021).

28. Tiraferri, A. & Elimelech, M. Direct quantification of negatively charged functional groups on membrane surfaces. *J. Memb. Sci.* **389**, 499–508 (2012).

Chapter 5

5. Chapter 5: Nanoporous PEGDA ink for High-Resolution Additive Manufacturing of Scaffolds for Organ-on-a-Chip

5.1 Preface

In the previous chapter, we introduced the hydrophilic ink for 3D printing of functional capillary microfluidic devices. Although the formulations demonstrated their efficacy for high-resolution 3D printing, they are still not suitable for 3D cell culture and organ-on-a-chip applications that require porosity and adequate cell attachment. In this manuscript, we try to address this limitation by developing a porous ink based on PEGDA. We evaluate the material's cytotoxicity on various cell lines and characterizes its effect on cell attachment. In comparison to nonporous wells, cell coverage for Human umbilical vein endothelial cells (HUVEC) increased fourfold in porous wells, with even higher coverage observed for Human foetal lung (IMR-90), indicating enhanced cell attachment. These cell lines were chosen due to their wide range of applications, as well as their sensitivity to toxicity. We also demonstrate the practical application of this material by utilizing it to develop an OoC.

This chapter is a manuscript of a research article intended for submission: “Nanoporous PEGDA ink for High-Resolution Additive Manufacturing of Scaffolds for Organ-on-a-Chip”, **V. Karamzadeh**, M. Shen, F. Lussier, and D. Juncker.

5.2 Abstract

Organ-on-a-chip (OoC) systems, prominent in drug discovery and personalized medicine, are typically made of polydimethylsiloxane (PDMS). However, PDMS faces challenges in replicating complex geometries, as it is made by replica molding and can only replicate surface structures, limiting its potential for physiologically relevant 3D OoC models. In contrast, 3D printing allows for easier production of complex structures. Poly(ethylene glycol) diacrylate (PEGDA-250) has been adopted for light-engine based 3D printing and microfluidic device manufacturing due to its ease of fabrication, resistance to small molecule absorption, and indications of biocompatibility. Here, we introduce a constitutively nanoporous PEGDA ink formed by including a porogen that is removed following photopolymerization. Using this ink, complex microstructures and membranes as thin as 27 μm were 3D-printed. With increasing porogen concentration in the ink, 3D-printed constructs with increasing porosity and diffusion rates could be made all while preserving printing resolution. We conducted systematic cytotoxicity studies following ISO standards for four different cell lines (IMR-90, MDA-MB-231, 293T, and HUVEC), providing a more comprehensive assessment of biocompatibility than previous studies. Viability greater than 80% was achieved, and nanoporous substrates showed fourfold coverage by endothelial cells compared to nonporous ones. Finally, we introduce a tumor-on-a-chip model comprising a 3D printed microporous gyroid scaffold for growing stromal cells in 3D around a central opening filled with hydrogel and a cancer cell spheroid. Following co-culture over 14 days, cell proliferation and endothelial sprouting within the spheroid were observed. The nanoporous PEGDA ink is a promising biomaterial for high-resolution 3D printing for making new constructs for cell culture and OoC models thanks to its printability, biocompatibility, cell adhesion, and porosity.

5.3 Introduction

Organ-on-a-chip (OoC) systems have emerged as a promising alternative *in-vitro* tool in various fields, including drug discovery, physiological monitoring, and personalized medicine [1–3]. These systems utilize microfluidics and tissue engineering to replicate the structure and function of human organs[4]. Leveraging 3D cell culture and microfluidics, OoC platforms have become an alternative to both *in-vitro* 2D culture—due to their increased biological relevance—and *in-vivo* animal testing, owing to their more controllable and reproducible nature. OoCs comprise microfluidic channels designed for 3D cell culture, with polydimethylsiloxane (PDMS) being most commonly used to house OoC[4,5]. However, PDMS has limitations, including the potential to absorb small hydrophobic molecules, which can result in inaccurate assessments of drug toxicity and efficacy[6]. Additionally, it can be challenging to fabricate complex structures with PDMS because it is made by replica molding and can only replicate surface structures, while for example 3D printing allows for easier production of complex 3D structures[7]. Thus, researchers are exploring alternative natural and synthetic materials to enhance OoC capabilities.

The cost-effectiveness and versatility of 3D printing have made it an attractive approach for fabricating OoC platforms[8–11]. Compared to classical microfabrication methods, the cost per device does not increase with increasing complexity or batch size, making it easier to customize the design. Moreover, the technical knowledge required to operate 3D printers can be acquired quickly and easily than most other manufacturing methods due to the largely automated nature of the process[12]. However, the 3D printing methods faces a trade-off between build volume and voxel resolution and print time, and cannot produce large polymer structures with geometrical features at the sub-micrometer scale, such as the ones present micro- and nanoporous materials.

Recent studies have addressed this challenge by using different approaches such as salt porogen leaching[13,14], aqueous two-phase emulsion[15], and polymerization-induced phase separation[16,17]. The salt porogen leaching method is limited to creating micropore sizes due to the salt particle size, while two-phase emulsion requires careful optimization to ensure the immiscible phases remain uniform throughout the printing process. Polymerization-induced phase separation, on the other hand, is better suited for DLP 3D printing, as it utilizes a stable miscible porogen in the ink and can create complex nanoporous structures with tunable porosity and interconnected nanopore. While these approaches have been used for different applications, it has not been applied for microfluidics, where nanoporosity with high printability and resolution is desirable. Moreover, most of these techniques necessitate post-processing with expensive instruments, such as supercritical drying[16,17]. For example, Dong et al. demonstrated a method that combines vat-photopolymerization (VP) 3D printing of 2-Hydroxyethyl methacrylate (HEMA) monomer and polymerization-induced phase separation to create 3D objects with nanoporosity by removing cyclohexanol and 1-decanol porogens[17]. The 3D-printed nanoporous structures showed improved cell attachment compared to non-porous ones. However, this method has limitations when it comes to OoC applications. For instance, the high concentration of photoinitiator (PI) (4%) in the HEMA-based formulations can be harmful to more sensitive cells, and HEMA-based formulations may not be stable in water. In contrast to HEMA-based formulations, polyethylene glycol diacrylate (PEGDA) with a molecular weight lower than 300 offers several advantages, such as improved biocompatibility, stability in water, and printability due to improved reaction kinetic[18,19]. These properties make PEGDA more suitable for OoC applications.

Poly(ethylene glycol) (PEG) is a biocompatible and hydrophilic biomaterial that finds wide use in tissue engineering and pharmaceutical applications[17]. By incorporating acrylate or

methacrylate functional groups, PEG becomes photocurable, and suitable for VP 3D printing. PEGDA, with a low molecular weight, has gained significant attention as an alternative material to PDMS for manufacturing microfluidic devices where its properties depend on its molecular weight (MW). For instance, PEGDA with a MW of 500~6000 Da is used as hydrogel due to its high-water content and porosity, while low-MW PEGDA crosslinks into rigid plastics. The Miller group has demonstrated the use of PEGDA with an MW of 6000 Da and 3400 Da, and food dye as a photoabsorber (PA) in VP 3D printing, to fabricate intricate structures, such as an acellular vascularized alveolar unit capable of ventilation[20,21]. Low-MW PEGDA is transparent, biocompatible, impermeable to water, and can be modified to introduce functionalities that make it more suitable for biological applications. Compared to PDMS, PEGDA-250 is easier and less expensive to manufacture and exhibits innate resistance to absorption of small molecules, making it more desirable for drug testing applications[22]. However, low-MW PEGDA has limitations including low permeability and low cell attachment compared to PDMS[18]. Nonetheless, low-MW PEGDA has shown great potential for high-resolution 3D printing, particularly for microfluidic devices.

To enable high-resolution 3D printing of biomicrofluidic devices, several groups have developed formulations based on PEGDA-250 as the monomer and phenylbis(2,4,6-trimethylbenzoyl) phosphineoxide (BAPO) as the photoinitiator (PI)[19,23–26]. The Folch group has demonstrated the ability to 3D-print microchannels with a cross-section of 27 µm wide and 1-mm-tall using low-MW PEGDA with Isopropylthioxanthone (ITX) PA. Conversely, Nordin's group has printed microchannels with a smaller cross-section of 18 × 20 μm^2 using 2-nitrophenyl phenyl sulfide (NPS) PA[23,26]. However, current formulations require 24 h washing and plasma treatment to achieve biocompatibility and cell attachment[18,23]. Furthermore, although it is crucial to evaluate

cytotoxicity using ISO standards, only one study performed cytotoxicity assessment using these standards for the EA.hy926 cell line[18]. Therefore, there is an unmet need for a biocompatible PEGDA ink with inherent nanoporosity suitable for nutrient exchange, high biocompatibility, and suitable cell attachment.

Here, we present a novel biocompatible PEGDA bioink with inherent nanoporosity (hereafter referred to as P-PEGDA) achieved through the use of a non-reactive PEG porogen. Furthermore, we conducted a thorough evaluation of the material's cytotoxicity on various cell lines and characterized the effect of the porogen on cell attachment. We then utilized the P-PEGDA ink to develop an innovative OoC platform featuring three levels of microchannels and a gyroid scaffold, which enabled long-term co-culture up to 14 days, 3D cell migration, proliferation, and endothelial sprouting within the spheroid. Our findings indicate that the developed porous PEGDA ink is a promising biomaterial for high-resolution VP 3D printing of OoC devices.

5.4 Results

5.4.1 Characterization and Design Criteria for P-PEGDA ink

Current inks for VP 3D printing mainly rely on a monomer and a PI, which results in nonporous structures. In this study, we present a novel ink formulation that includes a hydrophilic PEGDA monomer and a porogen solvent, offering a solution to this limitation. By simply washing the 3D printed object with water, the porogen can be easily removed, leaving behind nanoporous structures **(Figure 5.1a)**. Our approach is faster, more cost-effective, and simpler compared to previously reported methods that depend on supercritical drying to remove the porogen in a controlled way[16]. This approach enables the printing of high-resolution microstructures with nanoporosity, making it suitable for use in OoC devices.

The PEGDA-based ink suitable for OoC application had to meet the following criteria: (a) 3D printable with high resolution, (b) having high transparency suitable for high-resolution fluorescence microscopy, (c) being biocompatible and suitable for long-term cell culture, and (d) having sufficient cell attachment. Based on these criteria, we developed an ink consisting of PEGDA-250 as the hydrophilic monomer, PEG-200 as the porogen, TPO as the PI, and ITX as the PA **(Figure 5.1b)**. These criteria are essential to ensure that the formulation could be used effectively for fabrication of complex OoC devices.

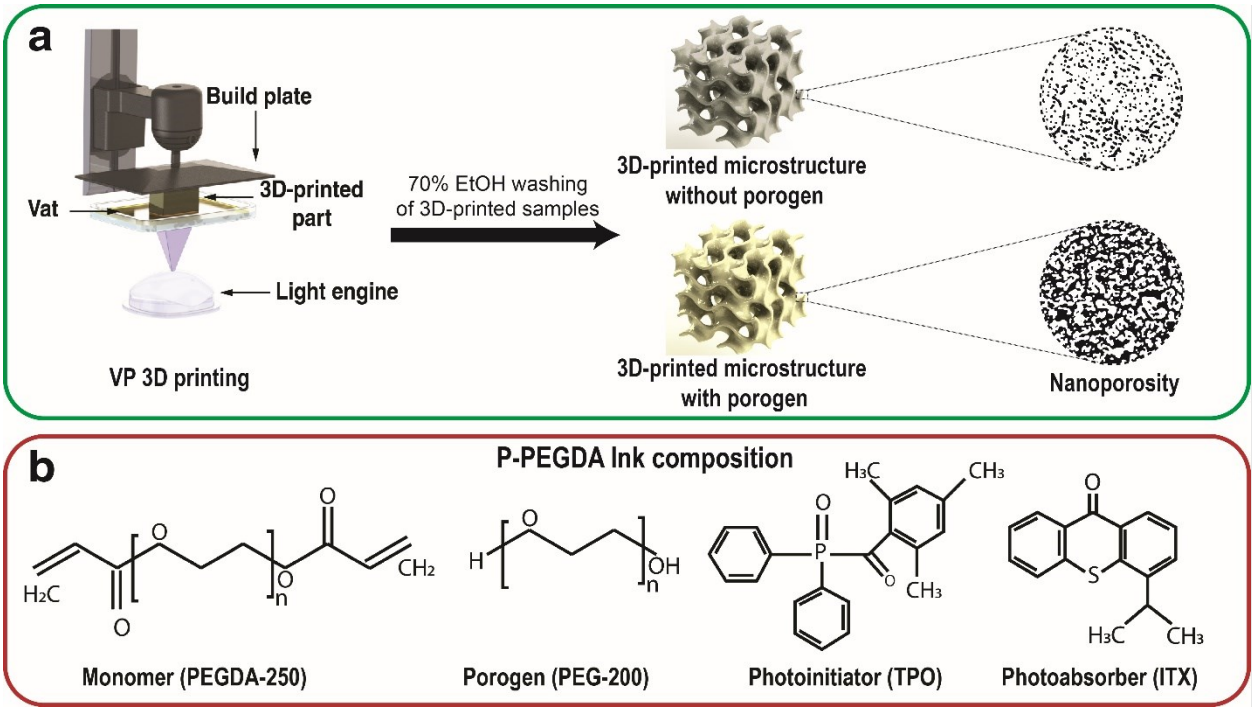

Figure 5.1. Schematic of the 3D printing process and the ink composition. (a) The fabrication process starts with 3D printing of an object to achieve microporosity, followed by washing steps to leach out the PEG porogen to form nanopores. The black areas in the images indicate the porosity of the structures. **(b)** P-PEGDA ink composition including PEGDA-250 monomer, PEG-200 porogen, TPO PI TPO and ITX PA.

We included PEG-200 as a porogen in our formulation, which is crucial for creating a porous structure. PEG-200 was chosen as the porogen for its ability to dissolve in hydrophilic monomers and easily diffuse out of the cured structure, leaving behind pores. It is also non-toxic, FDA-

approved, and has been widely used in biomedical applications[26,27]. The rationale behind using a porogen is to create a porous structure which can allow for oxygen exchange and facilitate removal of toxic and unreacted components in 3D printed structures. In our case, PEG-200 was found to be compatible with the PEGDA-250 and the PI, making it a suitable choice for making nanoporous inks and improving cell attachment.

The choice of PI for our PEGDA-based formulation for OoC applications requires careful consideration of several factors, including adequate absorbance at 385 nm, low cytotoxicity, and compatibility with the monomer. After narrowing down the options to lithium phenyl-2,4,6-trimethyl benzoyl phosphinate (LAP), BAPO, and diphenyl(2,4,6-trimethylbenzoyl)phosphine oxide (TPO), we chose TPO as the optimal PI for several reasons. Firstly, TPO is highly soluble in PEGDA-250 and has shown low cytotoxicity compared to BAPO[28,29], meeting the requirements of our formulation. Although LAP has the lowest cytotoxicity, it has very low solubility in PEGDA-250. Secondly, TPO has a maximum absorption at 380 nm, but with a wavelength window extending to up to 425 nm making it suitable for VP 3D printing, which is the most commonly used wavelength. Lastly, we observed that 3D-printed samples using TPO as the PI exhibited less yellowing compared to samples printed with BAPO, resulting in 3D-printed structures more suitable for fluorescence microscopy. Overall, the use of TPO as the photoinitiator in our ink formulation satisfies the necessary criteria for our OoC application and provides optimal performance.

In order to achieve high-resolution 3D printing with the P-PEGDA ink, a PA was necessary to improve the vertical resolution and prevent clogging of conduits caused by uncontrolled light penetration and scattering. ITX was chosen as the PA due to its high efficiency at 385 nm, which is the optimal wavelength for our printing process. Additionally, ITX has been previously used

with PEGDA-250 for high-resolution 3D printing and has very low cytotoxicity, making it suitable for tissue engineering applications[22]. In addition, compared to other PAs such as NPS, ITX is less cytotoxic and yellowish. Therefore, the use of ITX in our ink formulation helps to meet the necessary criteria for our OoC application, including 3D printability with high resolution, high transparency for fluorescence microscopy, and cytocompatibility.

In addition, In VP 3D printing, the resolution of embedded features in the Z direction is mainly dictated by the depth of light penetration into the ink. Characterization of the light penetration depth of the ink is crucial to optimize the printing parameters such as layer exposure time and layer thickness. We measured the penetration depth of light for different porogen concentrations at various exposure times to optimize the printing parameters for high accuracy in the Z direction. As shown in **Figure 5.2c**, the addition of PEG porogen increased the penetration depth. PEG porogen may act as a plasticizer, which can increase the mobility of the polymer chains in the material, leading to a more open and less dense network structure. This also contributes to the reduction of light scattering and the increase in the penetration depth of light.

The high-resolution printing capability of our ink enabled us to achieve excellent printability and accuracy, producing complex and precise geometries such as torus knots that would be difficult to achieve with other fabrication methods. Torus knots are constructed mathematically by taking a circle in the torus and moving it around the torus in a certain way. The resulting knot is defined by two integers (p,q), which determine its overall geometry. The values of p and q indicate the number of times the knot winds around the minor and major axis of the torus, respectively. Using P-PEGDA (10%), we were able to successfully 3D print a grammy knot with a diameter of 300 μm, a (3,13)-torus knot with a diameter of 240 μm, and two-(2,5)-torus knots passing each other with a diameter of 340 μm **(Figure 5.2a)**. Moreover, we demonstrated the versatility of our

ink by 3D printing objects like gyroid (**Figure 5.2d**), using P-PEGDA with different porogen concentrations. The transparency of P-PEGDA ink is maintained for concentrations of 0% and 10% porogen; however, it decreases for concentrations above 10% (**Figure 5.2e**). This reduction in transparency can be attributed to the increased presence of pores within the material, which results from higher porogen concentrations. As the number of pores rises, light scattering within the material becomes more pronounced, leading to a decrease in transparency. These findings suggest that a 10% porogen concentration is optimized for applications requiring both fluorescence microscopy and porosity.

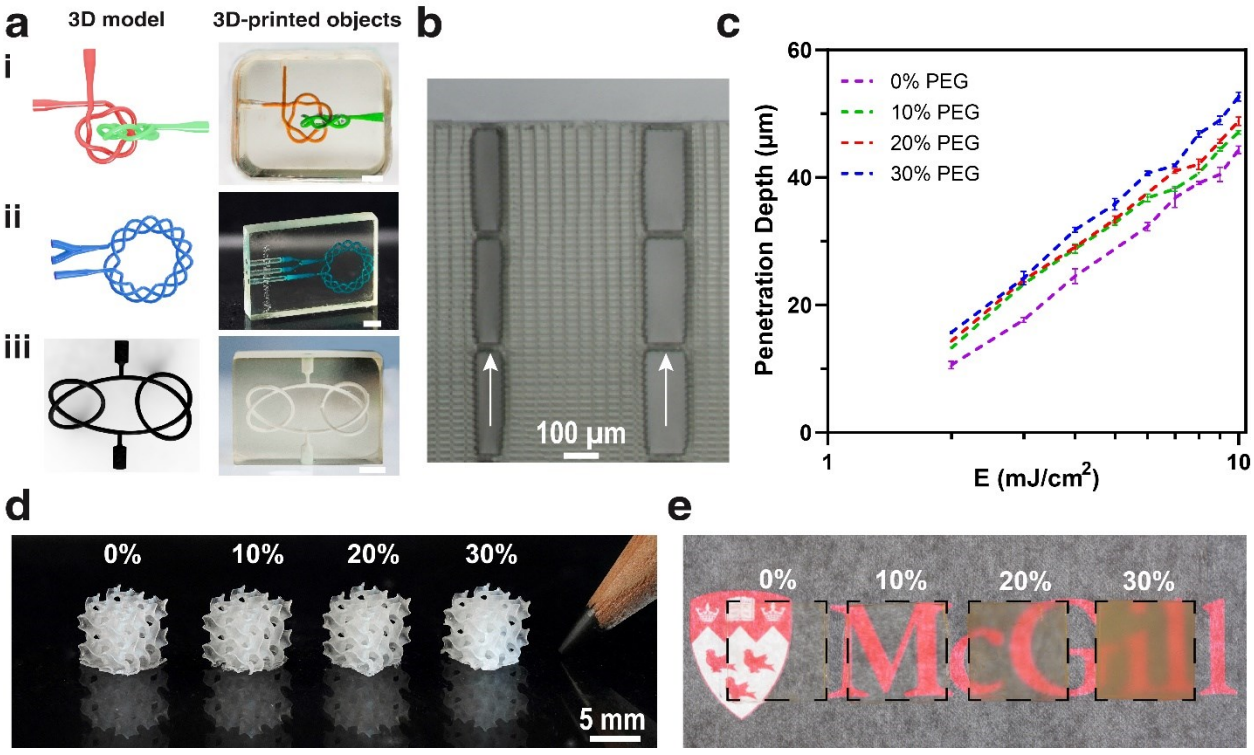

Figure 5.2. 3D printability of P-PEGDA ink. (a) 3D printed complex and intricate models with 10% porogen: **(i)** two-(2,5)-torus knots passing each other with a diameter of 340 µm, **(ii)** (3,13)-torus knot with a diameter of 240 µm, **(iii)** grammy knot with a diameter of 300 µm. **(b)** 3D printed stacked microchannels separated with 27-µm-thick membranes (indicated by white arrow). Scale bar: 2 mm. **(c)** Penetration depth characterization of P-PEGDA with different concentrations of porogen. Representative of three independent experiments (N = 3). The error bar represents standard deviation. **(d)** 3D-printed gyroid with

a dimension of 5 mm^3 at different porogen concentrations. **(e)** 3D printed 3D squares at different porogen concentrations. Higher porogen concentrations result in decreased transparency of the 3D printed parts.

Additionally, the ability to 3D print monolithic and embedded microchannels is crucial for microfluidic and OoC applications. These microchannels serve as the fundamental building blocks for complex OoC devices. To demonstrate the printability of our ink, we characterized the 3D printing resolution by 3D printing a stack of channels separated with a thin 27 μm membrane, using a formulation containing 10% porogen **(Figure 5.2b)**. The successful printing of these intricate structures, membranes and microfluidic channels shows the potential of the P-PEGDA ink for high-resolution 3D printing of complex microstructures for applications such as OoC devices.

5.4.2 Effect of porogen concentration on material properties

To visualize the pores formed in the 3D-printed object, the printed samples were immersed in water to leach out the porogen and create voids within the structure. We performed a quantitative analysis of the pore size distribution using image analysis to evaluate the pore size dependency in the 3D printed parts to porogen concentration. We varied the concentration of PEG porogen in the ink to evaluate its effect on pore size distribution. We measured 40 individual pores from scanning electron microscope (SEM) images and analyzed the pore size distribution. We found that the pore size distribution was narrow for lower porogen concentrations but became broader at higher concentrations which might be related to the increasing diffusion of porogen during the printing process **(Figure 5.3c-d)**. Additionally, the average pore size increased from 5 nm to 30nm for a porogen concentration of 30% compared to the nonporous samples. This observation is consistent with previous studies that have shown that higher porogen concentrations can lead to larger pore sizes in 3D-printed structures[14]. As the PEG concentration increases, the porogen-to-monomer ratio also increases, resulting in larger pore sizes.

To investigate the effect of porogen concentration on weight loss in our formulations, we fabricated 3D-printed disks with varying porogen concentrations and measured their weight immediately after printing. Following crosslinking, the disks were submerged in water for 48 h to ensure complete removal of the porogens, and then dried and weighed again to determine weight loss. Our findings indicate that weight loss increased as porogen concentration increased, with disks containing 30% porogen experiencing a mass loss percentage of 26%, while those with 0% porogen only lost 2% of their initial weight **(Figure 5.3b)**. This trend is due to the greater amount of porogen available for removal during incubation in water in disks with higher porogen concentrations.

By incorporating a porogen into PEGDA, which is inherently hydrophilic before crosslinking, and subsequently removing it through washing after polymerization, a more hydrophilic material with a reduced contact angle is obtained (**Figure 5.3a**). The porogen's addition creates pores within the material, increasing its surface area and disrupting the matrix structure, potentially providing additional sites for water molecule interaction. This process may lead to a rise in hydrophilic sites, resulting in enhanced hydrophilicity of the material. Furthermore, the porogen's low molecular weight could contribute to the disruption of the PEGDA matrix, yielding a more disordered and less dense network. This factor may also play a role in increasing the material's hydrophilicity and reducing its contact angle (CA). The contact angle decreased from 67° CA for the nonporous objects to 29° CA for the objects 3D printed with 30% porogen.

In addition to the SEM analysis, we also carried out a diffusion test utilizing 3D-printed rods to investigate diffusion of small molecules through the P-PEGDA structure. We washed the samples for 24 h to remove the porogen. Samples were then immersed in a solution of 10 μM fluorescein in pH 7.4 phosphate buffer saline, and fluorescence images were acquired by confocal

microscopy near the middle height of the polymeric rod. By probing a single plane far from both the top and bottom parts of the pillar, negligeable diffusion from fluorescein molecule is expected for the probed time. Hence, the increase in fluorescence results from radial diffusion of fluorescein molecules. Our results show that the addition of porogen increase diffusivity of fluorescein (**Figure 5.3e**), demonstrating the presence of interconnected nanopores networks in the 3D-printed structures. This experiment provided complementary information to the SEM analysis and confirmed the material's porosity, which is crucial for various biomedical applications such as OoC and tissue engineering.

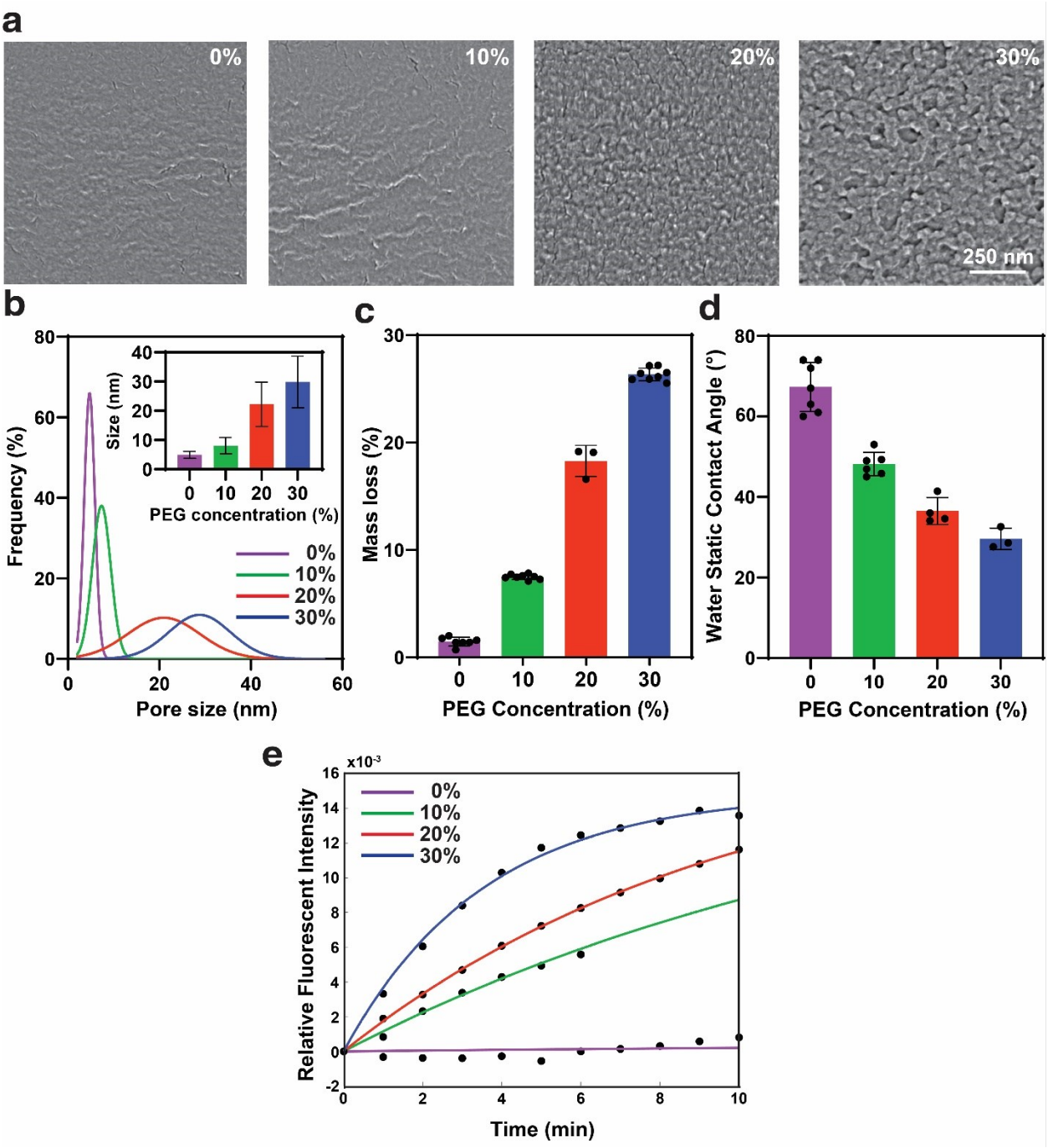

Figure 5.3. Characterization of P-PEGDA ink for different concentrations of PEG porogen. (a) SEM images show the porosity at different porogen concentrations. **(b)** Pore size distribution in the 3D-printed parts with P-PEGDA at different concentrations of porogen. Insert shows the average for size for different concentrations. In each case 40 random pores were analyzed. **(c)** mass loss of P-PEGDA after 48 h of incubation in DI water. **(d)** Static water contact angle for P-PEGDA for different porogen concentrations.

(e) diffusion of fluorescein (340 g/mol) through the 3D printed objects with different porogen concentrations. The error bar represents standard deviation.

5.4.3 Cytocompatibility

To further demonstrate the advantages of our P-PEGDA ink, we evaluated its cytotoxicity based on two ISO standards, namely ISO 10993-12:2009 and ISO 10993-5:2009[30]. The former standard involves incubating the cell media with the 3D-printed object and then culturing cells using the media, while the latter is more sensitive and based on direct co-culture of 3D-printed parts with the cells. ISO 10993-12:2009 provides guidance on the determination of the potential for a medical device to cause skin irritation, while ISO 10993-5:2009 provides guidance on the determination of the potential for a medical device to cause cytotoxicity. We selected several cell types, including IMR, MDA-MB-231, 293T, and HUVEC, for a cytotoxicity assay. The PrestoBlue assay was used to evaluate cell viability.

We investigated the impact of washing time and the ITX PA on the biocompatibility of 3D-printed objects for 293T cell line. Unreacted components during the printing process may affect the biocompatibility of the printed parts, but our results showed that washing with 70% ETOH after printing can enhance biocompatibility. We found that the cell viability for the printed objects was initially lower than 70% without washing but increased significantly after 12 h of washing (**Figure 5.4c**). The addition of 0.8% ITX did not negatively affect cell viability, as the samples with and without ITX showed similar increases in cell viability after washing. These results suggest that a 12 h washing period is sufficient to ensure biocompatibility of 3D-printed objects.

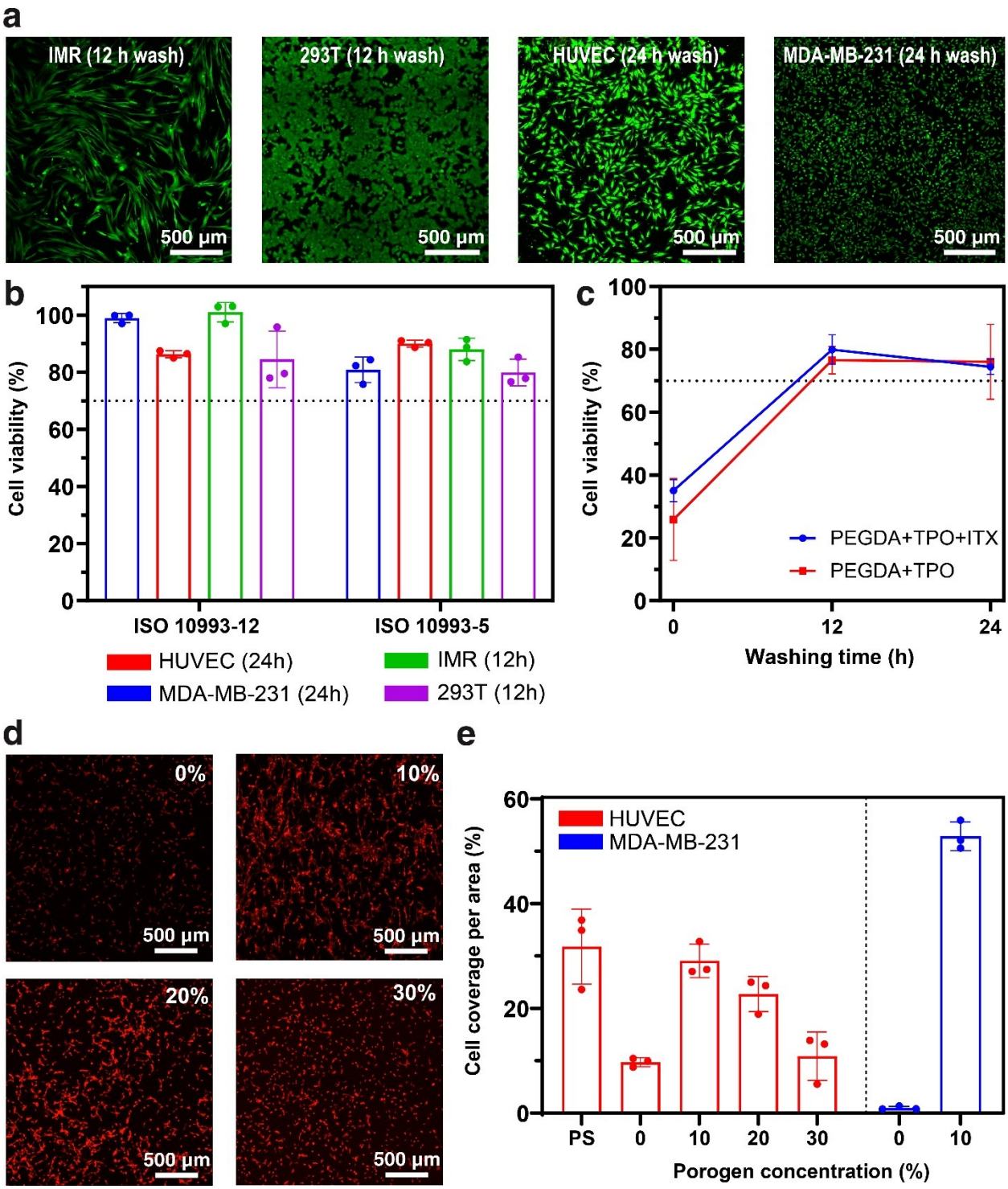

Figure 5.4. Cytotoxicity and cell attachment on P-PEGDA ink. (a) Fluorescence images of cells (IMR-90, 293T, HUVEC, and MDA-MB-231) following 48 h of culture in a well-plate in the presence of 3D-printed samples washed in 70% EtOH for 12 h or 24 h. **(b)** Cell viability for various cell types for 3D-printed disks with different washing time, assessed by incubation with cell media (ISO 10993-12) and direct

co-culture with the cells (ISO 10993-5). The line in (b) and (c) represents the minimum viability in accordance with the standards. (c) Cell viability of 293T cells analyzed using the ISO 10993-5 standard protocol for P-PEGDA ink with and without ITX PA, as a function of wash time. The results show low toxicity of the PA and enhanced biocompatibility for washed samples. **(d)** Cell attachment for HUVEC cells cultured on 3D-printed wells with P-PEGDA at different porogen concentrations. **(e)** Cell coverage per projected area on plasma-treated polystyrene (tissue culture plastic) and 3D-printed wells with different porogen concentrations for HUVEC and MDA-MB-231 cell lines. Representative of three independent experiments (N = 3). The error bar represents standard deviation.

In addition, we tested the biocompatibility of the formulation by evaluating the cell viability for four different cell lines based on two different standards, ISO 10993-12:2009 and ISO 10993-5:2009. Our results showed that a 24 h washing period can achieve a cell viability of 80% for all cell lines, which meets the minimum requirement (>70%) of both standards (**Figure 5.4a-b**). For example, the cell viability of HUVEC after 24 h was 90% for the ISO 10993-5:2009 standard. Moreover, we found that the cell viability was generally higher for the ISO 10993-12:2009 standard than the ISO 10993-5:2009 standard. It is important to note that the washing step is crucial in removing any unreacted components that may be present in the 3D-pritned part, as this can affect cell viability. The optimal washing time may vary depending on the application; for instance, a microfluidic device designed for a short assay may require little to no washing, while working with more sensitive cell types like induced pluripotent stem cells (iPSC) may require elongated washing time. These findings confirm that the material is suitable for OoC applications, as it demonstrates high biocompatibility across multiple cell lines and meets the required standards for cell viability.

PEGDA ink has garnered significant attention in biomicrofluidics and OoC applications due to its 3D printability and biocompatibility. However, existing PEGDA inks lack both cell attachment and nanoporosity. Thus, prior research endeavored to enhance cell attachment on

nonporous 3D printed PEGDA samples by employing plasma treatment, which necessitates the utilization of costly instrumentation[17]. Additionally, this approach may prove ineffective for internal structures that remain unexposed to plasma. In this study, we demonstrate that introducing nanoporosity to 3D printed scaffolds with porous-PEGDA formulation promotes cell attachment compared to nonporous PEGDA scaffolds. Previous studies have also shown that scaffolds with nanoporosity enhance cell attachment significantly[16].

To assess cell attachment, we fabricated microwells using both P-PEGDA and nonporous PEGDA via 3D printing, and then seeded fluorescently labeled HUVEC or MDA-MB-231 cells into the microwells. Cell attachment behaviors within each microwell were visualized using fluorescence microscopy after 24 h, and cell coverage was quantified via Image analysis. The results showed that for HUVEC cells, coverage in P-PEGDA containing 10% and 20% porogen was significantly better than the non-porous PEGDA formulation (**Figure 5.4d**). In fact, we observed cell coverage in P-PEGDA (10%) similar to that observed for plasma-treated polystyrene (tissue culture plastic), the gold standard material for 2D cell culture. We observed a similar trend in MDA-MB-231 cells, where a fifty-fold increase in cell attachment was observed in P-PEGDA (10%) microwells (**Figure 5.4e**). Consequently, 3D scaffolds with inherent nanoporosity demonstrate promising potential for OoC applications involving 3D cell culture. The increased cell adhesion on nanoporous scaffolds can be attributed to several factors. First, the nanoporous scaffolds provide a larger surface area for cells to adhere[31]. Second, the nanoporous topography can enhance cell anchorage, by allowing more filopodia to attach firmly to the surface[32].

5.4.4 OoC application

To demonstrate the potential of the developed porous ink, we developed an OoC platform using a formulation containing 10% porogen. The formulation with 10% porogen exhibited

superior cell attachment and transparency, making it suitable for OoC applications where both cell attachment and transparency are critical.

Conventional OoCs with capillary stop valves (CSVs) primarily employ 2D microfluidic designs that restrict cell interactions to a single plane or height[34–37]. CSVs[38] are integrated into these designs to provide better control over fluid flow and compartmentalization, allowing for localized and precise manipulation of the cellular microenvironment. However, this limitation in dimensionality leads to an inability to accurately mimic the complex 3D environment found in native tissues and organs, as cells *in-vivo* interact with their surroundings in all three dimensions. The 2D context in these classical OoC designs can limit cellular behavior, function, and response to stimuli. Moreover, conventional OoC devices only allow for exposure to side channel cell types through single-level channels, which may not accurately represent the spatial organization and cell interactions found in the microenvironment.

We developed a novel OoC system to investigate cancer and stromal cell interactions. To achieve this, we designed a microfluidic device with three levels of microchannels that confine the cancer spheroid in the middle chamber at different heights, allowing for exposure to more stromal cells (**Figure 5.5a-c**). The scaffold is connected to the central channel via 30 microfluidic CSVs with diameter of 250 μm. Note that the CSVs operate in both central and radial flow directions as shown in **Figure 5.5d-e**. In our work the first operation was to seed the gyroid scaffold with the edges forming peripheral stop valve with hydrogel prepolymers containing stromal cells, allowing it to gel and thereby immobilizing the cells on the scaffold. Next, the cancer spheroid was seeded in the central chamber. Thanks to the CSVs, either the spheroid chamber or the scaffold peripheral to the spheroid chamber may be seeded with hydrogels in any given order, without unwanted solutions overflowing into the other compartments (**Figure 5.5d-e**). Furthermore, the 3D CSV

layout with the gyroid scaffold was thus covered with cells along the Z axis, that could freely migrate in 3D up to a height of 500 µm.

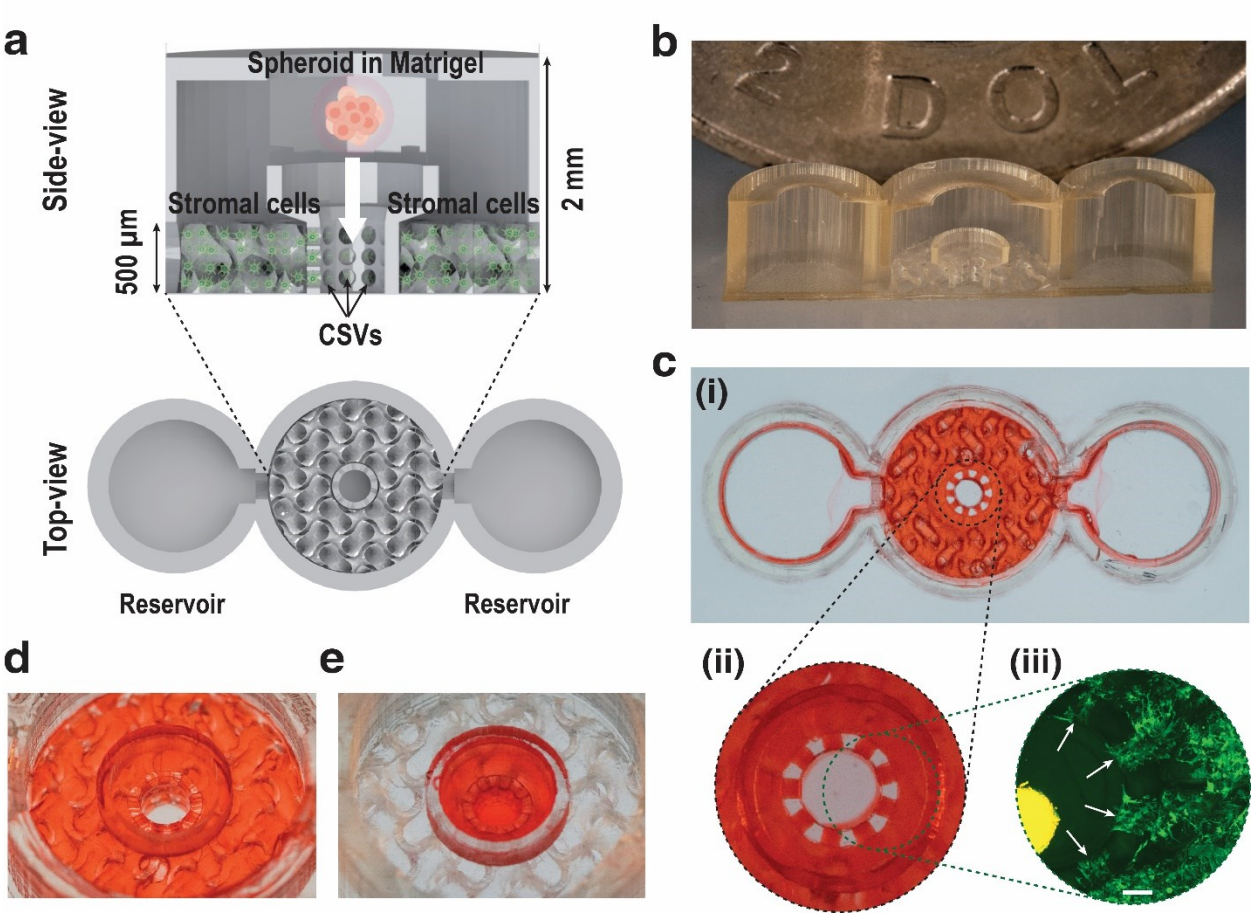

Figure 5.5 OoC device featuring CSVs and a Gyroid Scaffold. (a-b) Schematic representation of the device layout, including two reservoirs connected to a central gyroid scaffold, and three-level CSVs. (b) Isotropic view of the 3D OoC device cross-section. (c) (i) Top view of the OoC device filled with food dye, demonstrating the functionality of the stop valves. (ii) Zoomed-in view of (i), highlighting the functionality of stop valves. (iii) showing the presence of stromal cells halted at the CSV (white arrows) (scale bar: 200 µm). (d-e) Illustration of the bidirectional functionality of CSVs during the seeding process.

We were able to 3D print 45 OoC chips in a single print run, demonstrating the high throughput of our approach. Our design represents a significant improvement over conventional spheroid-on-a-chip devices that only allow for exposure to side channel cell type through channels

at a single level. Additionally, we utilized a gyroid scaffold to culture the stromal cells, providing a highly porous and interconnected structure. Gyroids have been studied as scaffolds for tissue engineering and regenerative medicine due to their unique shape and high surface-to-volume ratio[39,40]. The interconnected nature of the gyroid scaffold may also allow for cell migration and tissue integration, promoting tissue regeneration[41,42]. Our design rationale was based on the importance of spatial organization and the need for more physiologically relevant 3D culture systems. We successfully improved the design of tumor-on-a-chip devices by incorporating complex structures, such as a gyroid scaffold and CSVs at three different heights to increase the exposure of the cancer spheroid to stromal cells (**Figure 5.6a-b**), using the P-PEGDA ink. Our approach maintained a high level of biocompatibility while enabling the fabrication of complex models that better mimic *in-vivo* conditions.

We first evaluated the long-term co-culturing performance of the device by seeding tdTomato+ MDA-MB-231 spheroids in the middle chamber with GFP+ IMR-90 in the gyroid chamber. Media replenishment was performed bi-daily, and we conducted live-cell confocal imaging on day 1, day 8, and day 14 (end-point). Throughout the entire time-course, both MDA-MB-231 and IMR-90 maintained their physiological morphology inside the device **(Figure 5.6a)**. Moreover, at day 8, we observed bi-directional migration of both cell lines, where multiple IMR-90 cells migrated into the spheroid chamber at various heights, and vice versa **(Figure 5.6b)**. As shown in the confocal image at day 14, both cell types continued to migrate towards each other.

To further evaluate the utility of our OoC using a more sensitive cell type, we co-cultured GFP+ MDA-MB-231 spheroids with mCherry+ HUVEC cells in the gyroid chamber. The co-culture was maintained for up to 12 days, and confocal images were taken at the endpoint. Similar to our previous co-culture setup, both HUVEC and MDA-MB-231 maintained their physiological

morphology throughout the time-course. We observed bi-directional migration of both cell types, with HUVEC forming vessels surrounding the shell of the cancer spheroid (white arrow), and integration of the cancer spheroid into the vasculature (yellow arrow) **(Figure 5.6d-f)**. Furthermore, the chemokine CXCL12 has been associated with the promotion of directional cell migration. In our co-culture setup, we observed an elevated level of CXCL12 throughout the entire experimental time course, with the exception of the endpoint **(Figure 5.6c)**. This heightened CXCL12 signal appears to correlate with the observed cell migration, suggesting a chemotactic role. Interestingly, as the cells came into proximity at the endpoint, the CXCL12 signal diminished, possibly indicating that the chemotactic requirement was reduced upon successful cell interaction. Based on these findings, we conclude that our organ-on-a-chip model is suitable for long-term 3D cell interactions.

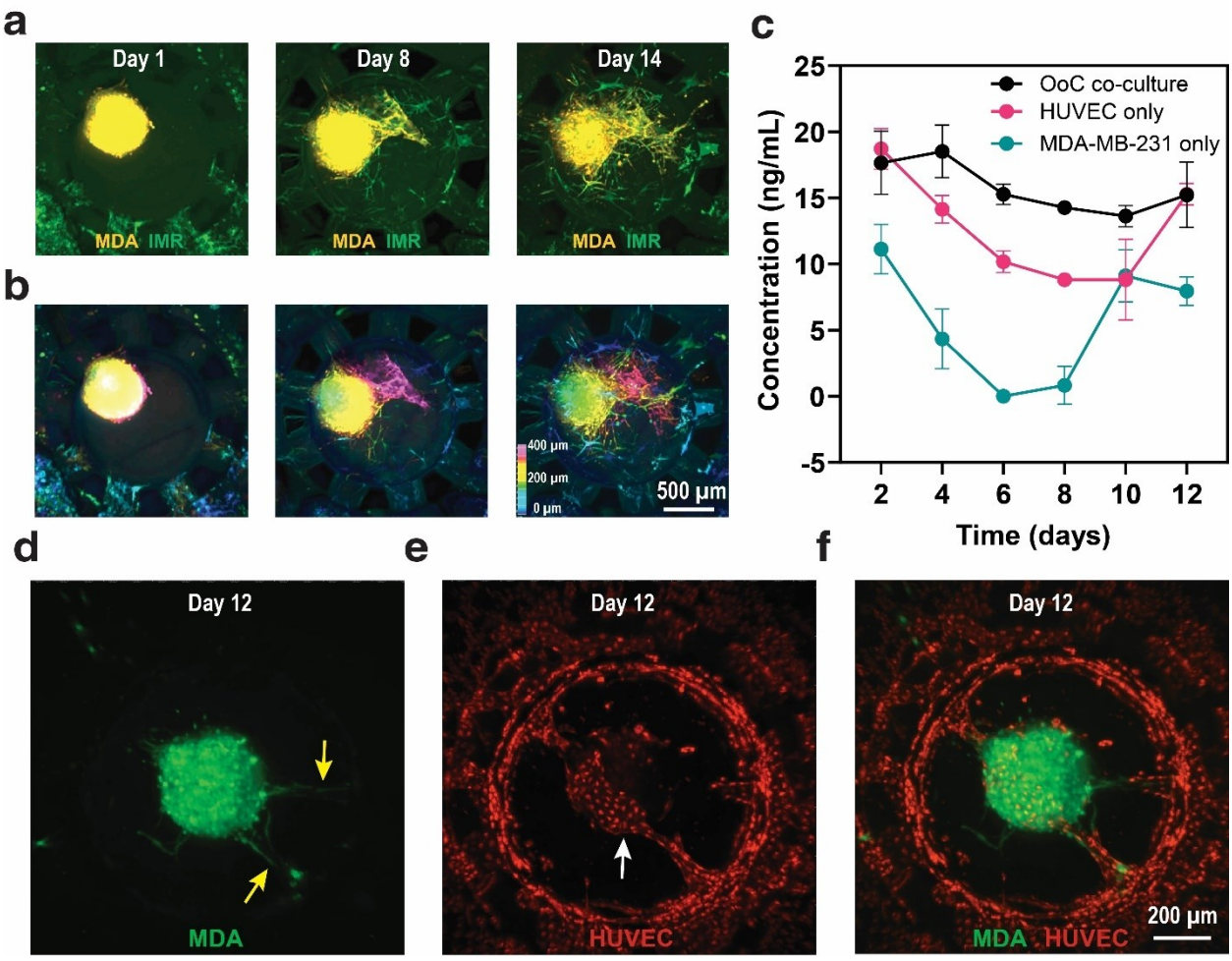

Figure 5.6 Co-culture of cancer and stromal cells in the OoC device. (a) 3D confocal microscopy images of tdTomato+ MDA-MB-231 spheroid co-cultured with GFP+ IMR-90 cells at different time points in the OoC platform. (b) Depth color map for the height range of 400 µm showing bi-directional migration of cells. (c) CXCL12 secretion under different culture conditions, showing increased concentration for OoC co-culture that induce cell migration. 3 biological repeats and 20 technical repeats were done for each condition and time course. (d-f) Confocal microscopy images of MDA-MB-231 breast cancer cells spheroid co-cultured with HUVEC cells, demonstrating vessel formation and integration of the cancer spheroid into the vasculature (white and yellow arrows, respectively)

5.5 Discussion and Conclusion

In this study, we have successfully developed a high-resolution nanoporous PEGDA ink for fabricating OoC devices using VP 3D printing method. 3D printing is growing rapidly technology and contributing to advancing tissue engineering by facilitating the production of

intricate and complex microstructures that are challenging to produce using conventional methods. While previous PEGDA inks show great potential for VP 3D printing, modifications are often necessary to make them suitable for OoC applications. Moreover, although achieving submicron porosity is critical for TE applications, it remains challenging to 3D print macroscopic structures with nanoporosity due to the tradeoff between printing resolution and footprint. P-PEGDA addressed these challenges and enabled the printing of intricate structures with an average pore size from 5 nm and 30 nm, controllable by varying the concentration of the porogen. With the capability to 3D print membranes as thin as 27 μm, our approach facilitated the fabrication of complex structures with fine details. We confirmed the porosity of the material using fluorescein diffusion tests, and systematic cytotoxicity studies following ISO standards for four different cell lines demonstrated high biocompatibility, with viability greater than 80% achieved. Moreover, the nanoporous substrates showed a fourfold increase in coverage by endothelial cells and a 50-fold increase for MDA-MB-231 cells compared to nonporous substrates, indicating strong cell attachment and improved cell interaction for successful in-vitro studies.

By leveraging the design flexibility of 3D printing, we introduced a tumor-on-a-chip model comprising a 3D printed microporous gyroid scaffold for growing stromal cells in 3D around a central opening filled with hydrogel and a cancer cell spheroid. The OoC platform supported long-term cell interaction, bidirectional migration of both cell types, and the potential for vascularization, both in 3D across the height of the scaffold. These accomplishments address the limitations of traditional PEGDA inks and 2D OoC devices. Our 3D OoC model, integrated with vascularization, provides a more physiologically relevant microenvironment for cell interactions compared to traditional 2D models. However, some challenges remain, such as ensuring reproducible cell

seeding in 3D, which is an avenue for potential improvement. Additionally, connecting the developed OoC to a recirculating system could further enhance the biomimetic nature of the model.

The development of our high-resolution nanoporous PEGDA ink has implications for the advancement of tissue models, drug discovery, and regenerative medicine. With this material, researchers can print structures with submicron porosity, allowing for the creation of more biomimetic scaffolds. In conclusion, our study demonstrates significant advancements in overcoming the limitations of traditional PEGDA inks in terms of cell attachment and nanoporosity. The development of this novel biomaterial for 3D printing and tissue engineering paves the way for more accurate and physiologically relevant in-vitro studies.

5.6 Materials and Methods

3D printing

All objects were designed in SolidWorks® computer aided drafting software, exported as "STL" files, and 3D-printed with Miicraft Prime 110 (Creative CADworks, Concord, Canada) with a projected pixel size of 40 μm. All objects reported in this work are printed with a layer thickness of 20 μm. Immediately after printing, to remove unpolymerized ink and clean channels, closed channels were vacuumed, washed with isopropanol (Fisher Scientific, Saint-Laurent, Quebec, Canada) several times using a syringe, and dried under a stream of pressurized nitrogen gas.

P-PEGDA Formulation and Preparation

Inks in this study consist of the monomer, poly (ethylene glycol) diacrylate (PEGDA, MW250, Sigma), the poly (ethylene glycol) (PEG, MW200, sigma) porogen, the photoinitiator, TPO (0.5 w/w) and the photoabsorber, ITX (0.8 w/w). The P-PEGDA was prepared by mixing

the above-mentioned components at the desired concentration for 30 min. All inks are stored in amber glass bottles after preparation.

Videos and image stacking

Videos and images were taken using a Panasonic Lumix DMC-GH3K and Sony α7R III. For focus stacking, Imaging Edge Desktop (Sony) was used to take the sequence of images on different focal planes. Then, CombineZP was used to process the images. Imaging at the microscale was done on an inspection microscope (Nikon Eclipse LV100ND) at 5x magnification. Some images were taken with a stereo microscope (Leica SMZ-8) fitted with a digital camera (Lumix GH3 DSLR, Panasonic).

Penetration depth measurements

In order to measure the effect of porogen on the penetration depth of light, a drop of the formulation was placed on a glass slide and exposed to different exposure times at a light intensity of 5 mW/cm^2. After rinsing uncured ink with 70% ethanol, we measured the thickness of patterned regions using a stylus profilometer (DektakXT, Bruker Co.). Absorbance measurements of the P-PEGDA were performed by triplicate using a NanoDrop (ND-1000).

Contact angle measurements

A volume of 2-3 µl DI water was placed on the top surface of 3D-printed samples and imaged using a Panasonic Lumix DMC-GH3K. The side view images were imported to Image-J to measure the static contact angle using the contact angle plugin.

SEM

The Hitachi SU-8230 SEM was used to characterize the pore structure of the 3D printed objects at an operating voltage of 3 kV. Before the SEM measurements, the samples were washed,

dried, and then coated with a 4 nm thick platinum layer. Pore sizes were measured from the cross-sectional SEM images by measuring 40 random pores in ImageJ.

Mass loss

Disk-shaped samples with a diameter of 8 mm and a thickness of 3 mm were 3D-printed. All the samples were weighed after printing. The samples were then soaked in 1x PBS and shaken on an orbital shaker for 48 h. Afterward, the samples were removed from the PBS and weighed to determine the mass loss.

Data analysis

The error bars displayed in the figures represent the standard deviation. GraphPad Prism 9 was used for data analysis.

Cytotoxicity Testing

The cytocompatibility assays were performed in compliance with International Organization for Standardization (ISO) standards for the development of medical devices. Cells were seeded in a 24-well plate at a seeding density of 10k per well. Immediately after cell seeding, post-treated disks were placed directly on top of the cell layer. As controls, cell-only wells was also seeded with the same cell density. Quantitative cell viability measurements via PrestoBlue™ (Thermofisher, USA) were taken every 24h for a time course of three days. Microscopy images were taken daily using a Ti2 inverted microscope and analyzed using NIS-Element (Nikon, Japan). Three biological replicates were done for each of the three above-mentioned conditions. For the PrestoBlue™ cell viability assay measurement, two technical replicates were performed for each biological repeat.

Diffusion assay

Permeability of the P-PEGDA ink was evaluated by confocal fluorescence microscope. Posts of 500 μm diameter and 5 mm height were 3D printed and immobilized into an observation chamber. The pinhole of the confocal microscope was set to1.2 Airy Unit and a single plane at around 200 μm above the base of the post was imaged. Then, a 1 μM Fluorescein isothiocyanate (FITC) solution in miliQ was introduced within the chamber, and fluorescence images were acquired every minute, while keeping the shutter off in between measurements to prevent photobleaching of the dye. By imaging a section away from the based and the top of the 3D-printed posts, the radial diffusion of FITC in the P-PEGDA is expected to account for increasing fluorescence intensity during the time of the experiment. Images were analyzed by a cutom matlab script, where the center of the post was automatically detected via the MatLab function imfindcircle. A circular mask was generated and separated into 9 distinct sectors. These sectors were individually applied onto the fluorescence images acquired in time to assess the homogeneity of the radial diffusion of FITC within the post. A second integration mask was generated to measure the fluorescence intensity outside the post and used to normalize the fluorescence intensity and account for photobleaching. In analogous to fluorescence recovery after photobleaching experiment (FRAP), and due to the radial diffusion of fluorescent molecule into a circular non-fluorescent material, a non-linear least-square function was fitted to the normalized intensity. The fit-function was f(t)=A(1-exp(-λt))+ x_o where A and λ are fit parameters and x0¬ the initial fluorescence intensity into the post.

5.7 References

1. Ashammakhi, N. *et al.* Microphysiological systems: next generation systems for assessing toxicity and therapeutic effects of nanomaterials. *Small Methods* **4**, 1900589 (2020).

2. Low, L. A., Mummery, C., Berridge, B. R., Austin, C. P. & Tagle, D. A. Organs-on-chips: into the next decade. *Nat. Rev. Drug Discov.* **20**, 345–361 (2021).

3. Liu, H. *et al.* Advances in Hydrogels in Organoids and Organs-on-a-Chip. *Adv. Mater.* **31**, 1902042 (2019).

4. Nahak, B. K., Mishra, A., Preetam, S. & Tiwari, A. Advances in Organ-on-a-Chip Materials and Devices. *ACS Appl. bio Mater.* **5**, 3576–3607 (2022).

5. Teixeira Carvalho, D. J., Moroni, L. & Giselbrecht, S. Clamping strategies for organ-on-a-chip devices. *Nat. Rev. Mater.* 1–18 (2023).

6. Regehr, K. J. *et al.* Biological implications of polydimethylsiloxane-based microfluidic cell culture. *Lab Chip* **9**, 2132–2139 (2009).

7. Campbell, S. B. *et al.* Beyond polydimethylsiloxane: alternative materials for fabrication of organ-on-a-chip devices and microphysiological systems. *ACS Biomater. Sci. Eng.* **7**, 2880–2899 (2020).

8. Carvalho, V. *et al.* 3D printing techniques and their applications to organ-on-a-chip platforms: A systematic review. *Sensors* **21**, 3304 (2021).

9. Gold, K., Gaharwar, A. K. & Jain, A. Emerging trends in multiscale modeling of vascular pathophysiology: Organ-on-a-chip and 3D printing. *Biomaterials* **196**, 2–17 (2019).

10. Goldstein, Y. *et al.* Breaking the third wall: Implementing 3D-printing techniques to expand the complexity and abilities of multi-organ-on-a-chip devices. *Micromachines* **12**, 627 (2021).

11. Ravanbakhsh, H. *et al.* Emerging Technologies in Multi-Material Bioprinting. *Adv. Mater.* **33**, 2104730 (2021).

12. Naderi, A., Bhattacharjee, N. & Folch, A. Digital Manufacturing for Microfluidics. (2019) doi:10.1146/annurev-bioeng-092618.

13. Mu, X. *et al.* Porous polymeric materials by 3D printing of photocurable resin. *Mater. Horizons* **4**, 442–449 (2017).

14. Nguyen, T. H. M. *et al.* Porous structures prepared by a novel route: Combination of digital light processing 3D printing and leaching method. *J. Manuf. Process.* **67**, 46–51 (2021).

15. Ying, G. *et al.* Aqueous Two-Phase Emulsion Bioink-Enabled 3D Bioprinting of Porous Hydrogels. *Adv. Mater.* **30**, 1805460 (2018).

16. Dong, Z. *et al.* 3D Printing of Superhydrophobic Objects with Bulk Nanostructure. *Adv. Mater.* **33**, (2021).

17. Dong, Z. *et al.* 3D printing of inherently nanoporous polymers via polymerization-induced phase separation. *Nat. Commun.* **12**, 1–12 (2021).

18. Warr, C. *et al.* Biocompatible PEGDA Resin for 3D Printing. (2020) doi:10.1021/acsabm.0c00055.

19. Urrios, A. *et al.* 3D-printing of transparent bio-microfluidic devices in PEG-DA. *Lab Chip* **16**, 2287–2294 (2016).

20. Grigoryan, B. *et al.* Multivascular networks and functional intravascular topologies within biocompatible hydrogels. *Science* **364**, 458–464 (2019).

21. Grigoryan, B. *et al.* Development, characterization, and applications of multi-material stereolithography bioprinting. *Sci. Rep.* **11**, 3171 (2021).

22. Naderi, A., Bhattacharjee, N. & Folch, A. Digital Manufacturing for Microfluidics. *Annu. Rev. Biomed. Eng.* **21**, 325–364 (2019).

23. Kuo, A. P. *et al.* High-Precision Stereolithography of Biomicrofluidic Devices. *Adv. Mater. Technol.* **4**, 1–11 (2019).

24. Gong, H., Bickham, B. P., Woolley, A. T. & Nordin, G. P. Custom 3D printer and resin for 18 μm × 20 μm microfluidic flow channels. *Lab Chip* **17**, 2899–2909 (2017).

25. Gong, H., Beauchamp, M., Perry, S., Woolley, A. T. & Nordin, G. P. Optical approach to resin formulation for 3D printed microfluidics. *RSC Adv.* **5**, 106621–106632 (2015).

26. Sanchez Noriega, J. L. *et al.* Spatially and optically tailored 3D printing for highly miniaturized and integrated microfluidics. *Nat. Commun. 2021 121* **12**, 1–13 (2021).

27. Alconcel, S. N. S., Baas, A. S. & Maynard, H. D. FDA-approved poly (ethylene glycol)–protein conjugate drugs. *Polym. Chem.* **2**, 1442–1448 (2011).

28. Nguyen, T. N. T. *et al.* Surface PEGylation of hollow mesoporous silica nanoparticles via aminated intermediate. *Prog. Nat. Sci. Mater. Int.* **29**, 612–616 (2019).

29. Kim, G.-T. *et al.* Cytotoxicity, Colour Stability and Dimensional Accuracy of 3D Printing Resin with Three Different Photoinitiators. *Polymers (Basel).* **14**, 979 (2022).

30. Zeng, B. *et al.* Cytotoxic and cytocompatible comparison among seven photoinitiators-triggered polymers in different tissue cells. *Toxicol. Vitr.* **72**, 105103 (2021).

31. Ghasemi-Mobarakeh, L., Kolahreez, D., Ramakrishna, S. & Williams, D. Key terminology in biomaterials and biocompatibility. *Curr. Opin. Biomed. Eng.* **10**, 45–50 (2019).

32. Grafahrend, D. *et al.* Degradable polyester scaffolds with controlled surface chemistry combining minimal protein adsorption with specific bioactivation. *Nat. Mater.* **10**, 67–73 (2011).

33. Dalby, M. J., Gadegaard, N. & Oreffo, R. O. C. Harnessing nanotopography and integrin–matrix interactions to influence stem cell fate. *Nat. Mater.* **13**, 558–569 (2014).

34. Busek, M. *et al.* Pump-less, recirculating organ-on-a-chip (rOoC) platform. *Lab Chip* **23**, 591–608 (2023).

35. Kim, S., Chung, M., Ahn, J., Lee, S. & Jeon, N. L. Interstitial flow regulates the angiogenic response and phenotype of endothelial cells in a 3D culture model. *Lab Chip* **16**, 4189–4199 (2016).

36. Nashimoto, Y. *et al.* Integrating perfusable vascular networks with a three-dimensional tissue in a microfluidic device. *Integr. Biol.* **9**, 506–518 (2017).

37. Lee, S. *et al.* Microfluidic-based vascularized microphysiological systems. *Lab Chip* **18**, 2686–2709 (2018).

38. Olanrewaju, A., Beaugrand, M., Yafia, M. & Juncker, D. Capillary microfluidics in microchannels: from microfluidic networks to capillaric circuits. *Lab Chip* **18**, 2323–2347 (2018).

39. Germain, L., Fuentes, C. A., van Vuure, A. W., des Rieux, A. & Dupont-Gillain, C. 3D-printed biodegradable gyroid scaffolds for tissue engineering applications. *Mater. Des.* **151**, 113–122 (2018).

40. Verisqa, F., Cha, J.-R., Nguyen, L., Kim, H.-W. & Knowles, J. C. Digital Light Processing 3D Printing of Gyroid Scaffold with Isosorbide-Based Photopolymer for Bone Tissue Engineering. *Biomolecules* **12**, 1692 (2022).

41. Su, J. *et al.* Three-dimensional printing of gyroid-structured composite bioceramic scaffolds with tuneable degradability. *Biomater. Adv.* **133**, 112595 (2022).

42. Qi, D. *et al.* 3D printed magnesium-doped β-TCP gyroid scaffold with osteogenesis, angiogenesis, immunomodulation properties and bone regeneration capability in vivo. *Biomater. Adv.* **136**, 212759 (2022).

Chapter 6

6. Chapter 6: High-Resolution Additive Manufacturing of a Biodegradable Elastomer with a Low-Cost LCD 3D printer

6.1 Preface

In the last two chapters, we presented two different formulations based on PEGDA for microfluidics and OoC applications. While the porous-PEGDA formulation is suitable for many OoC applications, numerous platforms for OoC and tissue engineering require the mechanical properties of soft tissues. Furthermore, in these works, the objects were 3D printed with a DLP-based 3D printer, which is less accessible compared to LCD 3D printers. In this chapter, we introduce POMaC formulations for VP 3D printing using very low-cost LCD printers and demonstrate the ability to create complex 3D structures with 80 μm resolution and tunable mechanical properties. With the POMaC ink, automated digital manufacturing of this biodegradable material becomes assembly-free. This feature should simplify the prototyping of devices for organ-on-chip platforms, soft robotics, flexible electronics, and sensors, among other applications.

This chapter is a manuscript of a research article intended for submission: “High-Resolution Additive Manufacturing of a Biodegradable Elastomer with an Ultra Low-Cost LCD 3D printer”, **V. Karamzadeh**, M. Shen, H. Ravanbakhsh, A. Sohrabi, M. Radisic, and D. Juncker.

6.2 Abstract

The Artificial organs and organs-on-a-chip are of great clinical and scientific interest and have recently been made by additive manufacturing, but depend on, and benefit from, biocompatible, biodegradable, and soft materials. Poly(octamethylene maleate (anhydride) citrate (POMaC) meets these criteria and has gained popularity, and as in principle, it can be photocured and is amenable to vat-photopolymerization (VP) 3D printing, but only low-resolution structures have been produced so fa. Here, we introduce a VP-POMaC ink and demonstrate 3D printing of high resolution (80 μm) and complex 3D structures using low-cost (~US$300) liquid-crystal display (LCD) printers. The ink includes POMaC, a diluent and porogen additive to reduce viscosity within the range of VP, and a crosslinker to speed up reaction kinetics. The mechanical properties of the cured ink were tuned to match the elastic moduli of different tissues simply by varying the porogen concentration. The biocompatibility was assessed by cell culture which yielded 80% viability and the potential for tissue engineering illustrated with a 3D printed gyroid seeded with cells. VP-POMaC and low-cost LCD printers make the additive manufacturing of high resolution, elastomeric, and biodegradable constructs widely accessible, paving the way for a myriad of applications in tissue engineering, implants, organ-on-a-chip, wearables, and soft robotics.

Keywords: 3D Printing, Elastomers, Tissue engineering, Additive manufacturing, Biomaterials, Photopolymerization

6.3 Introduction

Organ-on-a-chip platforms integrate microfabrication, tissue engineering, and microfluidics fundamentals to recapitulate relevant aspects of complex living organs *in-vitro*, including microarchitecture, microenvironment, functions of organs, and dynamic cell-to-cell

interaction[1,2]. Organ-on-a-chip engineering could revolutionize new compound screening, and biomarker discovery and, lead to the development of organ-specific drug screening systems[3]. Fabrication of organs-on-a-chip devices in a biomimetic manner requires great care to achieve tissue-like physiology *in-vitro*. These biofabrication techniques tend to be complex and labor-intensive, and they often require cleanroom facilities which lead to limited growth in the field of organ-on-a-chip. In response to these limitations, 3D printing using bioinks has become an increasingly popular alternative[4].

3D printing offers many advantages over conventional biofabrication processes for scaffold fabrication, including the ability to create 3D structures with predefined design and fabrication of complex 3D tissue constructs similar to biological systems in an automated, rapid and cost-effective manner[5,6]. Hydrogels are undoubtedly the most utilized biomaterials for 3D printing and 3D bioprinting due to their properties such as porosity, high water content and biocompatibility suitable for live cells[7]. Conventional hydrogels suffer from poor mechanical properties, uncontrollable degradability, and structural stability[8]. Furthermore, to prevent shrinkage and disintegration of the 3D-printed scaffolds, hydrogels must be kept hydrated during and after 3D printing. Additionally, 3D printing must be done in a wet environment to avoid dehydration and shrinkage of the 3D-printed layers.

Driven by the growing need for advanced materials in emerging technologies, research on novel biodegradable elastic polymers has increased, with synthetic, biodegradable elastomeric biopolymers[9,10] emerging as promising alternatives to hydrogels due to their tunable and stable mechanical and chemical properties, making them suitable for mimicking a wide range of soft biological tissues[11]. Citrate-based biomaterials have received considerable attention in the last few years due to their biocompatibility, degradability, and flexible designability[12–14]. One of the

promising citrate-based biomaterials is poly(octamethylene maleate (anhydride) citrate) (POMaC) elastomer which is a photo-curable elastomer allowing fast fabrication under mild conditions, degrades through hydrolysis reactions in aqueous solutions, and is synthesized from non-toxic monomers[15]. In addition to photocrosslinking of POMaC via the alkene moieties, it can be also thermally crosslinked via easter formation[15]. POMaC has also been successfully used as a key component of implantable pressure/strain sensors for tendons and tissue engineering, selected and proven for its biocompatibility, biodegradability, and mechanical properties. For example, Zhang et al. previously developed an angiogenesis assist device that enabled the merging of two seemingly opposing criteria: permeability and mechanical stability of the vasculature, in a microfabricated polymer-based scaffold for organ-on-a-chip engineering[16]. However, the assembly of the polymer structures involves multiple cumbersome photolithography steps and manual layer-by-layer assembly that hinder the use of POMaC for tissue engineering applications. Photolithography and 3D stamping technology are expensive, lengthy, and involve multistep procedures. 3D printing could provide an alternative solution to such limitations, however, elastomers are particularly challenging to 3D print due to their high viscosity, softness, and slow crosslinking kinetics compared to most common polymers and hydrogels[17].

To circumvent some of these challenges, 3D printing by extrusion of POMaC followed by photocuring has been explored as an alternative to direct photopatterning; however the high viscosity (>5000 cP) severely limits speed and resolution[18,19]. Radisic and colleagues developed a coaxial extrusion-based 3D printing of tubular POMaC microstructures with a Pluronic bath[18]. Poly(ethylene glycol) dimethyl ether (PEGDME) was mixed with POMaC to reduce viscosity and introduce porosity. Thanks to this approach, a variety of perfusable tubes with an inner diameter

of 500 μm and a wall thickness of 50 μm could be printed at much higher speed. However, this method cannot be used for non-tubular structures.

In an alternative strategy, Wales et al. used Poly(ethylene glycol) diacrylate (PEGDA) with a molecular weight of 700 Da as a copolymer crosslinker with POMaC to improve photoreaction kinetics[19]. POMaC could thus be 3D printed into simple shapes such as rings with a maximal spatial resolution of ~ 1 mm, which is inadequate for many applications. Additionally, PEGDA had a significant effect on the degradability and mechanical properties of POMaC, which may limit its usefulness in tissue engineering applications. As a result, there is a need for 3D printing of high-resolution and more complex structures made with POMaC.

Vat photopolymerization (VP) 3D printing is an agglomerative term that encompasses a variety of 3D photopolymerization printing methods, such as stereolithography (SLA) within the vat, which have collectively gained popularity in recent years. These techniques include high-end, expensive 2-photon photopolymerization systems costing > US$500K, widely used digital light processing (DLP, also called stereolithography) systems that typically cost between US$5,000 and US$15,000 with resolutions of up to 2560 × 1600 (~4M) pixels, and direct laser writers that offer slightly lower resolution and lower throughput but at a somewhat reduced cost of around $2000. Most printers are available as light engines with wavelengths of 405 nm, as well as 385 nm and 365 nm, which are often preferred due to the greater availability of inks, higher energy, and increased photo-crosslinking efficiency. More recently, liquid crystal display (LCD) 3D printers have become available at a very low cost of US$300, offering a resolution of 4K (3840 × 2160, ~ 8M pixel) and, for slightly more expensive models, 8K (7680 × 4320, ~33M pixels), significantly outperforming more costly DLP printers while only being available with 405 nm illumination.

LCD 3D printers have only recently been adopted and explored for research application[20–22], but have not been reported for printing of biomaterials.

Herein, we further analyze the challenges that prevented VP 3D printing of POMaC. We then formulate a POMaC ink (VP-POMaC) incorporating cross-linkers, photoabsorbers (PA), diluent, and porogens suitable for printing at a resolution tens-of-micrometers using very low-cost LCD 3D printers. The mechanical properties of prepolymer and polymerized VP-POMaC are characterized, including viscosity, hydrolytic degradation, compatibility of 3D printed constructs for 3D cell culture. Additionally, we fabricate complex POMaC constructs that were previously unattainable using conventional methods.

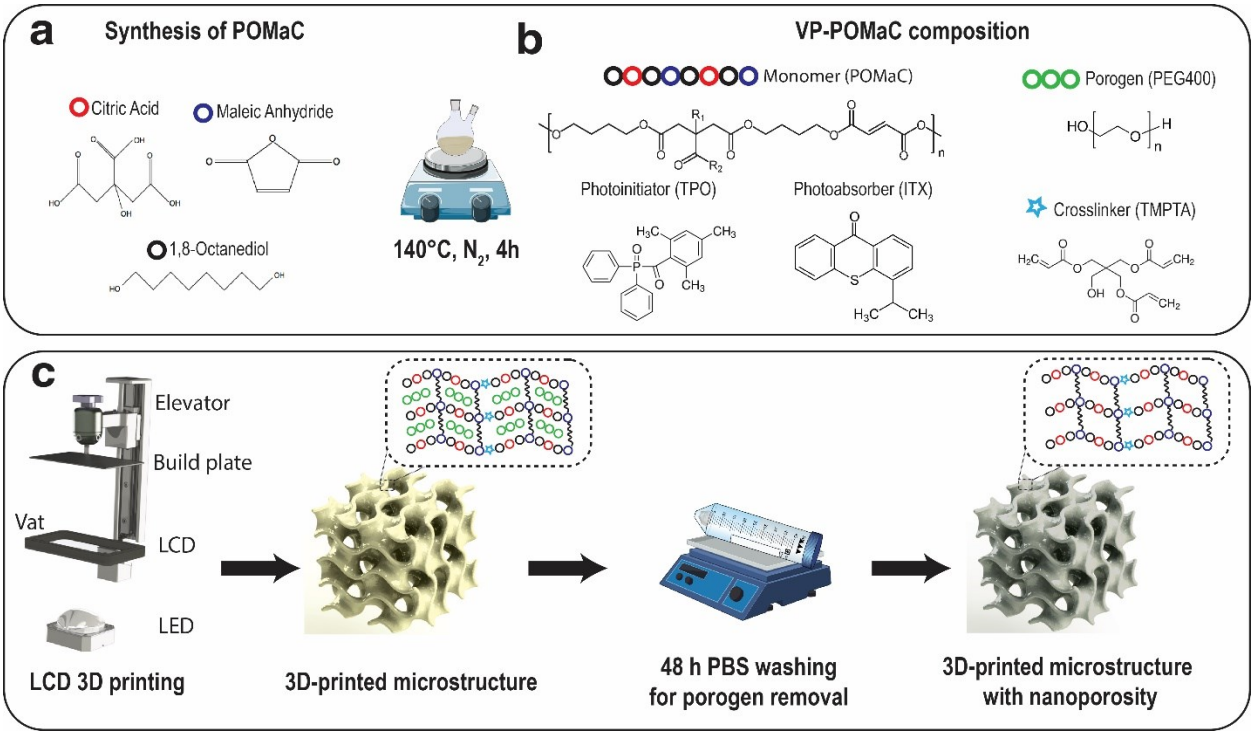

Figure 6.1 Schematic of the synthesizing and 3D printing process via LCD VP 3D printing. (a) POMAC prepolymer was synthesized by mixing three different monomers (citric acid, 1,8-octanediol, and maleic anhydride) at 140◦C for 4 h under N2 purge. **(b)** the VP-POMaC ink composition. **(c)** The fabrication process starts with LCD 3D printing of an object to achieve microporosity, followed by washing steps to remove the porogen to form nanoporosity.

6.4 Results

6.4.1 Characterization and Design Criteria for VP 3D printable POMaC

VP 3D printing of POMaC was challenging because of its low reaction kinetics and its high viscosity (>5000 cP), which, make it difficult to produce high-resolution structures, limit printing speed, and the ability to drain uncured ink from the prints, which collectively preclude its use for VP 3D printing. Indeed, slower reaction rate can lead to decreased resolution because of increased diffusion of the reactants.[23] Furthermore, it has been reported that a viscosity higher than 3000 cP is not suitable for VP 3D printing, as it would translate to an impractical vat-recoating period between layers of more than 1 min[24]. Additionally, the elasticity and comparatively low mechanical resilience of POMaC can cause damage to the 3D printed structure due to layer separation force.

In order to 3D print POMaC with an LCD VP 3D printer, we developed the VP-POMaC formulation depicted in **Figure 6.1** that meets the following criteria. (a) photocrosslinkable with high efficiency at the wavelength of 405 nm available in LCD VP 3D printers, (b) high absorbance at the same wavelength, (c) improved reaction kinetic compared to POMaC, (d) a lower viscosity to facilitate VP 3D printing and draining the uncured ink from microscale features, and (e) suitable biocompatibility for 3D cell culture. These criteria are important to ensure that VP-POMaC could be used effectively with an LCD 3D printer, and that the resulting 3D-printed structures would have the desired properties for tissue engineering applications.

A photoinitiator (PI) is required for VP 3D printing and for our purposes needs to be biocompatible, soluble in POMaC, and high absorption at 405 nm. Irgacure 2959 is commonly used as photoinitiator and was used with POMaC, but it has low absorption at wavelengths higher than 375 nm, making it unsuitable for use with 405 nm light. The requirement for sufficient

absorbance at 405 nm and low cytotoxicity narrowed down the available photoinitiator options to lithium phenyl-2,4,6-trimethyl benzoyl phosphinate (LAP), 2,4,6-trimethylbenzoyl)-phenylphosphine oxide (BAPO), and diphenyl (2,4,6 trimethylbenzoyl)phosphine oxide (TPO). LAP has the lowest cytotoxicity among these options, but it is not soluble in POMaC. Compared to BAPO, which is one of the most commonly used photoinitiators in VP 3D printing, TPO is less cytotoxic and has a less yellow color[25,26]. We thus used TPO, a type 1 photoinitiator that is readily soluble in POMaC at a high concentration (5% w/w). TPO has an absorption wavelength range of 380-425 nm, with a maximum absorption around 380 nm[27]. While not perfectly matched to the 405 nm light of commercially available 3D LCD printers, it nonetheless remains adequate for efficient polymerization of the POMaC ink. To improve the vertical resolution and prevent clogging of embedded conduits by uncontrolled light penetration through and scattering on cross-linked structures, a photoadsorber is required. We added isopropyl thioxanthone (ITX) as a photoabsorber as it exhibits very low cytotoxicity, and is suitable for tissue engineering applications[26,28].

Methacrylated/acrylated crosslinkers have been widely employed for free-radical-based polymerization in photosensitive inks. Trimethylolpropane triacrylate (TMPTA) has gained poularity as crosslinker due to its biocompatibility and the three double-bonds in its chemical structure, which increase the rate of double bonds in the ink and help to improve the reaction kinetics[29]. To facilitate free-radical-based polymerization of VP POMaC ink, we added 1% (w/w) of TMPTA (912 MW) and found that the gelation time was reduced from 11 s to 7 s . Importantly, TMPTA does not significantly change the mechanical properties of POMaC, so the 3D-printed material retains its desired mechanical behavior even after TMPTA has been added.

The high viscosity of POMaC is an obstacle to 3D printing, and needs to be reduced by either heating in the vat[30,31] or by adding a diluent (*i.e.,* a thinner as is used in paint or polish) to the ink[32,33]. Heating POMaC during the polymerization process could affect its stability and reactivity due to its dual crosslinking characteristic. The diluent is thus the preferred approach but it must be non-reactive and not participate in the crosslinking reaction, while it must leach out after polymerization. For example, reactive diluents such as PEGDA700 help reduce viscosity[19], but they participate in the crosslinking reaction. Prior works have shown that non-reactive diluents such as PEGDME could also enhance nutrient and oxygen exchange by forming nanopores into POMaC polymer scaffolds[11,34]. This allows for the production of 3D-printed parts with nanoporosity, which can be beneficial for tissue engineering applications. Hence, we explored the possibility of incorporating polyethylene glycol (PEG) with a molecular weight of 400 a miscible non-reactive material into the ink solution with the expectation that it would reduce viscosity, could be readily leached out after 3D printing thanks to its low molecular weight, and that it would also act as a porogen. PEG is less viscous and expected to be less toxic than PEGDME, which has an ether group. Indeed, PEG is also FDA-approved, water-soluble, and non-toxic and has been used in numerous biomedical and pharmaceutical applications.

By incorporating all the components introduced so far, we developed an optimized ink, VP-POMaC, which was composed of POMaC as the monomer, PEG400 as the porogen and diluent, TMPTA as the crosslinker, TPO as the photoinitiator, and ITX as the PA. We successfully 3D-printed transparent elastomeric microfeatures using VP-POMaC (**Figure 2**). The final construct is obtained after incubating it overnight in 70% ethanol to remove the porogen and unreacted ink components, turning the parts from translucent when freshly printed to their final transparent state.

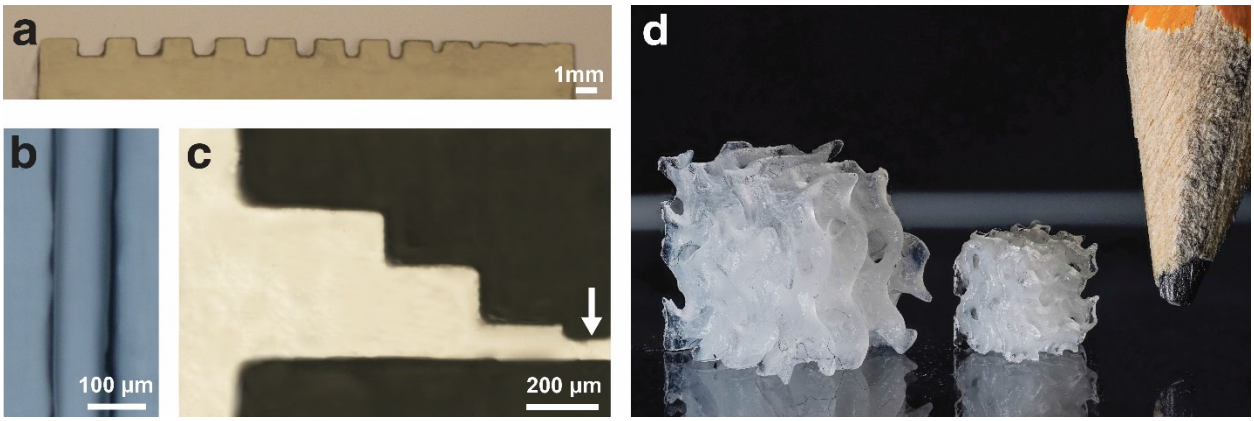

Figure 6.2. 3D constructs made by VP-POMaC ink illustrating its printability. (a) Side view of an array of 3D-printed open channels with different dimensions. **(b)** Top-view microscopy image of 3D-printed open channels as small as 100 µm. **(c)** Top-view microscopy image of 3D-printed features as small as 80 µm (white arrow). **(d)** Isometric view of 3D-printed complex gyroid structures with different dimensions. Objects in **(a-c)** were 3D-printed using 40% porogen, while the objects in **(d)** were 3D-printed using 50% porogen.

The LCD 3D printer used in this study has a footprint of 143 × 90 mm2 with a projected pixel size of 35 × 35 µm2 and 2.5 mw/cm2 power intensity. The printing parameters were optimized for producing detailed prints on a footprint approximating the one of a 96-well plate within a few minutes. While DLP-based 3D printers offer sharper pixel edge resolution and higher light intensity, LCD 3D printers are more affordable, have more pixels, and larger printing area. VP-POMaC is also compatible with DLP printers, and 3D structures were printed with shorter exposure times thanks to the higher light intensity of these printers (**Figure 6.S1, Supporting Information**). VP relies on a low adhesion membrane to minimize print failure, and fluorinated ethylene propylene (FEP) membranes are commonly used. Here, to further reduce the separation force, we used a perfluoroalkoxy (PFA) membrane that has a higher tensile strength. This allowed the printed layers to detach more easily and minimized the risk of damaging small features during printing. The layer thickness of 20 µm, in conjunction with a layer exposure time of 50 s, facilitates the production of a smooth surface finish with minimal layer artifacts. After separation in each

layer, the resting time of 2 s ensured complete ink recoating during the 3D printing process. Furthermore, the retraction speed was set at a low value of 80 mm/min to reduce the separation force that is proportional to the speed.

In VP 3D printing, the effective Z resolution for overhanging structures is mainly dictated by the penetration depth of light and the reaction kinetics of the ink. The light penetration in the ink can be characterized by measuring the thickness of polymerized ink for different exposure times (**Figure 5.S2, Supporting Information**). Although the exposure time required for curing each layer was reduced from 120 s to 50 s by adding TMPTA, it is still relatively long compared to commonly used non-elastomeric inks. This longer exposure time can lead to the diffusion of free radicals, which can affect the XY resolution of the 3D-printed structures. We evaluated the 3D printing resolution by printing open channels separated by 500 μm gaps with widths ranging from 50 μm to 500 μm in steps of 50 μm. The 50 μm channel was blocked, and the smallest successful 3D-printed channel was measured to be 110 μm, as shown in Figure 2a-b. The blockage of the 50 μm channel may have been caused by the scattering of light, the diffusion of free radicals generated during the reaction, or both. Previous research has investigated the potential impact of reactant diffusion and light scattering on the loss of resolution that is commonly observed in VP 3D printing35,36. Additionally, we successfully 3D-printed positive surface features with dimensions as small as 80 μm (**Figure 5.2c, Figure 5.S3, Supporting Information**). By using the VP-POMaC with 50% porogen and optimized exposure time in our 3D printing process, we successfully fabricated complex structures such as the gyroid with features as small as 100 μm (Figure 2d). The gyroid illustrates the capabilities of VP-POMaC and LCD printers for making elastic objects with nanoporosity and intricate microscale geometries that cannot be made by extrusion-based 3D printing or molding of POMaC.

6.4.2 Effect of porogen on printability, and on mechanical properties of VP-POMaC Ink

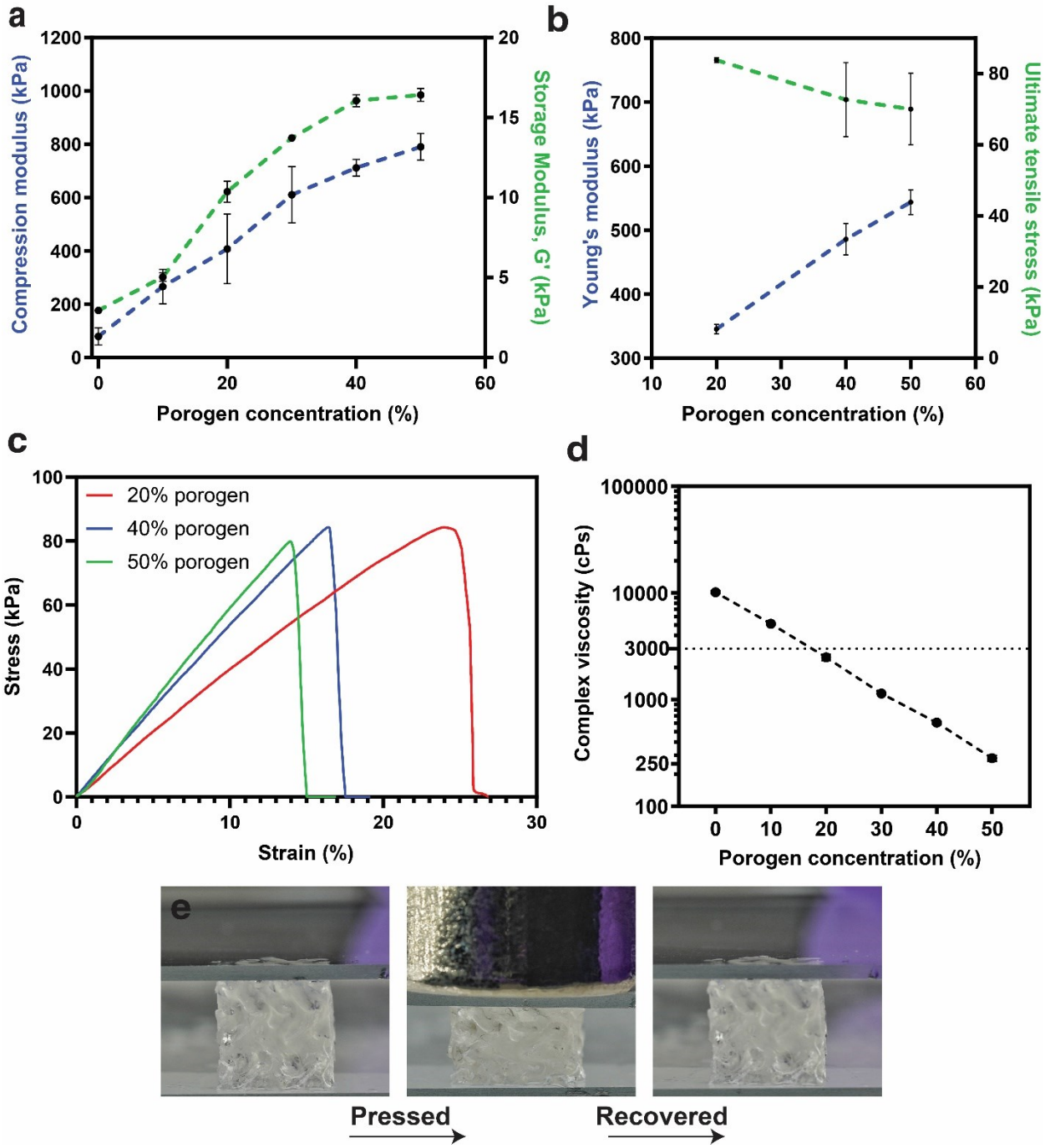

Figure 6.3. Effect of porogen on the mechanical properties of photocured POMaC. (a) Compression and final storage modulus for VP-POMaC with different concentrations of PEG porogen. **(b)** Young's modulus and ultimate tensile stress for VP-POMaC with different concentrations of porogen. **(c)** Representative stress–strain curves of samples 3D-printed with VP-POMaC prepared with various

concentrations of PEG. **(d)** Viscosity for different concentrations of PEG porogen. Error bars represent standard deviations. Representative of three independent experiments (N = 3). **(e)**. Images of a 3D-printed gyroid before, while under load, and after recovery.

We investigated the effect of porogen concentration on the mechanical properties of VP-POMaC using photorheology, compression, and tensile testing. It should be noted that due to the high viscosity of POMaC at concentrations lower than 20% of porogen, preparing samples for tensile testing was challenging, as the elevated viscosity made it difficult to 3D print the material. In contrast, photorheology is compatible with high-viscosity materials, and compression tests necessitate only small disc samples, which can be feasibly produced. As a result, tensile testing was only conducted for porogen concentrations within the 20-50% range, while photorheology and compression testing were conducted for concentrations of 0-50%. Unexpectedly, VP-POMaC with increasing porogen exhibited increasing compression (max. 790 kPa), storage (max. 16.42 kPa), and Young's modulus (max. 543 kPa) with maximal values found for the maximum porogen concentration of 50% tested in this study. Both compression and photorheology tests confirmed that formulations with a higher concentration of porogen had a higher modulus (**Figure 6.3a**). Specifically, the compression modulus increased from 80 kPa to 790 kPa as the porogen concentration increased from 0% to 50%. Tensile testing exhibited a similar trend (**Figure 6.3b**). Additionally, we observed that increasing the porogen concentration resulted in a more brittle material (**Figure 6.3c and Figure 6.S4, Supporting Information**). Our findings are in agreement with previously reported results on the effect of porogen concentration on the mechanical properties of elastomers[37].

Here, the porogen is primarily utilized as a viscosity-reducing agent to enhance printability. By introducing 50% PEG porogen, the viscosity of POMaC can be reduced from 10136 cP to 282 cP. (**Figure 6.3d**). We found PEG concentrations of 40% and 50% to be optimal for printing as

the reduced viscosity both facilitates that back-and-forth movement of the build plate and the post-printing cleaning, which involves the rinsing and drainage of residual ink, while it also leads to faster photoreaction kinetics.

The increased rigidity within increasing porogen observed in 3D-printed samples may be attributed to several factors. The decreased viscosity of VP-POMaC at higher porogen concentrations may enhance reaction speed due to improved mobility of reactive species. This increased mobility can lead to a higher probability of encounters between reactive species, resulting in a faster curing reaction and ultimately forming a more densely crosslinked network. Moreover, material shrinkage resulting from porogen removal after curing could contribute to an increase in the density of the polymer network. This observation is in agreement with the photorheology and swelling results presented in the subsequent sections. In-depth investigations, beyond the scope of this paper could offer additional insights into the underlying factors responsible for the observed increase in rigidity. In this study, we focused on the effects of porogen concentrations ranging from 0% to 50% on the mechanical properties of the VP-POMaC. It should be noted that this study did not investigate porogen concentrations higher than 50%; future research could explore the impact of higher porogen concentrations on the material's properties.

Our findings indicate that the mechanical properties of the VP-POMaC material can be tailored by adjusting the porogen concentration to potentially suit various tissue engineering applications. The storage modulus values, ranging from 2.94 kPa to 16.42 kPa with increasing porogen concentration from 0% to 50%, encompass the desired range for tissues such as skeletal and heart muscle tissues (6-25 kPa)[39–41]. However, it is higher than the range for brain tissue (0.1-1 kPa)[42] and liver tissue (0.5-3 kPa)[43].

6.4.3 Effect of porogen on the crosslinking rate of VP-POMaC

To investigate the impact of PEG porogen and TMPTA on POMaC's gelation time, we conducted photorheology tests to measure the storage modulus (G') and loss modulus (G") during UV light exposure. The gelation time was determined by the point at which G' crossed over G", indicating the material's transition from a gel to a solid state. Before crosslinking induced by UV light (<15 s), the G' and G" values were stable (**Figure 6.4a**). The addition of 1% TMPTA significantly reduced the gelation time from 11 s to 7 s in the photorheometer, illustrating the influence of low concentrations of the TMPTA crosslinker with three double bonds on reaction kinetics. This has notable benefits for 3D printing, where rapid polymer crosslinking during printing is desirable. The effect of porogen concentration on the crosslinking rate of the polymer is also considerable, as illustrated in **Figure 6.4b**. Increasing the porogen content exhibited a clear acceleration in crosslinking rate. This may be attributed to the significantly lower viscosity of the VP-POMaC ink at higher porogen concentrations (**Figure 6.3d**), which enables greater potential for increased free radical diffusion coefficient, resulting in a more pronounced impact on the crosslinking rate. The same underlying mechanism could explain the correlation observed between mechanical properties and porogen concentration.

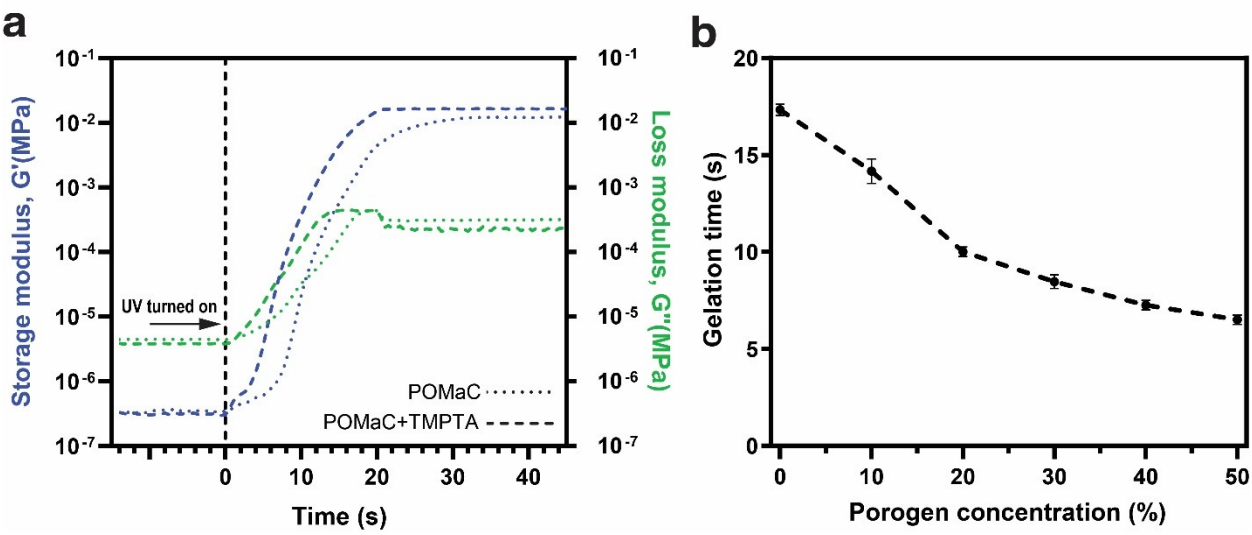

Figure 6.4. Crosslinking rate, gelation time of POMaC and VP-POMaC. (a) time sweep photorheology measurements of POMaC and VP-POMaC ink both with 40% porogen. The addition of TMPTA in the VP-POMAC ink formulation resulted in a decrease in gelation time from 11 s to 7 s as compared to the ink formulation without TMPTA. **(b)** Gelation time under UV illumination for different concentrations of porogen. The gelation time is reduced when the concentration of porogen is increased.

6.4.4 In vitro swelling and degradation

Biocompatible inks with low swelling/ shrinkage ratios (<50%) are favorable for tissue engineering and wound healing applications[44] as a low swelling ratio is essential for maintaining the architecture and fidelity of 3D-printed microstructures under physiological conditions. The swelling behavior of VP-POMaC inks was characterized by incubating them in PBS for up to 7 d. As shown in **Figure 6.5a**, the shrinkage increased for samples with higher concentrations of porogen. This could be ascribed to the higher porosity of samples with porogen which leads to higher water uptake. Notably, the shrinkage for all concentrations remained below 25%, indicating a low level that is suitable for tissue engineering applications.

Biodegradability is essential for tissue-engineered scaffolds, and the rate of degradation requires to match the tissue formation rate, to finally replace the regenerated tissue. Hence, the long-term performance of scaffolds *in-vivo* is strongly dependent on the degradation rate. The

polymer molecular structure and composition have a critical impact on the degradation rate. The ester bonds in the POMaC backbone are hydrolytically degradable, and depending on their relative content, they mediate controlled degradation rates[37,44]. When exposed to physiological conditions, POMaC degrades via surface erosion, a process that sequentially breaks the ester bonds between monomers.

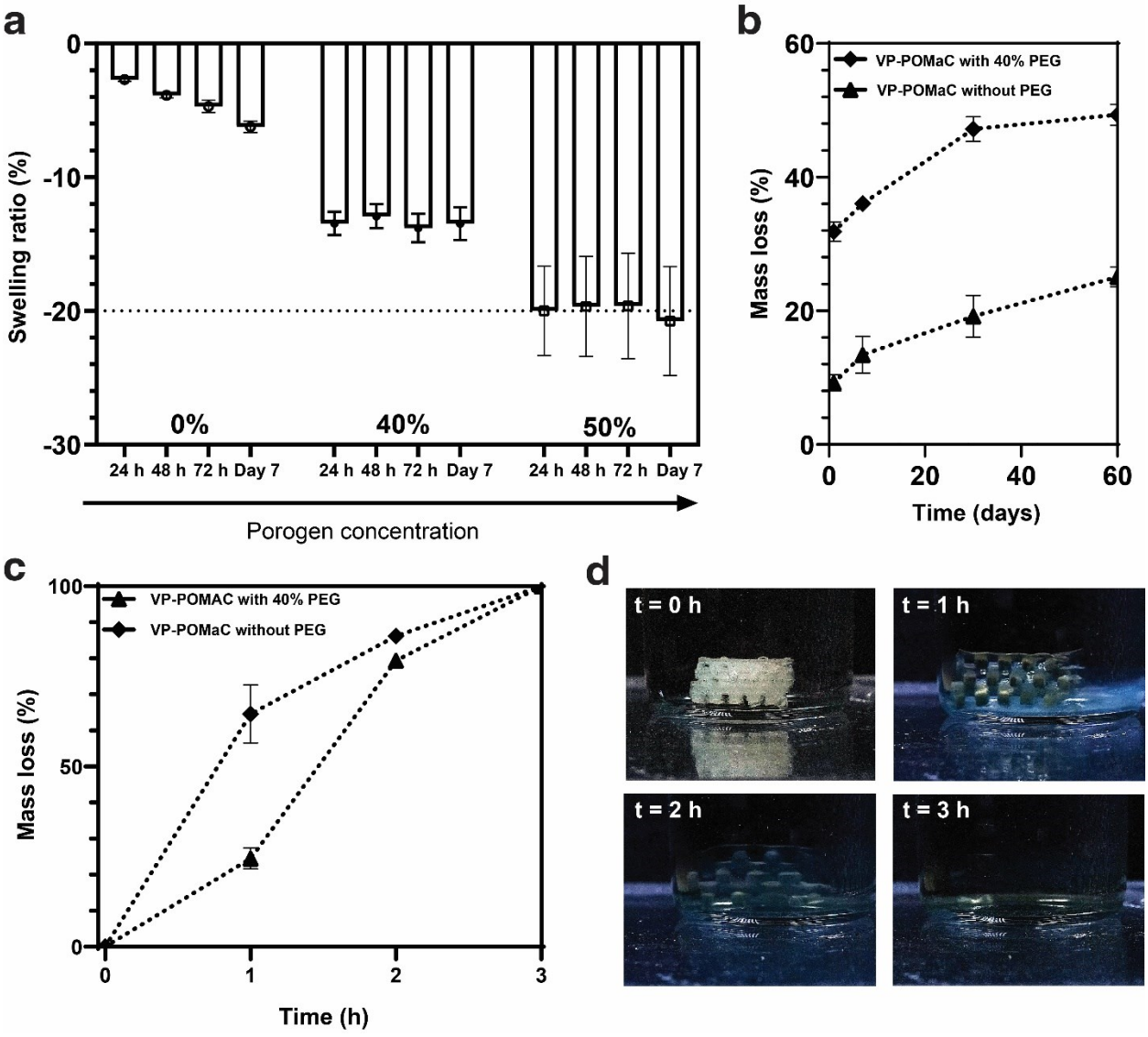

Figure 6.5. ***In-vitro*** **swelling and degradation of VP-POMaC. (a)** Swelling ratio over a week in PBS solution. **(b)** mass loss of VP-POMaC disks without porogen and with 40% porogen in PBS solution at 37°C over 60 days and **(c)** accelerated mass loss in 0.25M NaOH solution Representative of three

independent experiments (N = 3). **(d)** hydrolytic degradation via surface erosion of 3D printed woodpile structure with 40% porogen over time in 0.25 M NaOH solution (**See Video S2, Supporting Information**).

To investigate the *in-vitro* degradation of VP-POMaC, we fabricated disks via 3D printing and incubated them in phosphate-buffered saline (PBS) buffer (pH 7.4) and 1M NaOH at 37° C. As shown in **Figure 6.5b**, the samples containing 40% porogen experienced significant weight loss in PBS compared to pure VP-POMaC. The rate of degradation significantly slowed down after day 1, and samples with PEG porogen exhibited 50% mass loss after 60 days. The initial mass loss (~10%) is associated with soluble low molecular weight chains in the polymer, while the additional mass loss in the porous VP-POMaC samples is due to the leaching of water-soluble PEG porogen.

Polymers that contain ester linkages, such as POMaC, are more susceptible to hydrolytic degradation in the presence of NaOH (sodium hydroxide) which hydrolyses the ester groups and can speed up degradation. We investigated the accelerated degradation of POMaC at a concentration of 0.25 M sodium NaOH solution. 3D-printed structures were immersed in 0.25 M NaOH solution at room temperature with no agitation. The VP-POMaC samples completely degraded and dissolved after 3 h in an aqueous base solution (**Figure 6.5c, Supplementary Video S2**). **Figure 6.5d** shows the dissolution as time progresses. Most of photocurable inks are derived from acrylates and epoxides that are difficult to degrade once crosslinked. 3D printable materials such as POMaC can address the concerns about pollution issue for VP inks that are of increasing concern as 3D printing becomes more widely adopted.

6.4.5 Cytocompatibility and 3D cell culture

POMaC has been widely used for cell-based applications which require a high level of biocompatibility. As unreacted POMAC ink components remain in the 3D-printed part and are cytotoxic, extensive post-printing washing is needed to eliminate all unreacted residues prior to

cell culture. The washing step is also necessary for the pore formation via extraction of the porogen component. To achieve optimal biocompatibility and porosity, 3D-printed POMaC samples were washed with PBS and 70% EtOH for at least 48 h to remove any residual porogen and unreacted ink components. Throughout the washing process, we alternated the wash buffer between PBS and 70% EtOH every 12 h to best utilize POMAC's distinct swelling behavior in each buffer.

VP-POMaC was tested for cytocompatibility using the human lung fibroblast cell line (IMR-90) and human umbilical vein endothelial cells (HUVEC). The cell lines were chosen for their wide usage in research, as well as for their intolerance of sub-optimal culturing conditions. The cytocompatibility assays were performed in compliance with International Organization for Standardization (ISO) standards (10993-5:2009) for the development of medical devices. According to ISO 10993-5:2009 standard, the 3D-printed POMaC samples were post-treated with the above-mentioned washing process and directly co-cultured with our model cell lines in a 96-wellplate. In addition to a cell-only control condition, a previously developed POMaC formulation[34] was used as a cytocompatibility benchmark. Microscopy images and quantitative cell viability measurements via PrestoBlue™ were taken every 24 h for a time course of 3 days. As shown in **Figure 6.6a-d**, we observed that HUVECs and IMR-90 co-cultured with VP-POMaC or the benchmark POMaC formulation were morphologically indistinguishable compared to the cell-only control condition. Furthermore, the quantified cell viability (normalized to cell-only control) showed excellent biocompatibility (>80% for all time points) of both VP-POMaC and the benchmark POMaC formulation.

In addition, we cultured HUVEC cells on a 3D-printed cylindrical lattice gyroid structure as a demonstration of cell-populated 3D-printed POMaC structures for prospective tissue engineering applications. The scaffold was designed with voids with a minimum diameter of 200

μm. To enable cell attachment, the 3D-printed VP-POMaC structure was incubated in cell culture media supplemented with 40 μg/mL collagen I overnight at 4°C. The morphological characterization shows a satisfactory cellular adhesion to the scaffold, as illustrated in **Figure 6.6d-f**. In 3D culture, cells were found to proliferate throughout the entire scaffold for pore sizes between 200-400 μm. The scaffold exhibits autofluorescence in the green channel, which aids in visualization of its topography and of cell attachment. In summary, VP-POMaC ink shows good biocompatibility, cell adhesion and proliferation, making it a promising candidate for various tissue engineering applications.

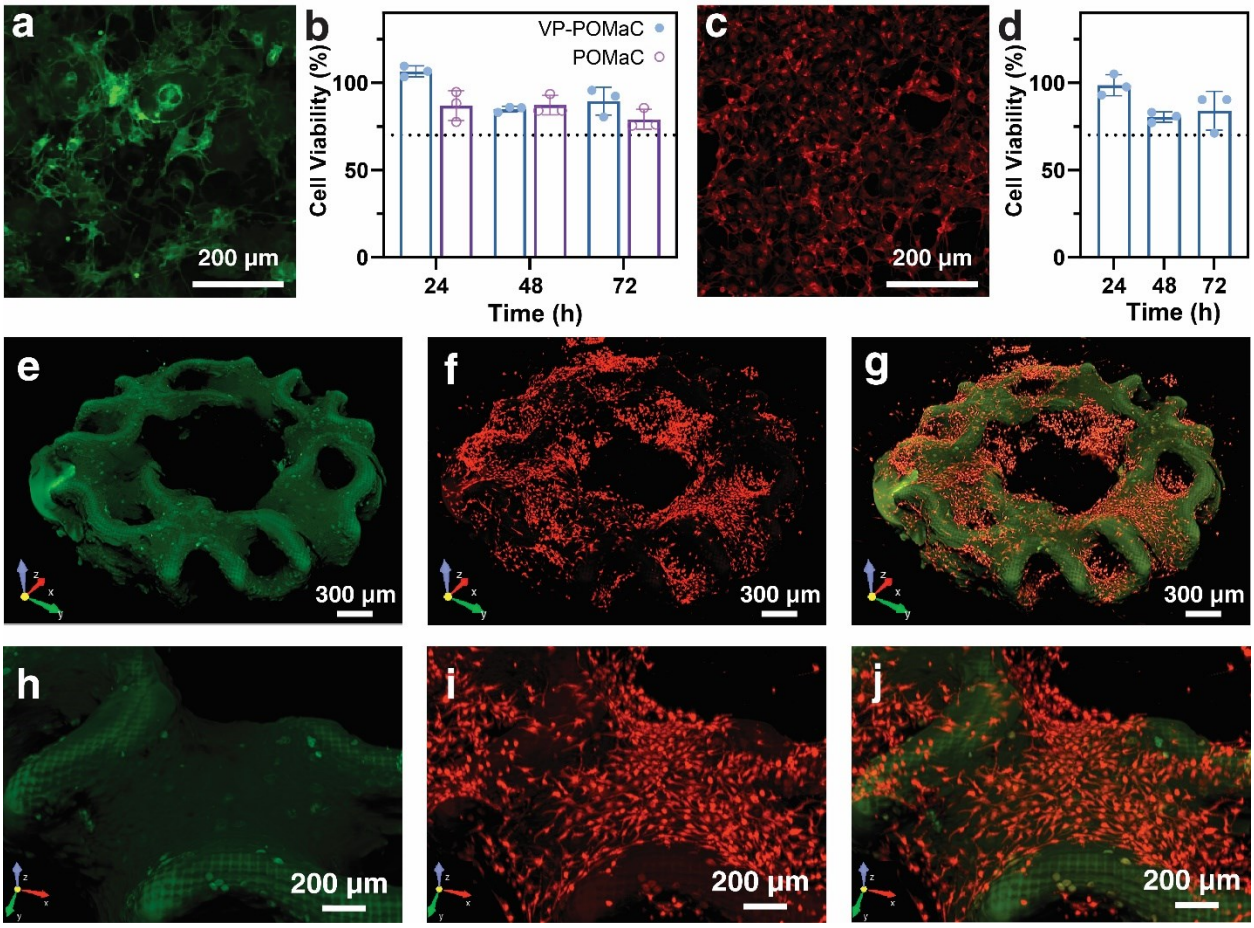

Figure 6.6. 3D cell culture on VP-POMaC scaffold. (a) Fluorescence images of GFP labelled IMR-90 human lung fibroblast cells following 48 h culture in a wellplate in presence of VP-POMaC. **(b)** IMR-90 cell viability when cultured with VP-POMaC or POMaC for up to 3 d. **(c)** Fluorescence image of mCherry-

labelled HUVEC cells following 48 h in a wellplate in the presence of VP-POMaC. **(d)** HUVEC Cell viability for 3 d. **(e-f)** 3D confocal microscopy images of HUVEC cells (red) cultured and adhered on an autofluorescent cylindrical gyroid scaffold (green) along with close-up images **(h-i)** A close-view of cultured HUVEC cells (red) reveals cellular proliferation on the scaffold (green).

6.5 Discussion and Conclusion

3D printing has transformed tissue engineering, offering unprecedented freedom in designing and fabricating intricate microstructures that are challenging to create using traditional fabrication methods. The use of elastic, biodegradable materials is desirable for many tissue engineering applications, and POMaC has emerged as a candidate material but has been difficult to shape by 3D printing. Here, we introduced VP-POMaC and the use of DLP and low-cost LCD printers for the fabrication of complex scaffolds that were unattainable with previous fabrication methods for POMaC.

This presents a notable breakthrough in the 3D printing of POMaC, achieving a resolution down to tens of microns with the smallest feature printed at 80 μm. The optimized exposure time of 30 s to 50 s per 20 μm layer constitutes a major improvement over the 4 min crosslinking time (per layer) required in previously reported manual stamping processes, which also entailed labor-intensive manual alignment and multiple masks for each scaffold, ultimately extending the total scaffold fabrication time to a day. The DM process for POMaC 3D printing is largely automated, eliminating the need for expensive equipment and manual labor while also enabling faster design iteration. In addition to the faster fabrication time, using this approach allows for the fabrication of more complex scaffolds, such as gyroid structures that were previously impossible to create. These complex scaffolds can be utilized in various tissue engineering and organ-on-a-chip (OoC) applications that demand precise designs.

By reducing the gelation time from 11 s to 7 s as measured by photorheology, adding a crosslinker with three double bonds, and decreasing the viscosity using PEG porogen, we successfully adapted POMaC for VP printing on the low-cost LCD 3D printer. The resulting POMaC constructs exhibit high biocompatibility (>80% cell viability) with fibroblast and endothelial cells. Their mechanical properties can be tailored to suit specific tissue engineering needs with a range of storage moduli (2.94-16.4 kPa) and compression moduli (79.3 - 790 kPa) suitable for various applications, such as skeletal and heart muscle tissues. This controllability of mechanical properties offers the potential to create biomaterials that more accurately recapitulate the tissue-specific biomechanical microenvironments, thereby enhancing the prospective efficacy of tissue engineering approaches. Additionally, this flexibility in the mechanical profile of the material broadens its application spectrum in non-biomedical fields. Moreover, compatibility with both DLP and low-cost 3D LCD printers (available for under $300) will open up new opportunities for VP-POMaC, tissue engineering, and VP printing,

Future work will be needed to investigate the effect of PEG porogen on the pore size, resolve the low printability at lower porogen concentrations, and validate or improve the bioink for high-resolution 3D printing down to the sub-ten-micrometer scale necessary for reproducing small embedded vasculature networks that correspond to the size range of capillaries. Beyond tissue engineering, the 3D-printed POMaC constructs also hold promise for use in wearables, soft robotics and possibly flexible electronics thanks to its biocompatibility and tunable elastomeric properties. Hence, the convenient and rapid fabrication of biodegradable, biocompatible, and elastic microstructured POMaC constructs using an affordable LCD 3D printer creates a wealth of opportunities not just for tissue engineering, implants, and organ-on-a-chip, but also for wearables and soft robotics.

6.6 Materials and Methods

3D printing

All objects were designed in SolidWorks, exported as "STL" files, and 3D-printed with a ELEGOO Mars 3 LCD 3D printer (ELEGOO, China) with a 35 μm pixel size and 4K monochrome LCD. All objects reported in this work are printed with a layer thickness of 20 μm and an exposure time of 50 s at a light intensity of 2.2 mW/cm^2. Immediately after printing, to remove unpolymerized ink, objects were washed with 70% EtOH (Fisher Scientific, Saint-Laurent, Quebec, Canada) several times, and dried under a stream of pressurized nitrogen gas. Then, the objects were immersed in 70% PBS for 48 h to remove the residual ink and porogen.

Synthesis of POMaC

Poly(octamethylene maleate (anhydride) citrate) (POMaC) was synthesized as described previously[46]. Briefly, maleic anhydride, citric acid, and 1,8-octanediol were mixed in a two-necked round bottom flask at a 2:3:5 molar ratio and melted at 160 °C under nitrogen purge, and the mixture was stirred for 2 h. The resultant prepolymer was then dissolved in 10 ml 1,6-dioxane and purified through drop-wise precipitation in deionized distilled water. Then the collected polymer was concentrated and dried under airflow for two days and stored at 4°C. Following drying, the prepolymer was analyzed using FT-IR spectroscopy (**Figure 6.S8, Supporting Information**), and the obtained data was consistent with the spectra reported in prior studies[15,19].

Formulation of VP-POMaC ink

Purified POMaC was mixed with a PEG (no. 202398; Sigma-Aldrich), which is miscible with both POMaC and water and has a low molecular weight, allowing it to be leached out after crosslinking of the polymer. Different concentrations of PEG, spanning from 10% (w/w) to 50%

(w/w), were used to quantify the effect of porogen on the mechanical, and reaction kinetic characteristics of the ink. TMPTA (no. 412198; Sigma-Aldrich) at a concentration of 1% (w/w) was added to the ink to decrease the onset time by providing more acrylate groups.

The PI, TPO (no. 415952; Sigma Aldrich), was mixed with the POMaC/PEG solution at a 2 % (w/w) concentration, after preliminary experiments were conducted to identify a concentration that produced prints of adequate resolution (i.e., lower concentrations did not consistently produce prints with satisfactory resolution, while higher concentrations did not necessarily cause any improvement). To assist in mixing the PI into the solution, the solution was heated on a hot plate at 60-90 °C for 2-5 min and then mixed for 30-120 min, depending on the progress of mixing. The other component of the ink was a PA, ITX (no. TCI0678; VWR International) was mixed with the ink at a concentration of 0.8% (w/w).

Videos and image stacking

Videos and images were captured using a Panasonic Lumix DMC-GH3K and Sony α7R III. Focus stacking was performed using Imaging Edge Desktop (Sony Imaging Products & Solutions Inc., Japan) to obtain a sequence of images at various focal planes. The images were then processed using CombineZP (available at https://combinezp.software.informer.com/). Microscale imaging was conducted on a Nikon Eclipse LV100ND inspection microscope at 5x magnification. Some images were captured using a Leica SMZ-8 stereo microscope equipped with a Lumix GH3 DSLR digital camera from Panasonic.

Photorheology

A Discovery HR-2 rheometer (TA-Instruments, DE, USA) was used in conjunction with the ultra-violet (UV) accessories to investigate the effect of porogen, and TMPTA on the storage

and loss moduli and the gelation time of the ink. A volume of 200 µL was added on the bottom plate of the rheometer and a time sweep test was performed while the sample was exposed to UV radiation for 45 s. The UV light intensity was set at 20 $mW.cm^{-2}$. The time sweep test was conducted at room temperature using a torsional frequency of 1 Hz and torsional strain of 1%. The experiment was performed for different study groups and the storage and loss moduli was recorded to find the onset time as well as the gelation time, i.e., the intersection of the loss and storage moduli curves.

Compression and tensile test

Disk-shaped samples were 3D-printed with a diameter of 10mm. The samples were then washed in 70% EtOH (Fisher Scientific, Saint-Laurent, Quebec, Canada) for 48 h before the compression test. A dynamic mechanical analyzer (DMA, Q800 TA-Instruments, DE, USA) was employed to quantify the compression modulus of the crosslinked samples. Tensile testing was carried out using an Instron 3360 electronic universal testing machine (Instron corporation, MA, USA).

Swelling/shrinkage

Disk-shaped samples were prepared similarly to samples for compression tests. All the samples were weighted after crosslinking. The samples were then soaked in PBS 1x and shaken over an orbital shaker for certain time periods up to 3 weeks. At each time point, the samples were removed from PBS, weighed, and resoaked in PBS for the next time point. The solution was changed at every time point to avoid saturation.

***In-vitro* degradation**

Three disk-shaped samples, each with a diameter of 8 mm and a thickness of 3 mm, were fabricated for performing degradation in PBS 1x and 1M NaOH at 37°C. After crosslinking, the samples were frozen at -80°C for 24 h and then lyophilized for 72 h using a ModulyoD 5L freeze dryer (Thermo Fisher Scientific) at 290 ± 10 μbar and room temperature. The samples were then weighed and soaked in PBS 1x or 1M NaOH for different time periods up to 8 weeks and 3 h, respectively. At each timepoint, a set of samples was collected, and the media was changed for other samples. At the final point, all samples were frozen, lyophilized, and weighed to find the remaining weight fraction.

Penetration depth measurements

In order to measure the penetration depth of light, a drop of the formulation was placed on a glass slide and exposed to different exposure times at a light intensity of 2.2 mW/cm^2. After rinsing uncured ink with 70% EtOH, we measured the thickness of patterned regions using a stylus profilometer (DektakXT, Bruker Co.).

Cell culture

The normal human fibroblast cell line IMR-90 (ATCC CCL-186) expressing the fluorescent protein GFP was cultured in Dulbecco's Modified Eagle Medium (Gibco, USA) containing 4.5 g/L D-glucose, 4.5 g/L L-glutamine, and 110 mg/mL sodium pyruvate. The media was further supplemented with 10% FBS and 1% penicillin-streptomycin (Gibco, USA). All cell lines were incubated at 37ºC with 5% CO2 supplementation. Human umbilical vein endothelial cells (HUVEC) expressing the fluorescent protein mCherry were kindly provided by Dr. Arnold Hayer of McGill University[46]. HUVEC cells were cultured in EGM-2 media (Lonza, USA). The cells were grown and passaged according to ATCC's recommendations.

Cytotoxicity Testing

The cytocompatibility assays were performed in compliance with International Organization for Standardization (ISO) standards (10993-5:2009) for the development of medical devices. POMaC disks with a thickness of 800 μm were made by UV curing 150 μL of VP-POMaC ink in a PDMS-coated 24-well plate. The disks washed for at least 72 h in PBS and EtOH to leach out any unreacted ink, as well as the porogen. IMR-90 cells were seeded in a 24-well plate at a seeding density of 10k per well. Immediately after cell seeding, post-treated POMaC disks were placed directly on top of the cell layer. As controls, cell-only wells, as well as cells co-cultured the literature POMaC formulation were seeded with the same cell density. Quantitative cell viability measurements via PrestoBlue™ (Thermofisher, USA) were taken every 24 h for a time course of three days. Microscopy images were taken daily using a Ti2 inverted microscope and analyzed using NIS-Element (Nikon, Japan). Three biological replicates were done for each of the three above-mentioned conditions. For the PrestoBlue™ cell viability assay measurement, two technical replicates were performed for each biological repeat.

3D Co-culture of POMaC and HUVEC

3D-printed POMaC structures were post-treated as described above. Additionally, they were incubated in cell culture media supplemented with 40 μg/mL collagen I overnight at 4 degrees Celsius to enable cell attachment to the surface of the structure. Trypsinized HUVEC cells were washed once in PBS, resuspended in EGM-2 media at a concentration of $1x10^6$ cells/mL, and supplemented with 10% growth factor reduced Matrigel® (Corning, USA). HUVECs were seeded in droplets onto the air-dried POMaC structure and incubated in the cell culture incubator for 1 h to allow cell attachment. Afterward, the POMaC structure was flipped upside-down, and the seeding was repeated for the opposite side. Finally, the co-culture was carefully transferred into

an ultra-low attachment 96-well microplate (Corning, USA) and cultured in EGM-2 media for at least 24 h prior to confocal imaging.

Fourier Transform Infrared (FT-IR)

To evaluate the synthesizing process, FTIR (Thermo-Scientific Nicolet 6700, Waltham, MA, USA) was conducted on the prepolymer and VP-POMaC (**Figure 6.S8**, Supporting Information).

Data analysis

The error bars displayed in the figures represent the standard deviation. GraphPad Prism 9 was used for data analysis.

6.7 Supplementary Information

6.7.1 Supplementary Videos

Video S1. Flexible gyroid structure

A flexible gyroid structure 3D-printed with VP-POMaC (40%) under load without a change in the shape.

Video S2. VP-POMaC degradation in NaOH

Rapid degradation of VP-POMaC at different NaOH concentrations

6.7.2 Supplementary Figures

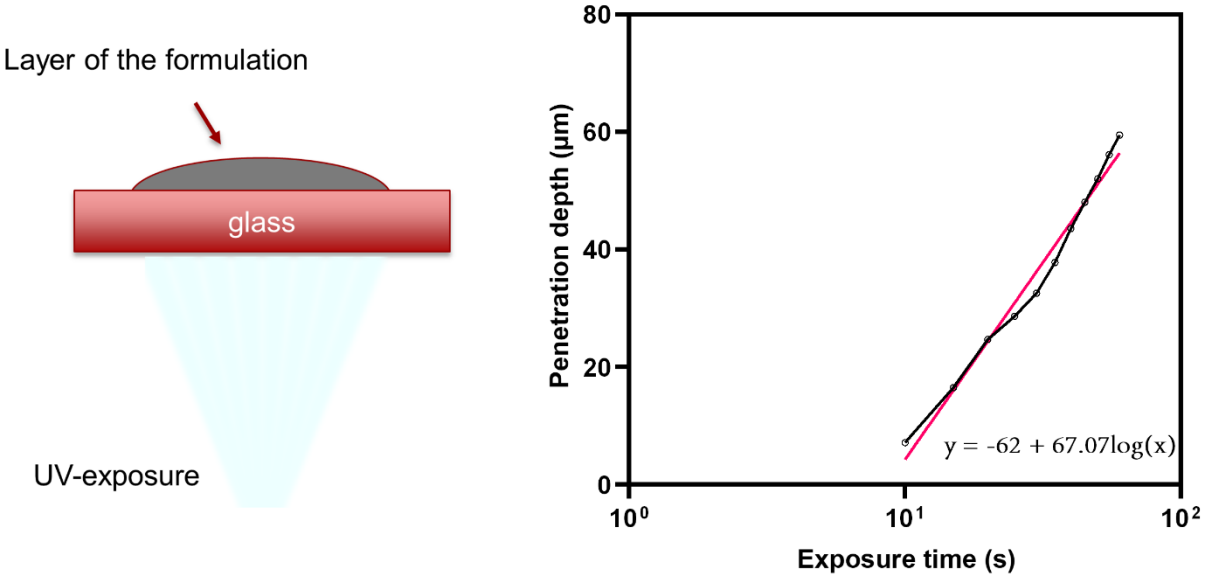

Figure 6.S6.7. Penetration depth characterization of the VP-POMaC with 40% PEG porogen.

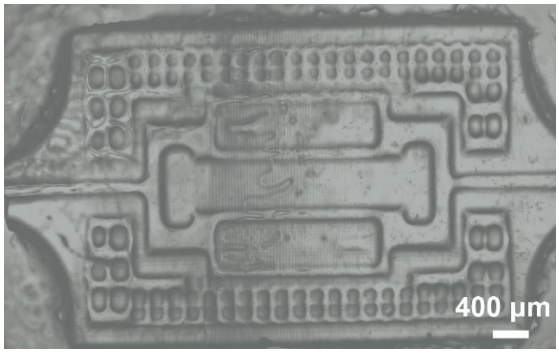

Figure 6.S6.8. 3D-printed Angiochip scaffold with open channels.

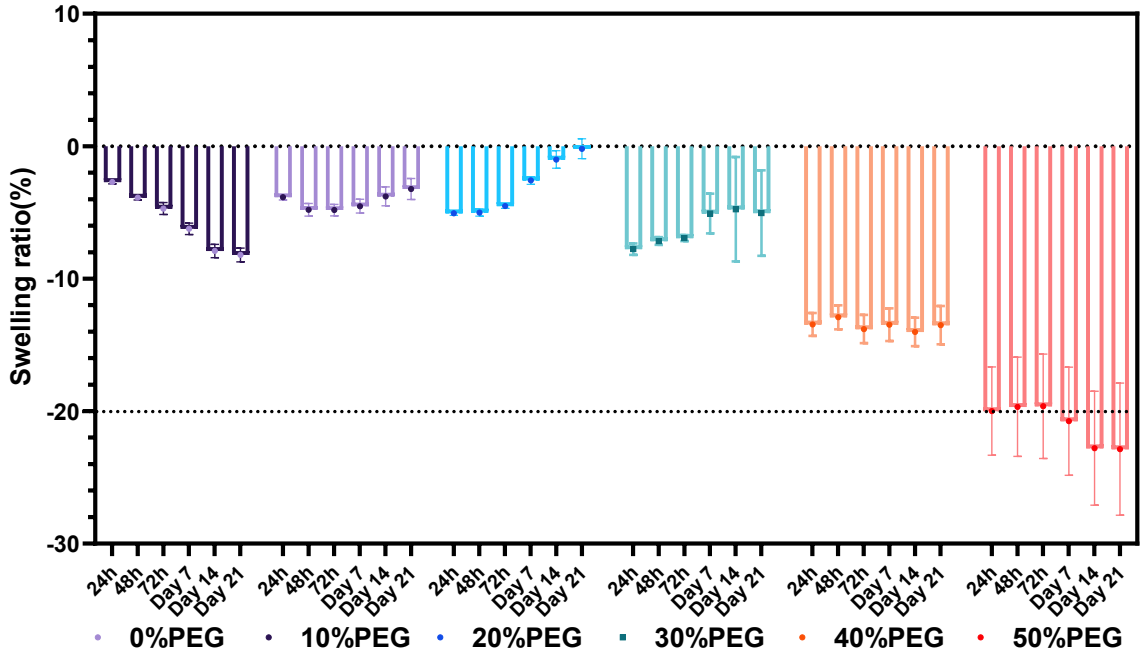

Figure 6.S6.9. Swelling behaviour of VP-POMaC over 21 days in PBS.

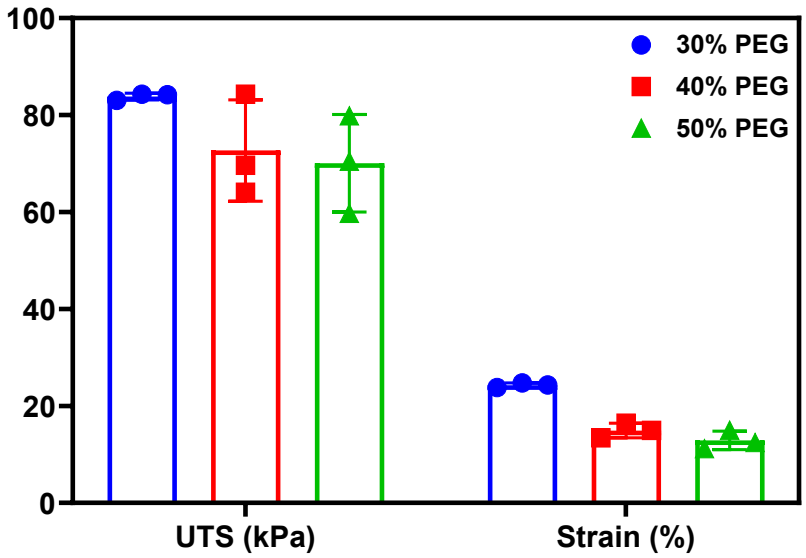

Figure 6.S.6.10. Ulitimate tensile stress (UTS) and maximum strain of VP-POMaC with different concentrations of porogen

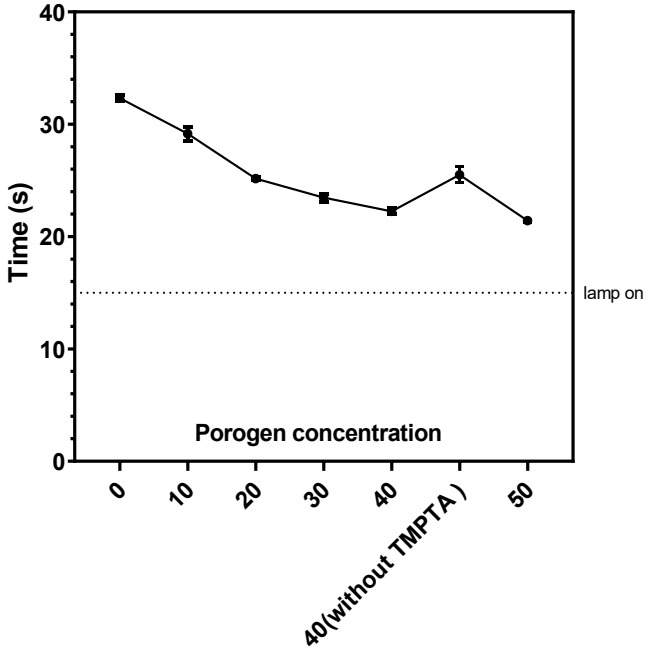

Figure 6.S6.11. Effect of TMPTA on the gelation time

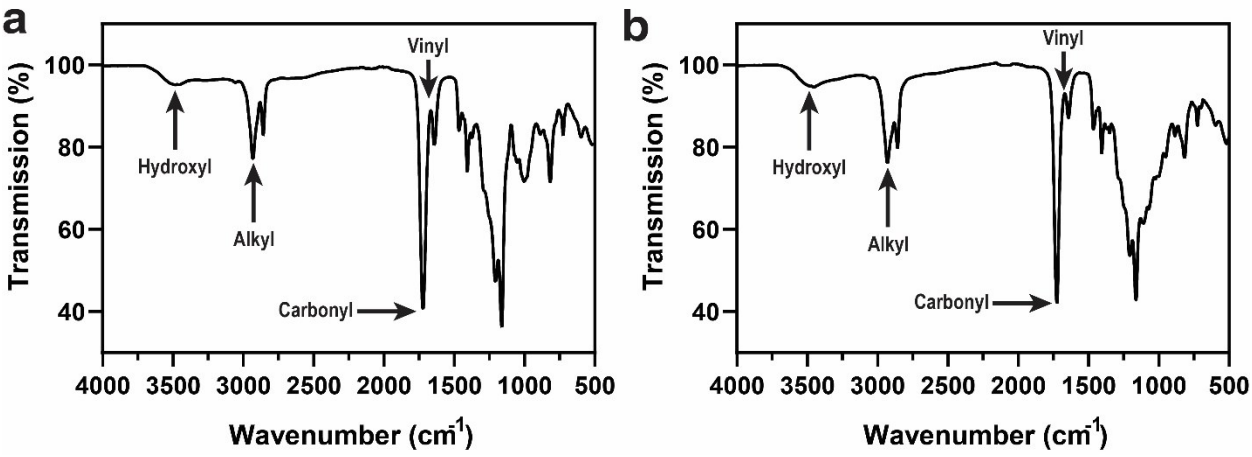

Figure 6.S6.12. FTIR charecterization of POMaC. (a) FTIR spectra of POMaC prepolymer**. (b)** FTIR spectra of VP-POMaC film. FTIR analysis verified the presence of various functional groups in the pre-polymer. FT-IR analysis of crosslinked VP-POMaC films reveals a decrease in the peak positioned at 1647 cm^{-1}, attributed to the vinyl group from maleic anhydride.

Table 6-1. 3D printing parameters of VP-POMaC

Layer thickness (mm)	Base layer exposure time (s)	layer exposure time (s)	Rest time after retract (s)	Lifting distance (mm)	Retract speed (mm/min)
0.020	120	30-50	2	5	80

6.8 References

1. Zhang, B., Korolj, A., Lai, B. F. L. & Radisic, M. Advances in organ-on-a-chip engineering. Nat. Rev. Mater. 1 (2018).

2. Ravanbakhsh, H. et al. Emerging Technologies in Multi‐Material Bioprinting. Adv. Mater. 33, 2104730 (2021).

3. Ma, C., Peng, Y., Li, H. & Chen, W. Organ-on-a-chip: a new paradigm for drug development. Trends Pharmacol. Sci. 42, 119–133 (2021).

4. Nahak, B. K., Mishra, A., Preetam, S. & Tiwari, A. Advances in Organ-on-a-Chip Materials and Devices. ACS Appl. bio Mater. 5, 3576–3607 (2022).

5. Ghosh, U., Ning, S., Wang, Y. & Kong, Y. L. Addressing unmet clinical needs with 3D printing technologies. Adv. Healthc. Mater. 7, 1800417 (2018).

6. Li, T., Chang, J., Zhu, Y. & Wu, C. 3D printing of bioinspired biomaterials for tissue regeneration. Adv. Healthc. Mater. 9, 2000208 (2020).

7. Puza, F. & Lienkamp, K. 3D printing of polymer hydrogels—from basic techniques to programmable actuation. Adv. Funct. Mater. 32, 2205345 (2022).

8. Fuchs, S., Shariati, K. & Ma, M. Specialty tough hydrogels and their biomedical applications. Adv. Healthc. Mater. 9, 1901396 (2020).

9. Zhang, F. & King, M. W. Biodegradable polymers as the pivotal player in the design of tissue engineering scaffolds. Adv. Healthc. Mater. 9, 1901358 (2020).

10. Kirillova, A. et al. Fabrication of biomedical scaffolds using biodegradable polymers. Chem. Rev. 121, 11238–11304 (2021).

11. Zhang, B. et al. Biodegradable scaffold with built-in vasculature for organ-on-a-chip engineering and direct surgical anastomosis. Nat. Mater. 15, 669–678 (2016).

12. Tan, X. et al. Development of Biodegradable Osteopromotive Citrate‐Based Bone Putty. Small 18, 2203003 (2022).

13. Davenport Huyer, L. et al. Tunable Bioelastomers: One‐Pot Synthesis of Unsaturated Polyester Bioelastomer with Controllable Material Curing for Microscale Designs (Adv. Healthcare Mater. 16/2019). Adv. Healthc. Mater. 8, 1970064 (2019).

14. Wang, M., Xu, P. & Lei, B. Engineering multifunctional bioactive citrate-based biomaterials for tissue engineering. Bioact. Mater. 19, 511–537 (2023).

15. Tran, R. T. et al. Synthesis and characterization of a biodegradable elastomer featuring a dual crosslinking mechanism. Soft Matter 6, 2449–2461 (2010).

16. Zhang, B. et al. Microfabrication of AngioChip, a biodegradable polymer scaffold with microfluidic vasculature Microengineered biomimetic systems for organ-on-a. Nat. Protoc. 13, (2018).

17. Paunović, N. et al. Digital light 3D printing of customized bioresorbable airway stents with elastomeric properties. Sci. Adv. 7, eabe9499 (2021).

18. Liu, C. et al. High Throughput Omnidirectional Printing of Tubular Microstructures from Elastomeric Polymers. Adv. Healthc. Mater. 2201346 (2022).

19. Wales, D. J., Keshavarz, M., Howe, C. & Yeatman, E. 3D Printability Assessment of Poly (octamethylene maleate (anhydride) citrate) and Poly (ethylene glycol) Diacrylate Copolymers for Biomedical Applications. ACS Appl. Polym. Mater. 4, 5457–5470 (2022).

20. Lo Giudice, A. et al. Evaluation of the accuracy of orthodontic models prototyped with entry-level LCD-based 3D printers: A study using surface-based superimposition and deviation analysis. Clin. Oral Investig. 26, 303–312 (2022).

21. Katsuyama, Y. et al. A 3D‐Printed, Freestanding Carbon Lattice for Sodium Ion Batteries. Small 18, 2202277 (2022).

22. Gallastegui, A. et al. Fast Visible-Light Photopolymerization in the Presence of Multiwalled Carbon Nanotubes: Toward 3D Printing Conducting Nanocomposites. ACS Macro Lett. 11, 303–309 (2022).

23. Kim, Y. T., Ahmadianyazdi, A. & Folch, A. A 'print–pause–print'protocol for 3D printing microfluidics using multimaterial stereolithography. Nat. Protoc. 1–17 (2023).

24. Schüller‐Ravoo, S., Feijen, J. & Grijpma, D. W. Preparation of flexible and elastic poly (trimethylene carbonate) structures by stereolithography. Macromol. Biosci. 11, 1662‐1671 (2011).

25. Kim, G.-T. et al. Cytotoxicity, Colour Stability and Dimensional Accuracy of 3D Printing Resin with Three Different Photoinitiators. Polymers (Basel). 14, 979 (2022).

26. Zeng, B. et al. Cytotoxic and cytocompatible comparison among seven photoinitiators-triggered polymers in different tissue cells. Toxicol. Vitr. 72, 105103 (2021).

27. Schneider, L. F. J., Cavalcante, L. M., Prahl, S. A., Pfeifer, C. S. & Ferracane, J. L. Curing efficiency of dental resin composites formulated with camphorquinone or trimethylbenzoyl-diphenyl-phosphine oxide. Dent. Mater. 28, 392–397 (2012).

28. Bhattacharjee, N., Parra-Cabrera, C., Kim, Y. T., Kuo, A. P. & Folch, A. Desktop-Stereolithography 3D-Printing of a Poly(dimethylsiloxane)-Based Material with Sylgard-184 Properties. Adv. Mater. 30, 1–7 (2018).

29. Yan, Z. et al. Strengthening waterborne acrylic resin modified with trimethylolpropane triacrylate and compositing with carbon nanotubes for enhanced anticorrosion. Adv. Compos. Hybrid Mater. 5, 2116–2130 (2022).

30. Patel, D. K. et al. Highly stretchable and UV curable elastomers for digital light processing based 3D printing. Adv. Mater. 29, 1606000 (2017).

31. Harri, K. et al. Novel photo-curable polyurethane resin for stereolithography. RSC Adv. 6, 50706–50709 (2016).

32. Peng, S. et al. 3D printing mechanically robust and transparent polyurethane elastomers for stretchable electronic sensors. ACS Appl. Mater. Interfaces 12, 6479–6488 (2020).

33. Ji, Z. et al. 3D printing of photocuring elastomers with excellent mechanical strength and resilience. Macromol. Rapid Commun. 40, 1800873 (2019).

34. Zhao, Y. et al. A Platform for Generation of Chamber-Specific Cardiac Tissues and Disease Modeling. Cell 176, 913-927.e18 (2019).

35. Beauchamp, M. J., Nordin, G. P. & Woolley, A. T. Moving from millifluidic to truly microfluidic sub-100-μm cross-section 3D printed devices. Anal. Bioanal. Chem. 409, 4311–4319 (2017).

36. Parra-Cabrera, C., Achille, C., Kuhn, S. & Ameloot, R. 3D printing in chemical engineering and catalytic technology: structured catalysts, mixers and reactors. Chem. Soc. Rev. 47, 209–230 (2018).

37. Davenport Huyer, L. et al. Highly elastic and moldable polyester biomaterial for cardiac tissue engineering applications. ACS Biomater. Sci. Eng. 2, 780–788 (2016).

38. Tan, K., Cheng, S., Jugé, L. & Bilston, L. E. Characterising skeletal muscle under large strain using eccentric and Fourier Transform-rheology. J. Biomech. 48, 3788–3795 (2015).

39. Ramadan, S., Paul, N. & Naguib, H. E. Standardized static and dynamic evaluation of myocardial tissue properties. Biomed. Mater. 12, 25013 (2017).

40. Jacot, J. G., McCulloch, A. D. & Omens, J. H. Substrate stiffness affects the functional maturation of neonatal rat ventricular myocytes. Biophys. J. 95, 3479–3487 (2008).

41. Hrapko, M., Van Dommelen, J. A. W., Peters, G. W. M. & Wismans, J. The mechanical behaviour of brain tissue: large strain response and constitutive modelling. Biorheology 43, 623–636 (2006).

42. Ayyildiz, M., Cinoglu, S. & Basdogan, C. Effect of normal compression on the shear modulus of soft tissue in rheological measurements. J. Mech. Behav. Biomed. Mater. 49, 235–243 (2015).

43. Zhan, Y., Fu, W., Xing, Y., Ma, X. & Chen, C. Advances in versatile anti-swelling polymer hydrogels. Mater. Sci. Eng. C 127, 112208 (2021).

44. Boutry, C. M., Kaizawa, Y., Schroeder, B. C., Chortos, A. & Legrand, A. A stretchable and biodegradable strain and pressure sensor for orthopaedic application. (2018).

45. Montgomery, M. et al. Method for the Fabrication of Elastomeric Polyester Scaffolds for Tissue Engineering and Minimally Invasive Delivery. ACS Biomater. Sci. Eng. 4, 3691–3703 (2018).

46. Zhang, B. et al. Microfabrication of AngioChip, a biodegradable polymer scaffold with microfluidic vasculature. Nat. Protoc. 13, 1793 (2018).

47. Hayer, A. et al. Engulfed cadherin fingers are polarized junctional structures between collectively migrating endothelial cells. Nat. Cell Biol. 18, 1311–1323 (2016).

Chapter 7

7. Chapter 7: Comprehensive Scholarly Discussion of All the Findings

7.1 Introduction

In this chapter, we will provide an in-depth and comprehensive scholarly discussion of all the findings from our research on utilizing VP 3D printing for various biocompatible formulations and their applications. By formulating suitable polymers, the capabilities of materials such as POMaC and PEGDA and technologies such as capillary microfluidics and organ-on-a-chip can be broadened, as demonstrated in the preceding chapters.

With the advent of low-cost LCD 3D printers, VP 3D printing has become increasingly popular, offering high-throughput capabilities and enabling the fabrication of complex geometries with high resolution. The advantages of VP printing over other 3D printing methods like fused deposition modeling (FDM) and selective laser sintering (SLS) are evident in its versatility, resolution and faster printing speeds[1,2]. The high resolution of VP printers is largely determined by the size of the projected pixels and the layer thickness in the vertical direction. However, factors such as ink viscosity, composition, and curing properties also contribute to the final print resolution and the overall quality of the printed structures. Biocompatible inks for VP 3D printing typically contain one or more monomer materials, a photoinitiator, and a photoabsorber that controls the depth of light penetration. This ensures precise spatial control over the polymerization process, leading to accurate and reproducible structures. Materials functionalized with acrylate, methacrylate, alkyne, and acrylamide groups are compatible with VP 3D printing, including

biomaterials such as hyaluronic acid-methacrylate, gelatin-methacrylate, and PEGDA, among others[3–5]. These materials provide opportunities to create biocompatible and tunable structures that can be tailored to specific applications. Although biocompatible resins, hydrogels, and elastomers have been successfully developed for VP printing, there remains a need for suitable biomaterials that meet specific application requirements, such as mechanical strength, biodegradability, and cell adhesion properties. These warrant continued research and development in this area, both in terms of material science and the optimization of printing process.

In this chapter, we will delve into the themes that emerged from our research, including the challenges we encountered and the solutions we developed to address them. We will discuss the impact of our findings on the broader scientific community and how our work contributes to the growing body of knowledge surrounding VP 3D printing and biocompatible materials. We will also acknowledge the limitations of our study and propose future directions for developing biocompatible formulations. Our findings ultimately demonstrate the potential of VP 3D printing as a valuable tool for fabricating complex and biocompatible structures for tissue engineering, biomicrofluidics, and other biomedical applications. By reflecting on our research in this chapter, we aim to provide a thorough understanding of the current state of the field and inspire further advancements in VP 3D printing technology and biocompatible materials.

7.2 Statement of the problem

PEGDA has emerged as a promising alternative material to PDMS in microfluidic and OoC applications. Several research groups have developed PEGDA-250 formulations capable of 3D printing microfluidic channels as small as 20 μm^2 [6–9]. However, the current formulations have limitations that must be addressed to enable broader applications. One of the key challenges is optimizing the hydrophilicity of PEGDA-250 formulations. While they are transparent,

biocompatible, and impermeable to water, they are typically hydrophobic or only mildly wettable (>65°), which falls outside the optimal hydrophilicity range for microfluidic CCs. To address this issue, post-print surface modification is necessary to obtain hydrophilic surfaces that provide sufficient capillary pressure for self-powered filling and drainage. Although plasma oxidation and silane treatment are common methods for surface modification of CC channels, they require expensive and non-accessible equipment and have low surface coating stability, which limits their applicability in non-technical settings. Thus, there is a need for the development of hydrophilic formulations that can be printed with high resolution using versatile 3D printing techniques, such as VP printing. The formulations should possess the required hydrophilic properties and be stable enough to avoid the need for additional post-processing steps. Such a formulation would enable the use of CCs for point-of-care testing applications, which require low-cost and easily accessible manufacturing tools.

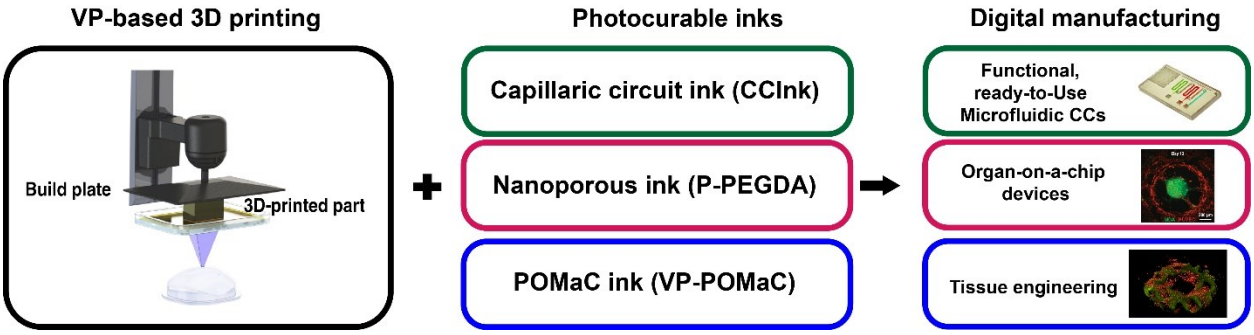

Figure 7.1. A summary of the inks developed in this dissertation. CCInk, P-PEGDA, and VP-POMaC are all compatible with VP 3D printing for the fabrication of CCs, OoC, and TE devices.

Another limitation of PEGDA-250 is that it does not provide sufficient cell attachment, which can hinder the usage of this material for 3D cell culture within the microfluidic channels. To improve cell attachment, additional post-treatment is required. This can involve the use of adhesion promoters or surface modifications to enhance the biocompatibility of PEGDA-250

formulations[10]. However, these processes are time consuming and require special equipment. Additionally, due to its low MW, it has very low gas permeability, which can limit gas exchange between the culture environment and the surrounding air. Thus, the development of a biocompatible PEGDA-based ink with improved cell attachment, high biocompatibility, and nanoporosity is crucial for various biomedical applications, including tissue engineering and drug discovery. Furthermore, PEGDA-250 is a rigid and non-degradable material, which may limit its suitability for some tissue engineering applications that require mechanical properties similar to soft tissues and slow degradation.

Citrate-based elastomers have gained significant attention in the field of biomaterials due to their biocompatibility, degradability, and tunable mechanical properties. One promising citrate-based biomaterial is POMaC elastomer, which is a photo-curable elastomer and has been successfully used as a key component of implantable sensors and TE. Although the current fabrication methods for POMaC involve multiple photolithography steps, 3D printing could provide an alternative solution to these limitations. Although several attempts using extrusion-based 3D printing have been made to 3D print POMaC, it is still a challenge to 3D print complex and intricate structures due to its slow reaction as well as high viscosity (>5000 cP). Therefore, there is a need to develop a POMaC formulation that is suitable for the VP 3D printing of OoC platforms with complex designs, while maintaining the desirable properties of it, such as its biocompatibility, degradability, and tunable mechanical properties. This dissertation focuses on the development of biocompatible formualtions suitable for VP 3D printing of OoC and microfluidic CCs. To address the limitations of current materials, novel inks were developed based on PEGDA-250 and POMaC, both of which demonstrated enhanced properties suitable for various biomedical applications (**Figure 7.1**).

7.3 Summary of proposed solutions, findings, and their limitations

This dissertation first presents the development of a hydrophilic PEGDA-based ink through co-polymerization of the monomer with hydrophilic crosslinkers. While native PEGDA-based CCs are considered hydrophilic, their contact angle of ~65° is too hydrophobic for aqueous solutions to self-fill. Although plasma treatment can increase hydrophilicity, it has been observed that 3D printed PEGDA-250 reverts to low hydrophilicity within 4 hours after plasma treatment. By incorporating hydrophilic crosslinkers, AA and MA, into the PEGDA monomer, the wetting behavior of the material improved significantly. The contact angle could be adjusted based on the percentage of the additive, with a 10% AA CCInk resulting in a contact angle of 35°, which meets the requirements for self-filling and valve-stopping capillary flow.

To evaluate the long-term stability of CCs fabricated using the developed CCInk, we conducted a 16-week stability assessment by measuring the contact angle with water over time on 3D printed chips stored at room temperature. Our results revealed that the contact angle remained stable throughout the duration of the experiment, which confirms that it is feasible to print CCs and store them for later use. This long-term stability is a valuable property for point-of-care devices and other applications that require reliable performance over extended periods. Utilizing 3D printing for embedded capillary valves allows for the regulation of expansion angles on either side of the valves, exceeding the traditional limit of 90 degrees and enabling the production of stronger TVs and SVs. A two-layered CC, consisting of a microfluidic chain reaction (MCR) with a total of nine capillary flow events—five on the top and four on the bottom layers—was fabricated to demonstrate the feasibility of a monolithic CC with embedded conduits. In addition, we explored the possibility of printing conduits with circular cross-sections while taking into account the limited resolution of the 3D printer. To improve circularity and minimize artifacts, we utilized

anti-aliasing and a low layer thickness of 20 µm. Following optimization, we were able to successfully 3D print circular channels with diameters as small as 160 µm.

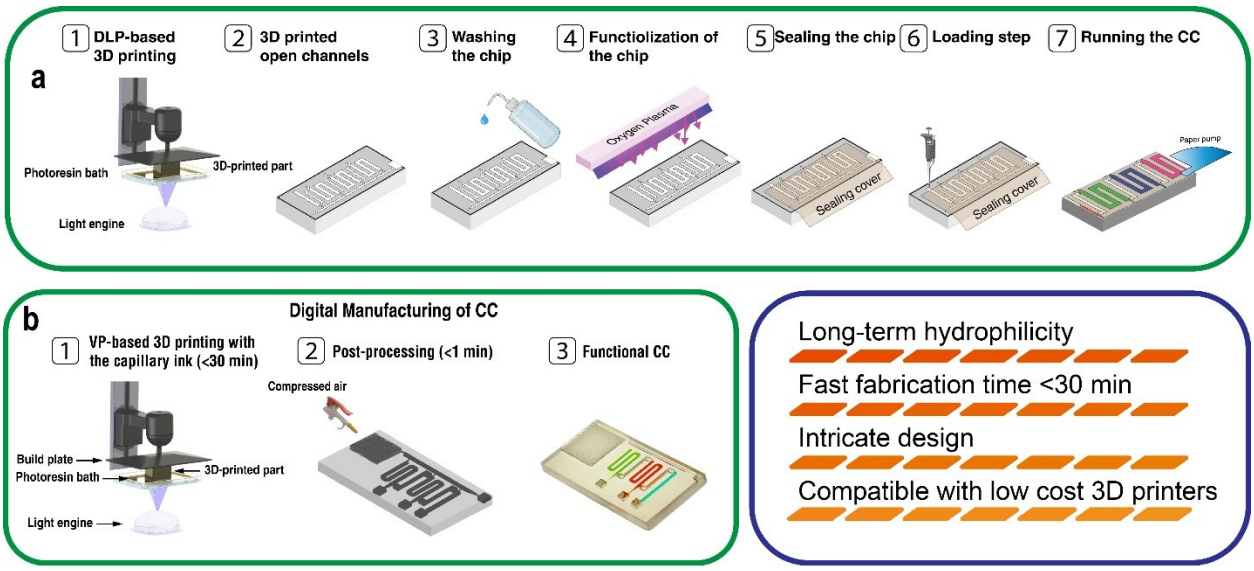

Figure 7.2. Comparison of previous fabrication methods for capillary microfluidic devices and the presented method in this thesis. (a) The conventional method involves multiple steps, including 3D printing of open channels, washing the chip, functionalizing the chip, sealing the chip with hydrophobic tape, and finally running the chip. (b) DM of CCs reduces fabrication time by minimizing post-processing time. Additionally, this approach allows for the fabrication of more intricate designs with long-term hydrophilicity.

In order to demonstrate the power and compatibility of our 3D printing technique, a proof-of-concept ELISA was developed to detect SARS-CoV2 antibodies by using a 3D printed interwoven circuit architecture. Additionally, external paper capillary pumps were replaced with an integrated 3D printed gyroid structure, realizing fully functional, monolithic CCs. We adopted a gyroid based on TPMS as the capillary pump.

The use of DM has the potential to lower the barriers associated with developing complex microfluidic chips, making them more accessible for distributed manufacturing. Compared to the previous fabrication method for CCs, which involved 3D printing open channels, followed by

temporary functionalization of the chip using a plasma machine, and then sealing the chip using a hydrophobic layer, the DM of CCs can significantly reduce the fabrication time and increase functionality by providing long-term hydrophilicity, the ability to have embedded 3D designs, and compatibility with low-cost 3D printers (**Figure 7.2**). This approach is especially beneficial for individuals with limited skills in microfluidics or manufacturing, as they can easily download a design and 3D print it at a low cost due to the affordable CCInk. This method significantly reduces the fabrication and design iteration time from a few hours to less than an hour. Its long-term hydrophilicity also makes it suitable and accessible for point-of-care devices where expensive equipment, such as plasma machines, is not available. As a result, various labs can utilize CC as a useful tool. However, improvements can be made. For instance, optimizing CCInk for compatibility with low-cost LCD 3D printers could broaden CC use. One GCP limitation is the weakening of capillary pressure as it drains, which could be addressed by designing a GCP with a gradient size. More robust GCPs could be 3D-printed using higher-resolution printers. Software generating STL files for CCs would make them accessible to users without design expertise. Other areas of improvement include eliminating pipetting steps, implementing automated actuation systems, and the capability to 3D-print hydrophilic and hydrophobic materials simultaneously, enabling the design of more complex capillary elements.

In VP 3D printing processes, inks typically consist of a monomer and a PI, resulting in non-porous structures. In **Chapter 5**, a novel formulation was proposed to address this limitation by incorporating a hydrophilic PEGDA monomer and a PEG-based porogen solvent. This approach enables the fabrication of high-resolution microstructures with nanoporosity, making the material suitable for OOC devices. The method offers advantages over previously reported techniques relying on supercritical drying, such as being faster, simpler, and more cost-effective.

The formulation employed PEG-200 as a porogen, which is essential for generating porous structures. PEG-200 was selected due to its capacity to dissolve in hydrophilic monomers and readily diffuse out of the cured structure, leaving behind pores. The printability of the ink was assessed by 3D printing complex objects, including gyroid structures and a stack of channels separated by a thin 27 μm membrane. Incorporating a porogen into PEGDA, which is inherently hydrophilic before crosslinking, and subsequently removing it through washing after polymerization, yielded a more hydrophilic material with a reduced contact angle. Lower porogen concentrations resulted in a narrow pore size distribution, while higher concentrations produced a broader distribution. Moreover, the average pore size increased from 5 nm to 30 nm when comparing a 30% porogen concentration to nonporous samples.

Experimental results demonstrated that a 24-hour washing period achieves 80% cell viability for all tested cell lines, meeting the minimum requirements of ISO 10993-12 and ISO 10993-5:2009 standards. In comparison to nonporous wells, cell coverage for HUVEC increased fourfold in porous wells, with even higher coverage observed for IMR, indicating enhanced cell attachment. HUVEC cell attachment to the scaffolds was similar to the cell culture plate control, suggesting that scaffolds with nanoporosity hold significant potential for 3D cell culture in OOC applications. To showcase the capabilities of the developed porous ink, an OOC platform was designed using a formulation containing 10% porogen. This composition offered improved attachment and transparency, making it suitable for OoC applications requiring both properties. A gyroid scaffold was utilized for culturing endothelial cells, providing a highly porous and interconnected structure that mimics the in vivo extracellular matrix. Proteomics analysis revealed increased extracellular matrix degradation, evidenced by the elevated secretion of MMPs by cancer cells. This study

confirms the potential of the developed P-PEGDA ink as a biomaterial for high-resolution VP 3D printing of OoC devices.

Despite the ink's promising performance in OoC and 3D culture applications, there is room for further improvement. The use of porogens with different MWs could modulate material porosity, expanding the range of nanopore sizes in 3D printed constructs. Investigating the impact of porogen composition on the mechanical properties of 3D printed components may provide valuable insights. The integration of an active pumping system or a gravity-driven pump into the OoC platform could facilitate dynamic fluid flow around cells. Future research might also explore oxygen permeability in 3D printed parts with varying porogen concentrations. Employing FITC-dextran with different MWs would enable a more in-depth evaluation of the material's porosity. Additionally, examining cell culture within embedded channels of 3D printed parts using both porous and non-porous inks could elucidate the influence of porosity on hypoxia.

In **Chapter 6**, we addressed the challenges impeding the VP 3D printing of POMaC and overcame them by formulating a POMaC ink containing cross-linkers, PAs, and porogens. We developed a POMaC-based ink that is biodegradable and elastic (<1000 kPa), making it suitable for TE applications. By adding 1% (w/w) of TMPTA (912 MW), we enhanced the free-radical-based polymerization of VP POMaC ink, reducing the gelation time by 4 seconds. Our approach employs ultra-low-cost LCD 3D printers (<$300) to fabricate elastic objects with nanoporosity and intricate geometries, such as gyroids with features as small as 80 μm, which are difficult to produce using molding or other extrusion-based 3D printing methods previously reported for POMaC.

We found that modulating the porogen concentration effectively adjusted the mechanical properties of 3D-printed parts, making this approach useful for applications requiring specific mechanical characteristics. The addition of 1% TMPTA considerably reduced the gelation time

from 11 s to 7 s, demonstrating the significant impact of low concentrations of the TMPTA crosslinker on reaction kinetics. Our biocompatibility tests revealed that HUVECs and IMR-90 co-cultured with VP-POMaC or the benchmark POMaC formulation were morphologically indistinguishable from the cell-only control condition, and both VP-POMaC and the benchmark POMaC formulation exhibited excellent cell viability (>80% for all time points). To demonstrate biocompatibility, we cultured endothelial cells on the 3D-printed cylindrical lattice gyroid scaffold and confirmed biodegradability in vitro. The POMaC ink enables assembly-free digital manufacturing of this material, and with the use of low-cost 3D printers, it could greatly facilitate the rapid prototyping of devices for OoC and TE applications.

The 3D printing of POMaC showed the potential to significantly reduce the fabrication time of POMaC scaffolds from days to hours, providing a faster design iteration time. In addition to the faster fabrication time, using this approach allows for the printing of more complex structures that were previously impossible to create. The traditional fabrication method for POMaC required a clean room facility and expensive masks, as well as requiring multiple manual steps. In contrast, the DM process for POMaC 3D printing is largely automated, eliminating the need for expensive equipment and manual labor (**Figure 7.3**). Although the VP-POMaC ink has substantially streamlined and automated the 3D printing process of this material for TE and OoC devices, there remains room for further advancements. The degradation rate of POMaC can be modulated by incorporating non-degradable crosslinkers, thereby allowing for adjustments in degradability based on specific applications. Moreover, this study examined porogen concentrations up to 50%; the effects of employing higher porogen concentrations on printability and mechanical properties warrant additional investigation. It would also be valuable to elucidate why 3D printed parts with elevated porogen concentrations exhibit increased rigidity.

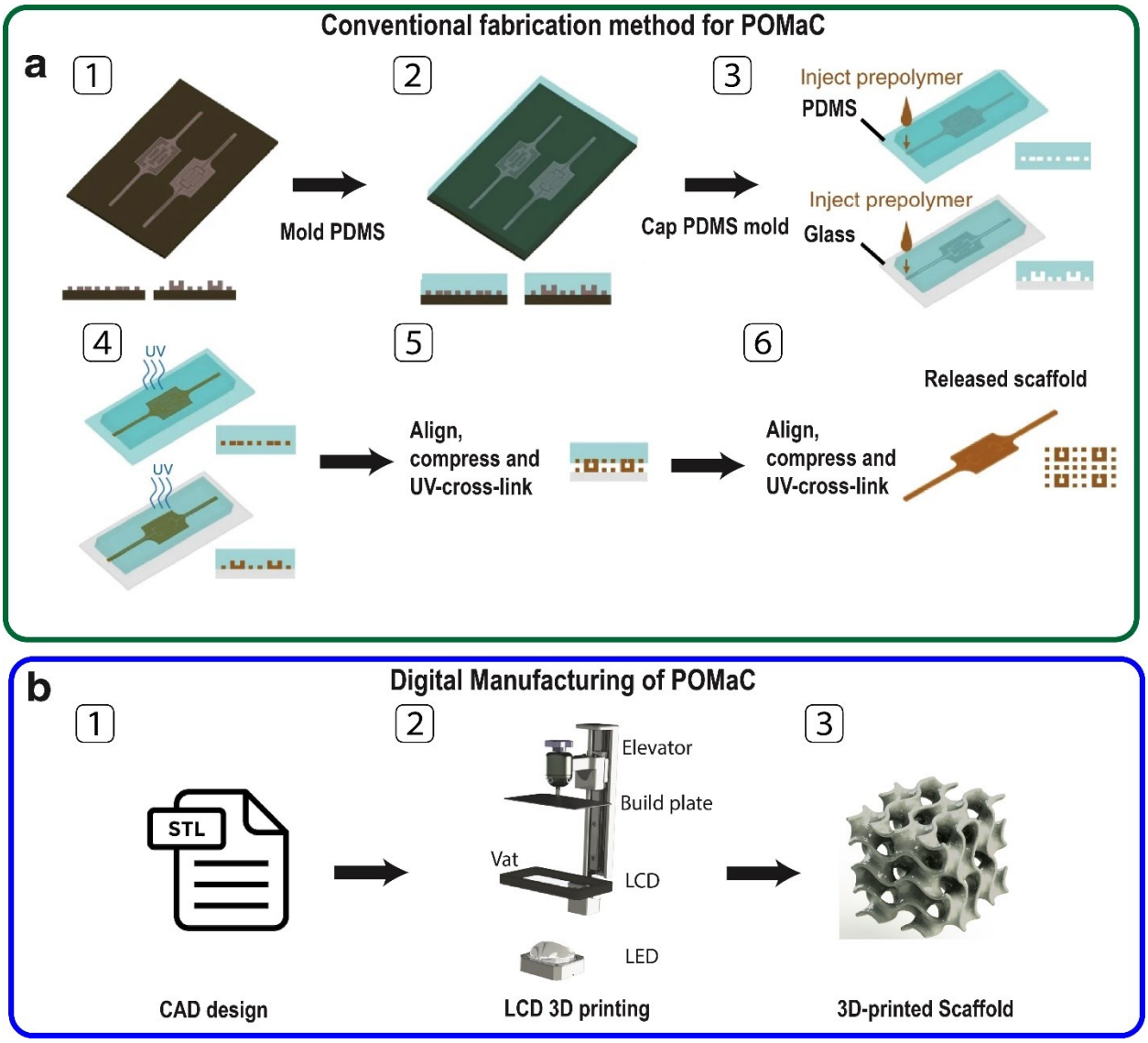

Figure 7.3. Conventional fabrication method for POMaC vs. VP-3D printing of POMaC. (a) The conventional approach involves multiple manual alignment and stamping steps. (b) With VP-3D printing of POMaC, models can be fabricated directly using a CAD file and a 3D printer, eliminating the need for expensive instruments.

Although the utilization of LCD 3D printers renders the technology more accessible to research laboratories, these printers are constrained by 405 nm LEDs. Given the ink's higher absorption at 385 nm, an enhanced resolution may be attainable through the use of advanced projectors with 385 nm light sources and smaller pixel sizes. This would facilitate the 3D printing of higher-resolution

features and the fabrication of embedded channels. Furthermore, implementing a heated vat could enable printing at elevated temperatures, where the ink exhibits reduced viscosity, potentially leading to improved resolution. Additionally, the application of porogens with higher molecular weights might result in increased pore size. By addressing these improvements in future studies, the applications of the VP-POMaC ink can be expanded.

7.4 Discussion and conclusion

In conclusion, this thesis presented three photocurable polymers for VP 3D printing, specifically tailored for tissue engineering, microfluidics, and OoC applications. The first project introduced the development of the hydrophilic CCInk for DM of CCs, which demonstrated the ability to produce complex structures with high precision while maintaining hydrophilicity. The CCInk have the potential to spur further development in various applications, such as point-of-care testing, microfluidics, and TE. This is largely due to the biocompatible nature of PEGDA, which makes it an ideal material for these types of applications.

The second approach focused on the formulation of a novel porous ink for VP 3D printing, which enabled the creation of high-resolution microstructures with nanoporosity. This ink exhibited promising results in terms of biocompatibility and potential use in OoC devices. The third approach overcame the challenges of VP 3D printing of POMaC by formulating a ink containing cross-linkers, PA, and porogens. This enabled the fabrication of elastic objects with nanoporosity and intricate geometries using low-cost LCD 3D printers.

One of the key advantages of the VP 3D printing, is the combination of affordability, versatility, scalability, functionality, and accessibility (**Figure 7.4**). By utilizing low-cost LCD 3D printers, the technology becomes more accessible to research laboratories with limited budgets, allowing for rapid prototyping and production of devices for TE, microfluidics, and OoC

applications. Additionally, the versatility of the developed inks enables the creation of complex structures with varying mechanical properties and porosities, catering to a wide range of applications. Scalability is another important aspect of the VP 3D printing approach, as the process can be easily adapted for large-scale production or scaled down for more intricate, high-resolution structures depending on the print process. The functionality of the developed biomaterials has been demonstrated through their biocompatibility, tunable hydrophilicity, and potential use in various biological models and devices. Furthermore, the accessibility of the materials and VP 3D printing ensures that researchers from various backgrounds can adopt and adapt these methods for their specific needs.

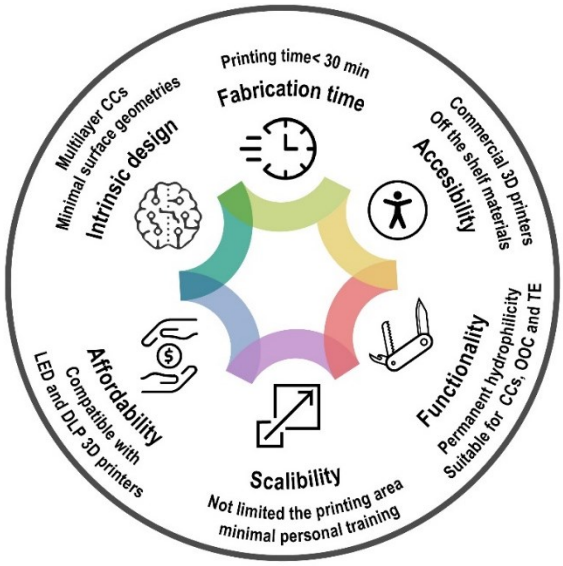

Figure 7.4. Summary of the broader impact of the current work. Key advantages of VP 3D printing include a combination of affordability, versatility, scalability, functionality, and accessibility.

Despite the success of these approaches, several opportunities for improvement and future research were identified. For the CCInk, examining different cross-linking strategies, and evaluating the long-term stability of the printed structures could lead to further advancements. In the case of the porous ink, investigating the effects of porogens with different MWs, and exploring

compatibility of the ink with LCD 3D printers are potential avenues for further development. For the VP-POMaC ink, modulating the degradation rate, examining higher porogen concentrations, and employing advanced projectors with 385 nm light sources and smaller pixel sizes could lead to enhanced performance and broader applications.

By addressing the identified limitations and building upon the achievements presented in this chapter, this work has the potential to pave the way for the development of more functional microfluidic and OoC devices. Future work includes designing inks with a tunable porosity from nano to micro range and combining inks with a multi-material 3D printing approach, to create more functional heterogeneous objects. Overall, the novel biomaterials and VP 3D printing method hold significant promise for the advancement of TE, microfluidics, and OoC research, enabling the creation of increasingly complex biological models and devices.

7.5 References

1. Ali, M. A., Hu, C., Yttri, E. A. & Panat, R. Recent advances in 3D printing of biomedical sensing devices. *Adv. Funct. Mater.* **32**, 2107671 (2022).
2. Ravanbakhsh, H. *et al.* Emerging Technologies in Multi-Material Bioprinting. *Adv. Mater.* **33**, 2104730 (2021).
3. Soman, P., Chung, P. H., Zhang, A. P. & Chen, S. Digital microfabrication of user-defined 3D microstructures in cell-laden hydrogels. *Biotechnol. Bioeng.* **110**, 3038–3047 (2013).
4. Hribar, K. C., Soman, P., Warner, J., Chung, P. & Chen, S. Light-assisted direct-write of 3D functional biomaterials. *Lab Chip* **14**, 268–275 (2014).
5. Billiet, T., Vandenhaute, M., Schelfhout, J., Van Vlierberghe, S. & Dubruel, P. A review of trends and limitations in hydrogel-rapid prototyping for tissue engineering. *Biomaterials* **33**, 6020–6041 (2012).
6. Naderi, A., Bhattacharjee, N. & Folch, A. Digital Manufacturing for Microfluidics. (2019) doi:10.1146/annurev-bioeng-092618.
7. Kuo, A. P. *et al.* High-Precision Stereolithography of Biomicrofluidic Devices. *Adv. Mater. Technol.* **4**, 1–11 (2019).
8. Beauchamp, M. J., Gong, H., Woolley, A. T. & Nordin, G. P. 3D printed microfluidic features using dose control in X, Y, and Z dimensions. *Micromachines* **9**, (2018).
9. Gong, H., Bickham, B. P., Woolley, A. T. & Nordin, G. P. Custom 3D printer and resin for 18 μm × 20 μm microfluidic flow channels. *Lab Chip* **17**, 2899–2909 (2017).
10. Warr, C. *et al.* Biocompatible PEGDA Resin for 3D Printing. (2020) doi:10.1021/acsabm.0c00055.

Chapter 8

8. Chapter 8: Conclusions and Outlook

8.1 Summary of scientific contributions

In this dissertation, we developed biocompatible formulations suitable for VP 3D printing of OOC and microfluidic CCs. To address the limitations of current materials, novel inks based on low-MW PEGDA and POMaC were designed, both of which demonstrated enhanced properties appropriate for various biomedical applications. Before this work, DM of CCs and POMaC scaffolds was not achievable due to the reliance on manual and non-automated processes. In this thesis, we introduced DM for monolithic, fully functional, and intrinsically hydrophilic microfluidic CCs. By employing light engine additive manufacturing, CCs were 3D printed using a PEGDA ink co-polymerized with AA crosslinker optimized for printability and hydrophilicity. This 3D printing approach supports advances in capillary valve design, embedded conduits with circular cross-sections that prevent bubble trapping, and interwoven circuit architectures used for immunoassays. Moreover, external paper capillary pumps were replaced with an integrated 3D printed gyroid structure, realizing fully functional, monolithic CCs. As a result, a computer-aided design file of a CC can be transformed into a CC by light engine 3D printing within a few minutes, paving the way for low-cost, distributed DM of fully functional, ready-to-use microfluidic systems.

Furthermore, we developed a novel biocompatible PEGDA ink with nanoporosity by utilizing a non-reactive porogen. We thoroughly assessed the material's cytotoxicity on various cell lines and characterized the impact of the porogen on cell attachment. We then demonstrated the application of porous P-PEGDA ink in developing an OoC platform for long term 3D culture.

Our findings suggest that the developed P-PEGDA is a promising biomaterial for high-resolution VP 3D printing of OOC devices.

Lastly, we introduced a method that significantly simplifies and automates the fabrication of a citrate-based biopolymer, POMaC, with high resolution using a 3D LCD printer. With an affordable desktop 3D printer (less than $300), we demonstrated the capability to create optically transparent submillimeter structures and complex structures such as gyroids. The optimized exposure time of 50 s per 20 μm layer constitutes a major improvement over the 4 min crosslinking time (per layer) required in previously reported manual stamping processes which also entailed labor-intensive manual alignment and multiple masks for each scaffold, ultimately extending the total scaffold fabrication time to a day. Employing this approach, we 3D cultured endothelial cells on a 3D printed gyroid scaffold. The POMaC ink enables assembly-free, automated digital manufacturing of this biodegradable material, which is expected to facilitate the prototyping of devices for organ-on-chip platforms, soft robotics, flexible electronics, and sensors, among other applications. The work presented in this thesis has contributed to the development of novel 3D printable photocurable inks for TE, OoC, and microfluidic applications. As a result of the developed inks and DM, for the first time, complex designs for POMaC scaffolds and monolithic CCs were 3D printed using commercial and low-cost VP 3D printers in less than 1 hour.

8.2 Recommendations for future directions

Utilizing the VP 3D printing method, this research has achieved enhanced functionality and tunability in biocompatible inks, paving the way for the development of more functional microfluidic and OoC devices. Nevertheless, further studies could improve upon the presented work in several ways and expand the use of DM for TE and microfluidics applications.

8.2.1 Development of open-source inks for low-cost LCD 3D printers

In **Chapter 4**, we demonstrated that complex designs can be 3D printed with a DLP-based 3D printer. Our preliminary result shows that the same designs can be printed using an LCD 3D printer by scaling up the design by 60%. However, 3D printing smaller embedded channels is not achievable using the current CCInk. Future work in the development of CCInk for low-cost LCD 3D printers should focus on several key areas to improve the performance and accessibility of the technology for capillary microfluidics. Further optimization of the CCInk formulation could enable the use of lower-cost LCD 3D printers while maintaining or improving print quality and functionality, possibly by investigating alternative PAs or other additives to enhance print resolution. For instance, we used ITX PA in the CCInk, which is highly efficient at 385 nm but has lower absorption at 405 nm, leading to an increase in the penetration depth of light and a loss of Z resolution. A screening of different PAs that are more effective at the 405 nm wavelength of LCD 3D printers can be conducted. One issue with these PAs is that they usually reduce the transparency of 3D printed parts, affecting their imaging and functionality. Using dyes that can provide sufficient absorption during printing and can be leached out afterward would be highly beneficial. Recent studies have shown that suitable dyes, such as Tartazine[1], Ponceau 4R[2], and Orasol orange dye[3], have high absorption at 405 nm and can improve the resolution in VP 3D printing[4]. In addition, the advent of LCD 3D printers with an emission wavelength of 385 nm could solve this problem in the future. Another challenge is the lower intensity of LCD 3D printers compared to DLP 3D printers, which leads to longer exposure times and slower reaction kinetics. This can be addressed by using crosslinkers with multiple acrylate groups to increase molarity of double bonds[5,6].

It's important to note the differences in power output of LCD 3D printers when compared to DLP printers. The power of LCD 3D printers typically reaches up to 3.5 mW/cm^2, while DLP printers can emit light intensities up to 100 mW/cm^2. This significant difference in power can impact the printing speed and resolution, with DLP printers generally allowing for faster crosslinking times due to their higher power output.

However, as demonstrated in Chapter 6, even with the lower power intensity of LCD 3D printers, the efficiency of the printing process can be significantly enhanced by adjusting the formulation of the photopolymer resin. In particular, the introduction of crosslinkers such as Pentaerythritol triacrylate (PETA) and trimethylolpropane triacrylate (TMPTA) into the resin formulation can boost the reaction kinetics, leading to a reduction in crosslinking time. The inclusion of these crosslinkers enables the attainment of rapid crosslinking even at the relatively low light intensity provided by the LCD 3D printer. This compensates for its lower power output, making it possible to achieve high-resolution printing using an LCD printer.

Additionally, exploring new material combinations or modifications to the current CCInk formulation could result in improved biocompatibility, which would broaden the range of applications for CCInk in TE and microfluidic devices. For instance, utilizing biocompatible ink, CCs could be designed to facilitate automated cell staining for streamlined cell analysis workflows with minimized manual handling, or engineered for targeted growth factor delivery in OoC platforms, promoting improved biomimetic conditions. Currently, AA affects biocompatibility and cell adhesion, limiting its application for TE and OoC. In **Chapter 5**, we showed that the contact angle can also be modulated by the incorporation of PEG porogens. Further investigation can be done on the P-PEGDA ink for its use in CCs. The advantage of P-PEGDA ink is its enhanced biocompatibility and cell adhesion compared to CCInk.

Research into scaling up the production of CCs would be necessary to facilitate larger-scale manufacturing and development, potentially for point-of-care applications, by possibly improving post-processing techniques or using LCD 3D printers with 8K resolution. Encouraging open-source development of formulations and 3D printing parameters, as well as developing inks with off-the-shelf components, could accelerate the adoption of the technology and foster collaboration within the microfluidics research community, helping to refine and expand the applications of CCInk. By addressing these potential avenues for future work, the development of CCInk for low-cost LCD 3D printers could have a significant impact on the accessibility, affordability, and functionality of advanced microfluidic and TE devices.

8.2.2 Making CCs more user-friendly

To make CCs more user-friendly and suitable for point-of-care applications, future work should focus on several key areas. First, minimizing the number of pipetting steps is crucial. This can be achieved by delivering antibodies in the channels and drying them on the chip for later reconstitution by sample addition. Including mixers along the flow path of the CC would enable rapid, uniform, and efficient reagent reconstitution, ensuring even distribution and delivery of reagents.

Additionally, designing CCs with pre-dried reagents that only require the addition of the sample, which could also serve as a wash buffer, would simplify the assay process. Recent studies have shown the uniform reconstitution of dried reagents in CCs[7,8]. For assays that require additional liquid delivery steps, integrating blisters filled with liquid onto the CC could provide a convenient solution. Using 3D printing, features that are compatible with commercial blisters can be added to CCs. Lancing structures within the CC could be used to pierce the blisters and dispense liquids as needed.

Second, integrating on-chip aliquoting/overflow structures for accurate sample volume metering would make device operation more user-friendly. This has been done previously for CCs 3D printed with open channels, but it has not been implemented for closed-channel designs[9]. By leveraging 3D printing, gyroid capillary pumps can be used for draining excess liquid. Furthermore, incorporating user-friendly features such as visual indicators, intuitive instructions, or easy-to-handle designs would enhance the overall usability of the CC, particularly for non-expert users. By addressing these potential avenues for future work, making CCs more user-friendly would have a significant impact on the accessibility, affordability, and functionality of advanced microfluidic and point-of-care devices.

8.2.3 Improved functionality of CCs

Future work in improving the functionality of CCs should focus on several key areas, utilizing advanced 3D printing techniques and materials to enhance the capabilities of capillary microfluidic devices. First, integrating gyroid capillary pumps with a gradient size could provide constant negative pressure, ensuring precise control over fluid flow and enabling more complex assays. Other TPMS structures, such as Schwarz-P and Neovius, can also be tested as potential capillary pumps[10,11].

Second, the use of multi-material 3D printing could enable the fabrication of CCs with hydrophilic and hydrophobic areas, providing greater control over fluid movement and enabling the manipulation of specific fluidics within the device. This could lead to more advanced and highly customizable CCs, tailored to specific applications and requirements, and facilitate the development of new components. Hydrophobic ink, such as hexanediol diacrylate/lauryl acrylate (HDDA/LA) resin[12], forms a solid polymer that is sufficiently hydrophobic, can be used. Ameloot group recently demonstrated the development of CCs with distinct hydrophilic and hydrophobic

areas using multi-material 3D printing, creating functional stop valves[13]. However, their 3D printing method is based on binder jetting, which is costly, and the material development requires special equipment. In addition to traditional multi-material VP 3D printing methods based on vat exchange, a newer approach called the two-wavelength strategy can be used[14,15]. This technique involves using two different wavelengths of light to initiate and control polymerization, enabling the simultaneous printing of materials with distinct properties. By having hydrophilic and hydrophobic monomers, local hydrophilicity can be achieved using this approach. Furthermore, by utilizing this approach, it would be possible to create CCs with highly integrated and diverse features, such as the incorporation of responsive or stimuli-sensitive materials for advanced control and sensing capabilities.

Another avenue for future work could involve the integration of sensing elements within the CCs, such as electrochemical or optical sensors. This would enable real-time monitoring and analysis of assays, potentially providing faster results and enhancing the overall functionality of the device. Integrating such sensors could also pave the way for the development of smart, self-contained point-of-care CCs that can perform complex assays autonomously and provide immediate feedback to the user.

8.2.4 Development of software to automatically generate STL files

Future work should also focus on the development of specialized software that can automatically generate STL files for CCs and OoC, streamlining the design and fabrication process for microfluidic devices. Currently, designing complex microfluidic systems requires significant manual effort and expertise in CAD software. Automating this process would not only save time and resources, but also enable researchers and practitioners with limited experience in 3D design to create customized CCs for their specific needs.

One potential approach to this challenge is to develop a software platform that can take user-defined parameters, such as the desired geometry, dimensions, volume, and features of the model, and automatically generate the corresponding STL file. This could involve the implementation of parametric design principles and algorithms that can rapidly generate optimized and customizable designs based on user input. Such a platform could integrate pre-defined microfluidic elements (e.g., mixers, valves, and pumps) that can be easily incorporated into the final design, further simplifying the design process for users. Furthermore, incorporating machine learning algorithms within the software could enable the automated optimization of CC designs based on user-defined performance criteria. Machine learning and deep learning have recently been employed in 3D printing to optimize the printing process and predict mechanical properties and cell viability[16–20]. This would allow the software to learn from previous designs and simulations, iteratively refining the design parameters to achieve optimal performance.

Another potential approach to achieving this goal is to leverage existing parametric design software, such as nTopology, Surface Evolver which generate models based on user-defined inputs. nTopology has been used in multiple recent studies to generate complex designs that are hard to achieve using traditional CAD software[21–23]. By incorporating specific design rules and constraints related to CCs, the software could be customized to generate STL files for capillary microfluidic devices automatically. This would enable users to create custom designs by simply inputting their desired specifications, such as channel dimensions, capillary pump structures, and volume of reagents. Another aspect to consider is the integration of simulation tools within the software platform to enable users to virtually test and optimize the performance of their designs before fabrication. By making the software open-source, researchers can contribute to the development of the platform, sharing their expertise and experience to improve and expand its capabilities.

In summary, the development of specialized software to automatically generate STL files for CCs has the potential to significantly accelerate the design and fabrication of microfluidic devices, making them more accessible and enabling researchers and practitioners to create highly customized CCs tailored to their specific needs.

8.2.5 Improved functionality of OoC platform

Future research on improving the functionality of the organ-on-a-chip (OoC) platform could focus on several aspects. One such avenue for potential improvement is ensuring reproducible and uniform cell seeding within the 3D structures. This can be achieved by optimizing the cell seeding process and refining the microfluidic designs to facilitate consistent and uniform distribution of cells throughout the platform. Furthermore, the incorporation of a recirculating system into the OoC platform would better mimic native physiology by providing a continuous flow of nutrients, oxygen, and growth factors to the cells, thereby simulating the in vivo environment more closely. The use of gravity-driven pumps can be employed to establish a simple and low-cost circulation system, minimizing the need for external equipment and facilitating the long-term maintenance of cell cultures.

In the current platform, we used a regular gyroid structure, which may contribute to less uniform seeding and flow around the middle chamber. However, implementing a circular gyroid structure around the middle chamber could address these issues by providing a more organized scaffold for cell attachment and growth. The circular design would ensure an even distribution of cells and promote a more consistent flow of nutrients around the central chamber, resulting in a more physiologically relevant environment. Reducing the size of the gyroid structures within the OoC platform can also contribute to a more realistic tissue environment. Smaller gyroids offer a higher surface area for cell attachment and allow for more intricate tissue architectures to form. In

the case of VP-POMaC, we demonstrated the successful culturing of HUVEC cells on complex scaffolds. In the future, scaffolds 3D printed with VP-POMaC could be employed for vascularization studies, where multiple cell types can be cultured, and their interactions can be investigated.

8.2.6 Degradation rate modulation of VP-POMaC

Future work should also focus on modulating the degradation rate of VP-POMaC elastomers. Controlling the degradation rate is essential for achieving desired application-specific performance characteristics, such as scaffold lifetimes for TE applications and device performance for wearable devices. The challenge is to achieve this modulation without significantly altering the mechanical properties of the elastomer.

Several approaches can be considered for modulating the degradation rate of VP-POMaC elastomers. First, altering the composition by changing the ratio of different components in the polymer blend, such as incorporating more or fewer hydrolytically degradable polymers or using different polymer types, can influence the degradation rate. Initial studies on POMaC showed that the properties of the polymer can be tuned by changing the molar ratio of compositions at the time of synthesis[24]. Additionally, the degradation rate can be influenced by the crosslinking density of the polymer network, with a higher crosslinking density typically resulting in slower degradation, while lower crosslinking density leads to faster degradation[25]. Furthermore, the degradation rate can be affected by using polymers with varying MWs. Lower molecular weight polymers generally degrade faster than those with higher molecular weights[26]. Another factor that can influence the degradation rate is the porosity of the material. Higher porosity allows for faster penetration of water, enzymes, or other degradation agents, resulting in a faster degradation rate.

By systematically investigating these approaches, researchers can develop a comprehensive understanding of the interplay between the degradation rate, mechanical properties, and other factors, such as porosity, crosslinking density, and polymer composition for VP-POMaC. This will enable the development of VP-POMaC elastomers with tailored degradation rates suitable for various TE and OoC applications.

8.2.7 Higher resolution 3D printing of POMaC

In Future work should focus on enhancing the resolution of 3D-printed POMaC structures, particularly for applications in microfluidics where the fabrication of small channels remains a challenge. Based on the findings in **Chapter 6**, several strategies can be explored to improve resolution in POMaC 3D printing.

One approach involves employing a 3D printer with an emission wavelength closer to the absorbance peak of VP-POMaC (385 nm). The photoinitiator has a high absorbance at this wavelength, leading to reduced exposure times and diminished diffusion of free radicals, which can adversely impact resolution. Additionally, the ITX photoabsorber is more effective at 385 nm, resulting in less light penetration through the material. Another strategy to enhance resolution is to utilize digital light processing (DLP)-based 3D printers with a smaller projected pixel size, which can offer several advantages over LCD-based systems. DLP printers are known for their uniform illumination and smaller pixel sizes, which can further augment resolution. By employing DLP printers with a 385 nm emission wavelength, the resolution of POMaC structures can be improved.

In addition to printer technology, material selection and optimization play a crucial role in achieving higher resolution. The Radisic group has developed novel citrate-based materials, such

as PICO, which possess lower viscosities than POMaC[27,28]. These materials could potentially replace POMaC in future applications, provided that they undergo further optimization to ensure compatibility with high-resolution 3D printing processes. Moreover, to facilitate the fabrication of small microfluidic channels, future work can investigate the development of POMaC formulations with lower viscosity. This would make it easier to remove unreacted polymer after printing, ultimately enhancing the achievable resolution. In summary, future work should concentrate on improving the resolution of 3D-printed POMaC structures by investigating alternative printer technologies, and material formulations.

8.2.8 Modulation of Pore Size from Nanometer to Micrometer Range

In **Chapter 5** and **Chapter 6**, we successfully demonstrated 3D printing of microstructures with nanoporosity using both VP-POMaC and P-PEGDA inks. To further optimize these materials for diverse applications, future work should aim to modulate porosity over a broader range, spanning from nanometers to micrometers. This could be achieved by investigating various porogens with different MWs and concentrations and incorporating different crosslinkers, which may also influence pore size.

For example, previous research has shown that micrometer-scale pore sizes can be achieved using polyethylene oxide (PEO) with a molecular weight of 300 kDa[29]. Additionally, a recent study demonstrated that pore sizes between 500 nm and 1 μm can be obtained by utilizing 1-decanol as a porogen[30]. Investigating a wider range of porogens and crosslinkers could significantly enhance the customization of pore sizes in 3D-printed microstructures. Furthermore, future work should focus on expanding the range of achievable pore sizes and optimizing the combinations of porogens, crosslinkers, and printing parameters. By doing so, it would be possible

to fabricate 3D-printed microstructures with tailored porosity suitable for tissue engineering, drug delivery, and OoC.

8.3 Closing remarks

As the start of this PhD project, the fabrication of CCs relied on manual post-printing steps and expensive equipment. Moreover, PEGDA-based inks were not suitable for OoC applications, and the production of POMaC scaffolds was fully manual and extremely time-consuming. The work presented in this dissertation outlines a path toward truly DM of CCs, PEGDA-based OoC devices, and POMaC scaffolds by leveraging VP 3D-printing technology and the developed novel inks. Through the utilization of the VP 3D printing method, this research has successfully enhanced the functionality and tunability of biocompatible inks, setting the stage for the development of more advanced and versatile microfluidic and OoC devices. This progress marks a significant step forward in the field, opening up new possibilities for the rapid and customized fabrication of microfluidic and tissue engineering platform based on POMaC and PEGDA biomaterials.

8.4 References

1. Grigoryan, B. *et al.* Functional intravascular topologies and multivascular networks within biocompatible hydrogels. *Science (80-.).* **464**, 458–464 (2019).

2. van Bochove, B., Hannink, G., Buma, P. & Grijpma, D. W. Preparation of designed poly (trimethylene carbonate) meniscus implants by stereolithography: challenges in stereolithography. *Macromol. Biosci.* **16**, 1853–1863 (2016).

3. Dong, M. *et al.* Digital Light Processing 3D Printing of Tough Supramolecular Hydrogels with Sophisticated Architectures as Impact-Absorption Elements. *Adv. Mater.* **34**, 2204333 (2022).

4. Murphy, C. A., Lim, K. S. & Woodfield, T. B. F. Next Evolution in Organ-Scale Biofabrication: Bioresin Design for Rapid High-Resolution Vat Polymerization. *Adv. Mater.* **34**, 2107759 (2022).

5. Erkoc, P. *et al.* Photocurable pentaerythritol triacrylate/lithium phenyl-2, 4, 6-trimethylbenzoylphosphinate-based ink for extrusion-based 3D printing of magneto-responsive materials. *J. Appl. Polym. Sci.* **137**, 49043 (2020).

6. Ahn, D., Stevens, L. M., Zhou, K. & Page, Z. A. Rapid high-resolution visible light 3D printing. *ACS Cent. Sci.* **6**, 1555–1563 (2020).

7. Gökçe, O., Castonguay, S., Temiz, Y., Gervais, T. & Delamarche, E. Self-coalescing flows in microfluidics for pulse-shaped delivery of reagents. *Nature* **574**, 228–232 (2019).

8. Gervais, T., Temiz, Y., Aubé, L. & Delamarche, E. Large-Scale Dried Reagent Reconstitution and Diffusion Control Using Microfluidic Self-Coalescence Modules. *Small* **18**, 2105939 (2022).

9. Parandakh, A. *et al.* 3D-printed capillaric ELISA-on-a-chip with aliquoting. *Lab Chip* (2023).

10. Chouhan, G. & Bala Murali, G. Designs, advancements, and applications of three-dimensional printed gyroid structures: A review. *Proc. Inst. Mech. Eng. Part E J. Process Mech. Eng.* 09544089231160030 (2023).

11. Sengsri, P., Fu, H. & Kaewunruen, S. Mechanical properties and energy-absorption capability of a 3D-printed TPMS sandwich lattice model for meta-functional composite bridge bearing applications. *J. Compos. Sci.* **6**, 71 (2022).

12. Warr, C. A. *et al.* 3d-printed microfluidic droplet generator with hydrophilic and hydrophobic polymers. *Micromachines* **12**, 91 (2021).

13. Achille, C. *et al.* 3D Printing of Monolithic Capillarity-Driven Microfluidic Devices for Diagnostics. *Adv. Mater.* **33**, 2008712 (2021).

14. Chen, J. *et al.* 3D-Printed anisotropic polymer materials for functional applications. *Adv. Mater.* **34**, 2102877 (2022).

15. Schwartz, J. J. & Boydston, A. J. Multimaterial actinic spatial control 3D and 4D printing. *Nat. Commun.* **10**, 791 (2019).

16. Qin, J. *et al.* Research and application of machine learning for additive manufacturing. *Addit. Manuf.* 102691 (2022).

17. Khan, M. F. *et al.* Real-time defect detection in 3D printing using machine learning. *Mater. Today Proc.* **42**, 521–528 (2021).

18. Alejandrino, J. D. *et al.* A machine learning approach of lattice infill pattern for increasing

material efficiency in additive manufacturing processes. *Int. J. Mech. Eng. Robot. Res.* **9**, 1253–1263 (2020).

19. Xu, H. *et al.* Prediction of cell viability in dynamic optical projection stereolithography-based bioprinting using machine learning. *J. Intell. Manuf.* 1–11 (2022).

20. Khadilkar, A., Wang, J. & Rai, R. Deep learning–based stress prediction for bottom-up SLA 3D printing process. *Int. J. Adv. Manuf. Technol.* **102**, 2555–2569 (2019).

21. Flores-Jiménez, M. S., Garcia-Gonzalez, A. & Fuentes-Aguilar, R. Q. Review on Porous Scaffolds Generation Process: A Tissue Engineering Approach. *ACS Appl. Bio Mater.* (2023).

22. Hsiao, K. *et al.* Single-digit-micrometer-resolution continuous liquid interface production. *Sci. Adv.* **8**, eabq2846 (2022).

23. Doyle, S. E. *et al.* Printing between the lines: Intricate biomaterial structures fabricated via negative embodied sacrificial template 3D (NEST3D) printing. *Adv. Mater. Technol.* **6**, 2100189 (2021).

24. Tran, R. T. *et al.* Synthesis and characterization of a biodegradable elastomer featuring a dual crosslinking mechanism. *Soft Matter* **6**, 2449–2461 (2010).

25. Krongauz, V. V. Crosslink density dependence of polymer degradation kinetics: photocrosslinked acrylates. *Thermochim. Acta* **503**, 70–84 (2010).

26. Bartnikowski, M., Dargaville, T. R., Ivanovski, S. & Hutmacher, D. W. Degradation mechanisms of polycaprolactone in the context of chemistry, geometry and environment. *Prog. Polym. Sci.* **96**, 1–20 (2019).

27. Davenport Huyer, L. *et al.* One-Pot Synthesis of Unsaturated Polyester Bioelastomer with Controllable Material Curing for Microscale Designs. *Adv. Healthc. Mater.* **1900245**, 1900245 (2019).

28. Savoji, H. *et al.* 3D printing of vascular tubes using bioelastomer prepolymers by freeform reversible embedding. *ACS Biomater. Sci. Eng.* **6**, 1333–1343 (2020).

29. Ying, G. L. *et al.* Aqueous Two-Phase Emulsion Bioink-Enabled 3D Bioprinting of Porous Hydrogels. *Adv. Mater.* **30**, 1–9 (2018).

30. Dong, Z. *et al.* 3D printing of inherently nanoporous polymers via polymerization-induced phase separation. *Nat. Commun.* **12**, 1–12 (2021).